

THE DESIGN AND REALISATION OF
ELECTRONICALLY TUNABLE DIELECTRIC RESONATOR
MICROSTRIP FILTERS

BALBIR SINGH VIRDEE B.Sc.(Hons), M.Phil.

A thesis submitted in partial fulfilment of the
requirements of the University of North London
for the degree of Doctor of Philosophy

THIS RESEARCH PROGRAMME WAS CARRIED OUT IN THE
SCHOOL OF ELECTRONIC AND COMMUNICATIONS ENGINEERING
AND APPLIED PHYSICS

JANUARY 1996

To

My Father

For the integrity and leadership he gave each task

My Mother

For providing a stable and organized home

My Wife

For giving me inspiration and encouragement

Acknowledgements

I wish to thank Prof.R.G.Meadows and Dr.A.J.Parsons for their advice, encouragement and supervision throughout the course of this research.

I also wish to thank the technical staff who assisted with practical matters of the work, especially Mr.B.Patel.

Finally, I would like thank my wife, Neelam, for without her patience and support this work would not have been possible.

Abstract

Many of today's sophisticated communication systems, particularly those operating in the microwave frequency range, have a growing demand for highly selective and frequency agile filters with fast tuning rates. At microwave frequencies above 2GHz, filters that combine both tuning speed and high selectivity are difficult to realise. Unloaded Q values in the range of 1000 are required for reasonable selectivity. At present, these requirements with the exception of tuning speed are mainly fulfilled by electronically tuned filters employing yttrium iron garnet (YIG) resonators. An alternative solution to this problem is to utilise high-Q dielectric resonators (DRs) in-conjunction with an appropriate tuning mechanism to realise tunable filters. DRs can provide unloaded Q-factors comparable to waveguide resonators (typically 10,000 @ 10GHz), but at a substantially lower weight and smaller volume. DRs are also compatible with a microstrip environment which eliminates the need for microstrip to waveguide adaptors. This thesis is devoted to the study of the design and realisation of electronically tuned microwave filters employing dielectric resonators.

Knowledge of the values of the coupling coefficient between a pair of DRs is essential for the design of both the bandpass and bandstop filters using these resonators. This necessitates the use of an accurate expression for the coupling coefficient which was derived by performing an electromagnetic

analysis on the DR structure. This analysis also took into account the effects of the actual circuit environment such as the resonator support spacer and the dimensions of the enclosure. The experimental data presented shows very good agreement with the computed data.

Novel techniques for the tuning of the DR operating in its fundamental $TE_{01\delta}$ mode are presented. These tuning configurations incorporating GaAs varactor diodes have been investigated to determine a circuit which greatly perturbs the DR fundamental mode. The amount of tuning that can be obtained by these methods exceeds more than 60MHz of the unperturbed value of resonant frequency with acceptable amount of Q-factor degradation. These tuning characteristics are superior to similar devices reported to date. A simple analytical expression is also derived for determining the tuning range of such a structure.

Techniques for the design of novel electronically tunable DR bandpass and bandstop filters having either a Chebyshev or Butterworth response are presented. Design for prescribed response, starting from a low-pass lumped-element prototype filter is outlined. The bandpass filter structure consists of cascaded resonators, with the end resonators coupled to microstrip arcs on a substrate, whereas, the bandstop filter consists of a microstrip line with resonators mounted at intervals of one-quarter-wavelength. Tuning is achieved by varying a bias voltage to the varactor. The measured performances of several practical devices operating in the

S-band are presented, these agree closely with theory. The centre frequency of these filters is within 2.46% and the bandwidth is within 3.75% of the desired values.

Contents

Chapter 1 Introduction

1.0	Introduction	1
1.1	The Need for Electronically Tunable DR Filters	2
1.2	Scope of this Thesis	3
	References	7

Chapter 2 Dielectric Resonators

2.0	Introduction	9
2.1	Historical Overview	10
2.2	Dielectric Resonator Materials	12
2.3	Theoretical Dielectric Resonator Models	14
	2.3.1 The Cohn Models	15
	2.3.2 Itoh & Rudokas Model	20
	References	25

Chapter 3 Characterisation of DR Coupling in a Microstrip Environment

3.0	Introduction	30
3.1	Coupling Coefficient Between a Microstrip Line and a DR	31
	3.1.1 Experimental Characterisation of Coupling Coefficient Between a DR and a Microstrip Line	35
3.2	Coupling Coefficient Between Two DRs	38
	3.2.1 General Coupling Analysis Between Two DRs	39
	3.2.2 Improved Analysis of Coupling Coefficient Between Two DRs	41
	3.2.3 Evaluation of Theoretical Results	51
3.3	Conclusions	53
	References	54

Chapter 4 Microstrip Topologies for Electronically Tuning

DR TE_{01δ}-mode Resonant Frequency

4.0	Introduction	65
4.1	Tuning Mechanisms	66
4.2	Tuning Mechanism Chosen	69
4.3	Varactor Diodes	70
4.3.1	P-N Junction Diode	70
4.3.2	Types of Varactor Diodes	71
4.4	Figures of Merit	74
4.4.1	Quality Factor	74
4.4.2	Cut-off Frequency	75
4.4.3	Tuning Ratio	77
4.5	Selected Varactor Diode	77
4.6	Novel Tuning Topologies	78
4.7	Input/Output Coupling Structure	79
4.8	Tuning Configurations	82
4.9	Analytical Expression for the Tuning Range	85
4.10	Expression of the Tuning Range as a Function of the Tuning Voltage	89
4.11	Experimental Results of the Varactor Tuning Configurations	92
4.12	Effect of Tuning Loop on the Tuning Configuration	94
4.12.1	Evaluation of Results	95
4.13	The Effects of Large Signal Levels on Tuning Configuration Performance	96
4.14	Conclusions	98
	References	100

Chapter 5 Electronically Tunable DR Bandpass Filters

5.0	Introduction	131
5.1	Important Definitions	133
5.2	Equivalent Structure of a DR Coupled Filter	134
5.3	Proposed Design Method 1	135
5.3.1	Design 1	140
5.4	Proposed Design Method 2	141
5.4.1	Design Procedure	148

5.4.2	Design 2	149
5.4.3	Evaluation of Designs	155
5.5	Tunable DR Filter Designs	157
5.5.1	Evaluation of Designs	157
5.6	Conclusions	159
	References	160

Chapter 6 Electronically Tunable DR Bandstop Filters

6.0	Introduction	190
6.1	Tuning Configuration	192
6.2	DR Bandstop Filter Design	193
6.2.1	Design Specification of Fixed Frequency DR Bandstop Filters	198
6.2.2	Measured Performance of the Bandstop Filters	199
6.3	Tunable DR Bandstop Filter Design	200
6.4	Conclusions	201
	References	202

Chapter 7 General Conclusions and Suggestions for Future Work

7.0	Conclusions	216
7.1	Suggestions for Future Work	223

Publications	225
---------------------	-----

Appendix A	Program DRCOUP for computing the coupling coefficient between a pair of DRs	A1
-------------------	--	----

Chapter 1

Introduction

1.0 Introduction

With the increased use of continuously tunable microwave receivers, there is a large and growing demand for narrow band, frequency agile filters which are tunable over a broad band of frequencies in the microwave frequency range. Moreover, with the move towards ever smaller rugged systems the emphasis has been on compactness, low cost, and reliability.

Figure 1.1 shows a block diagram of the proposed common spare payload for European DBS system [1]. The two output multiplexers can be tuned via telecommand, thus allowing broadcasts in any frequency band allocated for DBS in the various operating countries. The manifold multiplexers incorporate five four-pole elliptic filters which are mechanically tunable with a tuning range of $\pm 40\text{MHz}$ [2]. The use of tunable output multiplexers enables a number of countries to share a spare satellite which could be reconfigured to the specific requirements of any one of the sharing countries. Reconfigurable components, such as tunable filters, ultimately reduces the operational costs of the satellite. The undesirable feature, however, of these mechanically tuned filters are their relatively complex construction and the slow tuning speeds or slew rates.

Obviously, different requirements for microwave system will lead to the development of various types of tunable filters with a performance matched to the system demands. For example, the important prerequisite of filters for use in a power combiner of a cell site base station for mobile radio is a high quality-factor capable of handling power in the range of tens of watts [3]. For airborne and spaceborne systems, such as satellite communications, the most important factors for filters (and other components) are usually a heavy constraint on both size and weight, and strict requirements on the device tuning speed for frequency hopping or for rapidly tuning the receiver front-end filter/preselectors [4].

Most of the requirements mentioned above with the exception of tuning, can already be fulfilled by a resonant ceramic device called a dielectric resonator (DR). This device was discovered in 1939 by Richtmyer [5], however, practical applications for dielectric resonators did not begin to appear until the late 1960's when they were first used as resonating elements in waveguide filters [6,7].

1.1 The Need for Electronically Tunable DR Filters

Most microwave filters implemented with DRs are tuned or adjusted mechanically. This is achieved by perturbing the field distribution surrounding the DR through the movement of metallic or dielectric objects, either manually or electrically, by using a step motor for example [8].

It is obvious that mechanical tuning involves mechanical parts in motion. It is therefore slow, inaccurate and hence not highly reliable. Even if this approach may be satisfactory in some cases, it is certainly not suitable for applications such as frequency hopping where tuning speeds of the order of about 1GHz/ms are needed. Moreover, some skill is needed on the part of the engineer or technician making the adjustment on site, and this can therefore be expensive.

Electronic tuning of DR filters over a wide range while still preserving their characteristics is highly desirable, especially for use in non-accessible systems such as airborne or spaceborne systems, or in areas of high sophistication such as cellular radio systems.

1.2 Scope of this Thesis

The overall objective of this work is to investigate and design fully functional electronically tunable microstrip DR bandpass and bandstop filters. The filter requirements sought are:

1. Continuous tunability,
2. Low response time (less than 0.1GHz/ μ s),
3. Broad tuning bandwidth with minimum degradation in passband or stopband performance,
4. Narrow passband or stopband to achieve relatively fine frequency discrimination,
5. Light weight,

6. Small size,
7. Low cost.

From amongst the numerous techniques available the varactor diode was found to be the most suitable tuning mechanism for low power operation. The use of varactors is mainly dictated by its low power requirements, low loss and high tuning speed (in excess of 1GHz/1 μ s) [1]. Varactors offer also a continuous frequency tuning and potential advantages in size, weight and cost.

A brief summary of the contents is now given.

Chapter 2, reviews the historical background of dielectric technology. Various approximation methods, including magnetic wall and waveguide models for the analysis of dielectric resonators, are reviewed in brief. It is shown that these models, although providing basic tools for understanding of the behaviour of the field in dielectric resonators, do not give accurate results. This is primarily due to the fact that they do not represent the exact structure of dielectric resonators.

Practical dielectric resonator filter design requires data of resonator coupling. Because of the large number of parameters involved, it is not feasible to obtain the quantity of experimental data adequate for all needs. Therefore, it is essential to have a formula for the coupling coefficient that is sufficiently accurate to be practical for design purposes. In Chapter 3, generalised formula for coupling coefficient

between a DR and a microstrip, and also between two DRs is presented. These two kinds of coupling used in the realisation of microstrip DR filters are discussed in Chapters 5 & 6. Analysis is then performed based on the electromagnetic fields in the DR structure and formulas are derived for magnetic dipole moment and stored energy of the DR enabling the computation of coupling coefficient. Finally, measurements of coupling coefficients are made to ascertain the accuracy of the coupling formula.

In Chapter 4, an overview of the different tuning techniques available and their relative advantages are discussed. A tuning mechanism is selected and novel microstrip tuning topologies incorporating the mechanism are investigated to determine a circuit which greatly perturbs the DRs fundamental TE_{016} mode with limited quality factor degradation. Finally, the effects of large r.f. signal on the performance of the tuning configuration selected are examined.

In Chapter 5, the design procedure for direct coupled DR microwave bandpass filters based on "classical" filters such as Butterworth and Chebyshev is described using two methods. Design formulae are derived which relate the filter specifications to the element values of low-pass prototype filters. Computer simulation of the filters is presented enabling their performance to be predicted. Experimental filters were constructed to verify the proposed methods. Finally, this method was employed in the design of novel

tunable filters. The experimental performance of these devices are also presented.

In Chapter 6, the results of the analysis described in the previous chapter on the coupling between a DR and a propagating transmission line are utilised in the design of DR bandstop filters. A formula is derived which expresses the external Q of each DR in a bandstop filter in terms of the element values of the normalised low-pass prototype and the parameters of the frequency transformation. Several fixed and tunable bandstop filters are designed and tested. The tunable filters represent a new development in microwave filters.

References

1. Uher, J. and Hofer, J.R., "Tunable Microwave and Millimeter-Wave Band-Pass Filters," IEEE Trans. on Microwave Theory & Tech., vol.MTT-39, No.4, April 1991, pp643-653.
2. Rosenberg, U., Rosowski, D., Rumber, W., and Wolk, D., "Tunable Manifold Multiplexers - A New Possibility for Satellite Redundancy Philosophy," Proc. MIOP Int. Conf. (West Germany), Feb. 1989.
3. Howson, D.P. and Mahmoud, M.S., "Electronic Tuning of High Q VHF Cavity Resonators," Report No.370, University of Bradford, Postgraduate School of Electrical and Electronic Engineering 1986.
4. Lammers, U.H.W. and Stiglitz, M.R., "Microwave Dielectric Resonator Tuning," Report No. AFCRL-TR-74-0497, Oct.1974, Air Force Cambridge Research Laboratories (LZ), Hanscom AFB, Massachusetts 01733.
5. Richtmyer, R.D., "Dielectric Resonators," J.Appl. Phys., vol.10, June 1939, pp391-398.
6. Harrison, W.H., "A Miniature High-Q Bandpass Filter Employing Dielectric Resonators," IEEE Trans. on Microwave Theory & Tech., vol.MTT-16, No.4., April 1968, pp210-218.
7. Cohn, S.B., "Microwave Bandpass Filters Containing High-Q Dielectric Resonators," IEEE Trans. on Microwave Theory & Tech., vol.MTT-16, No.4, April 1968, pp218-227.

8. David, G.H., "Dynamic Frequency Allocation Increases Cellular Efficiency," Communication Eng. Int., Nov.1986.

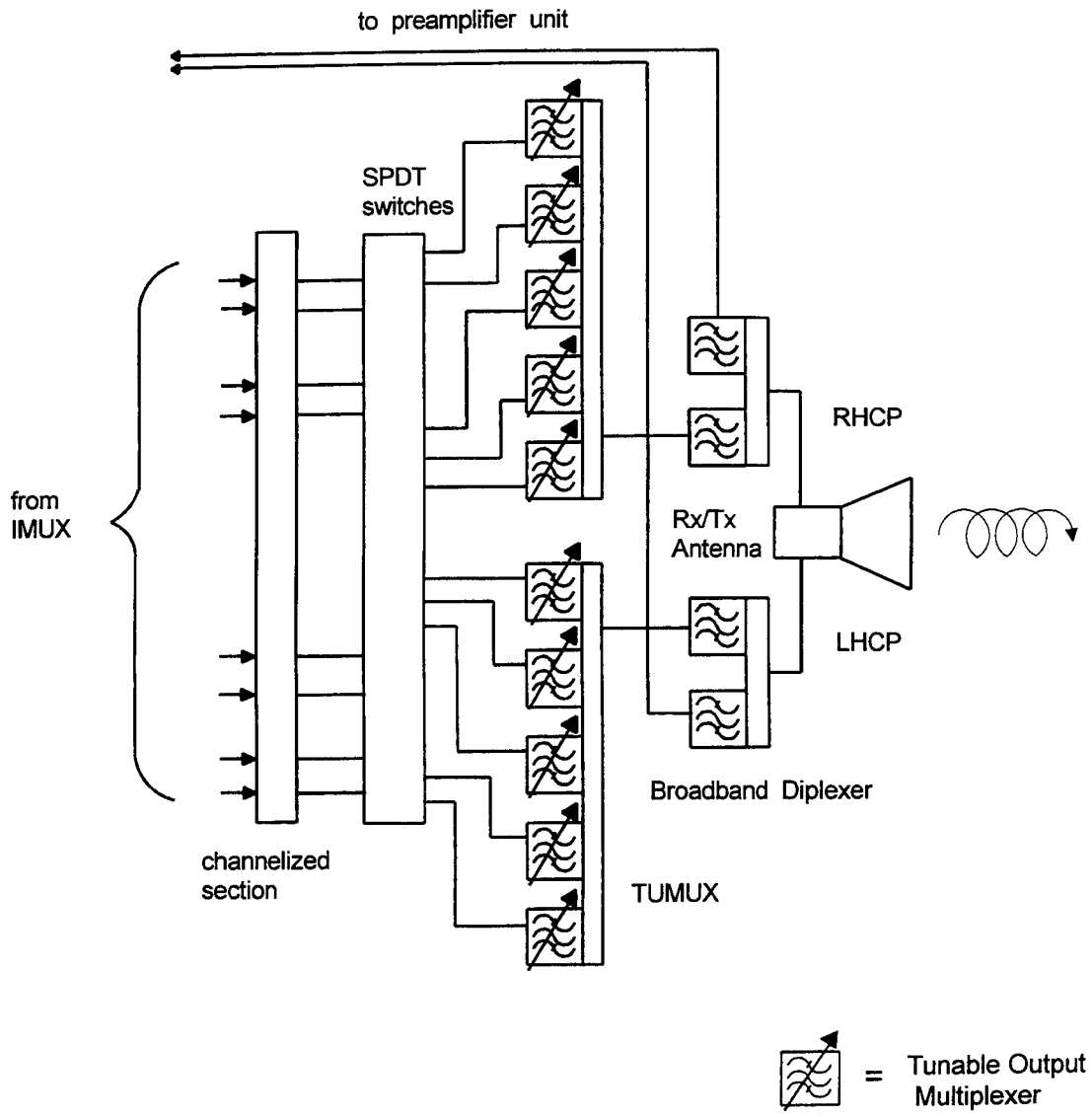


Figure 1.1 Block diagram of proposed common spare payload for European DBS containing tunable output multiplexers (TUMUX).

Chapter 2

Dielectric Resonators

2.0 Introduction

The dielectric resonator is a microwave component, comparable in characteristics and much smaller in size, to the existing metallic resonant cavities. It is made of a low-loss, temperature-stable, high-permittivity and high-Q ceramic material. Because of its small size, low cost, and ease of integration in MICs/MMICs, its applications in active and passive microwave circuits has been rapidly increasing [1,2,3].

The electrical properties of a dielectric resonator are dependent upon its geometry, as well as its immediate surroundings. The most commonly used shape of dielectric resonator is a cylindrical disc which can vary in size from a diameter and height of several millimetres to several centimetres, while its relative permittivity, ϵ_r , can vary between 10 to 100. The ceramic element functions as a resonator due to internal reflections at the interface between the dielectric resonator material and the surrounding medium. This results in confinement of energy within, and in the close vicinity of, the dielectric resonator, which therefore forms a resonant structure.

This chapter introduces the dielectric resonator and outlines its historical developments. The dielectric resonator material properties and the various material compositions used

in the manufacture of the resonator are discussed in brief. A brief discussion on two approximate models currently used to represent the dielectric resonator is also presented.

2.1 Historical Overview

The history of the dielectric resonator antedates the invention of the transistor by at least a decade. The first known publication on dielectric resonators is by R.D.Richmyer from Stanford University in 1939 [4]. Richmyer showed that unmetallised dielectric objects (sphere and toroid) can function as microwave resonators. However, in those troubled times, his theoretical work failed to generate significant interest, and practically nothing happened in this area for the next 25 years. There was only a small interruption of this hiatus. This was a paper by Schlicke in 1953 [5] reporting on super high dielectric constant materials ($\epsilon_r \geq 1000$ or more).

In the early '60s, researchers from Columbia University, Okaya and Barash [6,7], rediscovered dielectric resonators during their work on high dielectric constant materials (rutile), paramagnetic resonance and masers. Their work provided the first analysis of modes and resonator design. Nevertheless, the dielectric resonator was still far from practical applications. Materials such as TiO_2 (otherwise known as rutile) exhibited excessive temperature instability ($\sim 1000\text{ppm}/^\circ\text{C}$) causing correspondingly large resonant frequency changes with temperature. For this reason, these high Q

elements were not used. In the late '60s, S.B.Cohn, W.H.Harrison and their co-workers at Rantec Corp. [8,9] performed the first extensive theoretical and experimental evaluation of the dielectric resonator. The rutile ceramics that were used for experiments had isotropic dielectric constants of the order of 100. Again, poor temperature stability prevented development of practical RF components.

Cohn [8] stated in his early paper that in order to utilise dielectric resonators as microwave filters some form of temperature stabilization would be required. He observed that the development of a material having a relative dielectric constant of 100, a loss tangent of 0.0001 and a temperature coefficient, $\tau_f < 50\text{ppm}/^\circ\text{C}$, would solve this problem.

In the 12 years following Cohn's statement, the high temperature instability of dielectric resonator materials was solved. The first temperature compensated low-loss dielectric resonator material was Barium Tetratitanate (BaTiO_9) first reported on by Hartwig and Ready [10] of Raytheon. This material had a relative dielectric constant of 38 and a temperature coefficient of $-49\text{ppm}/^\circ\text{C}$, at 9.0GHz, which is just below the $50\text{ppm}/^\circ\text{C}$ mentioned by Cohn. However, the materials were in scarce supply and not available commercially.

The next major breakthrough in dielectric resonator material technology came from Japan in 1979. Toshio Nishikawa, Yohei Ishikawa and Hiroshi Tamura [11] of the Murata Company in Kyoto, Japan, had produced ceramic materials that had a

temperature coefficient of between +5 and -12ppm/°C and a loss tangent of 1.6×10^{-4} between -55°C to +100°C. These devices became commercially available at reasonable price. After this, the theoretical work and utilisation of dielectric resonators expanded very rapidly.

Recent developments in ceramic technology have made possible the manufacture of new ceramics with:

1. A relative permittivity generally ranging from 35-100; this particular range was found to allow a good confinement of electromagnetic energy in the bulk of the dielectric resonator,
2. Very low intrinsic losses ($\tan\delta=0.0001$), which means quality factors as high as 10,000 (at 4GHz) can be obtained, and
3. A controllable frequency temperature coefficient over the range -9 to +12ppm/°C.

Production tolerances ± 0.5 , ± 1 and $\pm 2\text{ppm}/^\circ\text{C}$ can be easily obtained by varying the chemical composition of the material.

2.2 Dielectric Resonator Materials

The important properties of the ceramic material to be used for dielectric resonators are:

1. The Q factor, which is equal to the inverse of the loss

tangent,

2. The temperature coefficient of the resonant frequency, τ_f , which includes the combined effects of the temperature coefficient of the dielectric constant and the thermal expansion of the dielectric,
3. The dielectric constant, ϵ_r .

The Q , τ_f , and ϵ_r values required for various applications differ, and in general a proper combination can be achieved by choosing an appropriate material and composition. Until several years ago, the lack of suitable materials possessing Q , τ_f , and ϵ_r all of acceptable values severely limited dielectric resonator applications.

High Q dielectric resonators with complex Perovskite structure, such as $\text{Ba}(\text{Zn}_{1/3}\text{Ta}_{2/3})\text{O}_3$, were developed in the mid '70s. Since then, several materials have been developed from this group such as $\text{Ba}(\text{Zr},\text{Zn},\text{Ta})\text{O}_3$ and $\text{Ba}(\text{Sn},\text{Mg},\text{Ta})\text{O}_3$ with relative permittivities of 30 and 25, respectively, having very high Q values: twice and four times higher than that of $(\text{Zr}-\text{Sn})\text{TiO}_4$. These are used from 10GHz up to millimetric frequencies.

It is not yet established if any of the dielectric materials in current use, Table 2.0, has overall superiority over the others, since many factors, such as ease of ceramic processing and ability to hold tolerances on the dielectric

properties, must also be considered. The performance limitations, if any, of the lower dielectric constant material remain to be determined, since most component work reported thus far has used dielectric resonators possessing ϵ_r in the range of 37-100. The lower dielectric constant material performance is likely to be more sensitive to shielding due to a higher proportion of the resonator fields being outside the resonator structure.

The temperature coefficient, τ_f , of the resonator can be controlled in some materials, by modifying the composition, to be anywhere within +9 to -9ppm/°C [12].

The quality factor, Q , of the dielectric resonator decreases with the increasing frequency. Typically the product $f_0(\text{GHz}) \times Q_0$ is constant. Some degradation of the Q is usually incurred in component applications. Losses due to housing walls, dielectrics, and adhesives used to support the resonators, and other effects may significantly reduce the Q .

2.3 Theoretical Dielectric Resonator Models

Accurate calculations of the resonant frequency and electromagnetic fields associated with dielectric resonators are much more complicated than those associated with hollow waveguide resonators. Usually numerical techniques are required to obtain characteristics of dielectric resonators and cavity resonators loaded with dielectrics [13]. Because large size matrices are usually involved in the numerical calculations of

electromagnetic fields and resonant frequencies of a dielectric/dielectric-loaded resonator and also because large number of mathematical operations have to be performed, a high computer time and memory are required for the analysis of dielectric and dielectric-loaded resonators. Consequently, many investigators have resorted to approximate techniques for the calculations of the resonant frequencies and the electromagnetic field of dielectric and dielectric-loaded resonators. However, except for special cases, these methods are capable of giving results which are accurate to 1% [14]. Examples of approximate techniques are the magnetic wall model introduced by Cohn [8] and the modified dielectric rod waveguide model by Itoh and Rudokas [14]. A brief discussion of these models is presented in the following sections, before the analysis used in this work is presented in Chapter 3.

2.3.1 The Cohn Models

Before discussing this model we should analyse the behaviour of a wave in dielectric medium. Consider a plane wave incident on the interface of two different dielectric media as shown in Figure 2.1. Assuming that the direction of the wave is normal to the interface, part of the energy of the incident wave will be reflected back from the interface as a plane wave travelling in the negative direction in medium 1. The rest of the energy will cross the interface and propagate as a transmitted wave in medium 2. The reflection coefficient, which is the ratio

between the reflected and incident wave amplitude, is given by:

$$\Gamma = \frac{Z_2 - Z_1}{Z_2 + Z_1} \quad (2.1)$$

where Z_1 and Z_2 are intrinsic impedances of region (1) and (2) respectively and are given by:

$$Z_1 = \sqrt{\frac{\mu_o}{\epsilon_o \epsilon_{r1}}} \quad (2.2a)$$

$$Z_2 = \sqrt{\frac{\mu_o}{\epsilon_o \epsilon_{r2}}} \quad (2.2b)$$

Substituting (2.2) into (2.1) and simplifying one can calculate the reflection coefficient as a function of ϵ_{r1} and ϵ_{r2} as follows:

$$\Gamma = \frac{\sqrt{\frac{\epsilon_{r1}}{\epsilon_{r2}} - 1}}{\sqrt{\frac{\epsilon_{r1}}{\epsilon_{r2}} + 1}} \quad (2.3)$$

From equation (2.3) it can be seen that if medium 1 has a much higher dielectric constant than medium 2, then the ratio of $\epsilon_{r1}/\epsilon_{r2}$ is much higher than unity and the reflection coefficient is close to +1. In this case most of the energy of the wave is

reflected back to medium 1 and a standing wave pattern will be created. At the interface, as the reflection coefficient is close to +1, the electric field is maximum and the magnetic field is minimum. This is equivalent to an open circuit and approximate computation of resonant frequencies and the field inside a high permittivity dielectric are thus possible by assuming that the surface of dielectric is covered with a perfect magnetic wall.

This model is called the "first-order" model of the dielectric resonator in which all surfaces of the dielectric resonator are assumed to be magnetic wall, Figure 2.2. In this model, the resonant frequencies and the associated field distribution can be computed using the known procedures for the analysis of hollow cavity resonators. Depending on the dielectric constant, the computed results can vary from measured values by as much as 20% for the fundamental magnetic dipole mode ($TE_{01\delta}$) [15]. Therefore, this model is not very useful for any practical circuit design where accurate determination of resonant frequencies is required. However as the dielectric constant increases, this model gives more accurate values to resonant frequencies and the associated electromagnetic fields.

In 1968 Cohn [8] introduced the "second-order" model which considerably reduced the error in characterisation of dielectric resonators. In this model the circumference of cylindrical dielectric resonator is assumed to be a perfect

magnetic wall. The magnetic wall end caps are removed and replaced by air-filled hollow waveguides as shown in Figure 2.3. The modes in these waveguides are evanescent and the field decays exponentially in the z-direction away from each end of the dielectric resonator.

To reduce the radiation losses, the air-filled waveguides can be terminated by conductor plates, however, this modifies the resonant frequencies of the isolated dielectric shown in Figure 2.4. The effect of conductor plates on the resonant frequencies of the isolated dielectric resonator can be reduced to minimum if they are placed far away from dielectric ends ($L_1/L > 3$ and $L_2/L > 3$). The resonance condition is now written as [15]:

$$\beta \cdot L = \tan^{-1} \left(\frac{\alpha_1}{\beta} \coth \alpha_1 L_1 \right) + \tan^{-1} \left(\frac{\alpha_2}{\beta} \coth \alpha_2 L_2 \right) \quad (2.4)$$

where β , is the axial propagation constant in the dielectric; α_1 and α_2 are attenuation constants in region (1) and (2) respectively. These values are given by:

$$\beta^2 = k_o^2 \epsilon_r - \left(\frac{x_{o1}}{a} \right)^2 \quad (2.5a)$$

$$\alpha_1^2 = \left(\frac{x_{o1}}{a} \right)^2 - k_o^2 \epsilon_{r1} \quad (2.5b)$$

$$\alpha_2^2 = \left(\frac{x_{01}}{a} \right)^2 - k_o^2 \epsilon_{r2} \quad (2.5c)$$

In equation (2.5), x_{01} is the first root of the Bessel function $J_0(x)$, and k_o is the free-space wave number. Equation (2.4) can be solved by a simple iteration computer program to find the resonant frequencies of the structure shown in Figure 2.4 for the fundamental $TE_{01\delta}$ mode. The resonant frequencies of other higher order modes ($TE_{01\delta+p}$) can also be calculated by letting $L_1=L_2=\infty$ while the resonant frequencies of the dielectric shorted in both ends by metallic plates are obtained by assuming $L_1=L_2=0$. The errors are due to the existence of the electromagnetic field outside the magnetic wall boundary ($r=a$) which is neglected in this model. However, this is certainly an improvement over the "first-order" model.

This model can still be further improved by removing the magnetic wall from the circumference of the dielectric resonator and applying the continuity conditions of the tangential fields at the boundary ($r=a$). The field components inside and outside the dielectric are then used to find the change in the resonant frequency due to the removal of the magnetic wall by using a perturbation formula [16]. To use the perturbation method, the shielded dielectric resonator in Figure 2.4 is divided into 6 different regions as shown in Figure 2.5. The fractional change in the resonant frequencies of the resonator by perturbing its volume by ΔV is calculated

by the formula [16],

$$\frac{\omega - \omega_o}{\omega_o} = \frac{\iiint_{\Delta V} (\mu |H_o|^2 - \epsilon |E_o|^2) dV}{\iiint_V (\mu |H_o|^2 + \epsilon |E_o|^2) dV} \quad (2.6)$$

where the numerator represents the difference of the magnetic and electric energies stored in volume ΔV while the denominator is the sum of both energies in the unperturbed cavity. Parameters ω_o and ω are resonant frequencies of the unperturbed and perturbed cavity respectively. In the "second-order" model as the magnetic wall AB and CD shown in Figure 2.6 are removed outward, the ΔV consists of region (3), (4), and (5). Equation (2.6) then reduces to:

$$\omega = \omega_o \left(1 + \frac{W_{m3} + W_{m4} + W_{m5} - W_{e3} - W_{e4} - W_{e5}}{W_{m1} + W_{m2} + W_{m6} + W_{e1} + W_{e2} + W_{e6}} \right) \quad (2.7)$$

where W_{mi} and W_{ei} are the magnetic and electric stored energies in region i respectively. The resonant frequencies calculated by applying the perturbation correction will only differ by less than 1% from the measured values.

2.3.2 Itoh and Rudokas Model

The model proposed by T.Itoh and R.Rudokas [14] approximates a cylindrical dielectric resonator operating in the $TE_{01\delta}$ mode and

placed in a microstrip environment and enclosed in a metallic enclosure. Unlike the Cohn models, however, this model accounts for the existence of electromagnetic fields around the sides of the dielectric resonator ($r > a$). Like Cohn's "second-order" model the whole structure is divided into six different regions [8] as shown in Figure 2.6. The dielectric resonator occupies region (6), while regions (2), (4) and (5) are filled with air, and regions (1) and (3) represent the substrate. Conducting walls at $z = -L_1$ and $z = H + L_2$ represent the base and top cover of the box, respectively.

In order to derive the electromagnetic field components, a dielectric rod waveguide model is used to represent the actual physical length of the resonator. At each end of the resonator, a waveguide below cutoff is postulated. The lengths of these two waveguides below cutoff are made to coincide with the actual dimensions of the metal box shielding the resonator. This model is applied to the structure of Figure 2.6, together with the additional assumption that no fields exist in regions (3) and (5), and that the fields in regions (1) and (2) gradually diminish away from the dielectric resonator. Moreover, the fields in regions (1) and (2) are selected so that Maxwell's equation, the boundary conditions and continuity conditions are maintained. The requirement for the continuity of fields in the dielectric resonator leads to the following two equations for the $TE_{01\delta}$ mode.

$$\frac{J_0(k_{\rho 1} a)}{J_1(k_{\rho 1} a)} = - \frac{k_{\rho 2} a}{k_{\rho 1} a} \cdot \frac{k_0(k_{\rho 2} a)}{k_1(k_{\rho 2} a)} \quad (2.8)$$

$$\beta \cdot H = \tan^{-1} \left(\frac{\alpha_1}{\beta} \coth \alpha_1 L_1 \right) + \tan^{-1} \left(\frac{\alpha_2}{\beta} \coth \alpha_2 L_2 \right) \quad (2.9)$$

where β is the propagation constant in the dielectric resonator,

$k_{\rho 1}$ and $k_{\rho 2}$ are the radial wave numbers in the substrate and in air, respectively,

α_1 and α_2 are the attenuation constants in the substrate and in air, respectively,

H is the dielectric resonator height,

a is the dielectric resonator radius,

L_2 is the distance between the cover and the dielectric resonator,

L_1 is the substrate thickness,

J_0 and J_1 are Bessel functions of the 1st kind and order zero and order one, respectively, and

k_0 and k_1 are modified Bessel functions of the 2nd kind and order zero and order one, respectively.

With the following mathematical identities, the computation of the resonant frequencies is reduced to the calculation of $k_{\rho 1}$ and $k_{\rho 2}$:

$$k_{\rho 2} a = \sqrt{(k_0 a)^2 (\epsilon_{r6} - \epsilon_{r4}) - (k_{\rho 1} a)^2} \quad (2.10a)$$

$$k_{\rho 1} a = \sqrt{(k_0 a)^2 \epsilon_{r6} - (\beta a)^2} \quad (2.10b)$$

$$\alpha_1 = \sqrt{k_{\rho 1}^2 - k_o^2 \epsilon_{r1}} \quad (2.11a)$$

$$\alpha_2 = \sqrt{k_{\rho 1}^2 - k_o^2 \epsilon_{r2}} \quad (2.11b)$$

The accuracy of the results obtained using this model varies according to the spacing between the conductor walls and the dielectric resonator. For the isolated dielectric resonator case ($L_1=L_2= \infty$), the computed resonant frequency is typically 5% too high. For closer wall spacings, however, the error decreases since the effect of assuming zero field in regions (3) and (5) becomes less significant, resulting in errors of about 1% or less when compared with measured values. When L_1 and L_2 are equal to zero, the solution becomes exact.

The model is limited to the case of a dielectric resonator placed directly on a substrate, and does not include the effect of the spacer which is often used in practical circuits to support the resonator on the substrate. Moreover, the model assumes the side walls of the enclosure are far away from the dielectric resonator as to have no effect. In certain practical situations, this assumption does not hold.

For this research work, the development of a rigorous analysis was considered inappropriate due to the increased computational cost involved. Instead, the technique used by Itoh & Rudokas for modelling the dielectric resonator is used for analysing a dielectric resonator circuit structure which

takes into account the spacer and the side walls of the metallic enclosure. The analysis is described in detail in Chapter 3.

References

1. Plourde, J.K., Ren. C.L., "Application of Dielectric Resonators in Microwave Components," IEEE Trans. on Microwave Theory & Tech., vol.MTT-29, Aug.1981, pp754-770.
2. Okuyama, K., et al., "A Compact and Low Loss Dielectric Resonator for 800MHz Band Mobile Communication Base Stations," Asia-Pacific Microwave Conf., Dec.6-9, 1994, pp751-754.
3. Darwish, A.M., Ezzeddine, A.K., Hung, H.L.A., Phelleps, F.R., "A New Phase Noise Reduction Technique for MMIC Oscillators," 1992 IEEE MTT-S Digest, pp463-466.
4. Richtmyer, R.D., "Dielectric Resonators," J.Appl. Phys., vol.10, June 1939, pp391-398.
5. Schlicke, H.M., "Quasi-Degenerate Modes in High-Dielectric Cavities," J. Appl. Phys., vol.24, Feb.1953, pp187-191.
6. Okaya, A., "The Rutile Microwave Resonator," Proc. IRE, vol.48, Nov.1960, p1921.
7. Okaya, A., Barash, L.F., "The Dielectric Microwave Resonator," Proc. IRE, vol.50, Oct.1962, pp2081-2092.
8. Cohn, S.B., "Microwave Bandpass Filters Containing High-Q Dielectric Resonators," IEEE Trans. on Microwave Theory & Tech., vol.MTT-16, April 1968, pp218-227.
9. Harrison, W.H., "A Miniature High-Q Bandpass Filter Employing Dielectric Resonators," IEEE Trans. on Microwave Theory & Tech., vol.MTT-16, April 1968, pp210-218.
10. Hartwig, C.P., Ready, D.W., "Dielectric Loading for

Microwave Components," Raytheon Internal Memorandum M2575, Feb.1971.

11. Nishikawa, T., Ishikawa, Y., Tamura, H., "Ceramic Materials for Microwave Applications," Electronic Ceramics, Spring Issue, Special Issues on Ceramic Materials for Microwave Applications, Japan, 1979.
12. Trans-Tech, Inc. Catalogue on "A Designers' Guide to Microwave Dielectric Ceramics".
13. Zaki, K.A., and Atia, A.E., "Modes in Dielectric-Loaded waveguides and Resonators," IEEE Trans. on Microwave Theory & Tech., vol.MTT-31, 1983, pp1039-1044.
14. Itoh, T., Rudokas, R.S., "New Method for Computing the Resonant Frequencies of Dielectric Resonators," IEEE Trans. on Microwave Theory & Tech., vol.MTT-25, Jan.1977, pp52-54.
15. Kajfez, D., Guillon, P., "Dielectric Resonators," Artech House, 1985.
16. Harrington, R.F., "Time-Harmonic Electromagnetic Fields," McGraw-Hill, 1961.

Table 2.0 Properties of Dielectric Resonators.

Composition	Dielectric Constant	Q @ 10GHz	Temperature Coefficient ppm/°C	Frequency Range GHz	Manufacturer
Ba ₂ Ti ₉ O ₂₀	40	4,000	+2	1 to 50	Bell Labs.
BaTi ₄ O ₉	39	3,500	+4	1 to 50	Raytheon Trans.Tech
(Zr-Sn)Ti ₄ O ₉	38	4,000	-4 to -10 ^a	1 to 60	Trans.Tech Thomson-CSF Murata
Ba(Zn _{1/2} Tn _{2/3})O ₃	29	10,000	0 to +10 ^a	5 to 60	Murata
Ba(Zr,Zn,Ta)O ₃	30	10,000	0 to +10 ^a	10 to 60	Murata
Ba(Sn,Mg,Ta)	25	20,000	0 to +8 ^a	10 to 60	Murata
(Ba,Pb)Nd ₂ Ti ₅ O ₁₄	90	5,000 @1GHz	0 to +6 ^a	0.8 to 4	Murata Trans.Tech.

^aAdjustable with composition.

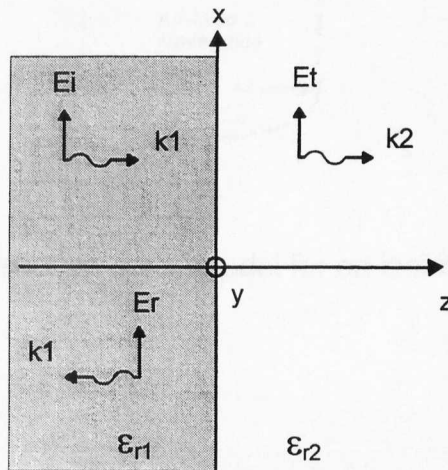


Figure 2.1 Plane wave incident to the interface of two dielectric media.

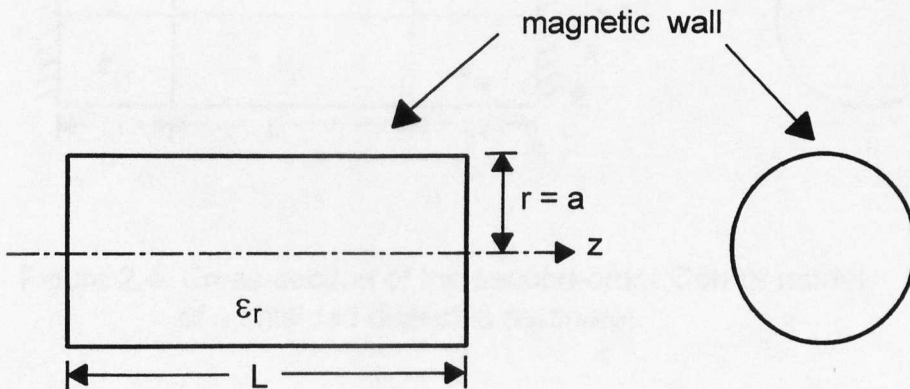


Figure 2.2 The cross-section of the first-order model for the analysis of the dielectric resonator.

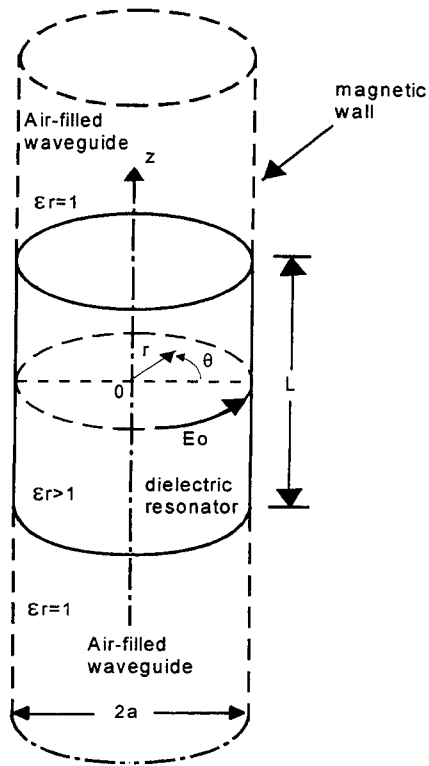


Figure 2.3 Cohn's second-order model for an isolated dielectric resonator.

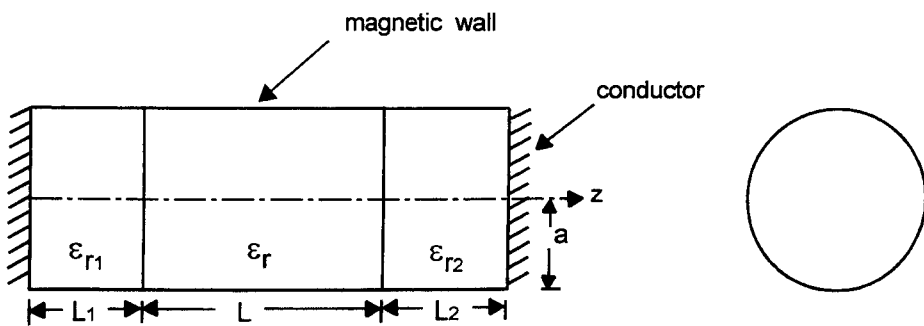


Figure 2.4 Cross-section of the second-order Cohn's model of a shielded dielectric resonator.

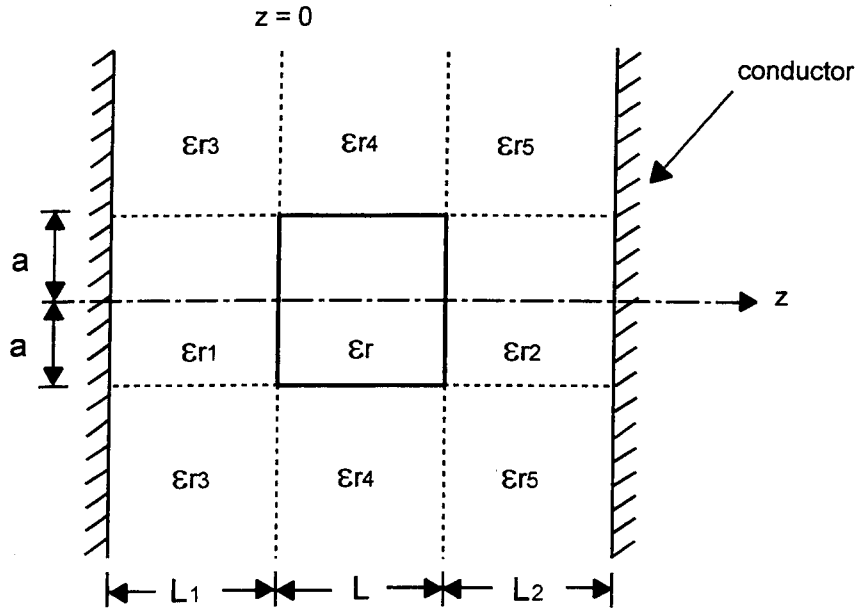


Figure 2.5 Cross-section of a shielded dielectric resonator.

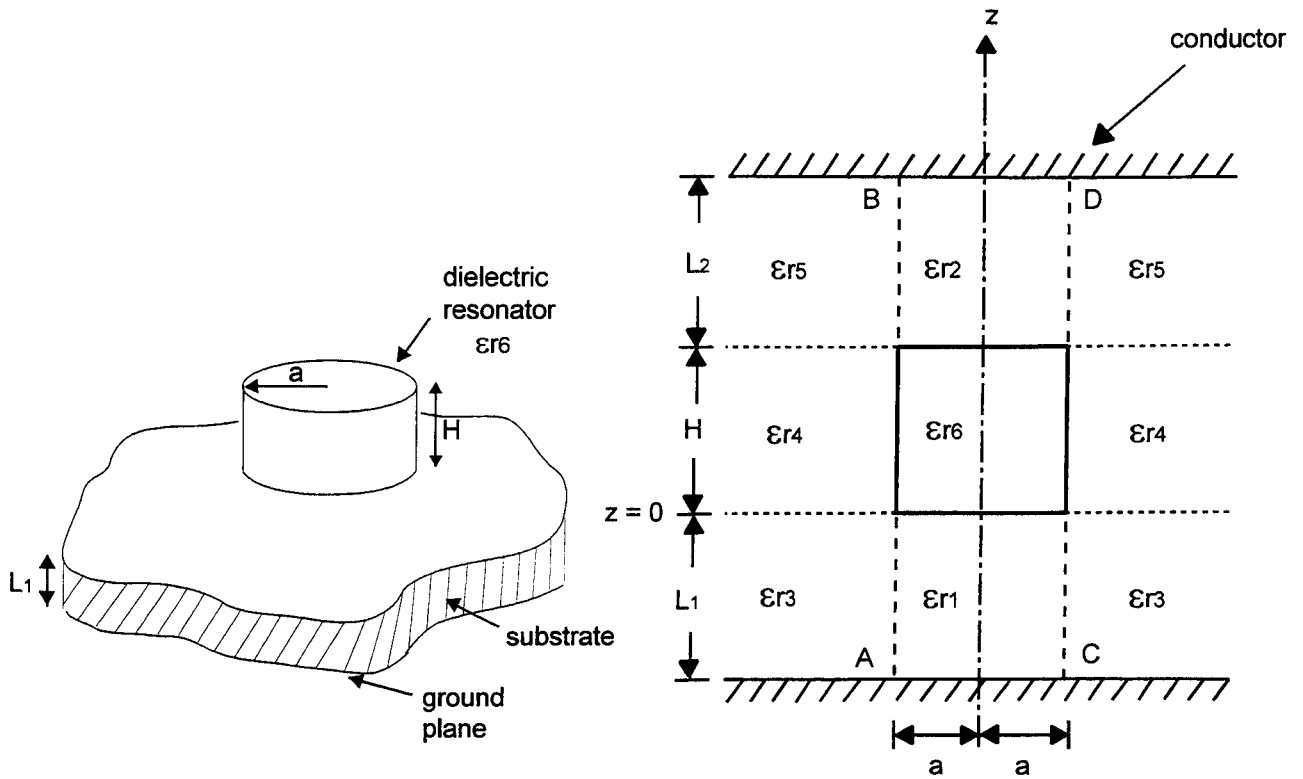


Figure 2.6 Itoh & Rudokas model of shielded dielectric resonator.

Chapter 3

Characterisation of DR Coupling in a Microstrip Environment

3.0 Introduction

To utilise dielectric resonators in bandpass filters, it is necessary to couple the resonators to each other, and to couple the end resonators to terminated transmission lines. The bandwidth, passband, and stopband responses depend upon the coupling values and number of resonators. Formulas exist for computing the coupling values for the required bandwidth with maximally flat or equal-ripple response shapes [1]. However, none of these relate the coupling coefficient between a pair of resonators to the physical and electrical parameters of the dielectric resonators, their centre-to-centre spacing, or the dimensions of the surrounding structure. In order to design microstrip DR filters it is therefore essential to characterise the coupling which exists between a DR and a microstrip line and also between a pair of DRs, to the physical and electrical parameters of the dielectric resonator.

In this chapter we start with a discussion of coupling between a DR and a microstrip line. Since extensive work on this type of coupling has been performed in the past [2,3] resulting in mathematical expressions which accurately characterise the coupling, only the salient results of this analysis will be presented. An analytical method is then used

to derive new expressions which characterise the coupling between a pair of DRs based on the electromagnetic fields in this structure. These expressions are then verified experimentally. The computed values of coupling coefficient show very good agreement with the experimental values. The coupling coefficient data presented in this chapter will be used in subsequent chapters for designing microwave DR filters.

3.1 Coupling Coefficient Between a Microstrip Line and a DR

When a DR is placed in the vicinity of a microstrip line, as shown in Figure 3.1, and excited in the $TE_{01\delta}$ mode, the transmission characteristics of the microstrip line are modified by the magnetic coupling. The electric coupling caused by the high dielectric constant of the DR can be assumed to be very small since most of the electric field of the microstrip line is not only concentrated under the microstrip but is also almost orthogonal to the electric field of the resonator [4]. The magnetic effect is an interaction between the magnetic field of the resonator and the magnetic field of the current in the microstrip line. This interaction can be regarded as mutual inductance.

The following assumptions are made in the analysis of the coupling between a cylindrical DR and the microstrip:

1. The width of the microstrip is much smaller than the diameter of the DR, which approaches the practical case.

2. The microstrip is thin, so field disturbances due to the presence of the microstrip and the radiation loss due to field mismatch are neglected.
3. The microstrip line carries only the TE quasi-TEM mode.
4. All dielectric materials are isotropic and lossless.
5. The dielectric constant of the DR is larger than that of the substrate.
6. The DR can be represented by a conducting loop having in series an inductance, L_r , a capacitance, C_r , and a resistance R_r . The resonance occurs at the angular frequency ω_o .

$$\omega_o = \frac{1}{\sqrt{L_r C_r}} \quad [5]$$

7. Only the TE_{018} mode is strongly excited and field distortion caused by other modes is very small [4,5].
8. The DR couples with the microstrip line through the mutual inductance, L_m .
9. All losses involved (i.e. in the dielectric resonator and substrate) are small enough to be neglected.

With these assumptions, the structure of Figure 3.1 can be represented [2] by a resonance circuit magnetically coupled with a transmission line, as shown in Figure 3.2, where L_1 , C_1 , and R_1 represent the equivalent parameter of the line and L_m is the mutual inductance.

In the coupling plane P-P', the equivalent circuit of Figure 3.2 can be further simplified to that of Figure 3.3. L, R, and C are represented by the following equations [7]:

$$L = \frac{L_m^2}{L_r} \quad (3.1)$$

$$C = \frac{L_r}{\omega_o^2 L_m^2} \quad (3.2)$$

$$R = Q_o \omega_o \frac{L_m^2}{L_r} \quad (3.3)$$

where
$$Q_o = \frac{L_r \omega_o}{R_r} \quad (3.4)$$

The coupling coefficient k is defined by:

$$k = \frac{R}{R_{\text{ext}}} \quad (3.5)$$

where R_{ext} is the resistance of the generator and the loaded impedance of the line. Since $R_{\text{ext}} = 2Z_o$, we obtain:

$$k = \frac{\omega_o Q_o L_m^2}{2Z_o L_r} \quad (3.6)$$

The external Q-factor which characterises the coupling of the resonator with the microstrip line is given by [2]:

$$Q_{\text{ex}} = \frac{Q_o}{k} = \frac{2Z_o L_r}{\omega_o L_m^2} \quad (3.7)$$

To determine the coupling coefficient it is necessary to evaluate the Q_{ex} -factor as a function of distance d between the microstrip line and the resonator. The factor which characterizes this variation is L_r/L_m^2 . A useful relationship to evaluate L_r/L_m^2 is now derived based on the above simplifying assumptions and approximating the DR in the $TE_{01\delta}$ mode by a magnetic dipole [7]. The voltage V_r induced in the magnetic dipole by the current, I , flowing in the microstrip line is:

$$V_r = j\omega_o L_m I \quad (3.8)$$

This induced voltage can be computed from the magnetic flux through the cross section in the microstrip substrate shown in Figure 3.4.

$$V_r = \int \bar{E} \cdot d\bar{l} = j\omega\mu_o \iint_A \bar{H} \cdot d\bar{A} \quad (3.9)$$

The magnetic energy stored in the resonator is:

$$W_m = \frac{1}{2} L_r I_r^2 \quad (3.10)$$

combining Equations (3.8), (3.9) and (3.10) and substituting into (3.7) and (3.6), the external quality factor and the coupling coefficients are given by:

$$Q_{ex} = \frac{4Z_o}{\omega_o \mu_o^2} \frac{W_m}{\left(\iint_A \overline{H} \overline{dA} \right)^2} \quad (3.11)$$

$$k = \frac{\omega_o Q_o \mu_o^2}{4Z_o} \frac{\left(\iint_A \overline{H} \overline{dA} \right)^2}{W_m} \quad (3.12)$$

W_m can be evaluated by using:

$$W_m = \frac{1}{2} \varepsilon_o \varepsilon_i \int_{V_i} \overline{E}_i \overline{E}_i^* dV_i \quad (3.13)$$

where ε_i = relative permittivity of the medium i

E_i = electric field vector in the medium i

V_i = volume of the medium i .

This analytical technique has been used by Guo et al [3] and has proved to closely correlate with the experimental results.

3.1.1 Experimental Characterisation of Coupling Coefficient Between a DR and a Microstrip line.

Accurate characterisation of coupling coefficient between a DR and a microstrip line is essential in the design of DR filters. In this section an accurate technique of measuring the coupling coefficient is described using a scalar network analyser. The measured data will be used to design, construct and test DR filters in the subsequent chapters.

The test fixture for measuring the coupling coefficient

basically consists of a 50Ω microstrip line coupled to the resonator in its TE_{015} mode, Figure 3.5. To minimise radiation loss, which would result in a lower effective Q-value, the circuit is mounted inside a metallic enclosure. The transmission characteristic of this configuration around the resonant frequency resembles a band-reject frequency response as shown in Figure 3.6.

The coupling coefficient, k , relates the different quality factors in the following way [8]:

$$Q_o = Q_L(1 + k) = kQ_{ex} \quad (3.14)$$

where Q_o , Q_L , and Q_{ex} are the unloaded, loaded, and external quality factors of the resonator coupled to the microstrip line. The loaded and unloaded Q-factors can be determined from the magnitude of the transmission coefficient S_{21} around the resonant frequency as measured with a network analyser. The magnitude S_{21} of the transmission coefficients corresponding to Q_o and Q_L measurement points S_{21U} and S_{21L} are [8]:

$$S_{21U} = S_{210} \sqrt{\frac{2}{1 + S_{210}^2}} \quad (3.15)$$

$$S_{21L} = \sqrt{\frac{1 + S_{210}^2}{2}} \quad (3.16)$$

The measurement point is determined by the quantity x as shown in Figure 3.6. The peak insertion loss, L_o , is given by:

$$L_o = -20 \log_{10} S_{21o} \quad (dB) \quad (3.17)$$

It can be shown that [8]:

$$x = 3 - 10 \log_{10} (1 + 10^{-L_o/10}) \quad (dB) \quad (3.18)$$

Figure 3.7 illustrates the above relationship and shows that for high values of L_o the Q_o and Q_L measuring points approach a 3dB separation from S_{21o} and $|S_{21}|=0$, respectively.

Q_o and Q_L can be determined from:

$$Q_o = f_o / \Delta f_o \quad (3.19)$$

$$Q_L = f_o / \Delta f_L \quad (3.20)$$

where f_o is the resonant frequency, Δf_o and Δf_L is the bandwidth of Q_o and Q_L , respectively. The coupling coefficient can therefore be determined using the ratio of loaded and unloaded quality factor given by Equation (3.14).

A computer program DR100 [9] was used to calculate the coupling coefficient of the dielectric resonator coupled with a microstrip. The comparison of the experimentally determined coupling coefficients with calculated data is given in Figure 3.8. The measured values are in good agreement with the

theoretical values for spacings exceeding about 13mm. For smaller spacings, the model deviates from the measured data by 10% due to neglect of the spacer used to support the dielectric puck on the substrate. However, the accuracy is adequate for most design purposes.

The measurements were carried out using a 50Ω microstrip line constructed on Cu217 dielectric substrate with $\epsilon_r=2.17$ and thickness of 0.794mm. The DR employed was a Transtech D8500 series with $D=17.145\text{mm}$ and thickness of 7.722mm made of $(\text{ZnSn})\text{TiO}_4$ with $\epsilon_r=36$. The resonant frequency of the DR dominant mode was 3.29GHz.

3.2 Coupling Coefficient Between Two DRs

To analyse the coupling between two DRs, we first need to establish an equivalent circuit for the system and then perform the electromagnetic field analysis to find a generalised relation between the coupling coefficient, k , and the spacing between the two resonators.

Figure 3.9 shows the arrangement considered. The cylindrical DRs are placed on a dielectric substrate and are magnetically coupled to each other and to the adjacent microstrip lines which carry the microwave energy into and out of the structure. The structure is enclosed in a rectangular metallic cavity below cutoff. The cavity serves as a shield, preventing radiation loss and undesired coupling to external fields.

The external field of the fundamental resonant mode resembles that of a magnetic dipole directed along the axis of the disk. Because of this, an energised resonator excites many hybrid modes. The amplitude of these waves attenuates with longitudinal distances, s , since the cavity is used below cutoff. The magnetic field of the waves excites the adjacent resonator and results in magnetic coupling between the pair of resonators. Because of the exponential decay of these waves, the coupling between non-adjacent resonators can be neglected.

In the following analysis the assumptions outlined earlier apply with the additional factor that the coupling between the the DRs is mainly due to the radial magnetic component H_p .

3.2.1 General Coupling Analysis Between Two DRs

The two DRs in Figure 3.9 operating in the $TE_{01\delta}$ mode, separated by a distance, s , can be modelled by the two magnetic dipoles which are represented by conducting loop in an arbitrary enclosure, as shown in Figure 3.10, [10]. If a current I_1 is caused to flow in loop-1, a magnetic dipole moment, m , will be developed by loop-1 such that,

$$\vec{m} = I_1 A \quad (3.21)$$

where A is the loop area. The magnetic energy stored in loop-1 is then given by:

$$W_m = \frac{1}{2} L_1 I_1^2 \quad (3.22)$$

If L_m designates the mutual inductance between the two loops, the voltage V_2 induced in loop-2 due to the current I_1 is given by:

$$V_2 = j\omega L_m I_1 \quad (3.23)$$

The same voltage is also given by the induction law:

$$V_2 = - \int \overline{E}_2 \overline{dI} = j\omega \int_A \overline{B}_2 \overline{dA} = j\omega \mu_o \int \int_A \overline{H}_2 \overline{dA} \quad (3.24)$$

If we consider \overline{H}_{m2} to be the mean value of the magnetic field \overline{H}_2 in loop-2, V_2 simplifies to:

$$V_2 = j\omega \mu_o \overline{H}_{m2} \overline{A} \quad (3.25)$$

By taking into account Equations (3.21) to (3.23) and Equation (3.24) the coupling coefficient can thus be written:

$$k = \frac{L_m}{L} = \frac{\mu_o \overline{H}_{m2} \overline{m}}{2W_m} \quad (3.26)$$

This formula for the coupling coefficient between two identical resonators applies in general and is only approximate since it characterises the resonator magnetic dipole by a simple conductive loop.

3.2.2 Improved Analysis of Coupling Coefficient Between Two DRs

The general formula (3.26), giving the coupling coefficient between two magnetic dipoles, is now applied to the DR structure depicted in Figure 3.9. The structure considered is a rectangular metallic cavity containing two DRs supported on a low loss dielectric spacer on a substrate. The DR and spacer are surrounded by air to their sides and the complete structure is symmetrical.

A cross sectional view of the structure is shown Figure 3.11 where, for the purpose of analysis, it has been divided into eight regions. For clarity only one resonator is shown. However, the other resonator and its supporting spacer would be situated in region four and three, respectively. The current density J_s shown in Figure 3.11 was introduced by Kajfez [7] to justify the magnetic field discontinuities between different regions observed in the Itoh and Rudokas model [11].

The same symbols have been used in the following analysis as those defined in reference [7] for consistency. Since the derivations in the following analysis are rather lengthy only the main results will be presented.

A more accurate representation of resonator magnetic dipole can be achieved by using the following definition of magnetic dipole moment [12,13]:

$$\bar{m} = \frac{1}{2} \iiint_V \bar{r} \times \bar{J} \, dV \quad (3.27)$$

When \bar{r} is the vector distance from an arbitrary fixed reference point (see Figure 3.12), J is the current density and the integration is performed over a volume enclosing the current distribution. Equation (3.27) can be applied to our DR structure shown in Figure 3.11. The current density in each region is given by:

$$\bar{J} = -\frac{1}{j\omega} \bar{\nabla} \times \mu^{-1} \bar{\nabla} \times \bar{E} \quad (3.28)$$

If E satisfies Helmholtz equation ($\bar{\nabla} \times \bar{\nabla} \times \bar{E} = k^2 \bar{E}$), then Equation (3.28) reduces to:

$$\bar{J} = -j\omega\epsilon\bar{E} \quad (3.29)$$

It can easily be shown [7] that the Helmholtz wave equation is verified in regions 1, 2, 4, 6 and 7 but not in regions 3, 5 and 8. The improved model of Kajfez supposes that the magnetic fields are null in regions 3, 5 and 8 and, to take in to account the jump in the field, he introduced the surface density current, as shown in Figure 3.11. However due to the symmetry of the system, these currents do not contribute to the creation of the magnetic dipole moment in the axial direction.

In summary, the contribution to the dipole magnet due to region 1,2,4, 6 and 7 is given by:

$$\bar{m}_i = -\frac{1}{2} j\omega\epsilon_i \iiint_V \bar{r} \times \bar{E}_i dV \quad (3.30)$$

while the contribution of region 3, 5 and 8 is given by:

$$\overline{m}_i = - \frac{1}{2j\omega\mu} \iiint_V \vec{r} \times \left[\vec{\nabla} \times (\vec{\nabla} \times \overline{E}_i) \right] dV \quad (3.31)$$

Since the electrical field of the resonant mode $TE_{01\delta}$ exist inside as well as outside, the DR, the integration should be performed over the total volume outside the DR in addition to the internal volume. It is worthwhile recalling here that most of the electrical energy is confined inside the DR and thus the contribution of the external electrical field is very small. We also need to take into account the total stored energy at resonance in the system, which is given by:

$$W_m = W_e = \frac{\epsilon_o}{2} \iiint_V \epsilon_r E_i^2 dV \quad i=1 \text{ to } 8 \quad (3.32)$$

Where the integration should be performed inside and outside the DR body.

The improved formula for the coupling coefficient between two resonant DRs is then given by:

$$k = \mu_o \overline{H}_\rho \frac{\left(- \frac{1}{2} j\omega \epsilon_i \iiint_V \vec{r} \times \overline{E}_i - \frac{1}{2j\omega\mu} \iiint_V \vec{r} \times [\vec{\nabla} \times (\vec{\nabla} \times \overline{E}_i)] dV \right)}{2 \left(\frac{\epsilon_o}{2} \iiint_V \epsilon_r E_i^2 dV \right)} \quad (3.33)$$

This expression can be written alternatively by the ratio of the algebraic sum of magnetic dipole moment to the algebraic

sum of the stored energies in every region of the structure:

$$k = \frac{\mu_o H_{o4} \sum_{i=1}^8 m_i}{2 \sum_{i=1}^8 W_i} \quad (3.34)$$

Using the cylindrical coordinate system (ϕ, ρ, z) , electric field expressions for the TE_{018} mode can be derived for each region separately from the solutions of Helmholtz wave equation for TE modes. For the TE_{018} mode, the magnetic field H_z is independent of ϕ , hence, from Maxwell's equation, the only other field components which exist are H_ρ and E_ϕ . The boundary conditions of zero tangential electric field at all PEC surfaces are applied to the E_ϕ field components in the appropriate regions (i.e. $E_{\phi 2}=0$ at $z=(L+L_2)$ and $E_{\phi 7}=0$ at $z=-(L_1+L_3)$). We also need to take into account the continuity of the tangential components of the electric, as well as the magnetic field at the interface between regions (i.e. $E_{\phi 1}=E_{\phi 6}$ and $H_{\rho 1}=H_{\rho 6}$ at $z=0$, $E_{\phi 6}=E_{\phi 2}$ and $H_{\rho 6}=H_{\rho 2}$ at $z=L$, $E_{\phi 1}=E_{\phi 7}$ and $H_{\rho 1}=H_{\rho 7}$ at $z=-L_1$, $E_{\phi 6}=E_{\phi 4}$ and $H_{\rho 6}=H_{\rho 4}$ at $\rho=a$, $E_{\phi 1}=E_{\phi 3}$ and $H_{\rho 1}=H_{\rho 3}$ at $\rho=a$).

The electrical field of the mode TE_{018} in the different regions are given by the following equations [14]:

$$E_{\phi 1} = E_o r_B R J_1(k_\rho \rho) \cosh(\alpha_1 z + \alpha_T) \quad (3.35)$$

$$E_{\phi 2} = E_0 \frac{\cos \frac{\phi_2}{2}}{\sinh \alpha_2 L_2} J_1(k_{\rho 1} \rho) \sinh \alpha_2 (z - L - L_2) \quad (3.36)$$

$$E_{\phi 3} = E_0 r_o R \frac{J_1(k_{\rho} a)}{k_1(k_{\rho 2} a)} k_1(k_{\rho 2} \rho) \cosh(\alpha_1 z + \alpha_T) \quad (3.37)$$

$$E_{\phi 4} = E_0 \frac{J_1(k_{\rho} a)}{k_1(k_{\rho 2} a)} k_1(k_{\rho 2} \rho) \cos(\beta z - \frac{\phi_1}{2}) \quad (3.38)$$

$$E_{\phi 5} = E_0 \frac{\cos \frac{\phi_2}{2}}{\sinh \alpha_2 L_2} \frac{J_1(k_{\rho} a)}{k_1(k_{\rho 2} a)} k_1(k_{\rho 2} \rho) \sinh \alpha_2 (z - L - L_2) \quad (3.39)$$

$$E_{\phi 6} = E_0 J_1(k_{\rho 1} \rho) \cos(\beta z - \frac{\phi_1}{2}) \quad (3.40)$$

$$E_{\phi 7} = E_0 r_B R \frac{\cosh(\alpha_1 L_1 - \alpha_T)}{\sinh \alpha_7 L_3} J_1(k_{\rho 1} \rho) \sinh \alpha_7 (z + L_1 + L_3) \quad (3.41)$$

$$E_{\phi 8} = E_0 r_B R \frac{J_1(k_{\rho} a)}{k_1(k_{\rho 2} a)} k_1(k_{\rho 2} \rho) \frac{\cosh(\alpha_1 L_1 - \alpha_T)}{\sinh \alpha_7 L_3} J_1(k_{\rho 1} \rho) \sinh \alpha_7 (z + L_1 + L_3) \quad (3.42)$$

The corresponding magnetic fields can be obtained by the following Maxwell equation:

$$\vec{H} = \frac{j}{\omega \mu_0} \vec{\nabla} \times \vec{E} \quad (3.43)$$

In the above equations, $J_1(k_{\rho 1} \rho)$ and $k_2(k_{\rho 2} \rho)$ are the normal and the modified Bessel function [14], respectively; $k_{\rho 1}$ and $k_{\rho 2}$ are the radial wave numbers given by the following eigenvalue

equations [7]:

$$\frac{J_0(k_{\rho 1} a)}{J_1(k_{\rho 1} a)} = - \frac{k_{\rho 2} a}{k_{\rho 1} a} \frac{k_o(k_{\rho 2} a)}{k_1(k_{\rho 1} a)} \quad (3.44)$$

$$k_{\rho 2} a = \sqrt{(k_o a)^2 (\epsilon_{r6} - \epsilon_{r4}) - (k_{\rho 1} a)^2} \quad (3.45)$$

$$k_o a = \omega_o \sqrt{\epsilon_o \mu_o} = \frac{\Pi}{150} f_{GHz} \cdot a_{mm} \text{ is the wave number in free space.}$$

The eigenvalue $k_{\rho 1} a$ of the resonator depends mainly on the DR's radius a , the working frequency, the dielectric constant of the DR and the surrounding medium.

The separation constants β , α_1 and α_2 designate respectively the propagation constant inside the DR in the z direction (see Figure 3.11, region 6), and the attenuation constants of the mode $TE_{01\delta}$ in regions (2) and (7). These constants are given by:

$$\beta a = \sqrt{(k_o a)^2 \epsilon_{r6} - (k_{\rho 1} a)^2} \quad (3.46)$$

$$\alpha_1 a = \sqrt{(k_{\rho 1} a)^2 - (k_o a)^2 \epsilon_{r1}} \quad (3.47)$$

$$\alpha_2 a = \sqrt{(k_{\rho 1} a)^2 - (k_o a)^2 \epsilon_{r2}} \quad (3.48)$$

$$\alpha_7 a = \sqrt{(k_{\rho 1} a)^2 - (k_o a)^2 \epsilon_{r7}} \quad (3.49)$$

The dielectric constants ϵ_{ri} ($i = 1, \dots, 6$) and the dimensions are defined in Figure 3.11. The phases ϕ_1 and ϕ_2 introduced by the spacings $z=0$ to $-(L_1+L_3)$ and $z=L$ to $(L+L_2)$ between the forward and the reverse travelling waves are given by:

$$\frac{\phi_1}{2} = \tan^{-1} \left[\frac{\alpha_1}{\beta} \cosh(\alpha_1 L_1) \right] \quad (3.50)$$

$$\frac{\phi_2}{2} = \beta L - \frac{\phi_1}{2} \quad (3.51)$$

where
$$r_B = \frac{\sqrt{\beta^2 + \alpha_1^2}}{\alpha_1} \quad (3.52)$$

$$R = \sqrt{A^2 + B^2} \quad (3.53)$$

$$A = 2 \cos \frac{\phi_1}{2} \cos \alpha_B \quad (3.54)$$

$$B = 2 \sin \frac{\phi_1}{2} \sin \alpha_B \quad (3.55)$$

$$\alpha_B = \tan^{-1} \left(\frac{\beta}{\alpha_1} \right) \quad (3.56)$$

$$\alpha_T = \tan^{-1} \left(\frac{A}{B} \right) \quad (3.57)$$

The contribution of the fields of different region to the

magnetic dipole moment is derived to be given by [14]:

$$m_1 = -j \pi \omega \varepsilon_1 E_o \frac{a^2}{k_\rho} J_1(k_\rho a) r_B R Tm(k_\rho a) \theta_1 \quad (3.58)$$

$$m_2 = -j \pi \omega \varepsilon_2 E_o \frac{a^2}{k_\rho} J_1(k_\rho a) \frac{\cos \frac{\phi_2}{2}}{\sinh \alpha_2 L_2} Tm(k_\rho a) Y_2 \quad (3.59)$$

$$m_3 = -j \pi \omega_o \varepsilon_o E_o \frac{a^2}{k_{\rho 2}} J_1(k_\rho a) r_B R Pm(k_{\rho 2} a) \theta_1 \left(\frac{\alpha_2^2 - k_{\rho 1}^2}{k_o^2} \right) \quad (3.60)$$

$$m_4 = -j \pi \omega_o \varepsilon_4 E_o \frac{a^2}{k_{\rho 2}} J_1(k_\rho a) Pm(k_{\rho 2} a) \theta_{1/2} L \quad (3.61)$$

$$m_5 = -j \pi \omega_o \varepsilon_o E_o \frac{a^2}{k_{\rho 2}} J_1(k_\rho a) \frac{\cos \frac{\phi_2}{2}}{\sinh \alpha_2 L_2} Pm(k_{\rho 2} a) Y_2 \left(\frac{\alpha_2^2 - k_{\rho 1}^2}{k_o^2} \right) \quad (3.62)$$

$$m_6 = -j \pi \omega_o \varepsilon_6 E_o \frac{a^2}{k_\rho} J_1(k_\rho a) Tm(k_\rho a) \theta_{1/2} L \quad (3.63)$$

$$m_7 = -j \pi \omega_o \varepsilon_o E_o \frac{a^2}{k_\rho} J_1(k_\rho a) r_B R \frac{\cosh(\alpha_1 L_1 - \alpha_T)}{\sinh \alpha_7 L_3} Tm(k_\rho a) Y_7 \quad (3.64)$$

$$m_8 = -j \pi \omega_o \varepsilon_o E_o \frac{a^2}{k_{\rho 2}} J_1(k_\rho a) r_B R \frac{\cosh(\alpha_1 L_1 - \alpha_T)}{\sinh \alpha_7 L_3} Pm(k_{\rho 2} a) Y_7 \left(\frac{\alpha_7^2 - k_{\rho 1}^2}{k_o^2} \right) \quad (3.65)$$

where

$$\theta = \frac{1}{\alpha_1} (\sinh(\alpha_1 L_1 - \alpha_T) + \sinh \alpha_T) \quad (3.66)$$

$$Y_2 = \frac{2}{\alpha_2} \sinh^2 \left(\frac{\alpha_2 L_2}{2} \right) \quad (3.67)$$

$$Y_7 = \frac{2}{\alpha_7} \sinh^2 \left(\frac{\alpha_7 L_3}{2} \right) \quad (3.68)$$

$$\Theta_{1/2} = \frac{\sin \frac{\phi_1}{2} + \sin \frac{\phi_2}{2}}{\frac{\phi_1}{2} + \frac{\phi_2}{2}} \quad (3.69)$$

$$Tm(k_{\rho 1} a) = \frac{2}{k_{\rho 1} a} - \frac{J_0(k_{\rho 1} a)}{J_1(k_{\rho 1} a)} \quad (3.70)$$

$$Pm(k_{\rho 2} a) = \frac{2}{k_{\rho 2} a} + \frac{k_o(k_{\rho 2} a)}{k_1(k_{\rho 2} a)} \quad (3.71)$$

The stored energy in the various regions can be obtained by using (3.32) and (3.35) to (3.42), and are given by [14]:

$$W_1 = \frac{1}{4} \Pi \varepsilon_1 E_o^2 a^2 L_1 r_B^2 R^2 J_1^2(k_{\rho} a) Tr(x) \left(\frac{\Theta_2}{2\alpha_1 L_1} + 1 \right) \quad (3.72)$$

$$W_2 = \frac{1}{4} \Pi \varepsilon_2 E_o^2 a^2 L_2 J_1^2(k_{\rho} a) \frac{\cos^2 \frac{\phi_2}{2}}{\sinh^2 \alpha_2 L_2} Tr(x) (\sigma_2 - 1) \quad (3.73)$$

$$W_3 = \frac{1}{4} \Pi \varepsilon_3 E_o^2 a^2 L_1 J_1^2(k_{\rho} a) r_B^2 R^2 Pr(x) \left(\frac{\Theta_2}{2\alpha_1 L_1} + 1 \right) \quad (3.74)$$

$$W_4 = \frac{1}{4} \Pi \varepsilon_4 E_o^2 a^2 L J_1^2(k_{\rho} a) Pr(x) (\Theta + 1) \quad (3.75)$$

$$W_5 = \frac{1}{4} \Pi \varepsilon_5 E_o^2 a^2 L_2 J_1^2(k_\rho a) \frac{\cos^2 \frac{\phi_2}{2}}{\sinh^2 \alpha_2 L_2} Pr(x) (\sigma_2 - 1) \quad (3.76)$$

$$W_6 = \frac{1}{4} \Pi \varepsilon_6 E_o^2 a^2 L J_1^2(k_\rho a) Tr(x) (\theta + 1) \quad (3.77)$$

$$W_7 = \frac{1}{4} \Pi \varepsilon_7 E_o^2 a^2 L_3 J_1^2(k_\rho a) r_B^2 R^2 \frac{\cosh^2(\alpha_1 L_1 - \alpha_T)}{\sinh^2 \alpha_7 L_3} Tr(x) (\sigma_3 - 1) \quad (3.78)$$

$$W_8 = \frac{1}{4} \Pi \varepsilon_8 E_o^2 a^2 L_3 J_1^2(k_\rho a) r_B^2 R^2 \frac{\cosh^2(\alpha_1 L_1 - \alpha_T)}{\sinh^2 \alpha_7 L_3} Pr(x) (\sigma_3 - 1) \quad (3.79)$$

where

$$\theta_2 = \sinh 2\alpha_T + \sinh 2(\alpha_1 L_1 - \alpha_T) \quad (3.80)$$

$$\sigma_2 = \frac{\sinh 2\alpha_2 L_2}{2\alpha_2 L_2} \quad (3.81)$$

$$\sigma_3 = \frac{\sinh 2\alpha_7 L_3}{2\alpha_7 L_3} \quad (3.82)$$

$$\theta = \frac{\sin \phi_1 + \sin \phi_2}{\phi_1 + \phi_2} \quad (3.83)$$

$$Tr(x) = \frac{J_o^2(x)}{J_1^2(x)} - \frac{2}{x} \frac{J_o(x)}{J_1(x)} + 1 \quad (3.84)$$

$$Pr(x) = \frac{k_o^2(x)}{k_1^2(x)} + \frac{2}{x} \frac{k_o(x)}{k_1(x)} - 1 \quad (3.85)$$

The radial component of the magnetic field $H_{\rho 4}$ created by DR1, which is mainly responsible for the coupling, can be obtained by using $E_{\phi 4}$ (Equation (3.38)) and Maxwells equation $\bar{H} = \frac{j}{\omega \mu_0} \bar{\nabla} \times \bar{E}$ and is given by:

$$H_{\rho 4} = \frac{j\beta}{\omega \mu_0} E_0 \frac{J_1(k_\rho a)}{k_1(k_{\rho 2} a)} k_1(k_{\rho 2} \rho) \sin\left(\beta z - \frac{\phi_1}{2}\right) \quad (3.86)$$

Now that we have all the necessary field expressions we can evaluate the coupling as a function of separation distance s using Equation (3.34).

A program DRCOUP was written to compute the above coupling coefficient and the theoretical results are compared with the measurements in the next section. The program listing may be found in Appendix A.

3.2.3 Evaluation of Theoretical Results

A computer program was developed to compute the coupling coefficient between two DRs based on the above equations. The accuracy of the above model was evaluated by using a test fixture, shown in Figure 3.13, which basically consists of a metallic housing enclosing the two resonators and 50Ω microstrip arcs etched on the substrate to provide input and output coupling. The substrate employed is Cu217 which had a dielectric constant $\epsilon_r=2.17$ and thickness=0.794mm. The DRs employed were commercially available from Trans. Tech. Inc.

with diameter=17.145mm and height=7.722mm made of (ZrSn)TiO₄ with $\epsilon_r=36$. The polyurethane foam spacers which supported the DRs above the substrate were chosen for minimal distortive effects on the electromagnetic field and had a permittivity of about 2.2 and thickness of 1mm.

Measured values of the coupling coefficient were calculated from the transmission response of the structure using a scalar network analyser. The transmission response of two identical resonators when placed next to each other resembles a bandpass filter having two peaks when the resonators are over-coupled, that is, when k is greater than k_c , where k_c is critical coupling yielding a maximally flat response. The transmission curve sketched in Figure 3.14 shows the typical shape of the peaks, and defines the parameters associated with the response. The coupling coefficient k may be computed from the centre frequency f_o , the peak separation Δf and the transmission dip ΔL (in dB) by means of the following relations [12]:

$$k = \frac{1}{\sqrt{1 - \left(\frac{k_c}{k}\right)^2}} \frac{\Delta f}{f_o} \quad (3.87)$$

$$\Delta L = 20 \log_{10} \left[\frac{1}{2} \left(\frac{k}{k_c} + \frac{k_c}{k} \right) \right] \quad \text{dB} \quad (3.88)$$

The factor

$$f(\Delta L) = \frac{1}{\sqrt{1 - \left(\frac{k_c}{k}\right)^2}} \quad (3.89)$$

is plotted as a function of ΔL in Figure 3.15. Note that this factor is near unity, deviating from unity by less 0.5% for $\Delta L > 14$ dB. By means of Figure 3.14 and measured values of Δf and f_0 , k was obtained for various centre-to-centre spacings of the resonators. The loop couplings were purposely kept weak to maximise ΔL , thus sharpening the peaks and making the measurement less sensitive to ΔL . At the largest values of s for which measurements were taken ΔL had diminished to about 3.0 dB, and the factor, Δf , was about 1.1.

Figure 3.16 shows the comparison between the theoretical and measured values of k as a function of s . From this graph we can see that the measured values are in excellent agreement with the computed values in the range of measurement.

3.3 Conclusions

New mathematical expressions have been derived to accurately characterise the coupling which exists between two identical dielectric resonators operating in their dominant mode in a microstrip environment. The effect of the metal enclosure and the low dielectric constant spacers to support the resonators have also been taken into account in the analysis. Based on these expressions a program DRCOUP has been developed to facilitate the calculation of this parameter. Comparison between theoretical and experimental results of coupling show very good agreement.

References

1. Matthaei, G.L., Young, L., and Jones, E.M.T., "Microwave Filters, Impedance-Matching Network and Coupling Structures," McGraw-Hill, New York, 1964.
2. Guillon, P., Byzery, B., Chaubet, M., "Coupling Parameters Between a Dielectric Resonator and a Microstrip Line," IEEE Trans. on Microwave Theory & Tech., vol.MTT-33, No.3, March 1985, pp222-226.
3. Guo, K.Z., Trinogga, L.A., Edgar, T.H., "DR Coupling: Improvement to an Existing Approach," Electronics Letters, 3rd March 1988, vol.24, No.5, pp285-287.
4. Day JR, W.R., "Dielectric Resonators as Microstrip-Circuit Elements," IEEE Trans. on Microwave Theory & Tech., vol.MTT-18, Dec. 1970, pp1175-1176.
5. Cohn, S.B., "Microwave Bandpass Filters Containing High-Q Dielectric Resonators," IEEE Trans. on Microwave Theory & Tech., vol.MTT-16, April 1968, pp218-227.
6. Skalicky, P., "Coupling Coefficient Between Dielectric Resonator and Microstrip Line," Electronics Letters, vol.17, Jan.1981, pp99-100.
7. Kajfez, D., and Guillon, P., "Dielectric Resonators," Artech House, 1986.
8. Khanna, A.P.S., "Q Measurement of Microstrip-Coupled Dielectric Resonators," Microwave & RF., Jan.1984, pp81-86.
9. Trinogga, L.A., Guo, K., Hunter, I.C., "Practical

- Microstrip Circuit design," Ellis Horwood, 1991.
10. Cohn, S.B., "A miniature High Q Bandpass Filter Employing Dielectric Resonators," IEEE Trans. on Microwave Theory & Tech., vol.MTT-16, April 1968, pp210-218.
 11. Itoh, T., and Rudokas, R.S., "New Method for Computing the Resonant Frequencies of Dielectric Resonators," IEEE Trans. on Microwave Theory & Tech., vol.MTT-25, Jan.1977, pp52-54.
 12. Cohn, S.B., and Torgow, E.N., "Investigations of Microwave Dielectric Resonator Filters," Rantec Corp., Calabases, CA, Seventh Quarterly Report 7, Contract DA-36-039-AMC-02267(E), 1 March 1965 - 31 May 1965.
 13. Collin, R.E., "Field Theory of Guided Waves," McGraw-Hill, 1960.
 14. Virdee, B.S., Internal Research Report, 1994.
 15. Abramowitz, M., and Stegun, I.R., "Handbook of Mathematical Functions," Dover Publications Inc., New York, 1965.

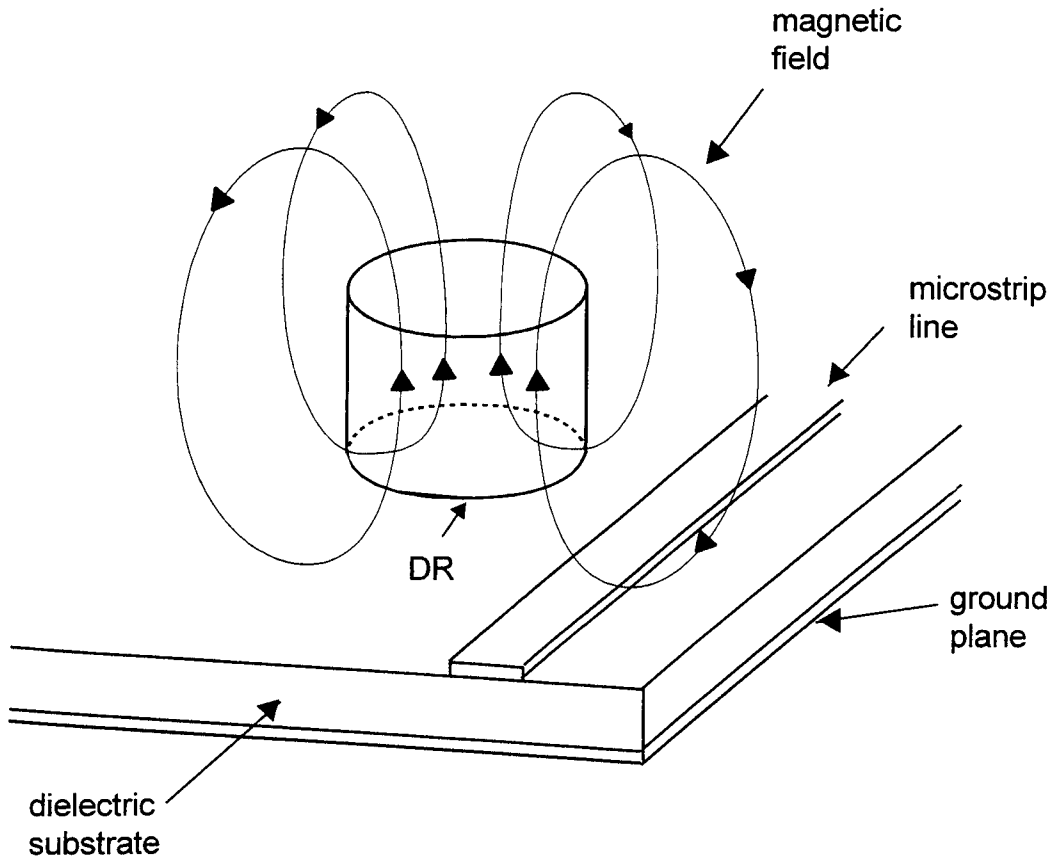


Figure 3.1 A dielectric resonator coupled with a microstrip line.

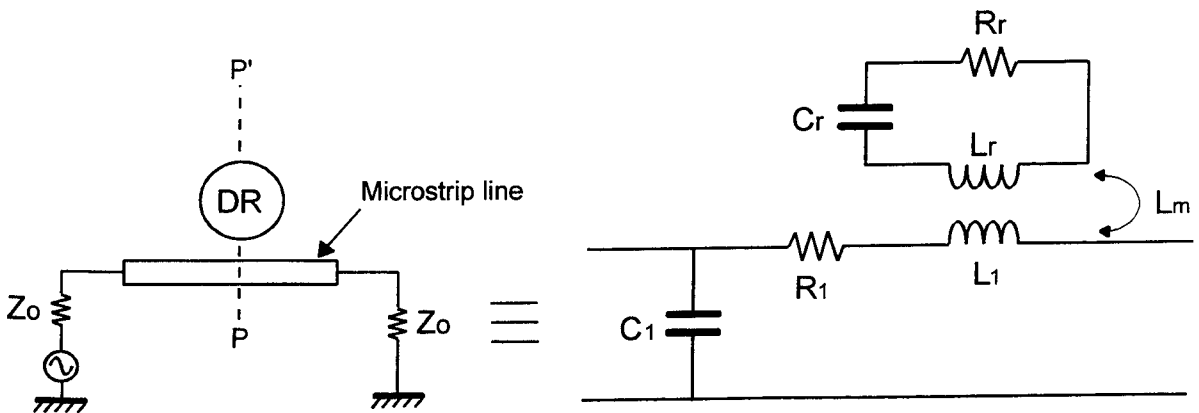


Figure 3.2 Equivalent circuit representing the coupling between a microstrip line and dielectric resonator.

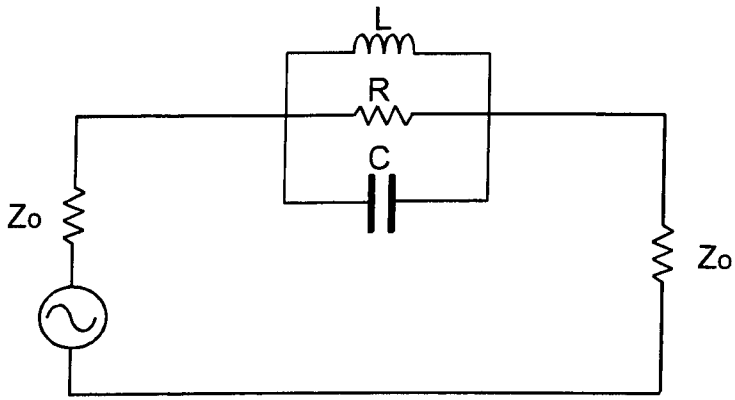


Figure 3.3 Simplified equivalent circuit of a dielectric resonator coupled with a microstrip line.

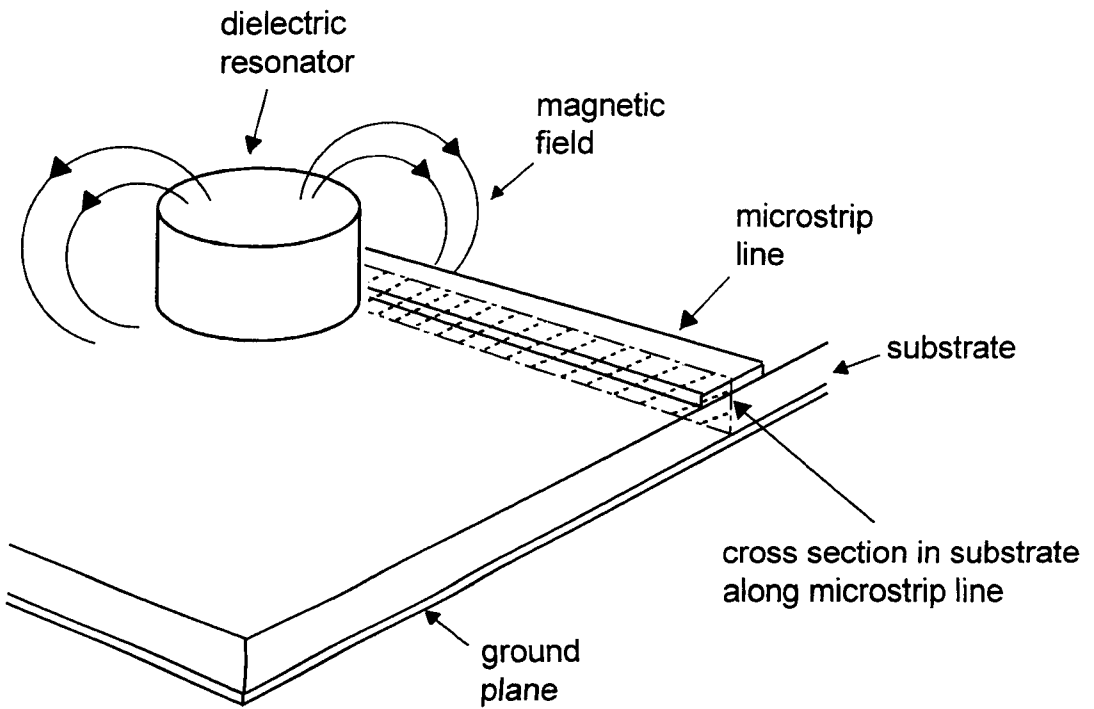


Figure 3.4 Magnetic flux linkage of the resonator field into the microstrip line.

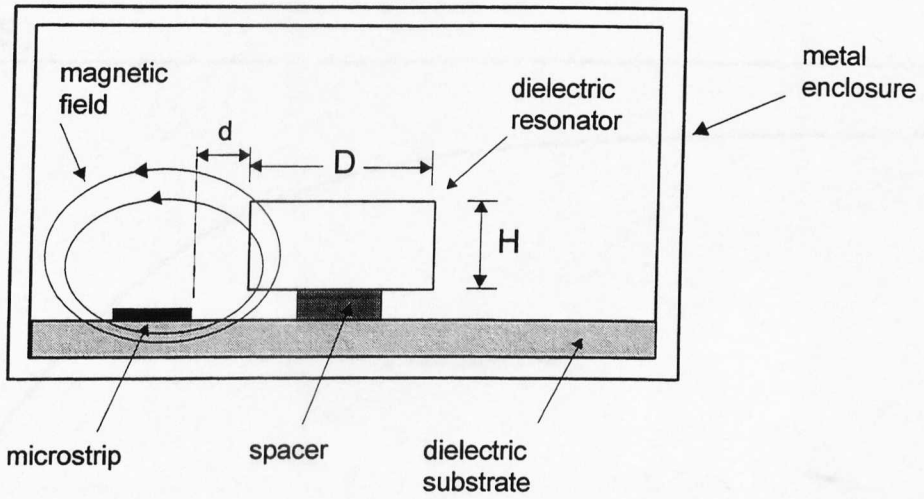


Figure 3.5 Configuration for coupling the TE_{018} mode of a dielectric resonator to a microstrip.

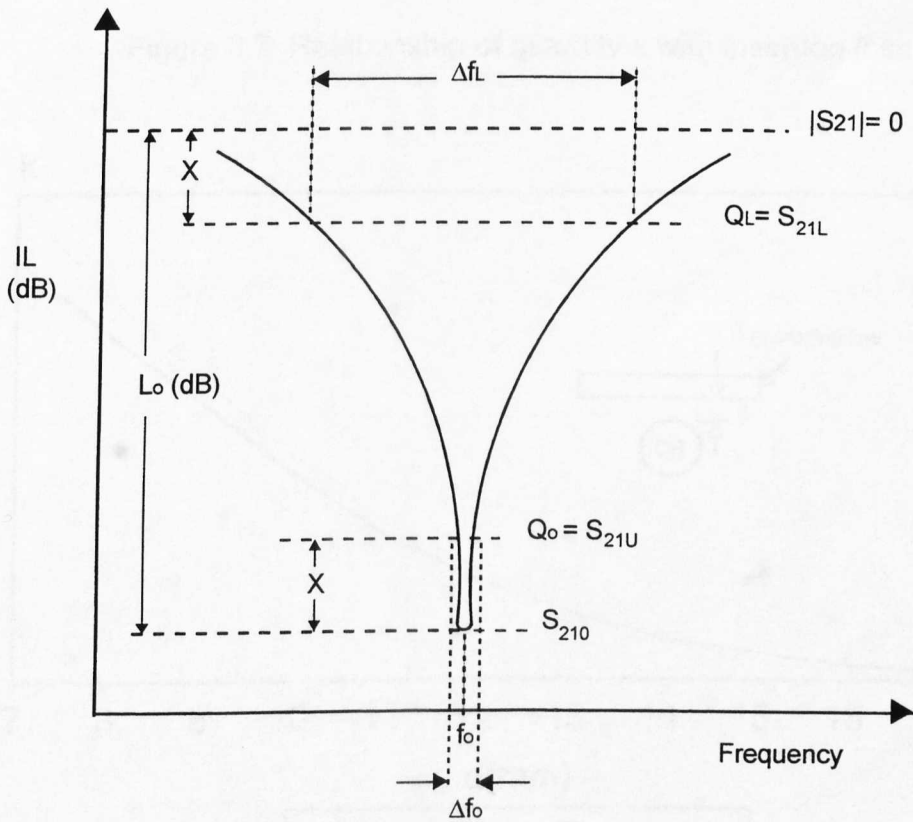


Figure 3.6 Typical transmission response of a dielectric resonator at TE_{018} mode coupled to a microstrip line.

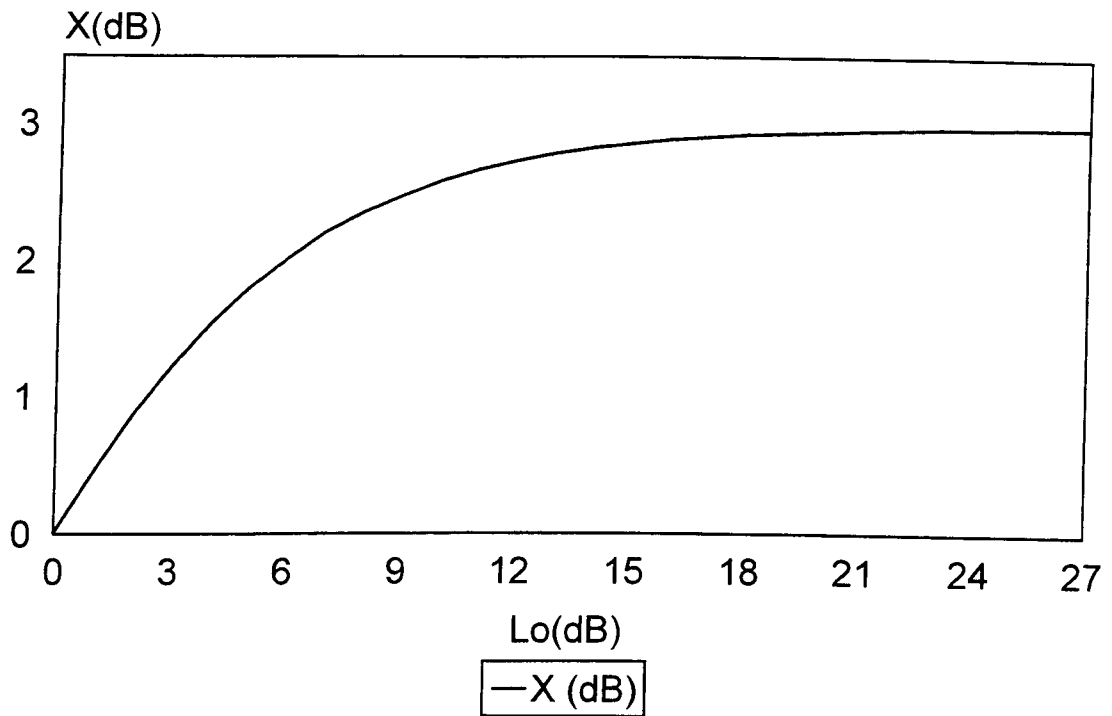


Figure 3.7 Relationship of quantity x with insertion loss.

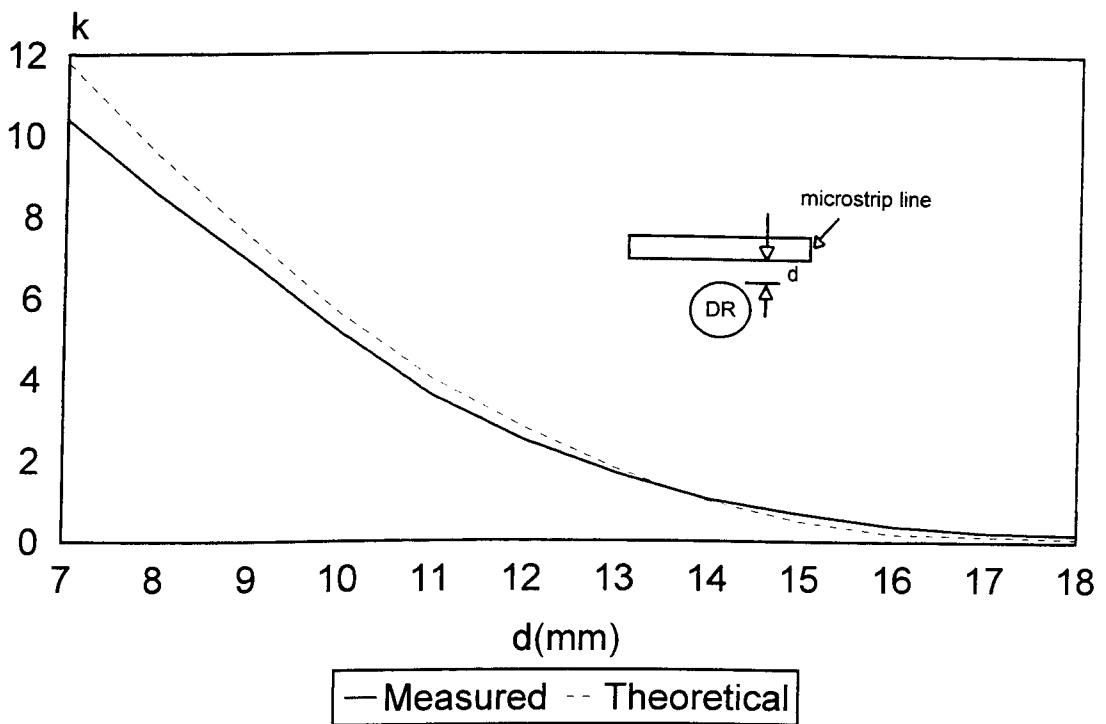


Figure 3.8 Coupling coefficient as a function of distance between the line and the resonator.

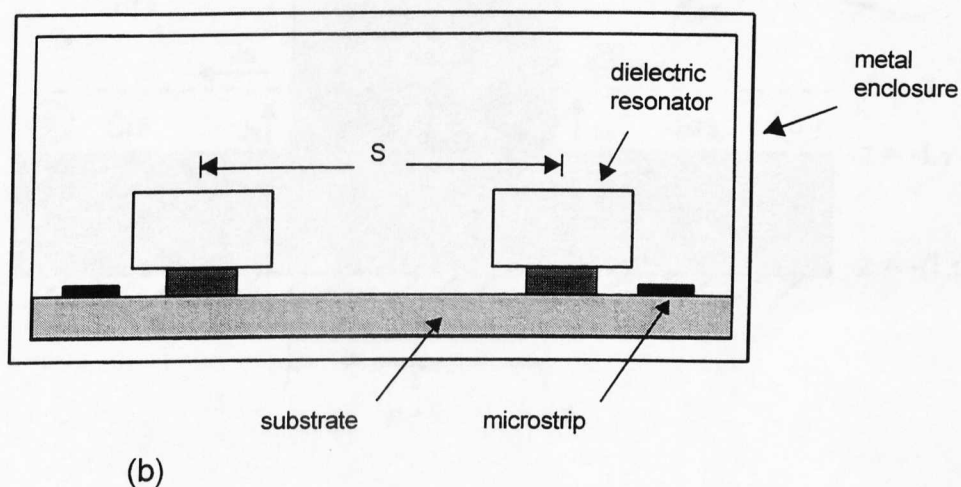
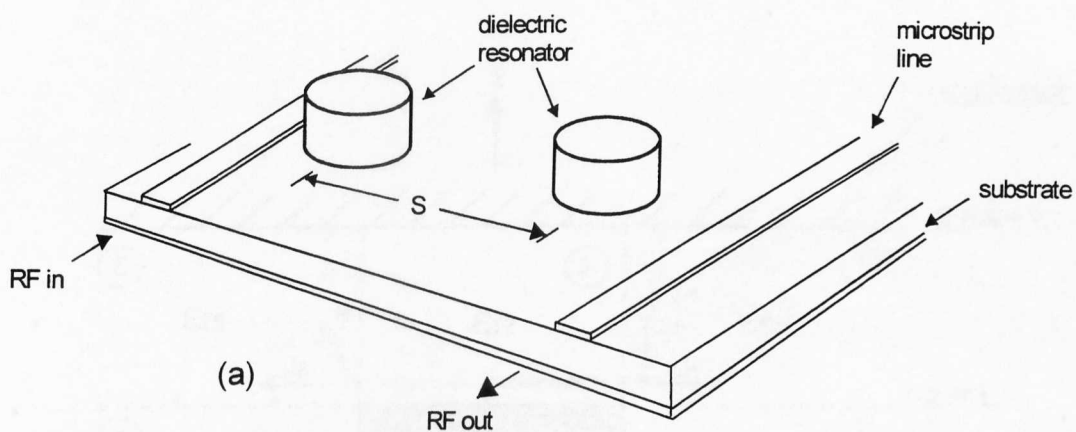


Figure 3.9 Configuration for coupling between two dielectric resonators.

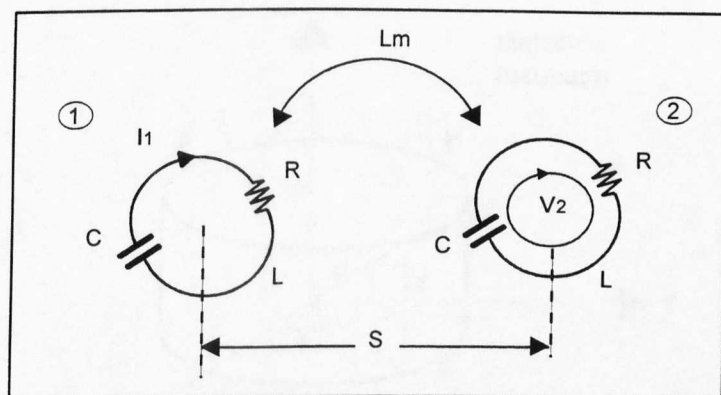


Figure 3.10 Representation of coupling between two dielectric resonators operating in the TE_{018} mode.

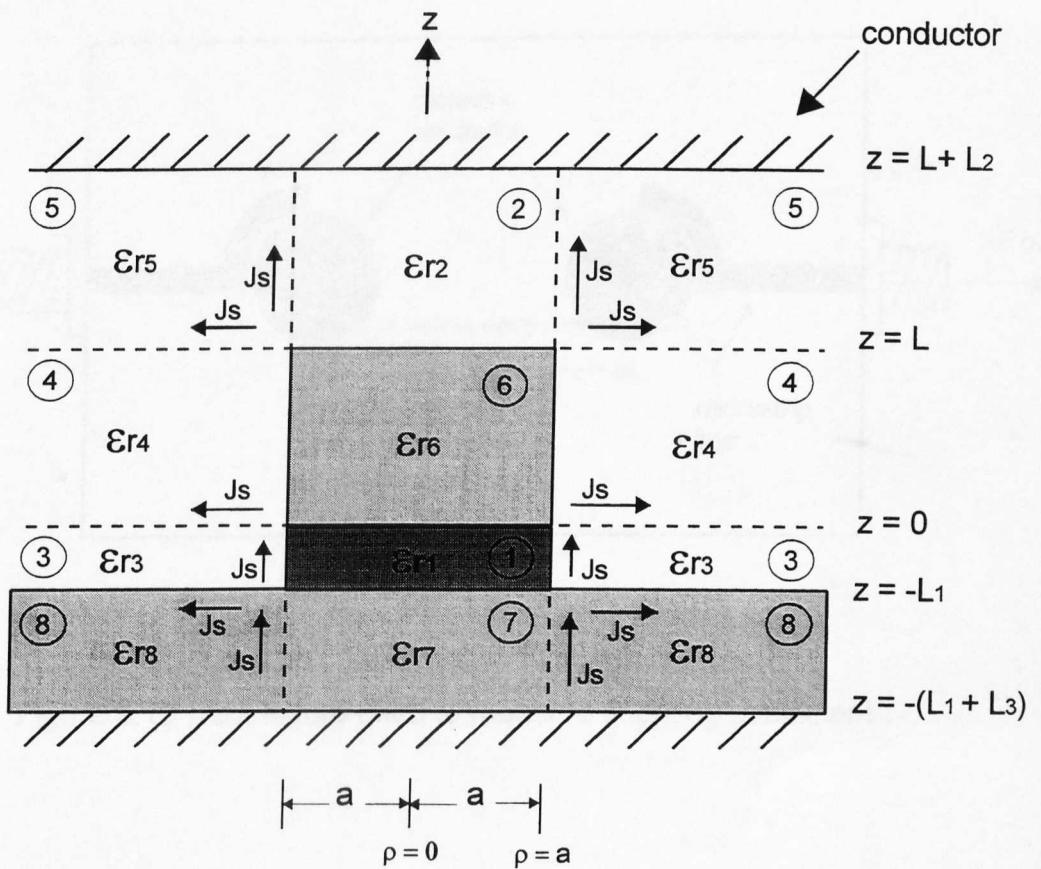


Figure 3.11 Improved model of a shielded dielectric resonator.

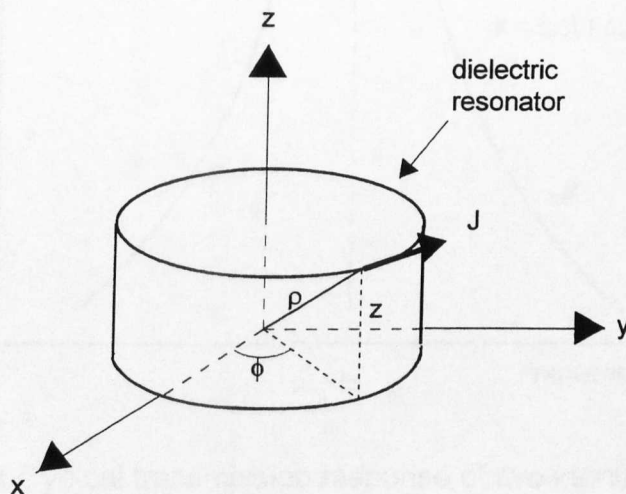


Figure 3.12 System coordinates for the magnetic dipole moment.

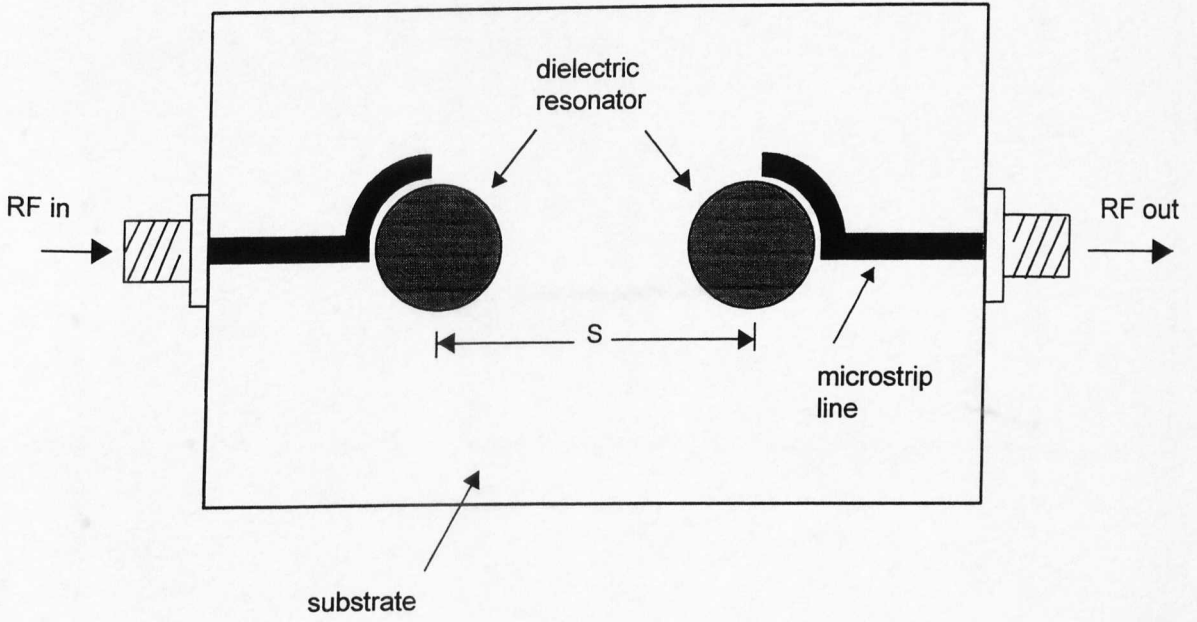


Figure 3.13 Test fixture used to measure coupling coefficient.

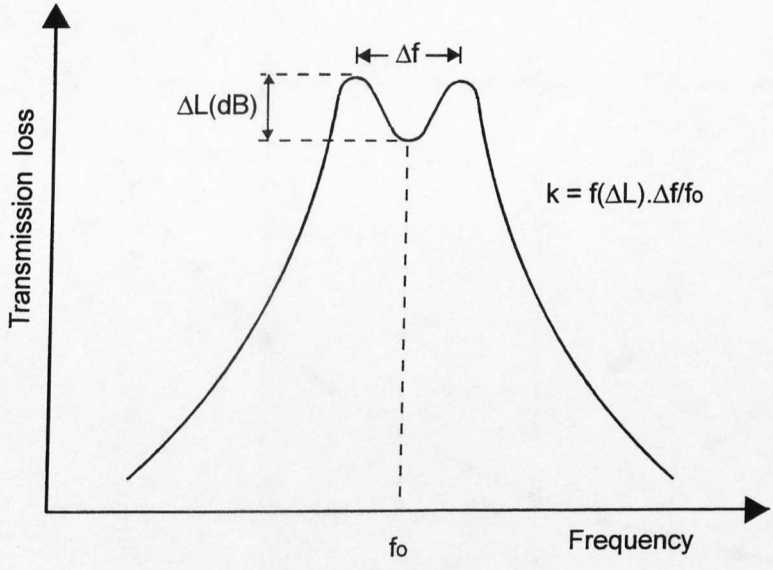


Figure 3.14 Typical transmission response of two identical dielectric resonators coupled to each other.

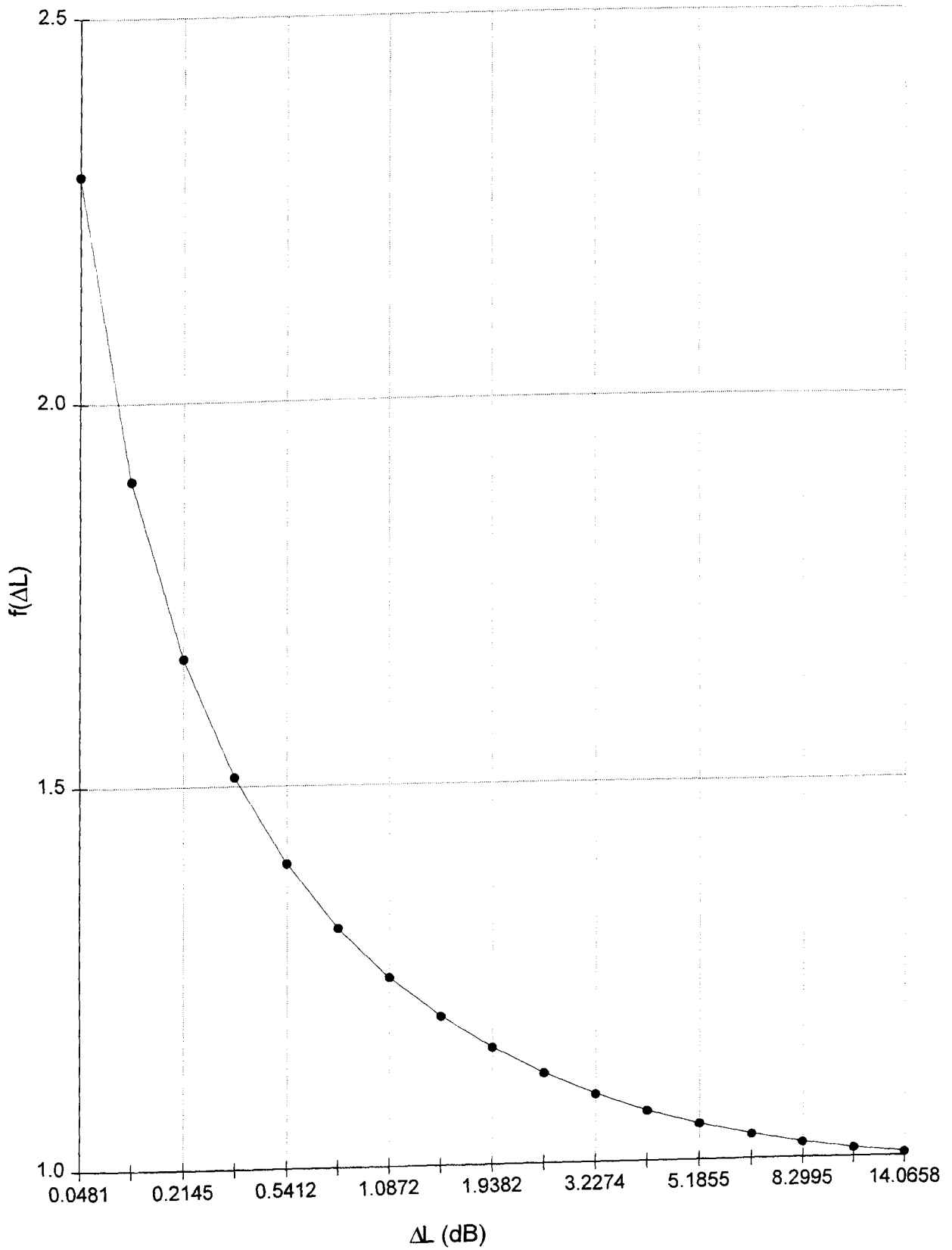


Figure 3.15 Graph of factor $f(\Delta L)$ used in the measurement of coupling coefficient between two DRs.

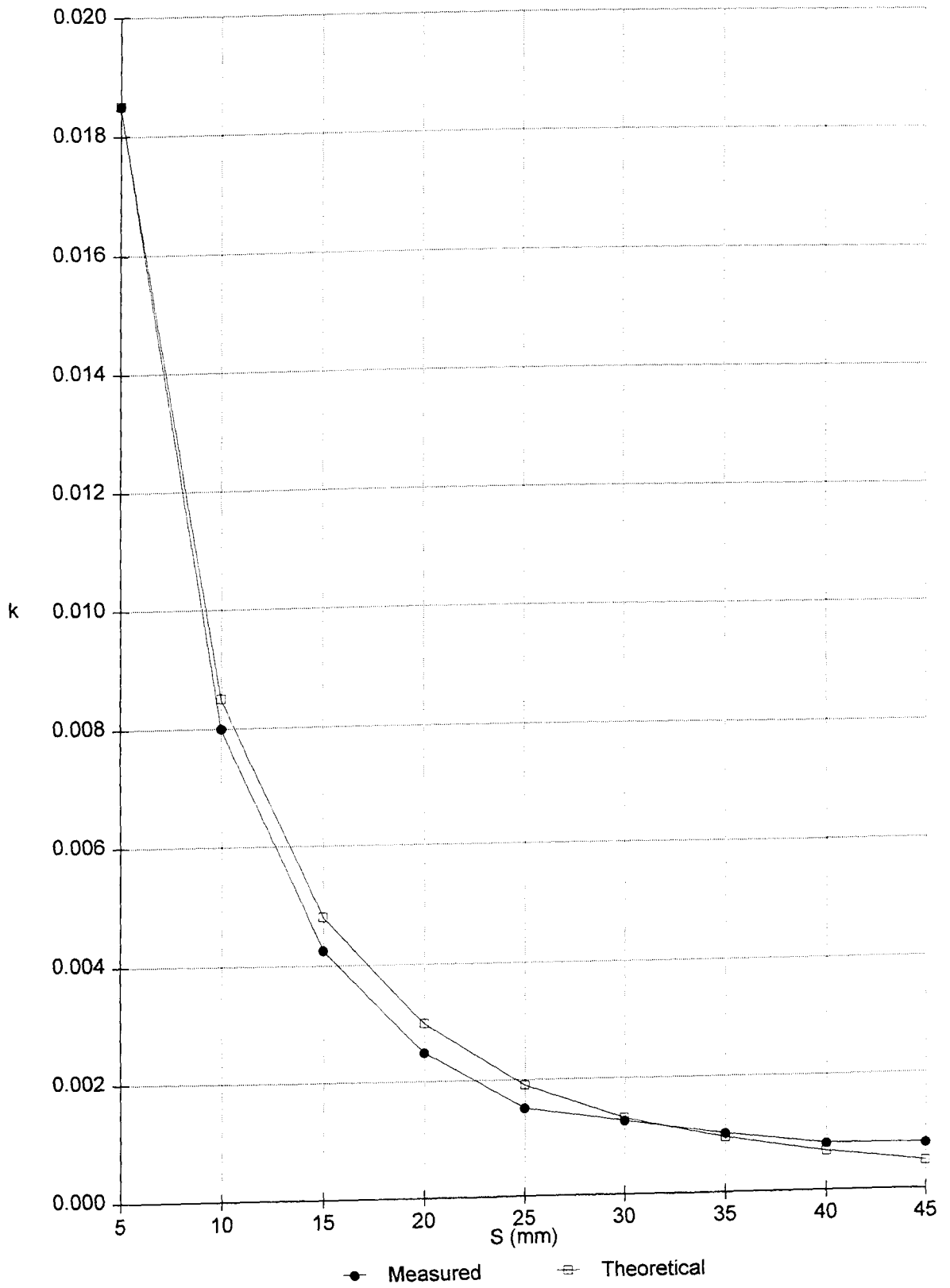


Figure 3.16 Coupling coefficient as a function of the distance between two resonators.

Chapter 4

Microstrip Topologies for Electronically Tuning DR $TE_{01\delta}$ -mode Resonant Frequency

4.0 Introduction

From Chapter 2 it was seen that shielded DRs possess capabilities that make them competitive with conventional microwave cavities and that the high Q obtainable is accompanied by the advantages of reduction in size and easier temperature stabilisation. Electronic tuning of such systems therefore has considerable importance since this enables DRs to be used where a high quality resonator and/or fast tuning are needed, e.g. in mobile radio base stations or in systems using dynamic channel allocation.

Tuning of DRs can essentially be accomplished by modifying the various electromagnetic fields supported by the resonator. There are three principal techniques, currently available which are capable of achieving this using non-mechanical methods:

- (a) Varactor tuning
- (b) Ferrite tuning
- (c) Optical tuning

From a practical point of view, however, the latter two techniques have a number of difficulties associated with them which will be discussed first in this chapter. As a consequence

the approach adopted in this thesis relies on the electronic tuning afforded by the coupling of varactor diodes to the DR.

This chapter commences with a review of the different tuning mechanisms currently available to tune a DR. Based on the selected tuning mechanism an experimental study of novel tuning structures is then presented. The tuning range of the DR and the effects of tuning on the quality factor are investigated. An analytical expression is developed which is used to predict the DR's frequency response and tuning capability. Finally, the effects of the large signal on this structure is also studied.

4.1 Tuning Mechanisms

A DR can be tuned over a bandwidth ($\approx 10\%$) by perturbing the resonators' magnetic field. This can be achieved by varying the air gap between the ceramic disc and the metal enclosure, with, for example, a movable metal plate or screw coaxial with the ceramic disc. The tuning mechanism involved here can be explained by the perturbational principle [1]. Namely, when a metal wall of any resonant cavity is moved inward, the change in resonant frequency is proportional to the difference in stored magnetic and electric energies with the displaced volume.

With electronic tuning, since there is no volume displaced, the frequency variation is related to the change in the energy stored in the reactances of the system. It is

evident that in both cases the adjustment of the resonant frequency to a prescribed value is based on the perturbation of the fringing fields outside the resonator. For a particular mode, the tuning range is determined by the amount of this perturbation. For example, if the tuning mechanism increases the stored magnetic energy with respect to the electric energy, the resonant frequency will shift towards higher frequencies [2], with a deviation proportional to the energy difference. If it decreases, the shift will be towards lower frequencies. A wide tuning bandwidth thus needs a strong perturbation which may drastically degrade the system quality. A compromise between the tuning bandwidth and DR qualities is necessary.

Dielectric resonator frequency control may be accomplished either by solid-state devices such as varactors or PIN diodes, or low-loss magnetic materials such as single-crystal Yttrium-Iron-Garnet (YIG) sphere ($f > 2\text{GHz}$) or disc-ferrite. The latter elements, which are based on the control of the magnetic field, lead to a limited tuning range (3% @ a centre frequency of 8GHz) [3-6]. However, like most of the mechanisms based on magnetic materials, methods utilising ferrite materials usually need a large and cumbersome electromagnet for producing the controlling magnetic field. Moreover, being current driven, their tuning speed is usually very low (e.g. $\sim 0.5\text{MHz/s}$) and subject to phase noise. Figure 4.1 shows the configuration used for this kind of tuning.

Faster tuning can be achieved by solid-state devices which are usually varactor diodes if continuous tuning is desired, or PIN diodes in the case of discrete tuning. Currently there are few papers which describe electronic tuning of a shielded DR. In reference [7], a dielectric resonator oscillator (DRO) tuned by PIN diodes is described. The tuning element consists of a conducting disc divided into four segments interconnected by PIN diodes and placed above the DR, Figure 4.2. Depending upon the conduction state of the diodes, the current-flow lines induced in the disc by the electrical field of the TE_{018} mode may be cut or not. The author reported perturbation results yielding a jump in frequency of about 40MHz at the centre frequency of 16GHz. No variation of the change in the value of the unloaded Q due to the tuning system was given.

Tuning employing a resonant loop using varactor diodes has been used [6,8,9,10] and is shown in Figure 4.3. It has been reported in reference [6] that a tuning range of 0.75% at the working frequency of 7.4GHz, with an unloaded Q above 1000, has been obtained. In reference [8], the authors used a loop with a single varactor and a bypass capacitor for the r.f. current to tune the DR. A theoretical investigation of this system shows that a tuning range as high as 30MHz at 1.2GHz can be obtained, depending on how tightly the resonator is coupled to the loop, and on the natural resonant frequency of the tuning loop. However, here also, the overall unloaded Q of the device is poor (<1000).

Another promising method of perturbing the DRs magnetic field is by optical means. This can be achieved by changing the conductivity of a layer of a photosensitive material deposited on the top surface of the DR by means of light from a laser or LED, as shown in Figure 4.4. Using this technique, tuning bandwidths of better than 0.1% have been achieved at X-band [11,12]. However, a major disadvantage of this method is that the external Q of the circuit degrades by about 30%. Moreover, light sources employed for fast modulation, such as He-Ne gas laser or GaAs LED produce a small frequency change (typically 0.4-0.5MHz @ $f_0=10\text{GHz}$). A comparison of the various tuning mechanisms is given in Table 4.1.

4.2 Tuning Mechanism Chosen

From amongst the numerous tuning techniques available careful comparative study showed that the varactor diode to be the most suitable tuning mechanism for low power requirements, since it offers low-loss and high tuning speed. Varactors offer also continuous frequency control and potential advantages in size, weight and cost.

The coupling of the varactor diode to the DR depends mainly on the mode to be tuned, the structure supporting the varactor, and the position of this structure with respect to the DR. For clarity of presentation, the structure supporting the varactor will be referred to as the tuning configuration,

and this will be discussed after the next section on varactor diodes.

4.3 Varactor diodes

The varactor diode is a nonlinear device and provides a voltage dependent variable capacitance. This property can be used in many applications, such as parametric amplification, harmonic generation, mixing, detection, and voltage-variable tuning.

Choosing a varactor for a particular microwave application is a critical step in any design, since it involves the selection of the important parameters to be optimised for best results. For example, the non-linearity feature of the varactor, which is a desired property in the design of parametric amplifiers or harmonic generators [13], may cause serious limitations in achieving linear tuning. In this section a review of the main properties of the semiconductor p-n junction is presented. This will enable us to understand, characterise, and consequently assist selection of the varactors to be used. A description of the physics of the p-n junction and the fabrication technologies are covered adequately in other texts and need not be repeated here. The interested reader is referred to references [14,15,16].

4.3.1 P-N Junction diode

The use of varactors to tune microwave circuits is mainly governed by four parameters:

- (i) Characteristic capacitance-voltage
- (ii) Junction capacitance at zero bias
- (iii) Series resistance
- (iv) Breakdown voltage

These parameters are in turn fixed by the type of semiconductor used and the techniques employed in fabrication.

The three most important semiconductors used in the fabrication of diodes in general are: germanium (Ge), silicon (Si), and gallium arsenide (GaAs). However, most of the varactor diodes currently in use are fabricated from Si, because of the low saturation current in Si diodes and the advanced state of Si technology. GaAs has found increasing application in recent years because of its high carrier mobility and low bulk resistivity (high Q) compared to Si (see Table 4.2). However, GaAs currently lags Si technology in development.

4.3.2 Types of Varactor Diodes

For a given semiconductor the characteristic capacitance-voltage of the varactor diode is mainly fixed by the dopant profile within the junction. In effect, if N designates the generalised doping distribution (N can be equal either to the acceptor N_A or to the donor N_D doping distributions), then N can be expressed as:

$$N = Bx^m \quad (4.1)$$

where x , considered positive, is the distance from the junction (see Figure 4.5). For $m=0$, we have $N=B=\text{constant}$ which corresponds to the abrupt junction uniformly doped. For $m=1$, $N=Bx$ and the doping profile is linearly graded. A junction having this profile is called a linearly graded junction. For $m<0$, the junction is said to be hyper-abrupt. The above cases are summarised in Figure 4.6(a) [14].

The depletion layer capacitance is related to the reverse voltage by the well-known relationship:

$$C_j(V) = C_o \left(1 - \frac{V}{\phi}\right)^{-\gamma} \quad (4.2)$$

where $\gamma = \frac{1}{m+2}$

and where $C_o=C(V=0)$ is the junction capacitance at zero bias. C_o is usually chosen to provide a reasonable level of capacitance reactance of the circuit; ϕ is the junction potential which depends upon the doping density and on the type of semiconductor (see Table 4.3). γ , the sensitivity, is an important parameter in characterising the varactor and is given by:

$$\gamma = \frac{dC_j}{C_j} = - \frac{d(\log C_j)}{d(\log V)} = \frac{1}{m + 2} \quad (4.3)$$

Table 4.4 shows the sensitivity relative to each type of diode.

The capacitance-voltage relationships of these junction diodes are shown in Figure 4.6(b). It can be seen that the hyper-abrupt diode has the highest sensitivity and gives rise to the largest capacitance variation.

For a simple resonant circuit comprised of an inductor, L , and a varactor with junction capacitance $C_j(V)$, the frequency-voltage relationship is given by:

$$f(V) = \frac{1}{2\pi \sqrt{C_j(V)L}} = f_o \left(1 - \frac{V}{\Phi}\right)^{\gamma/2} \quad (4.4)$$

where $f_o = \frac{1}{2\pi \sqrt{C_o L}}$ is the resonant frequency at zero bias.

Equation (4.4) shows that linear tuning can be obtained by choosing a hyper-abrupt junction with $\gamma=2$.

Substituting GaAs for Si diode in a real structure does not necessarily result in a better performance. It can be seen in Table 4.5 [17] that for high power (typically a few watts), wide band tuning range and good stability, silicon remains a better choice.

4.4 Figures of Merit

4.4.1 Quality Factor

Figure 4.7 shows a simplified equivalent circuit of a varactor diode without encapsulation. R_s designates the series equivalent resistance in the bulk semiconductor; R_p is the parallel equivalent resistance of generation-recombination, diffusion, and surface leakage currents; C_j is the junction capacitance. Both R_s and C_j generally decrease with reverse bias voltage while R_p increases.

The quality factor of the varactor, which is given by the ratio of the energy stored to the energy dissipated per cycle, can be expressed (see Figure 4.7 for parameter notation) by:

$$Q = \frac{\omega C_j R_p}{1 + \omega^2 C_j^2 R_p R_s} \quad (4.5)$$

It may be shown that the maximum Q is obtained at frequency, ω_o , where [18]:

$$\omega_o = \frac{1}{C_j (R_p R_s)^{1/2}} \quad (4.6)$$

and is given by:

$$Q_{\max} = \frac{1}{2\omega_o C_j R_s} = \left(\frac{R_p}{4R_s} \right)^{1/2} \quad (4.7)$$

The quality factor depends mainly on the bulk resistance loss, R_s , the breakdown voltage and the working frequency. To achieve a maximum Q , the resistance loss R_s must be reduced by restricting the thickness of the epitaxial layer. This places an upper limit on the width of the depletion layer. As a result, the breakdown voltage, which is generally set to be equal to the breakthrough voltage, and the tuning range become limited. Consequently, the power handling, fixed by the tuning voltage and the peak r.f. signal voltage, also becomes limited. The breakdown voltage thus creates a trade-off between high Q , tuning range, and power handling.

Equation 4.7 shows that the quality factor, Q , at resonance depends on the working frequency. Consequently, to characterise varactor diodes with respect to frequency, it is common to define two other figures of merit: (1) the cut-off frequency and (2) the dynamic cut-off frequency.

4.4.2 Cut-Off Frequency

The cut-off frequency, which is usually specified in manufacturers data sheets, is defined as the maximum working frequency of the diode and is defined by Equation 4.7, in which $Q=1$:

$$f_{cv} = \frac{1}{4\pi R_s C_j} \quad (4.8)$$

At zero bias, Equation 4.8 gives the upper frequency limit of the varactor:

$$f_{co} = \frac{1}{4\pi R_s C_o} \quad (4.9)$$

In practice R_s is relatively constant, consequently Equation 4.7 can be written in terms of Equation 4.8 as follows:

$$Q_{max} = \frac{f_{cv}}{f} \quad (4.10)$$

where f denotes the working frequency. It is thus easy to calculate the maximum Q at any working frequency. In the same manner, Q can be estimated at voltages other than the specified (usually Q is specified as $V_R = -4V$) by:

$$Q(V) = \frac{Q(-4)C(-4)}{C_j(V)} \quad (4.11)$$

The second figure of merit, the dynamic cut-off frequency, is defined as:

$$f_{cd} = \frac{1}{2\pi R_s} \left(\frac{1}{C_{jmin}} - \frac{1}{C_{jmax}} \right) \quad (4.12)$$

where C_{jmin} and C_{jmax} are the capacities, measured respectively at 0V, and breakdown voltage. The dynamic cut-off frequency gives an indication of the tuning range that can be achieved by a varactor.

4.4.3 Tuning Ratio

Another parameter providing an indication of the tuning range, which is often encountered in the literature, is the tuning ratio N defined by:

$$N = \frac{C_{\max}}{C_{\min}} = \frac{f_{\max}^2}{f_{\min}^2} \quad (4.13)$$

where C_{\max} and C_{\min} account for junction as well as parasitic capacitances. The tuning ratio is very sensitive to the parasitic capacitors introduced either by the package or the mounting environment. For tuning purposes a high N is always sought.

4.5 Selected Varactor Diode

As mentioned above (Table 4.5), although silicon varactor diodes remain a better choice for their wide tuning range, good temperature stability, and relatively high power handling the diode chosen was a GaAs device SMV1400-04 manufactured by Alpha Industries Inc. for the studies reported in this thesis. This device was selected for mainly two reasons, first it was a small surface mount device easily integrated in microstrip circuits, and secondly, it was cost effective. This second factor is particularly important since preliminary experiments indicated that a large number of circuits would need to be fabricated for investigation hence cost becomes a major

consideration. The electrical characteristics of this device are given in Table 4.6.

4.6 Novel Tuning Topologies

The tuning schemes employing varactor diodes reported earlier [6,8,9,10] mount the tuning configuration above the DR where the magnetic field of the $TE_{01\delta}$ mode exists undistorted, Figure 4.3. Although it is possible to produce as much as 56MHz of electronic tuning in an X-band DR [6], this technique is particularly cumbersome to implement in practice. Severe problems can also arise in applications which are susceptible to prolonged periods of intense vibration because the tuning circuits are prone to shake above the resonator, hence affecting its resonant frequency and the Q-factor of the overall system.

For a DR excited in the $TE_{01\delta}$ mode, the field configuration (Figure 4.8) and the energy distribution (Figure 4.9) around the DR suggests that the best arrangement consists of placing the tuning configuration below the DR where the electromagnetic energy is the strongest (see Figure 4.9). In this arrangement,

1. The tuning configuration can be realised on the microstrip substrate,
2. The magnetic coupling between the DR and the tuning configuration can be adjusted by altering the height of the spacer supporting the DR.

In the next section, the input/output coupling structure is selected based on empirical results before a detailed study of the novel tuning configurations employed are considered.

4.7 Input/Output Coupling Structure

The choice of an appropriate structure to couple energy in and out of a DR depends upon the following considerations:

1. Which mode is to be excited,
2. Which transmission medium is to be utilised (waveguide, coaxial line, microstrip line, etc...),
3. How much coupling is desired.

Modes with strong exterior magnetic fields, such as the $TE_{01\delta}$, are more effectively excited through coupling loops [17], which can assume, for example, the form of a bent coaxial probe, a circular sector microstrip line, or an offset straight line as illustrated in Figures 4.10(a), (b), and (c) respectively.

From empirical work performed [19] it was found that superior coupling is obtained when the DR is placed next to a curved microstrip line than when it is placed next to a straight line. In both cases the resonator proximity to the line was identical. A detailed investigation of this structure was carried out to ascertain the effect on the DR passband insertion-loss and Q-factor performance by the resonator

support height, length and radius of the input/output coupling arcs as follows.

A range of cylindrical spacers were made to support the resonator above the substrate. The spacers were made of a low-loss, low permittivity polyurethane form, details of their radius and height are given in Table 4.7 and the general circuit configuration shown in Figure 4.11.

Accurate location of the DR for each measurement was essential to generate accurate design data. A method of ensuring the resonator was precisely located in the same position in the circuit for each measurement had to be devised, as illustrated (Figure 4.11). A thin transparent plastic cover, with a circular hole cut out in the middle, was added to the test fixture. The resonator was then placed on top of the spacer through this locating hole. Each of the circuits was mounted in a 2"x2" metal enclosure with SMA connectors to make the connection to the test instrumentation.

To establish the relationship between the coupling arc length, arc radius, and spacer height on the DR passband insertion loss and Q factor, two separate groups of circuits were fabricated on substrate Cu217 with a dielectric constant of 2.17 and thickness of 0.794mm. The coupling arcs had a characteristic impedance of 50Ω , the arc length and radius for each circuit is specified in Tables 4.8 & 4.9.

Each of the circuits were tested in turn for different spacer heights using a scalar network analyser. Each

measurement consisted of determining the insertion loss, bandwidth, and centre frequency. The DR employed was a Transtech D8500 series with diameter=17.145mm and height=7.722mm made of $(\text{ZrSn})\text{TiO}_4$ with $\epsilon_r=36$. The results of these measurements are presented graphically in Figures 4.12 to 4.14.

From Figures 4.12(a) to 4.12(b) it can be seen that variation in the radius and lengths of the coupling arc has only a marginal effect on the resonant frequency of the resonator for all circuits. The frequency variation is almost exclusively attributed to the variation of spacer height. It can also be observed that as the resonator moves further away from the substrate it approaches its natural resonant frequency of 3.14GHz.

The transmission characteristics in Figure 4.13(a) to 4.13(b) show the dependency on all three parameters, namely, the spacer height, the coupling arc radius and length. We can see that the passband loss increases with increase in spacer height, and with reduction in the coupling arc length. As the radius of the arc is increased from 6.5mm to 8.5mm a further reduction in the loss is observed.

As with the loss, the resonator Q-factor is also a function of spacer height, arc radius and arc length, as shown in Figures 4.14(a) & 4.14(b). The Q-factor improves with an increase of spacer height, and with a reduction in the coupling arc length. As the radius of the arc was increased a

deterioration in the Q was observed. Q -factors from several hundred to several thousand can be obtained but this is at the expense of loss.

The requirement from the input/output coupling structure is that of low passband insertion loss, high Q , and high coupling. Since the Q is inversely related to the coupling, to maximise coupling a potentially high Q must be sacrificed. This will, as a result, have a detrimental effect on the selectivity of the DR circuit. Unfortunately, a trade-off between coupling and Q is inevitable. From the measured graphs circuit 2D was chosen as the input/output coupling structure for its relatively high Q and low loss properties. This structure will be used for all subsequent work.

4.8 Tuning Configurations

To realise a low cost tuning configuration for perturbing the DRs resonant frequency operating in the TE_{018} mode, the microstrip structure provides an obvious solution because of the ease with which this mode can be coupled to a microstrip line. This is accomplished by orienting the puck's magnetic moment perpendicular to the microstrip plane as shown in Figure 4.15. The whole structure is enclosed in a shielded environment to prevent any radiation loss. The degree of coupling between the puck and microstrip line has a direct effect upon output power, frequency stability, and harmonic content, as well as the puck's resonant frequency. It is also

well known [2] that in this mode more than 60 percent of the stored magnetic energy is located within the resonator, the remaining energy is distributed in the air around the puck, decaying rapidly with increased distance away from the puck surface. It is therefore essential that the tuning configuration be carefully designed to effectively perturb the fringing fields outside the puck and hence alter its resonant frequency.

Figure 4.16 shows the various methods employed in exciting the puck in the TE_{018} mode. The puck is coupled simultaneously to two 50Ω microstrip lines with curved coupling arcs to maximise the input/output coupling. Such a configuration behaves like a bandpass filter, as discussed in section 3.2.3.

The effect of varying the resonator support height, length and radius of the coupling arc have been extensively studied in the last section. For good overall performance of DR passband insertion loss and Q-factor, it was found that the aforementioned parameters should have the following dimensions: support height of 1mm, electrical length and radius of coupling arc of 70° and 8.5mm, respectively. These parameters will be kept constant for all subsequent tuning configurations.

The tuning configurations depicted in Figure 4.16 were fabricated using Cu217 substrate. Low pass filter arrangements were used for both supplying dc bias to the varactors, and for providing a d.c. ground. The high impedance microstrip lines used for this purpose were also etched on the tuning board.

Tests as described below were carried out on the effectiveness of these configurations as a means of electronically tuning the resonant frequency of the DR.

The tuning mechanism in each case is provided by varactor diodes. In Figure 4.16(a) to 4.16(d) the resonator is located at a plane one-quarter guide wavelength from the open-circuited end for effective magnetic coupling. Configurations outlined in Figures 4.16(e) to 4.16(g) have circular microstrip coupling sections loaded with varactor diodes. For analysis we can group these configurations in the same class as those in Figures 4.16(a) to 4.16(d). The second group of tuning configurations shown in Figures 4.16(h) to 4.16(l) consist of circular loops of microstrip line loaded with varactor diodes in the gaps as shown. In each case reverse bias d.c. voltage is applied to the varactor diodes, which causes their capacitance to change. This will alter the reactance of the microstrip to which they are connected, which results in a change in the electromagnetic fields of the lines. Since the resonant frequency of the DR is sensitive to its immediate surrounding, any change in the fields of the tuning lines will effect the fields of the DR, and hence change its resonant frequency. An alternative way of viewing the operation of the tuning mechanism is to consider the tuning circuit to be a resonant circuit coupled with the DR. If two coupled resonators have similar resonant frequencies, and one alters slightly, then the resonant frequency of the other is pulled. Based on these simple

electrical models we can verify the affect of the varactor on the proposed tuning circuits as shown in the next section.

4.9 Analytical Expression for the Tuning Range

For a given tuning mechanism, the tuning range depends upon the coupling between the DR and the tuning mechanism, and on the variable reactance of the loop. An approximate relationship expressing this dependence will be derived in this section.

Consider, for example, the configuration in Figure 4.16(c). At the plane of coupling, the transmission line can be treated as two-quarter wavelength impedance inverters terminated with two tuning varactors. The capacitance variation at the end of the inverter has been transformed into the inductive variation at the coupling plane as shown in Figure 4.17. At this plane the impedance may be expressed as,

$$Z_i = j\omega L_t = Z_t \left(\frac{Z_v + jZ_t \tan \beta l}{Z_t + jZ_v \tan \beta l} \right) \quad (4.14)$$

where $l = \frac{\lambda_g}{4}, \quad \beta = \frac{2\pi}{\lambda_g}$

therefore $Z_i = \frac{Z_t^2}{Z_v} \quad (4.15)$

since $Z_v = \frac{1}{j\omega C_v(V)} \quad (4.16)$

then $L_t = Z_t^2 C_v(V) \quad (4.17)$

where Z_t = characteristic impedance of coupled line.

$C_v(V)$ = effective capacitance of the varactor.

V = tuning voltage.

The equivalent circuit for a DR coupled with a microstrip line can be represented by a parallel tuned LCR circuit as shown in Figure 4.18, where $L_r C_r = 1/\omega_o^2$.

The total inductance in the DR can be modified because L_r and L_t are in parallel giving:

$$L_{rt} = \frac{L_r L_t'}{L_r + L_t'} \quad (4.18)$$

where $L_t' = L_t/2N_t^2$

N_t = the turns ratio of an ideal balanced transformer.

Hence, the inherent resonant frequency, ω_o , of the dielectric puck is given by:

$$\omega = \frac{1}{\sqrt{L_{rt} C_r}} = \omega_o \left(1 + \frac{N_t^2 L_r}{Z_t^2 C_v(V)} \right) \quad (4.19)$$

This equation indicates that variation in the varactor capacitance or the coupling between the DR and the tuning

circuit will produce a corresponding change in the tuning frequency.

The second group of configurations outlined in Figures 4.16(h) to 4.16(l) can be analysed by considering the equivalent circuit shown in Figure 4.19 [20,21]. Loops 1 and 2 represent the input and output lines, respectively. Loop 3 represents the DR and loop 4 the tuning mechanism. Figure 4.20 shows the simplified version of Figure 4.19. It can be easily seen that the modified resonant frequency will depend on the transformed impedance of the tuning mechanism Z_{bd} . The impedance Z_{bd} may be transformed as follows:

$$Z_{bd} = (\omega M_{34})^2 / Z_v = \frac{(\omega M_{34})^2}{R_v + j\omega L_v + 1/j\omega C_v}$$

$$= n_3^2 R_v + jn_3^2 \omega L_v - jn_3^2 / \omega C_v \quad (4.20)$$

where n_3 is the turns ratio between the resonator and the tuning mechanism and is related to the coupling, k_3 , given by:

$$k_3 = n_3^2 \frac{R_v}{R_r} \quad (4.21)$$

The equivalent circuit of Figure 4.20 can then be transformed to the one shown in Figure 4.21. Examination of this figure shows that the modified resonant frequency is given by:

$$\omega_o'^2 = \frac{1}{C_T L_T} \quad (4.22)$$

where C_T and L_T are, respectively, the total capacitance and inductance of the tuned system, and they are given by:

$$C_T = \frac{C_r}{\left(1 + n_3^2 \frac{C_r}{C_v}\right)} \quad (4.23)$$

$$L_T = L_r + n_3^2 L_v \quad (4.24)$$

Hence Equation 4.22 transforms to:

$$\omega_o'^2 = \omega_o^2 \left(\frac{1 + n_3^2 C_r / C_v}{1 + n_3^2 L_v / L_r} \right) \quad (4.25)$$

where $\omega_o^2 = 1/L_r C_r$ is the resonant frequency of the shielded puck. The above equation shows the dependence of the resonant frequency on the coupling, n_3 , the equivalent capacity of varactor, C_v , and the inductance of tuning loop, L_v .

For moderate coupling ($k=0.01$), Equation 4.25 can be further simplified, as shown in the next section. By doing so, the expression of the tuning range becomes simpler and the effects of C_v easy to analyse.

4.10 Expression of the Tuning Range as a Function of the Tuning Voltage.

The inductance of the tuning loop L_v , present in the denominator of Equation 4.25, varies slightly with the tuning voltage around the resonant frequency. Moreover, for moderate coupling ($k=0.01$), the turns ratio n_3^2 is of the order 10^{-2} . Hence, the term $n_3^2 L_v / L_r$ in the denominator of Equation 4.25 is much less than unity and therefore can be neglected. In this case, Equation 4.25 reduces to:

$$\omega_o'^2 \approx \omega_o^2 \left(1 + n_3^2 \frac{C_r}{C_v} \right) \quad (4.26)$$

By replacing n_3^2 by its expression given by Equation 4.21, Equation 4.26 can be written:

$$\begin{aligned} \omega_o'^2 &\approx \omega_o^2 \left(1 + k_3 \frac{R_r C_r}{R_v C_v} \right) \\ &\approx \omega_o^2 \left(1 + k_3 \frac{Q_{ov} C_o}{Q_o C_v} \right) \end{aligned} \quad (4.27)$$

where $Q_o = 1/\omega_o R_r C_r$ is the quality factor of the DR.
 $Q_{ov} = 1/\omega_o R_v C_o$ is the quality factor of the tuning circuit at the resonant frequency, ω_o , and zero bias voltage.

If I is the current in the equivalent circuit of Figure 4.21, then the power loss in the DR can be written:

$$P_o = R_r I^2 \quad (4.28)$$

In the same way, the power loss in the tuning mechanism is given by:

$$P_v = n_3^2 R_v I^2 = k_3 R_r I^2 = k_3 P_o \quad (4.29)$$

Hence $k_3 = P_v/P_o$ and Equation 4.27 transforms thus to:

$$\omega_o'^2 = \omega_o^2 \left(1 + \frac{P_v Q_{ov} C_o}{P_o Q_o C_v} \right) \quad (4.30)$$

Thus for $V_R=0V$, Equation 4.30 becomes:

$$\omega_o'^2 (0) = \omega_o^2 \left(1 + \frac{P_v Q_{ov}}{P_o Q_o} \right) \quad (4.31)$$

and for $V = aV$, Equation 4.30 becomes:

$$\omega_o'^2 (a) \approx \omega_o^2 \left(1 + \frac{P_v Q_{ov} C_o}{P_o Q_o C_a} \right) \quad (4.32)$$

Hence, combining Equations 4.31 and 4.32 yields:

$$\frac{\omega_o'^2(a) - \omega_o'^2(0)}{\omega_o'^2(0)} = \frac{\frac{P_v Q_{ov}}{P_o Q_o} \frac{(C_o - C_a)}{C_a}}{1 + \frac{P_v Q_{ov}}{P_o Q_o}} \quad (4.33)$$

Since most of the energy is stored in the DR ($P_o Q_o \gg P_v Q_{ov}$), Equation 4.33 simplifies to:

$$\frac{\omega_1^2 - \omega_o^2}{\omega_o^2} = \frac{P_v Q_{ov}}{P_o Q_o} \left(\frac{C_o - C_a}{C_a} \right) \quad (4.34)$$

The relationship 4.34 can be rewritten as:

$$\frac{f_1}{f_o} = \left(1 + \frac{P_v Q_{ov}}{P_o Q_o} \frac{(C_o - C_a)}{C_a} \right)^{1/2} \quad (4.35)$$

and for a small tuning range it transforms to:

$$\Delta f = f_1 - f_o = \frac{1}{2} \frac{f_{co}}{Q_o} \frac{P_v}{P_o} \left(\frac{C_o - C_a}{C_a} \right) \quad (4.36)$$

This important relationship shows some similarity with the one found in reference [22]. Although derived in the particular

conditions specified above, it allows us to draw some useful conclusions.

These are:

1. The tuning range is positive and depends on the range C_0 - C_v and on the cut-off frequency of the varactor diodes,
2. Since C_v is present in the denominator, a relatively high but nonlinear, tuning range might be obtained by this method,
3. The tuning range depends on the ratio of the energy stored in the tuning loop to the overall energy stored in the DR. A wide tuning range corresponds to a high ratio. Notice, however, that an excessive storage of energy in the tuning mechanism will result in a drop of the unloaded Q due to the losses in the varactor.

4.11 Experimental Results of the Various Tuning Configurations

Figure 4.22 shows how the introduction of the tuning mechanism influences transmission characteristic of the tuned DR. The curve (A) corresponds to the shielded DR without the tuning configurations. The resonant frequency in this case is about 3.29GHz. The curve (B) is the response when the tuning loop configuration in Figure 4.16(1) is introduced in the structure. This results in a frequency shift of 34.3MHz and an increase in insertion loss to 2.64dB. This change is mainly due to the perturbation introduced by the tuning structure.

Figure 4.23 shows the evolution of the characteristic response as a function of the tuning voltage for configuration 4.16(1) (with $D=2.0\text{mm}$ and $W=1.0\text{mm}$). The relatively large tuning range of 42.57MHz achieved is accompanied by a change in passband loss of about 3.2dB . The 3dB bandwidth of the resonant peak remains fairly constant at about 8.32MHz , implying that the loaded Q also remains constant. This indicates potential suitability as a tuning device for a filter where only the resonant frequency and not bandwidth is required to change. The insertion loss of 2.64dB at 0V bias represents an increase of about 1.38dB over the loss of the resonator without the tuning circuit in place. Notice also the nonlinear tuning which is due to the nonlinear nature of the varactor diodes.

The experimental results of the various tuning configurations are depicted in Table 4.10. The change in insertion loss and tuning bandwidth are for bias voltages between 0V and 30V . The resonant frequency of these circuits are centred around 3.29GHz . From this table we can see that tuning bandwidth in excess of 60MHz can be achieved using configurations in Figures 4.16(h) to 4.16(j). However, this is at the expense of intolerable variation in the resonator passband insertion loss. Since we are looking for a response with minimum variation in the insertion loss, configuration Figure 4.16(1) appears to satisfy our criterion. By choosing this configuration, however, we are sacrificing tuning bandwidth.

In the next section further investigations performed on this configuration are described to determine how the conductor width and radius of the tuning loop effects the overall tuning performance.

4.12 Effect of Tuning Loop on the Tuning Configuration

The radial dimension of the tuning loop is of prime importance since it fixes the position of the varactor with respect to the DRs azimuthal E-field. A maximum sensitivity will occur if the varactor senses the maximum field. Examination of the E-field distribution of an isolated DR [2], shown in Figure 4.24, indicates that a tuning loop, with a radius $b = 2a/3$, where a is the DR radius, will be the best choice. However, as the position of the maximum E-field depends on the proximity of its ground plane, its use in the microstrip structure employed and the restricted housing dimensions will inevitably distort its field distribution. It is therefore very difficult to exactly predict the offset position of the maximum E-field. A small diameter will prevent the varactor from sensing the maximum E-field, while an excessive diameter will introduce a direct input to output coupling leading to an unacceptable out-of-band rejection. Hence, it is essential to investigate experimentally the effect of varying the radius of the loop and its width to determine a value for these parameters which will give an optimum tuning response for a given varactor.

Several circuits were constructed on substrate Cu217 which had varying distance, D , between the resonant ring and the input/output coupling arcs as well as variation in their width, W . The varactor diodes used were surface mount devices of type SMV1400-04 manufactured by Alpha Ind. Inc.. The details of these circuits are given in Tables 4.11 to 4.14.

4.12.1 Evaluation of Results

Ideally the tuning configuration should provide a very large tuning range with no passband insertion loss change which should also be very low throughout the entire tuning range. Furthermore, the circuit Q -factor and 3db bandwidth should be independent of changes in bias voltage. Achieving all of these goals is not necessarily practically possible as the measured results in Figures 4.25 to 4.28 show. It may be seen that the resonant frequency of the tuning configurations, the insertion loss and the 3dB bandwidth generally tend to rise with increase in voltage, however, this is less pronounced for the 3dB bandwidth. Moreover, the Q -factor of the configuration tends to fall with increase in bias voltage. Since, the Q -factor and loss are inversely related to each other, a low Q and hence a wide tuning range is associated with high loss. Therefore, a trade-off between Q or tuning bandwidth and loss is envisaged. Although configuration 4E produces the largest tuning range, in excess of 180MHz, the change in loss over this range is

15.12 dB and the associated very low Q of 85 are unacceptable for practical situations.

The family of circuits 2A-2F, although providing a moderate tuning range, were considered suitable as tuning circuits because of their acceptable loss characteristics. Additional circuits were constructed, 2G to 2J, and their performance is shown in Figure 4.29. Clearly the tuning range for this group is from 28.8MHz to 53.7MHz depending on the degree of coupling with the input/output lines. The loss variation is between 1.82dB to 5.67dB. Both tuning range and loss tend to rise proportionally with weaker coupling with the input/output lines. Based on these results circuit 2F was chosen as the tuning configuration for all tunable filters in the subsequent chapters.

4.13 The Effects of Large Signal Levels on Tuning Configuration Performance

In the design of varactor tuned filters the varactor is assumed to be a linear circuit element. In reality, the varactor capacitance is a function of the instantaneous voltage across its terminals which is the sum of the d.c. bias voltage and the instantaneous r.f. signal voltage. Thus the varactor capacitance is a nonlinear circuit element with the current and voltage related by nonlinear differential equations. It has already been shown that the relationship between the instantaneous charge stored and the voltage across the

terminals of an ideal abrupt junction varactor is given by the following equation [23]:

$$\Delta V = \frac{\Delta q^2}{4C^2(V_B)(V_B + \phi)} + \frac{\Delta q}{C(V_B)} \quad (4.37)$$

where ΔV = Instantaneous voltage across the terminals

Δq = Instantaneous charge stored

V_B = Bias voltage

$C(V_B)$ = Varactor capacitance

From Equation 4.37 it can be seen that even if the charge following through the varactor were sinusoidal the terminal voltage would possess second harmonic distortion. In reality an infinite number of harmonics may be generated since this charge is not necessarily sinusoidal in nature. Consequently, the large signal behaviour of varactor tuned filters is not easily predicted by analysis, however, this information may be obtained through measurements of particular circuits.

The second harmonic and fundamental output powers of the varactor tuned configuration 2F were measured as a function of input power and varactor bias voltage, as shown in Figure 4.30.

Examining Figure 4.30 we can see that at 20dBm input power the second harmonic was 43dB down on the fundamental output at 5V bias. We can see that the slopes are nonlinear and rise very gradually for relatively low and high input powers and is

virtually linear for input power between 10dBm to 18dBm, for all bias voltages. Moreover, as the bias voltage increase there is a reduction in harmonic distortions. The physical basis for this is that the varactor capacitance becomes less sensitive to bias as the bias is increased. Unfortunately when the distortion level was below -58dB it was difficult to measure above the system noise, which was the case for input powers below 8dBm. No third or higher ordered harmonics were detected because of the very high unload Q-factor of the DR (>10,000 @4.5GHz) which prevents these harmonics from penetrating through to the output.

4.14 Conclusions

Novel microstrip tuning configurations have been developed that perturb the resonant frequency of the DRs TE_{018} mode. It has been demonstrated that the loop varactor loaded configurations can provide tuning bandwidths in excess of 5.6% at S-band. This exceeds any tuning method reported to date as indicated in Table 4.1. However, the configuration that was chosen for subsequent work exhibited high-Q and low-loss properties with a tuning range of only 1.3% at S-band. This tuning bandwidth still exceeds any tuning method reported to date with the exception of ferrite tuning. The configurations investigated are simple to construct and lend themselves to an inexpensive and reproducible manufacturing process. Furthermore, combined with the capabilities of the DRs make this kind of system very

competitive compared to the conventional conductor cavities. The characteristic curves presented allow an easy presetting of the system, along with the determination of the corresponding properties such as the tuning range, the loaded Q , the insertion loss, etc.. The techniques derived here may thus be successfully adapted to any other similar system working at different frequencies.

References

1. Harrington, R.F., "Time-Harmonic Electromagnetic Fields", New York, McGraw-Hill, 1961.
2. Kajfez, D., Guillon, P., "Dielectric Resonators," Artech House, Inc., 1986.
3. Kazeminejad S. et al., "Electronically Reconfigurable Cellular Mobile Radio Multicoupler," Fifth International Conference on Mobile Radio and Personal Communications, University of Warwick, U.K., Dec. 1989, pp103-104.
4. Krupka, J., "Resonant Modes in Shielded Cylindrical Ferrite and Single-Crystal Dielectric Resonators," IEEE Trans. Microwave Theory & Techniques, vol.MTT-37, No.4, April 1989, pp691-697.
5. Krupka, J., "Magnetic Tuning of Cylindrical H_{018} -mode Dielectric Resonators," IEEE Trans. Microwave Theory & Techniques, vol.MTT-37, No.4, April 1989, pp743-747.
6. Farr, A.N., Blackie, G.N., Williams, D., "Novel Technique for Tuning of Dielectric Resonators," Proc. 13th European Microwave Conference, Germany, 1983, pp791-796.
7. Nestic, A., "A New Method for Frequency Modulation of Dielectric Resonator Oscillators," Proceedings of 15th European Microwave Conference, 1985, pp403-406.
8. Lammers, U.H.W., and Stiglitz, M.R., "Microwave Dielectric Resonator-Tuning," Report No. AFCRL-TR-74-0497, Oct. 1974, Air Force Cambridge Research Laboratories (LZ), Hanscom AFB, Massachusetts 01733.

9. Popovic, N., "Novel Method of DRO Frequency Tuning with Varactor Diode," *Electronics Letters*, vol.26, No.15, 19th July 1990, p1162.
10. El-Moussaoui, A., Howson, D.P., "Electronic Tuning of a Dielectric Resonator at Microwave Frequencies," *IEE proceedings*, vol.136, Pt.H, No.6, dec.1989, pp502-504.
11. Herczfeld, P.R., Daryoush, A.S., Contarino, U.M., Rosen, A., Turski, Z., Khanna, A.P.S., "Optically Controlled Microwave Devices and Circuits," *IEEE MTT-S Int. Microwave Symposium Digest*, St. Louis, 1985, pp211-214.
12. Herczfeld, P.R., et al., "Optically Tuned and FM Modulated X-Band Dielectric Resonator Oscillator," *Proc. 14th European Microwave Conference*, Liege, 1984, pp268-273.
13. Davis, W.A., "Microwave Semiconductor Circuit Design," Van Nostrand Reinhold Company, New York, 1984.
14. Sze, S.M., "Physics of Semiconductor Devices," John Wiley & Sons, 1981.
15. Moll, J.L., "Physics of Semiconductors," McGraw-Hill, New York, 1964.
16. Smith, R.A., "Semiconductors," Cambridge University Press, 1979.
17. Manufacturers' catalogues: M/A, Alpha Ind. Inc., NEC Electronic Devices, Microwave Associates, Trans-tech.
18. Bahl, I., Bhartia, P., "Microwave Solid State Circuit Design," John Wiley & Sons, 1988.

19. Lande, G., "Electronically Tunable DR Microstrip Filters," Project Report, 1992/93, The University of North London.
20. Zaki, K.A., Chen, C., and Atia, A., "Modelling of Coupling by Probes in Dual Mode Cavities," IEEE MTT-S Digest, 1988, pp515-518.
21. Virdee, B., "Investigation of Different Microstrip Topologies for Tuning DR TE_{016} -mode Resonant Frequency," 1994 Asia-Pacific Microwave Conference, APMC'94, Tokyo, Japan, Dec.6-9.
22. Cawsey, D., "Wide-Range Tuning of Solid-State Microwave Oscillators," IEEE Journal of Solid State Circuits, April 1970, pp82-84.
23. Parry, R., "Microwave Frequency Dividers," Internal Research Report, Department of Electrical Engineering, The University of Leeds, 1981.

Table 4.1 Comparison of Tuning Range of Different Tuning Mechanisms

Tuning Mechanism	Tuning Range	Figure	Reference
Ferrite	3% @ 8GHz	4.1	[6]
PIN diode	0.25% @ 16GHz	4.2	[7]
Varactor diode	0.75% @ 7.4GHz	4.3(a)	[6]
	0.028% @ 14GHz	4.3(b)	[9]
	0.1% @ 950MHz	4.3(c)	[10]
Optical	0.14% @ 10.219GHz	4.4	[11,12]

Table 4.2 Semiconductor Properties

Semi-conductor	Energy Gap		Relative Permittivity ϵ_r	Electron mobility μ_e $\text{cm}^2\text{V}^{-1}\text{s}^{-1}$	Hole Mobility μ_h $\text{cm}^2\text{V}^{-1}\text{s}^{-1}$	Resistivity ρ $10^{-2}\Omega\text{cm}$
	eV	J.10 ⁻¹⁹				
Ge	0.66	1.06	15.7	3000	900	3.5
Si	1.12	1.79	11.7	800	300	8.0
GaAs	1.42	2.27	11.1	5000	250	1.8

Table 4.3 Built-in Potential

	Ge (p+n)	Si (p+n)	GaAs (p+n)
$\Phi(V)$	0.44	0.88	1.3

Table 4.4 Varactor Sensitivities

	Abrupt	Linearly graded	Hyperabrupt
m	0	1	<0 -1 -3/2 -5/3
γ	1/2	1/3	1 2 3

Table 4.5 Performance Comparison of Different Tuning Diodes

	Si		GaAs	
	Abrupt	Hyperabrupt	Abrupt	Hyperabrupt
Linearity	Fair	Good	Fair	Good-Best
Q or loss	Good	Fair	Best	Good
Post tuning drift characteristic	Very Good	Very Good	Fair	Fair
Settling time	Good	Best	Fair	Fair
Temperature stability	Good-Best	Fair	Best	Fair
Tuning range	Best	Fair	Fair	Fair
Power handling	Best	Good	Fair	Fair
Technology	Very Good	Good	Fair	Fair

Table 4.6 Electrical Characteristics of the Varactor SMV1400-04

Characteristics	Symbol	Value	Unit	Test Conditions
Reverse voltage	V_R	30.0	V	$I_R=10\mu A$
Capacitance	C_{T4}	1.0	pF	$V_R=4V, f=50MHz$
Capacitance ratio	N	3.5		
Capacitance tolerance	C	20%		
Quality value	Q	4800		$V_R=4V, f=50MHz$

Table 4.7 DR Support Spacers

Spacer	Radius R(mm)	Height H (mm)
1	3.0	1.72
2	3.0	2.61
3	3.0	3.70
4	3.0	4.64
5	3.0	5.53
6	3.0	6.54

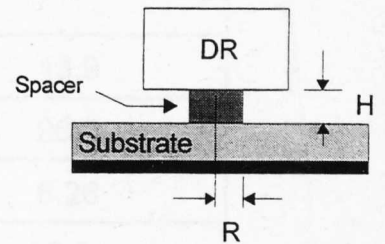


Table 4.8 DR Coupling Arc Parameters

Circuit	Radius R(mm)	Arc length ϕ
1A	6.50	100°
1B	6.50	90°
1C	6.50	80°
1D	6.50	70°
1E	6.50	60°

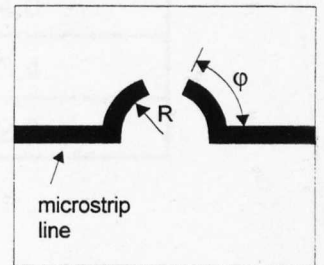


Table 4.9 DR Coupling Arc Parameters

Circuit	Radius R(mm)	Arc length ϕ
2A	8.50	100°
2B	8.50	90°
2C	8.50	80°
2D	8.50	70°
2E	8.50	60°

Table 4.10 Measured Performance

Tuning Configuration	Insertion Loss Variation ΔIL (dB)	Tuning Bandwidth Δf (MHz)
Figure 4.16 (a)	4.0	13.9
Figure 4.16 (b)	2.77	26.0
Figure 4.16 (c)	1.51	6.28
Figure 4.16 (d)	0.7	9.6
Figure 4.16 (e)	0.29	16.6
Figure 4.16 (f)	0.7	12.7
Figure 4.16 (g)	0.8	12.5
Figure 4.16 (h)	15.56	65.0
Figure 4.16 (i)	8.12	67.5
Figure 4.16 (j)	3.74	64.0
Figure 4.16 (k)	3.97	53.4
Figure 4.16 (l)	0.57	22.9

Table 4.11 Tuning Circuits 1A-1F

Circuit	Distance D(mm)	Width W(mm)
1A	1.0	0.5
1B	1.2	0.5
1C	1.4	0.5
1D	1.6	0.5
1E	1.8	0.5
1F	2.0	0.5

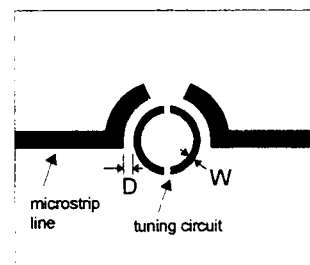


Table 4.12 Tuning Circuits 2A-2F

Circuit	Distance D(mm)	Width W(mm)
2A	1.0	1.0
2B	1.2	1.0
2C	1.4	1.0
2D	1.6	1.0
2E	1.8	1.0
2F	2.0	1.0

Table 4.13 Tuning Circuits 3A-3F

Circuit	Distance D(mm)	Width W(mm)
3A	1.0	1.5
3B	1.2	1.5
3C	1.4	1.5
3D	1.6	1.5
3E	1.8	1.5
3F	2.0	1.5

Table 4.14 Tuning Circuits 4A-4F

Circuit	Distance D(mm)	Width W(mm)
4A	1.0	2.0
4B	1.2	2.0
4C	1.4	2.0
4D	1.6	2.0
4E	1.8	2.0
4F	2.0	2.0

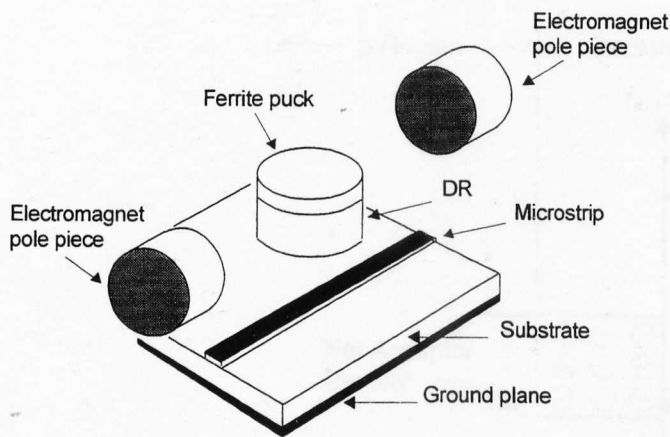


Figure 4.1 Ferrite tuning of a DR (reference [6]).

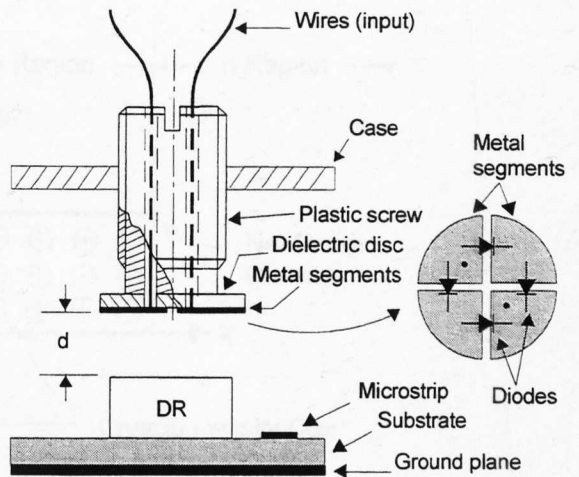


Figure 4.2 PIN diode tuning of a DR (reference [7]).

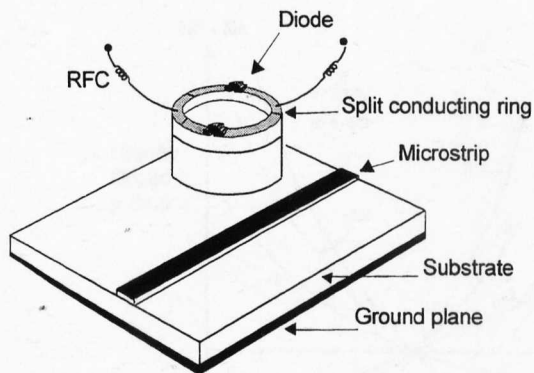


Figure 4.3(a) Varactor tuning of a DR (references [6,8]).

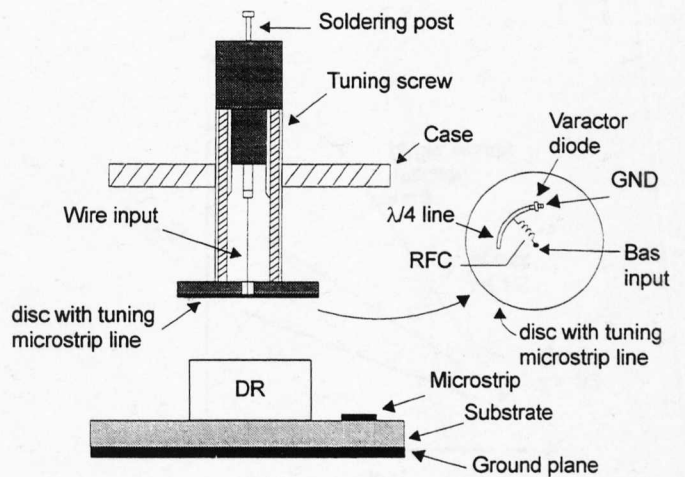


Figure 4.3(b) Varactor tuning of a DR (reference [9]).

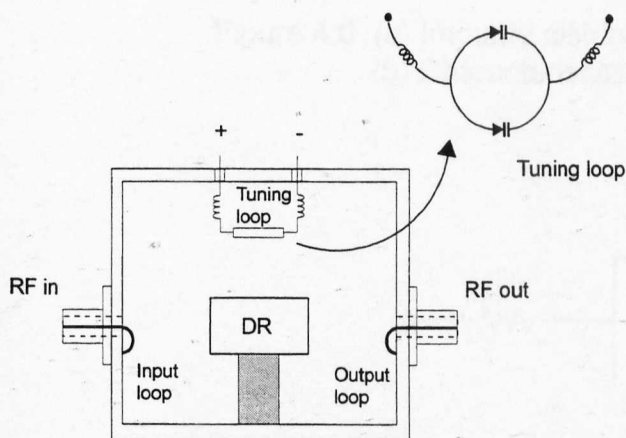


Figure 4.3(c) Varactor tuning of a DR (reference [10]).

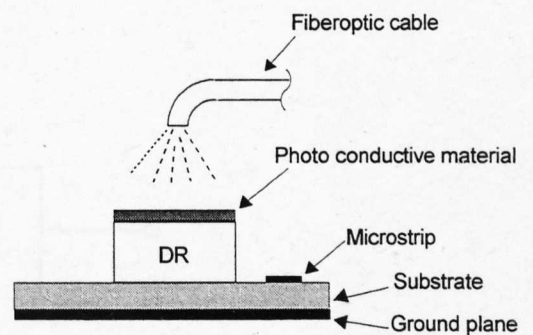


Figure 4.4 Optical tuning of a DR (references [11,12]).

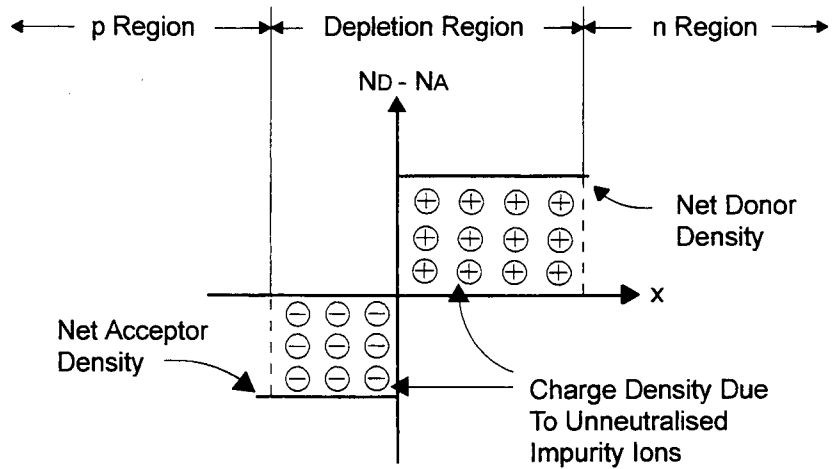


Figure 4.5 Space charge distribution of an abrupt p-n junction.

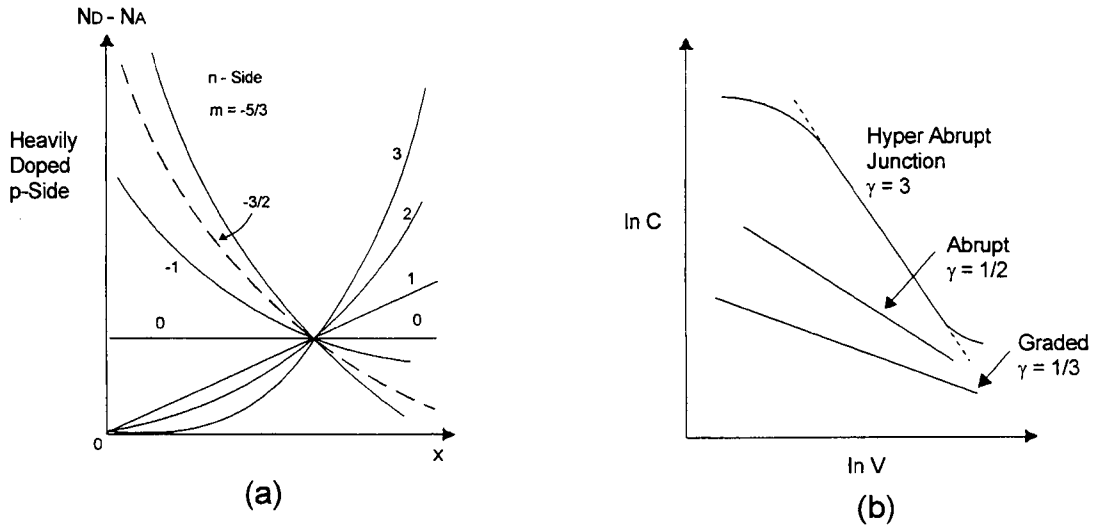


Figure 4.6 (a) Impurity distributions for varactors, (b) Characteristics C-V for various impurity distributions.

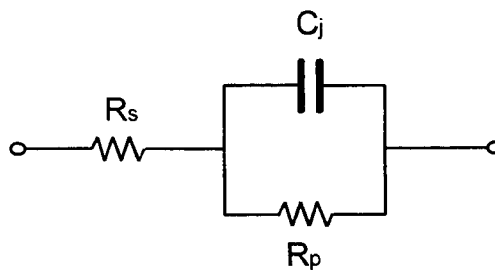


Figure 4.7 Simplified equivalent circuit of a varactor.

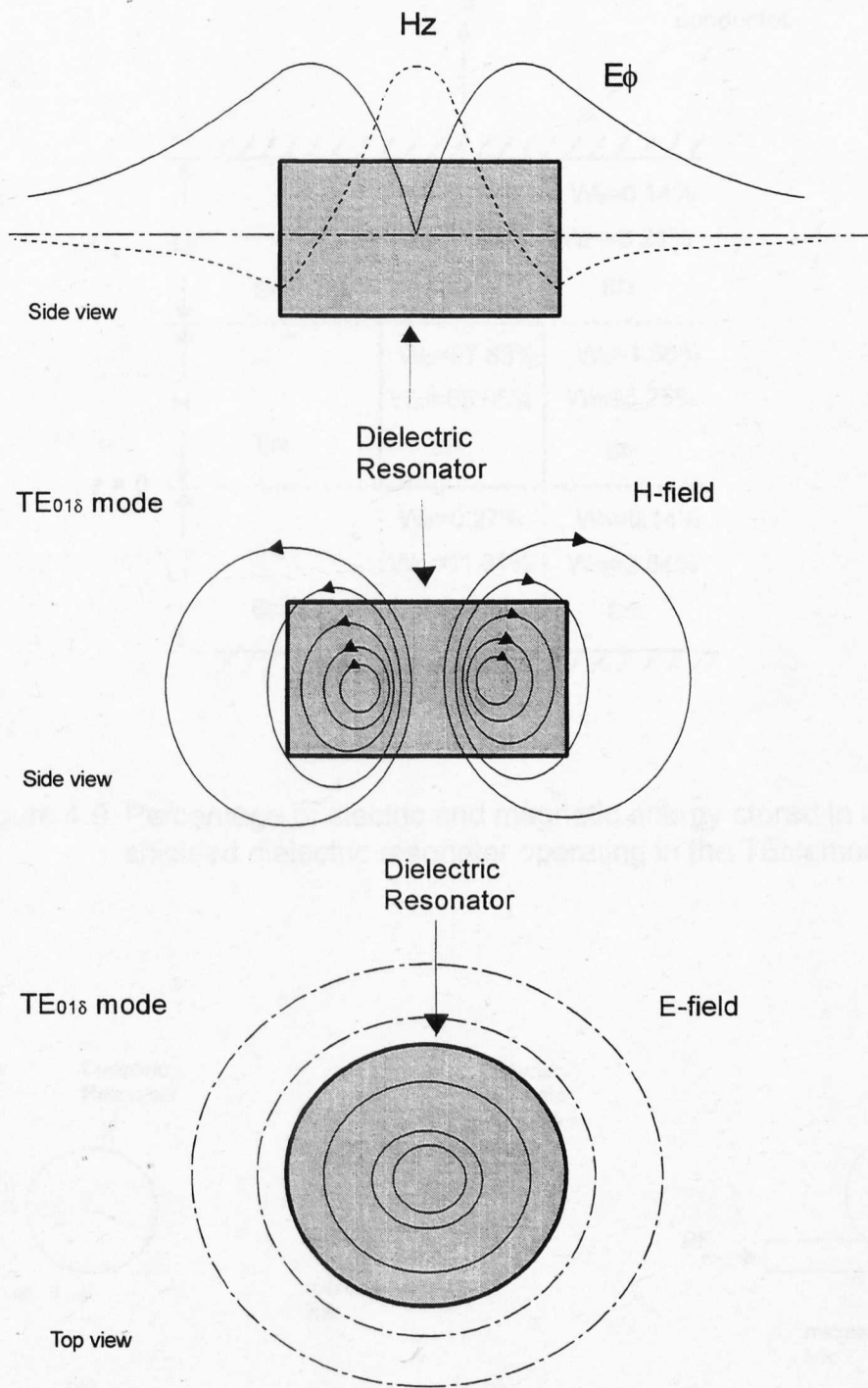


Figure 4.8 Field distribution of the $TE_{01\delta}$ mode of a dielectric resonator.

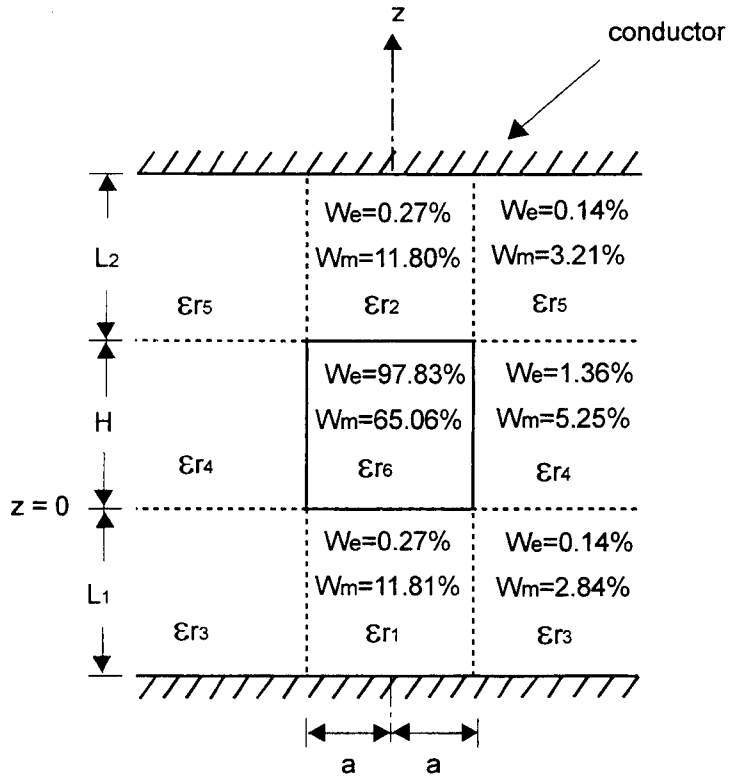


Figure 4.9 Percentage of electric and magnetic energy stored in a shielded dielectric resonator operating in the $TE_{01\delta}$ mode [2].

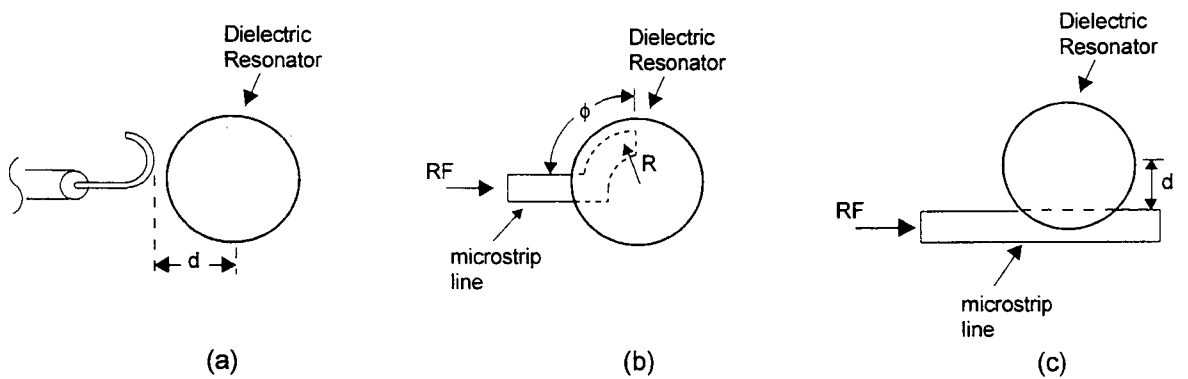


Figure 4.10 Methods of coupling to $TE_{01\delta}$ dielectric resonator mode.

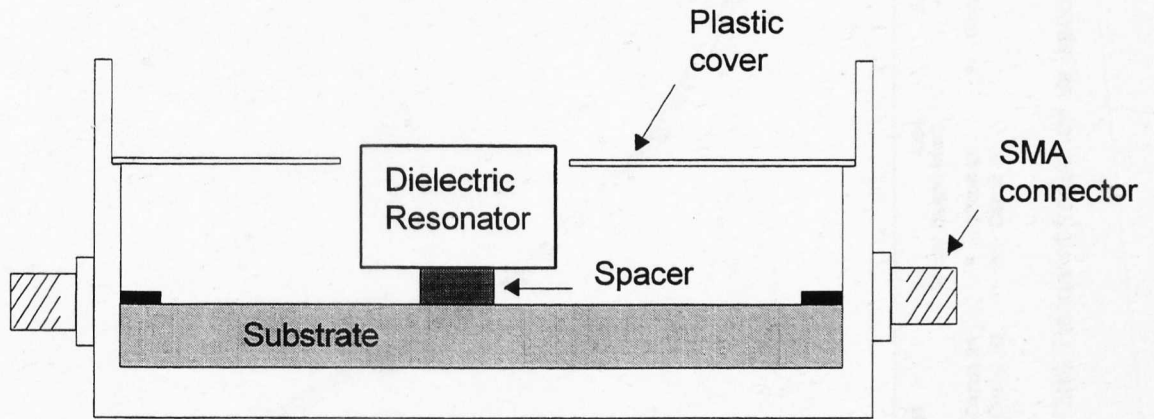


Figure 4.11 Test-fixture with dielectric resonator, spacer and plastic cover to locate the dielectric resonator.

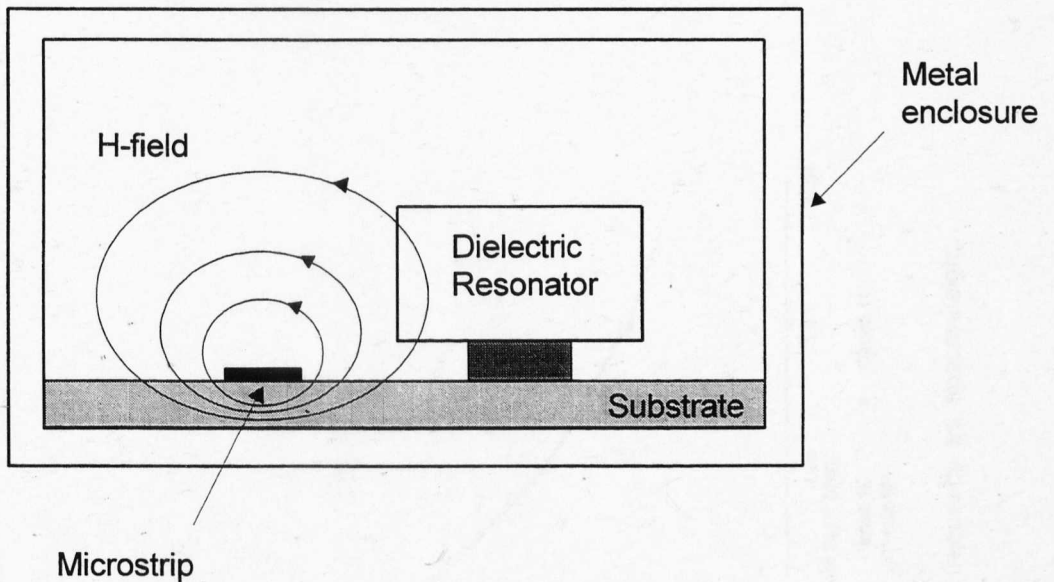


Figure 4.15 Configuration for coupling the TE_{018} mode to microstrip.

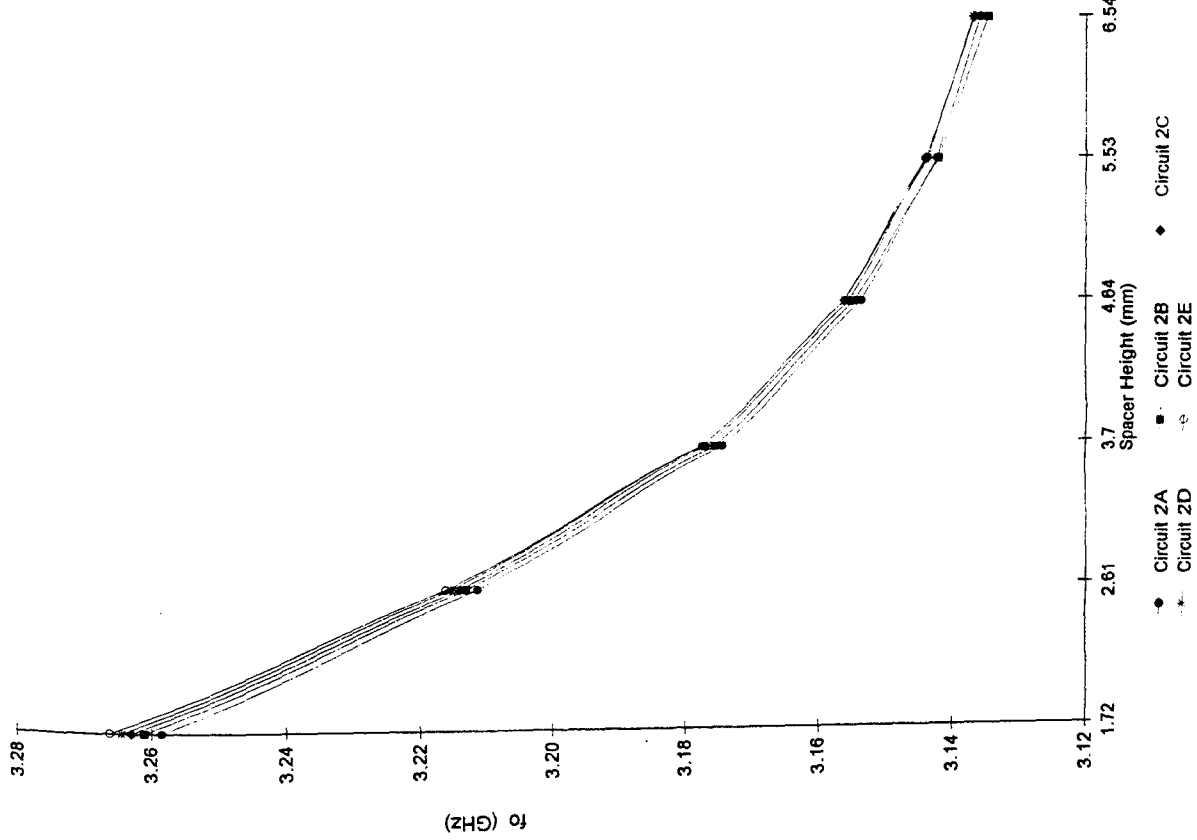


Figure 4.12(b) Resonant frequency vs spacer height.

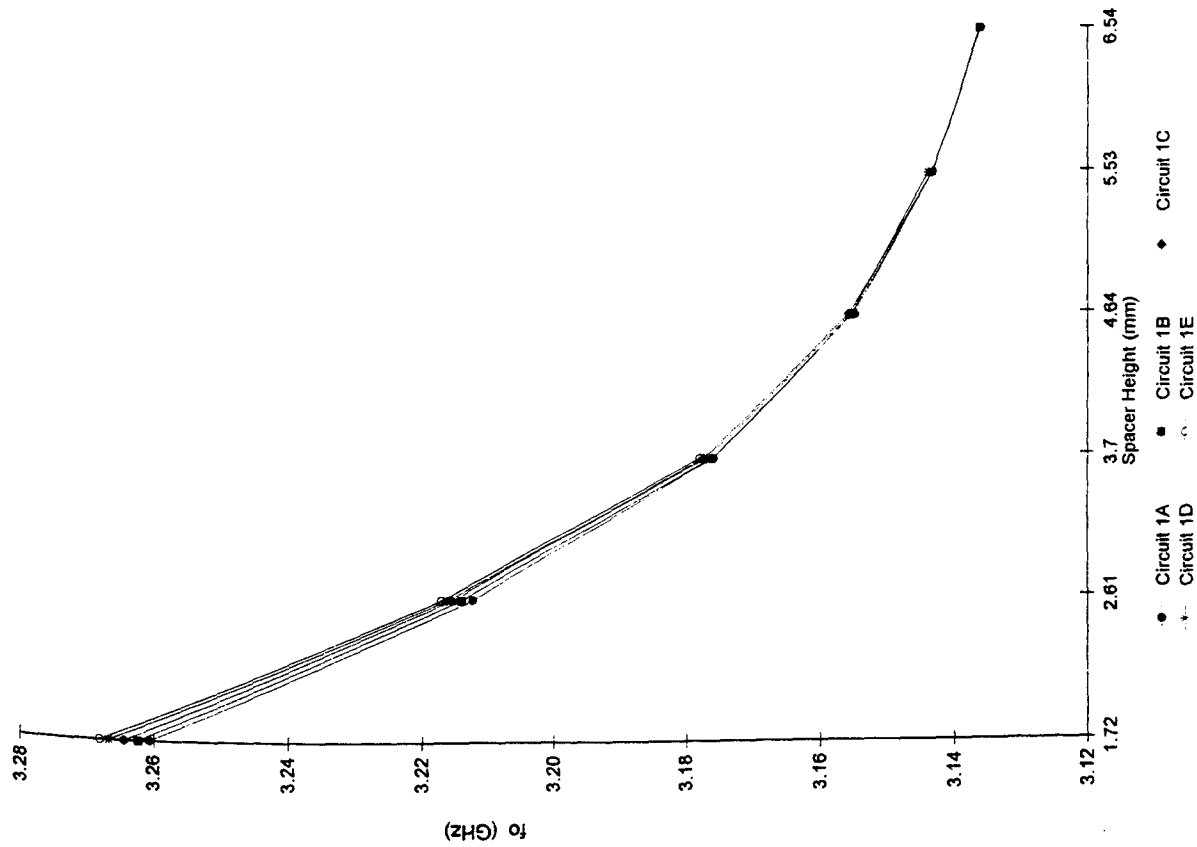


Figure 4.12(a) Resonant frequency vs spacer height.

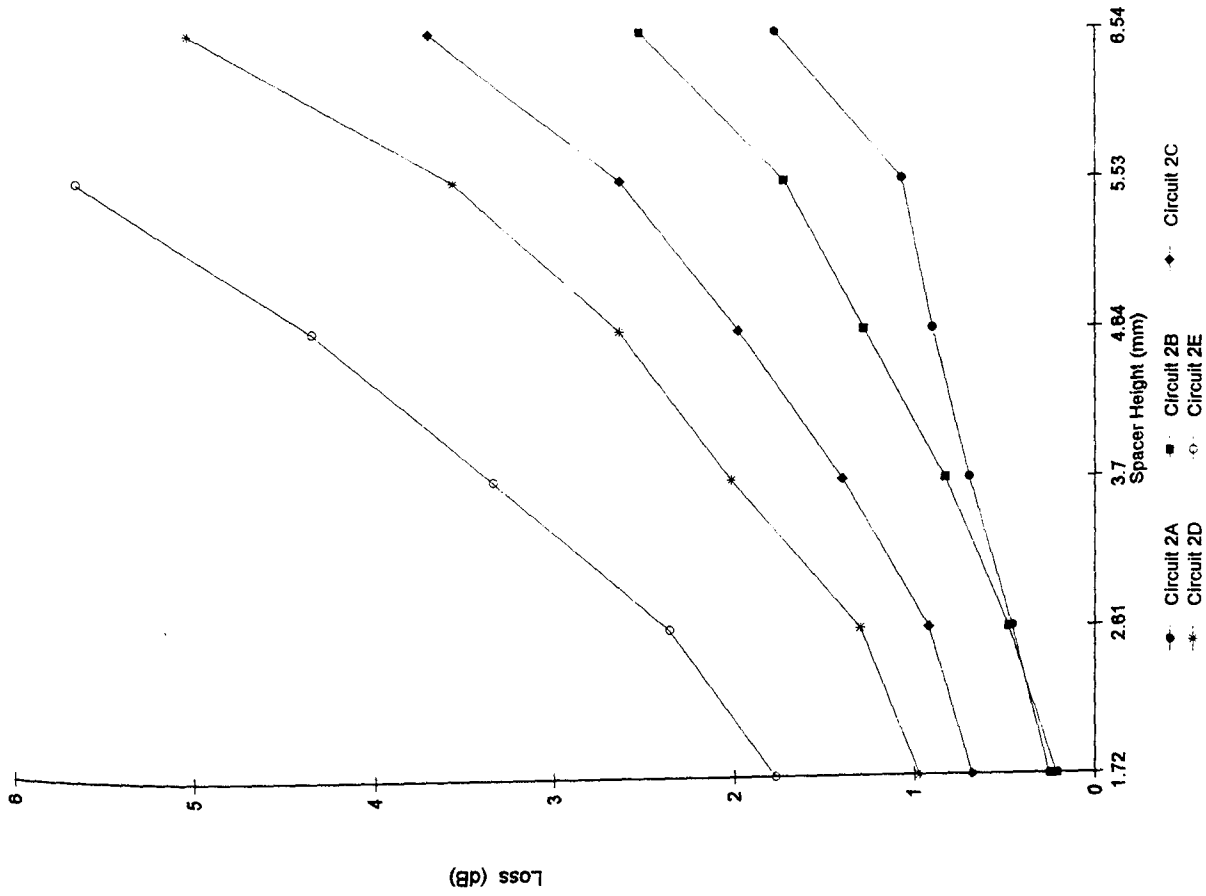


Figure 4.13(b) Insertion loss vs spacer height.

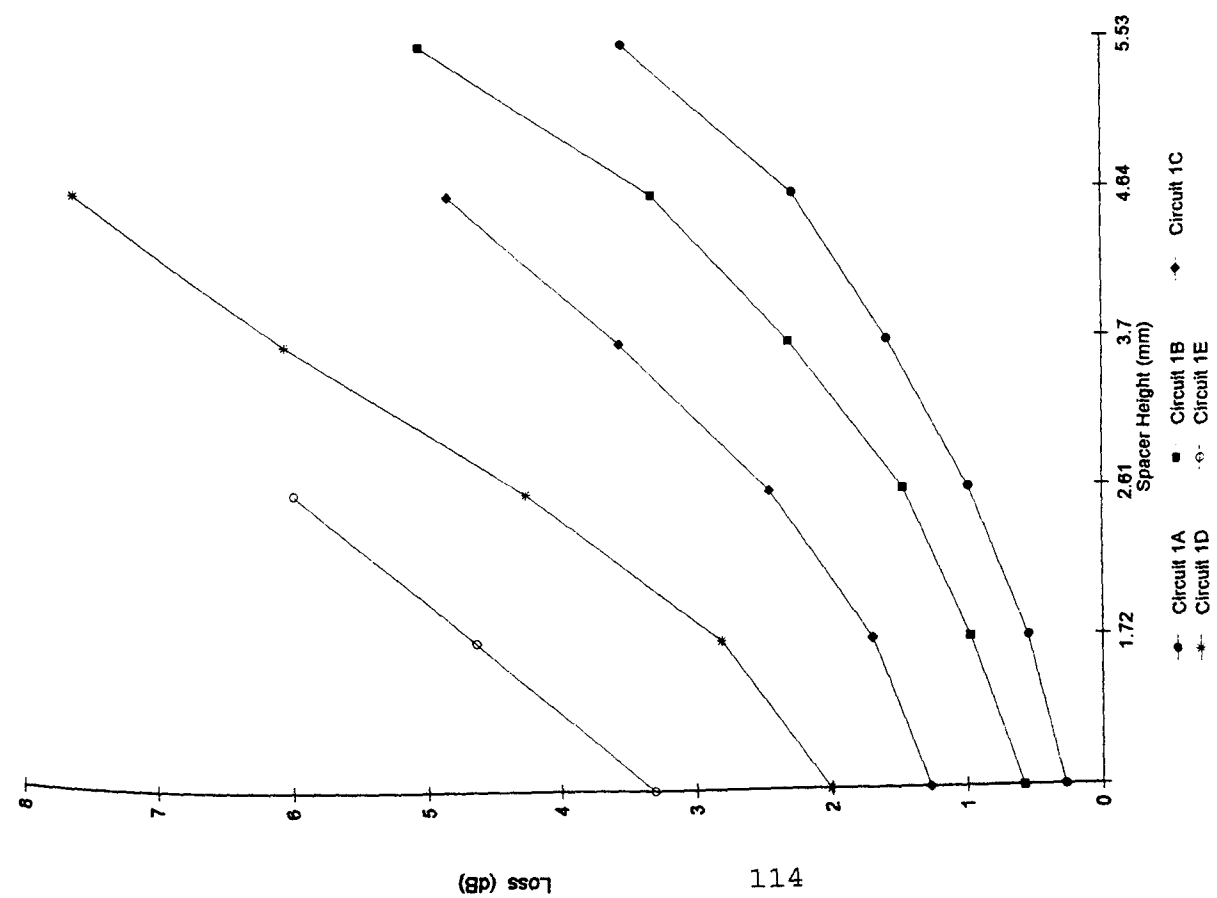


Figure 4.13(a) Insertion loss vs spacer height.

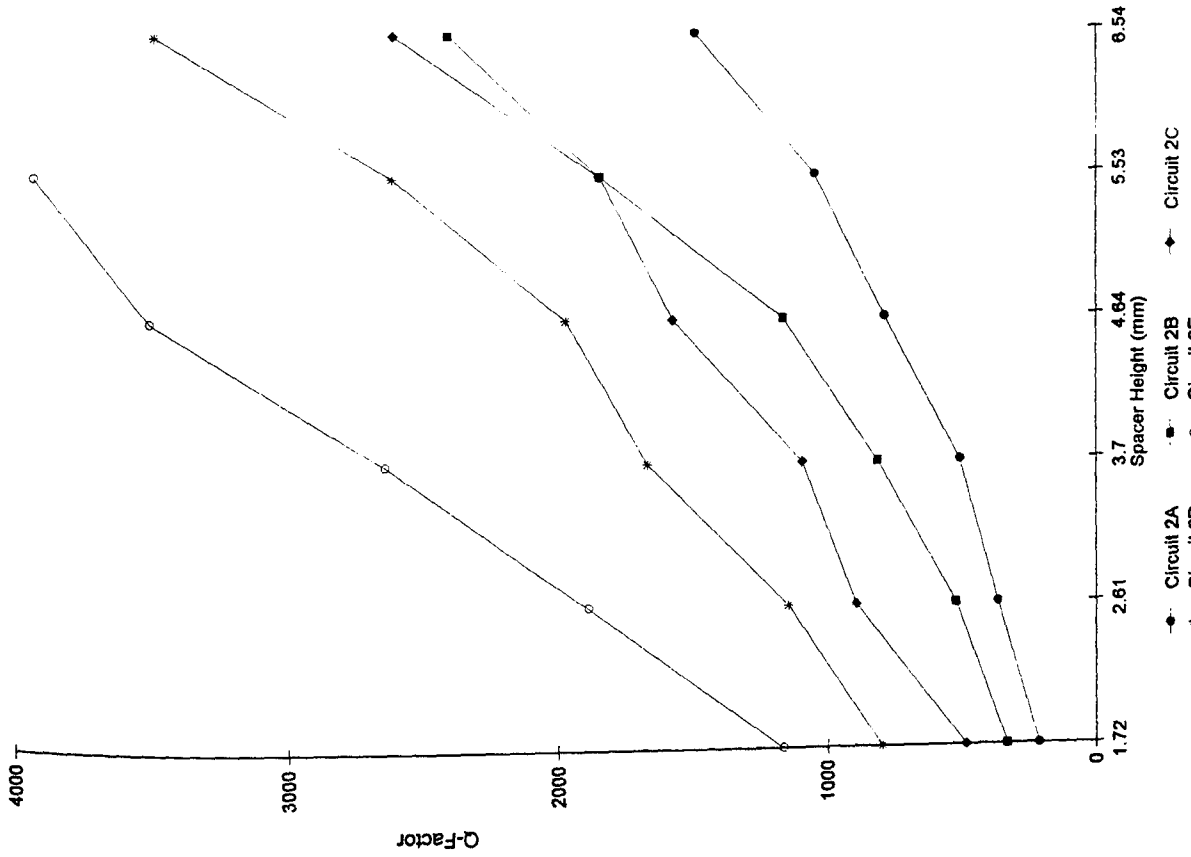


Figure 4.14(b) Unloaded Q-factor vs spacer height.

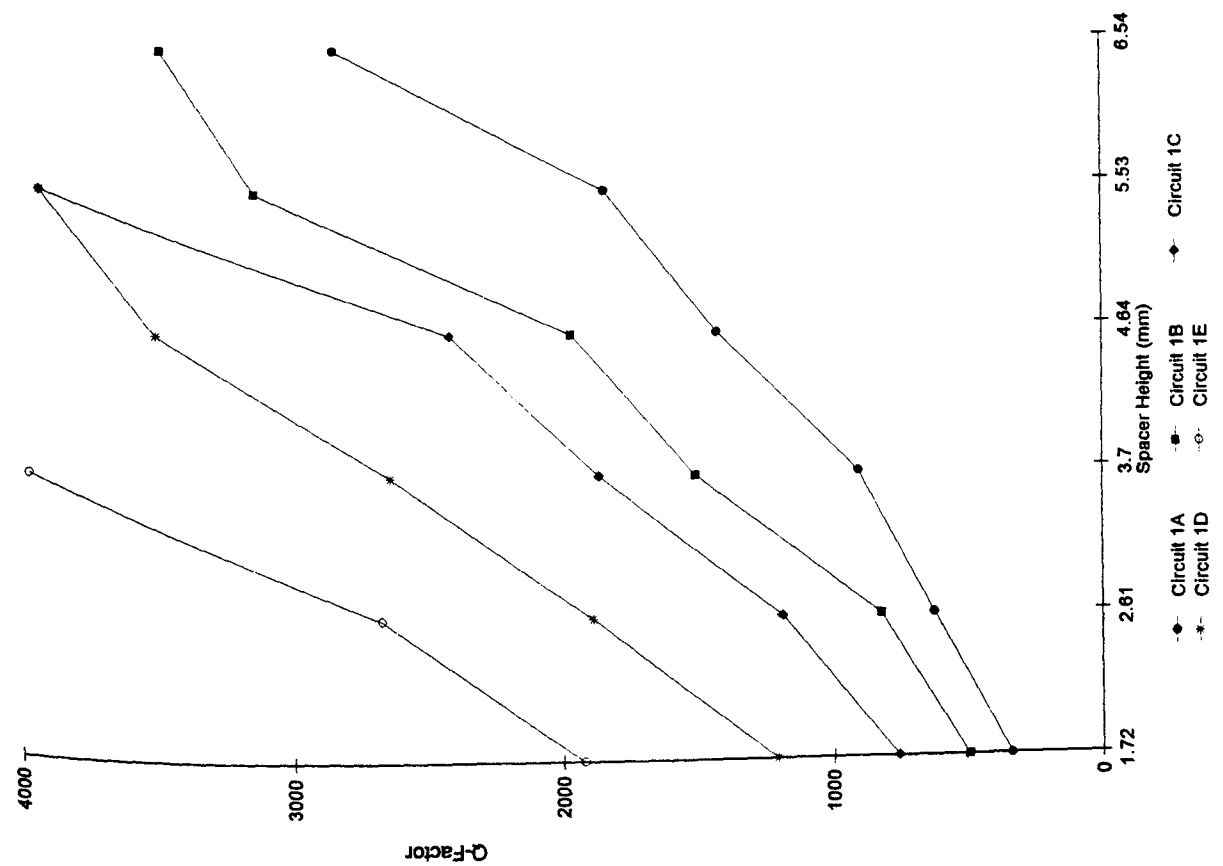


Figure 4.14(a) Unloaded Q-factor vs spacer height.

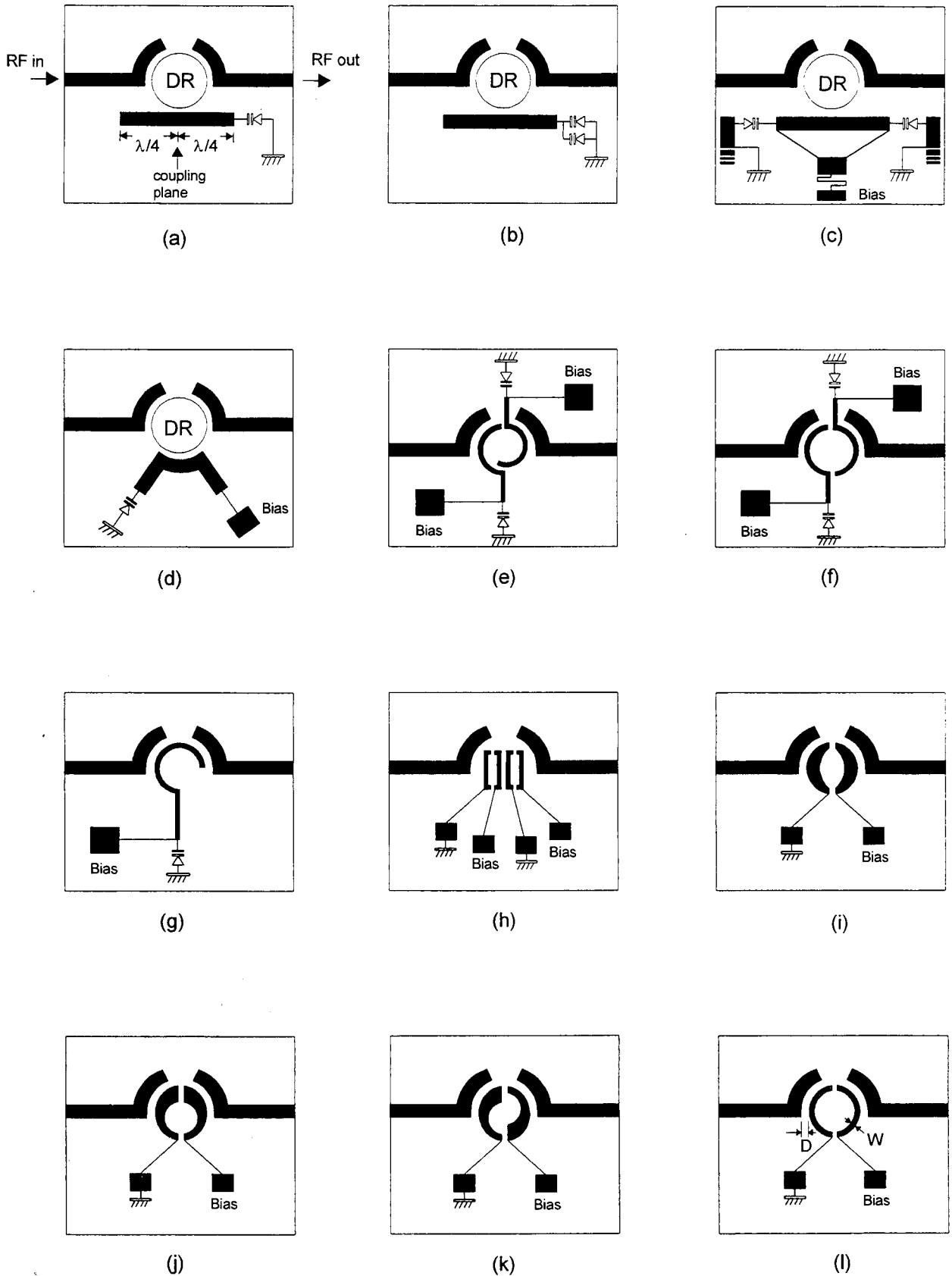


Figure 4.16 Different microstrip coupling topologies with constant input/output coupling arc length, $\phi=70^\circ$, and arc radius, $R=8.50\text{mm}$.

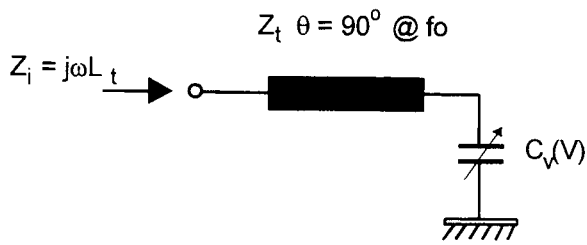


Figure 4.17

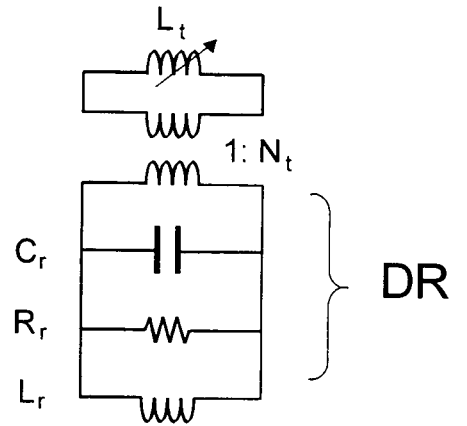


Figure 4.18

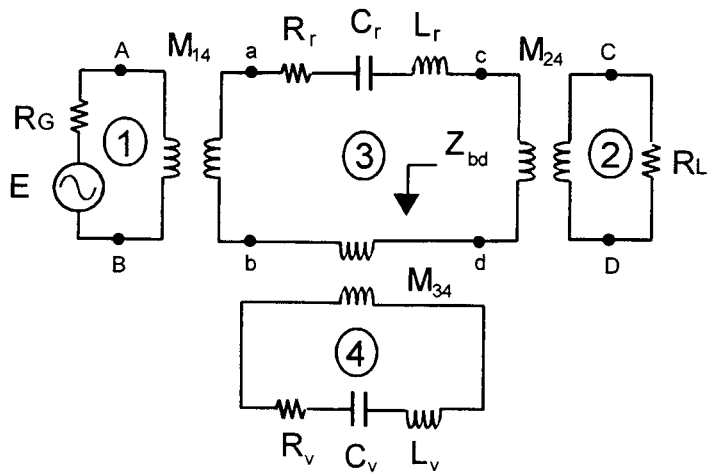


Figure 4.19

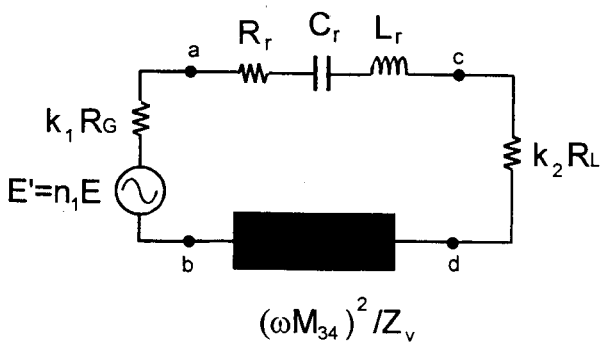


Figure 4.20

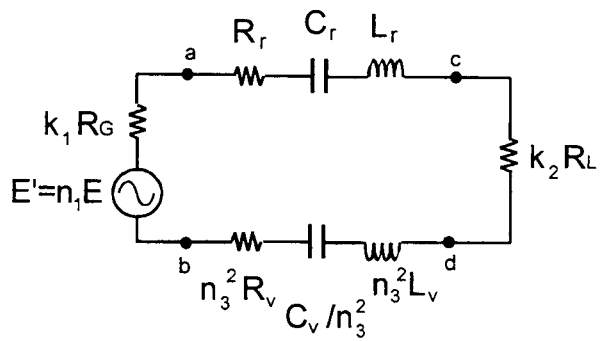


Figure 4.21

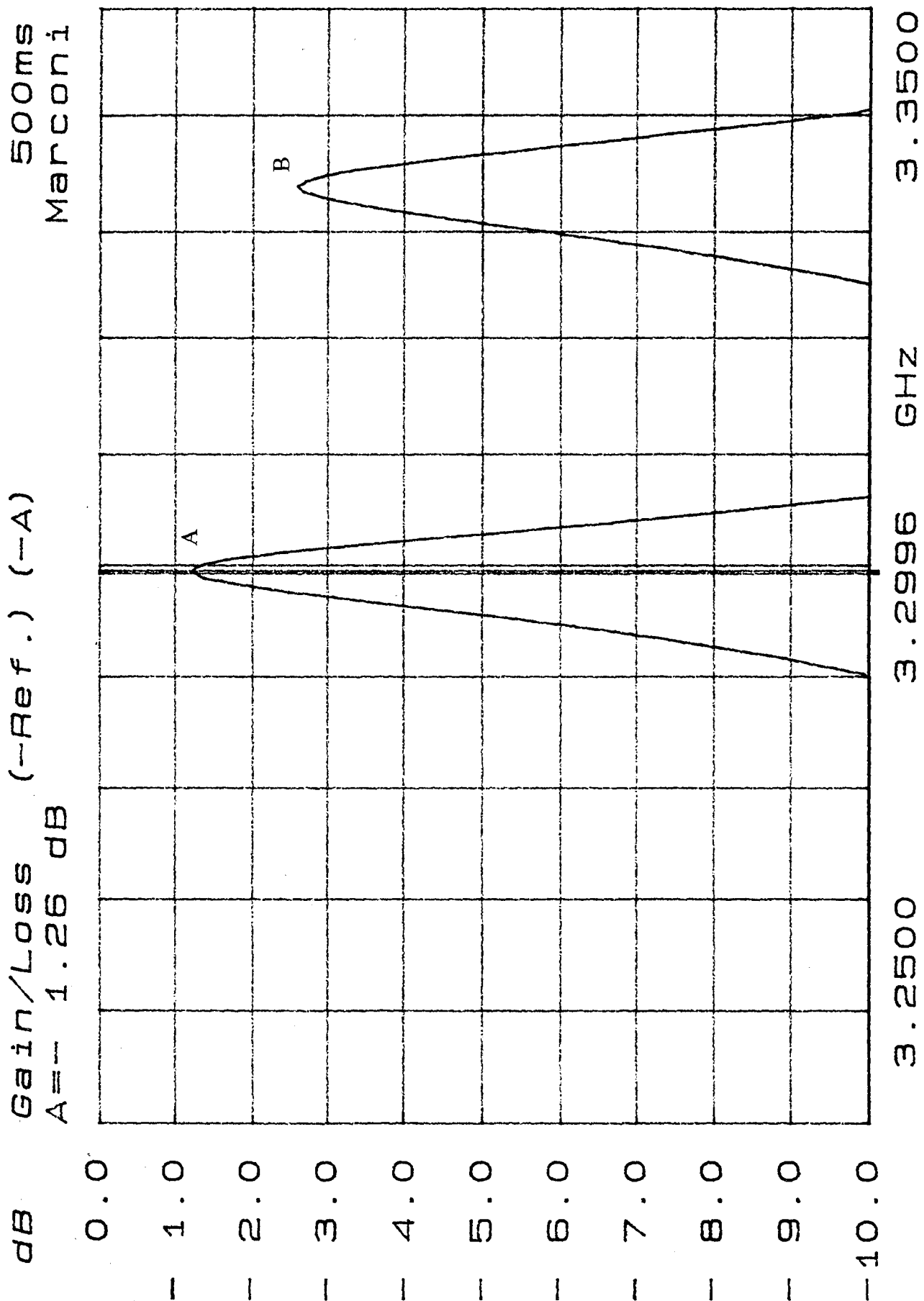


Figure 4.22 (A) Transmission response without tuning circuit.
(B) Transmission response with tuning circuit.

10 s
Marconi

Gain/Loss (-Ref.) (-A)
A=-2.64 dB

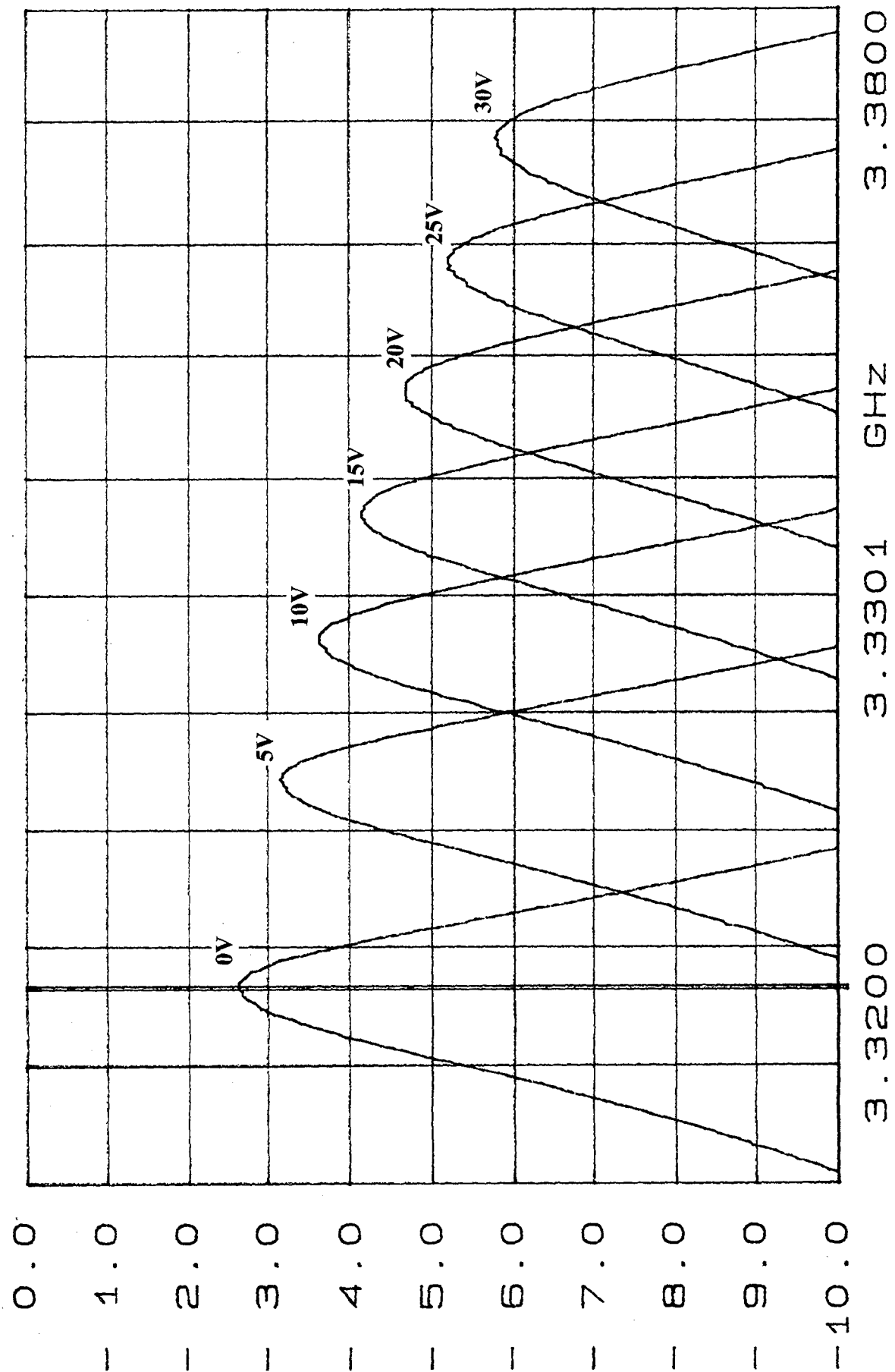


Figure 4.23 Characteristic responses of the tuned DR as a function of the tuning voltage.

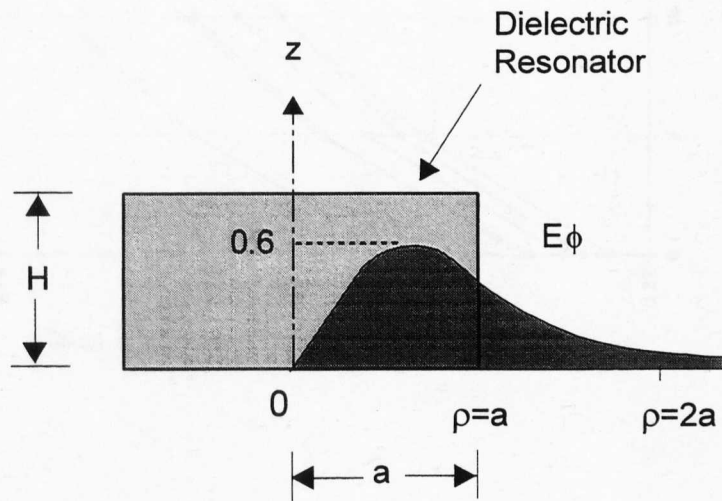


Figure 4.24 Electric field intensity versus radial distance.

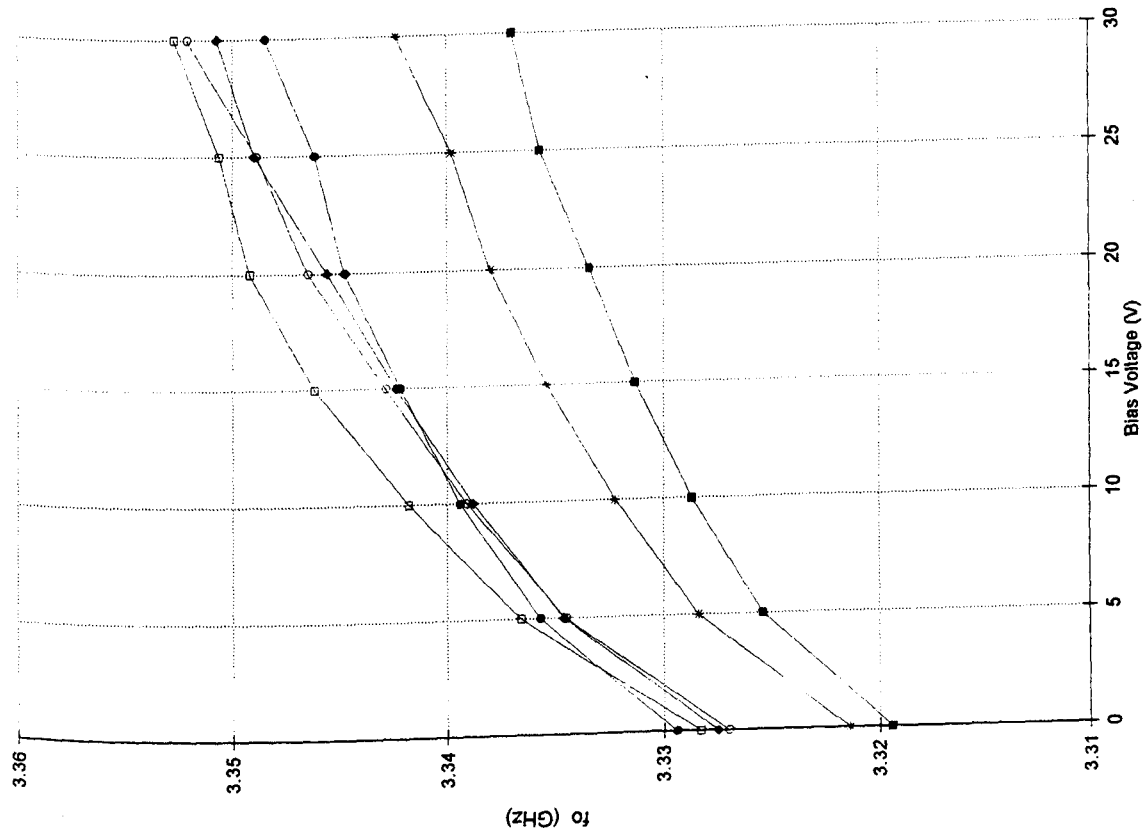


Figure 4.25(a) Resonant frequency vs tuning voltage.

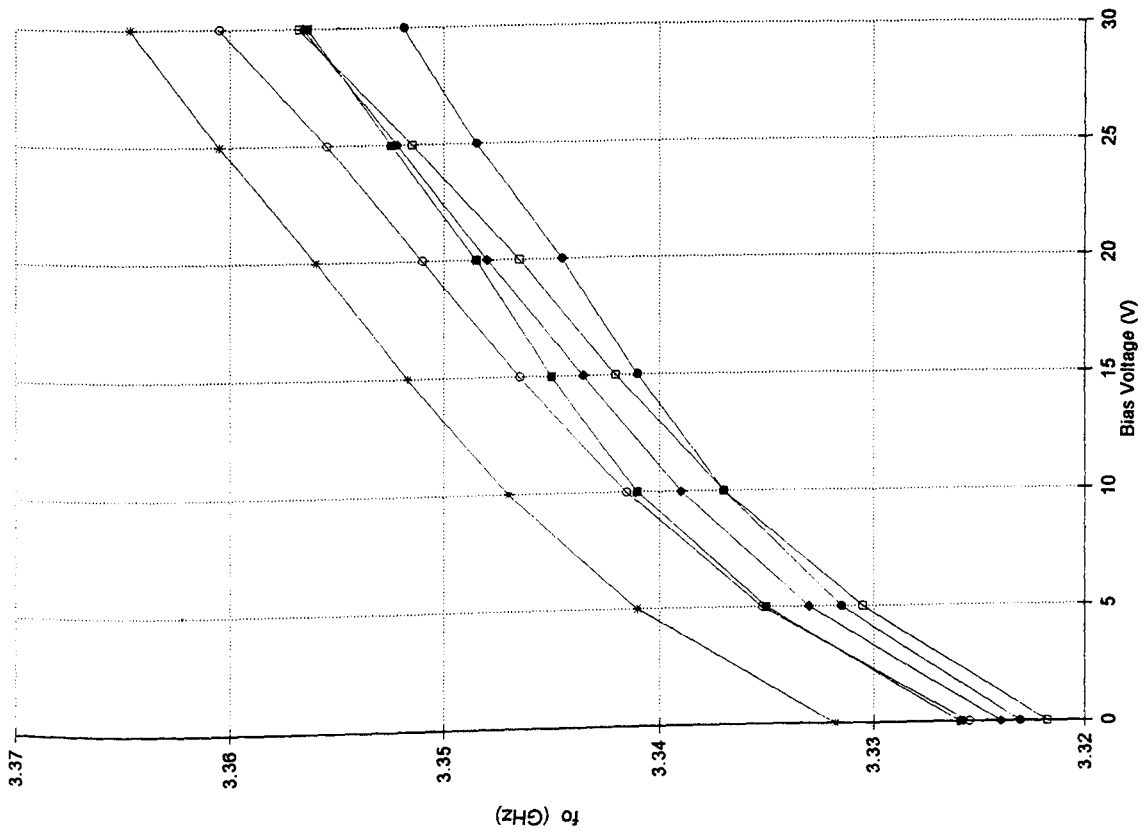


Figure 4.25(b) Resonant frequency vs tuning voltage.

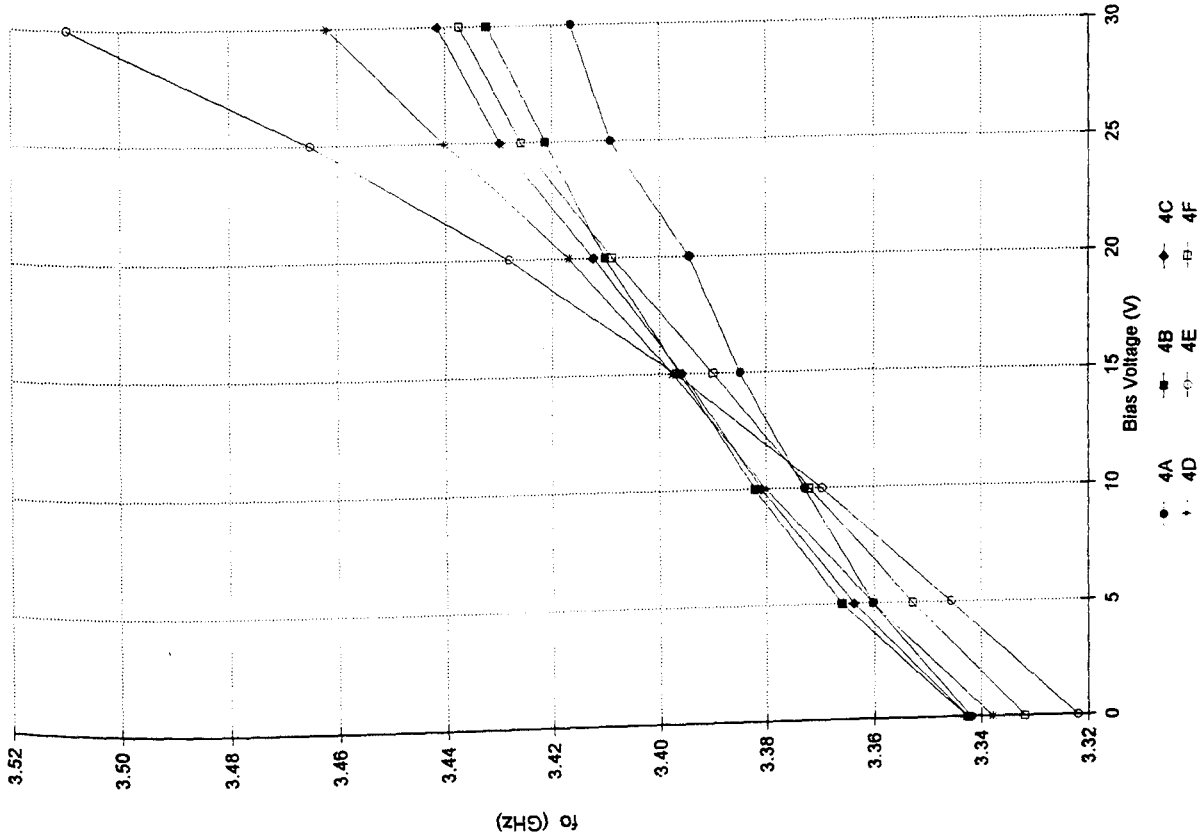


Figure 4.25(d) Resonant frequency vs tuning voltage.

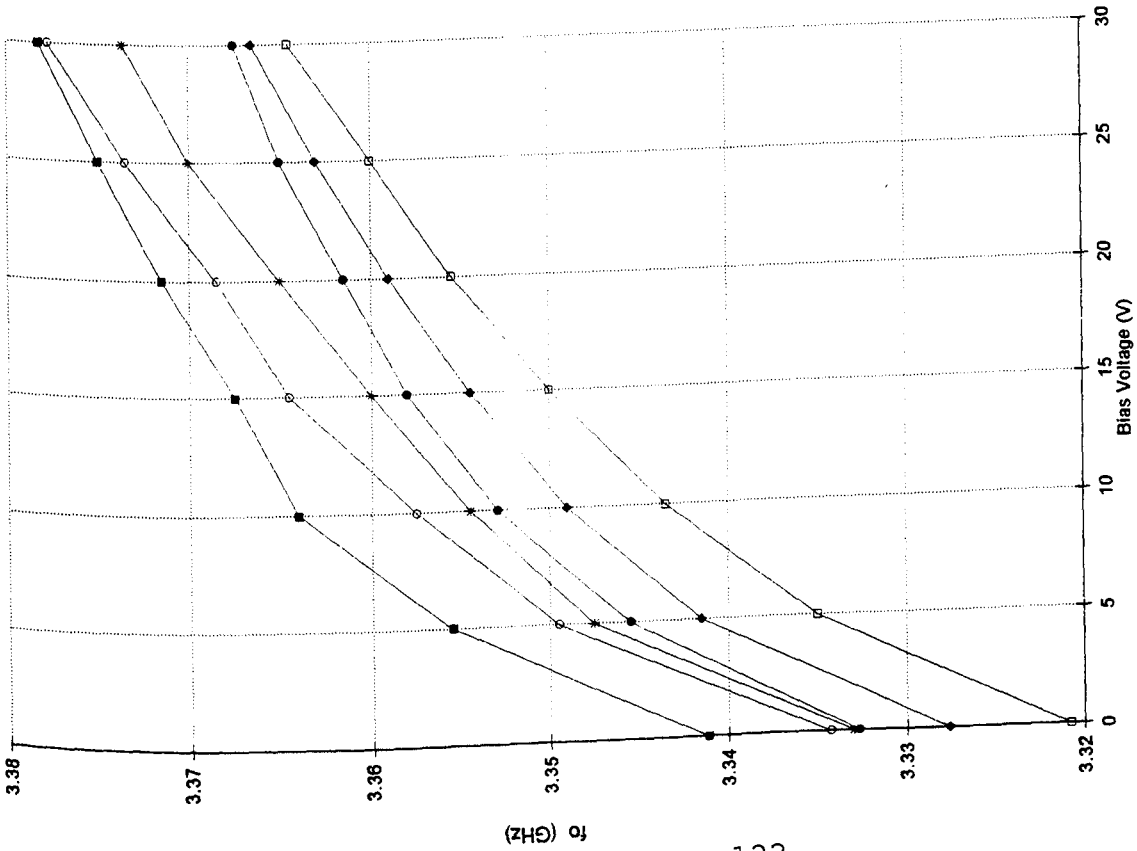


Figure 4.25(c) Resonant frequency vs tuning voltage.

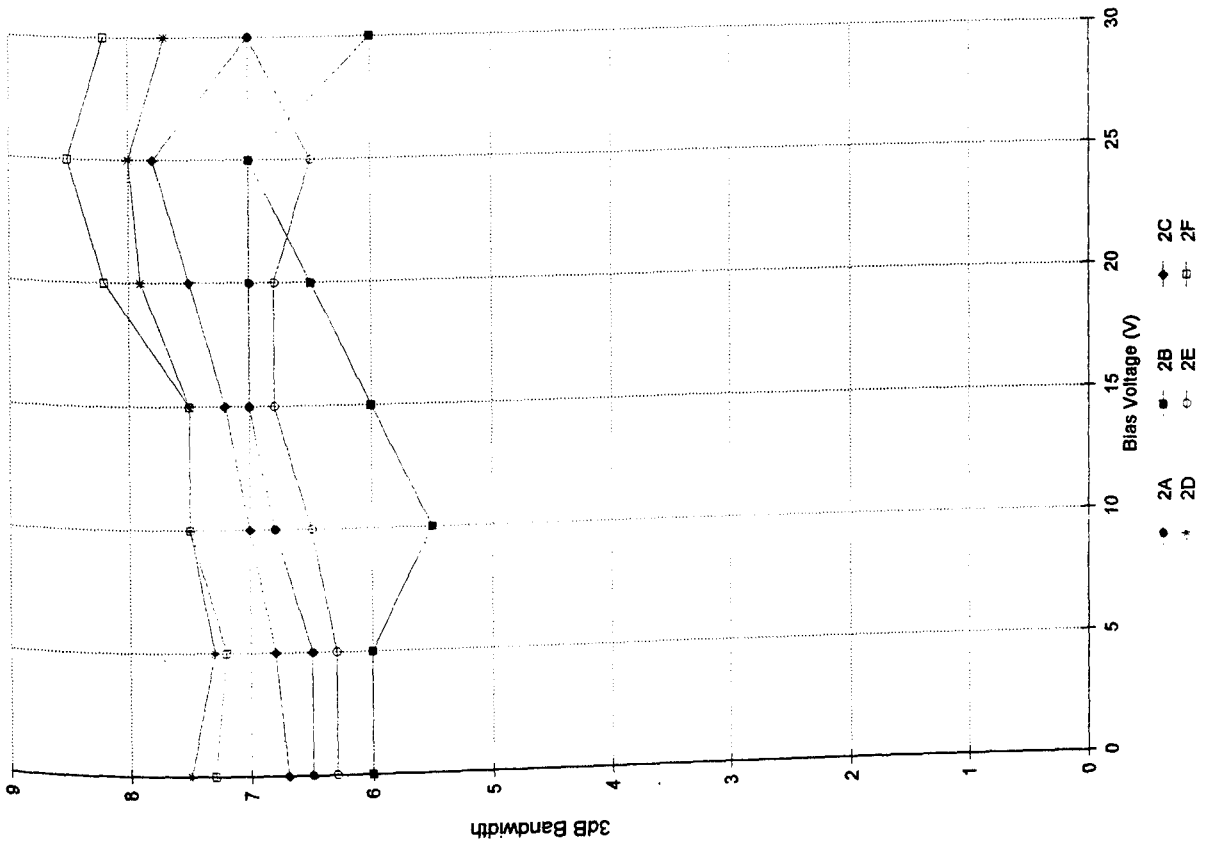


Figure 4.26(b) 3dB Bandwidth vs tuning voltage.

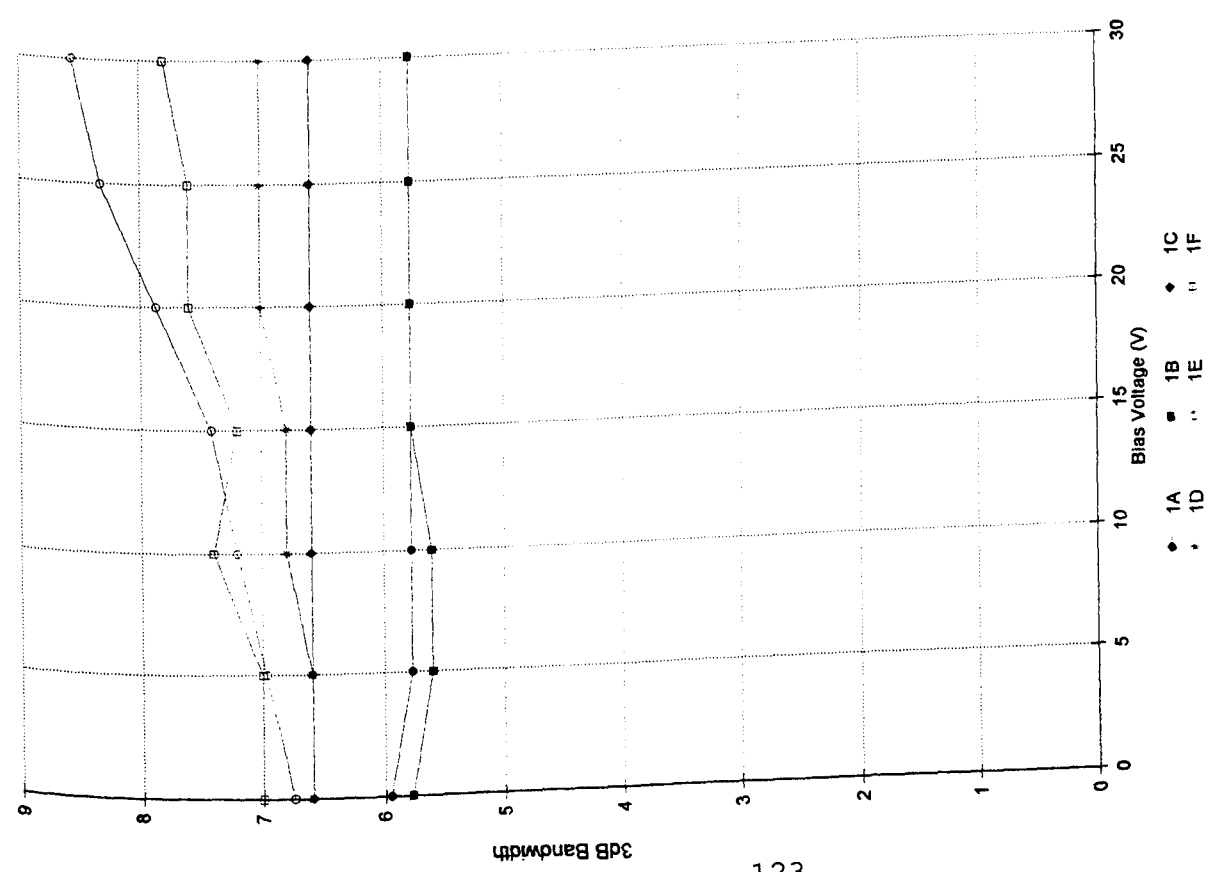


Figure 4.26(a) 3dB Bandwidth vs tuning voltage.

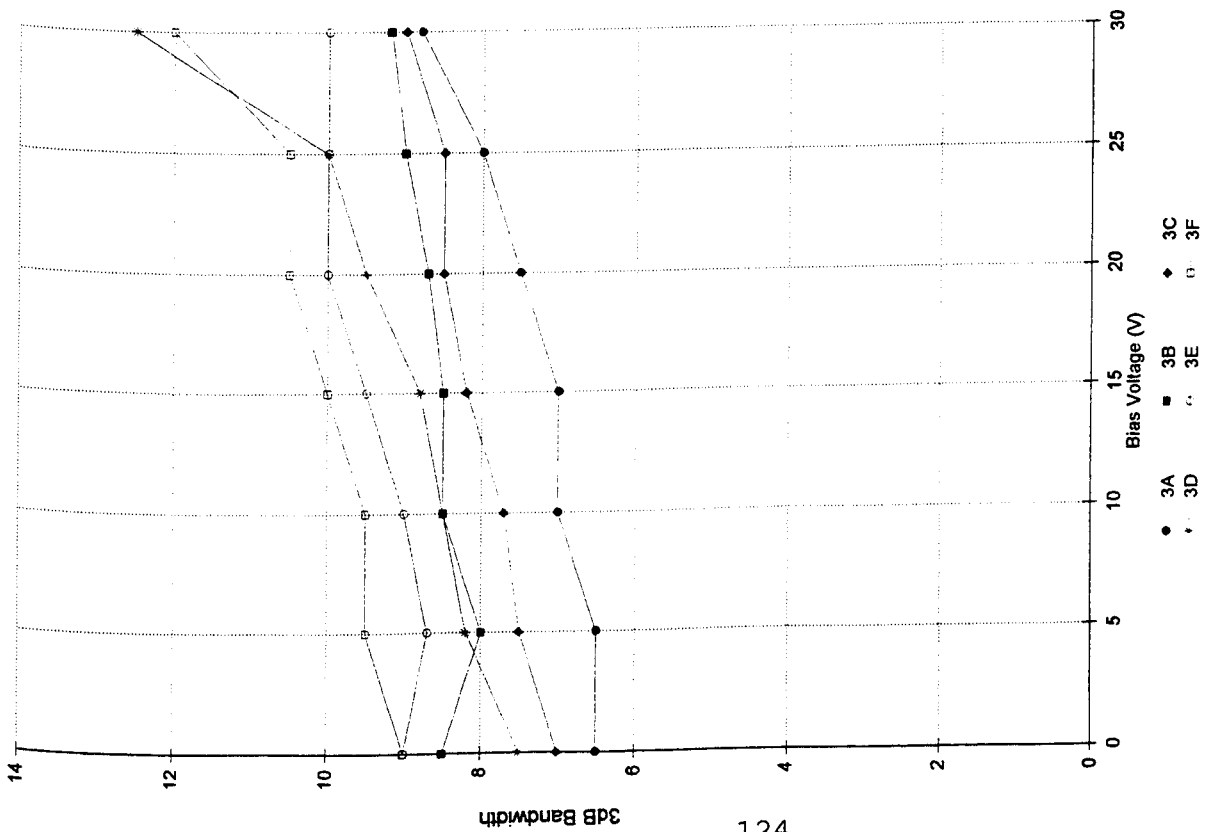


Figure 4.26(c) 3dB Bandwidth vs tuning voltage.

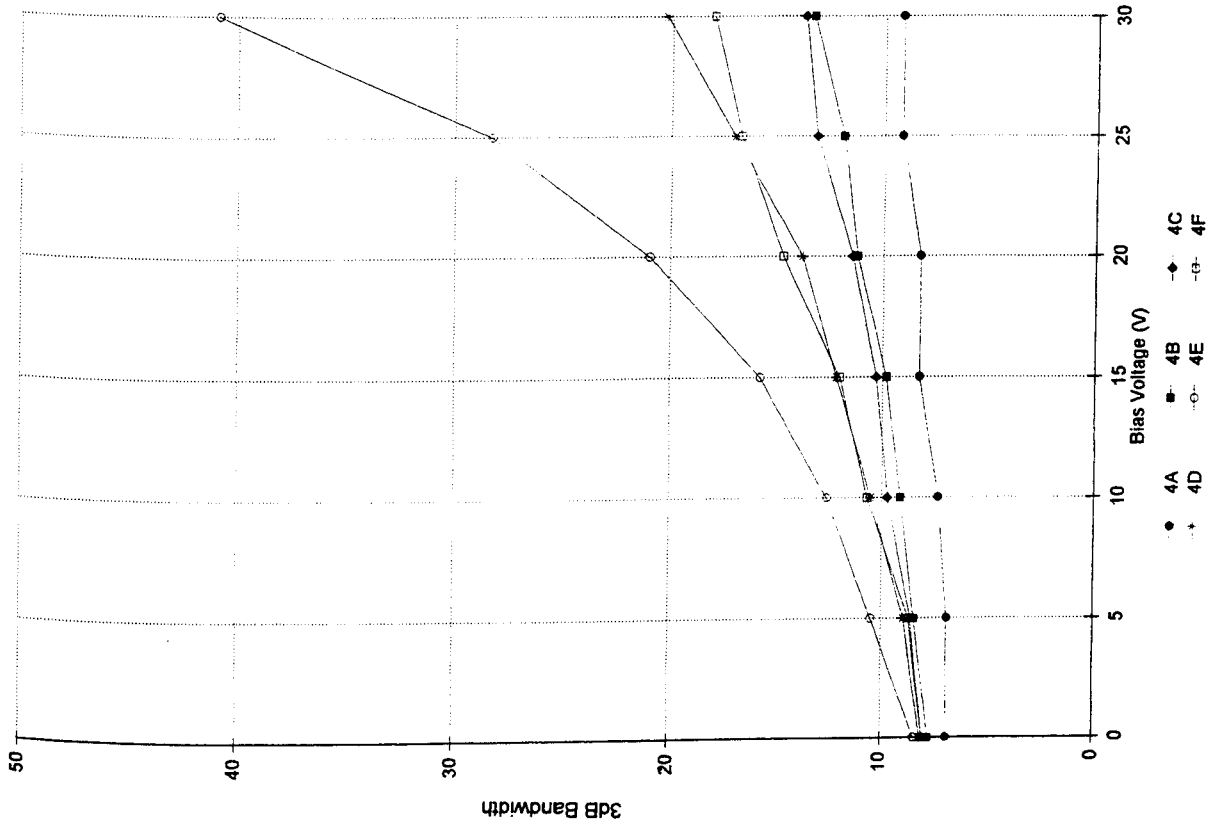


Figure 4.26(d) 3dB Bandwidth vs tuning voltage.

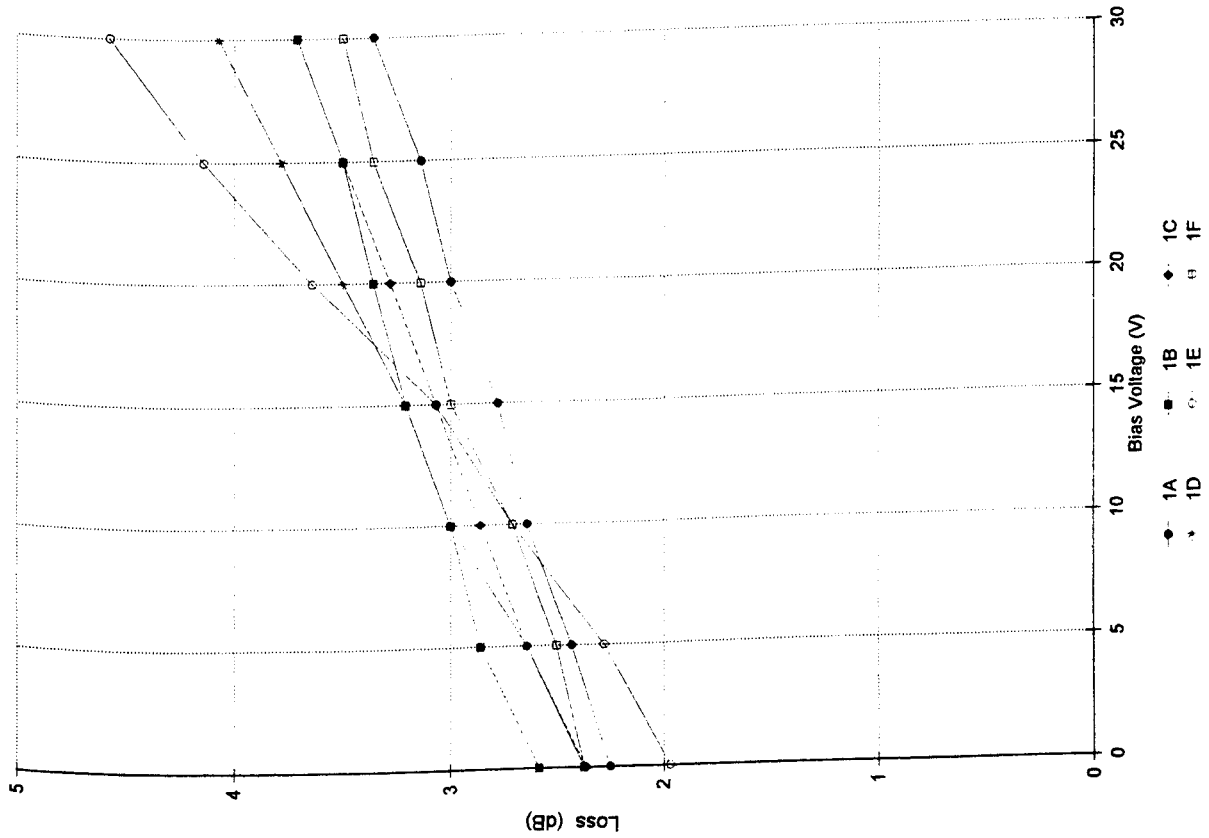


Figure 4.27(a) Insertion loss vs tuning voltage.

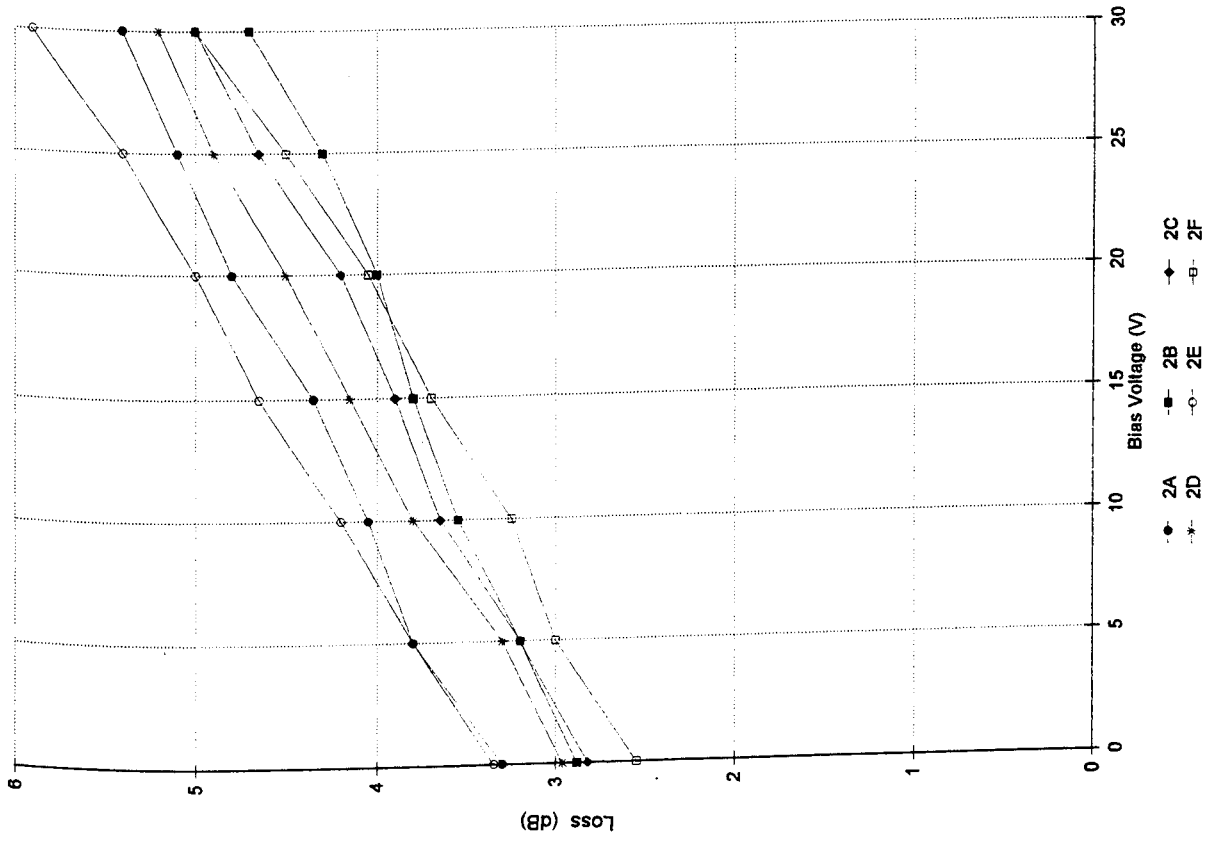


Figure 4.27(b) Insertion loss vs tuning voltage.

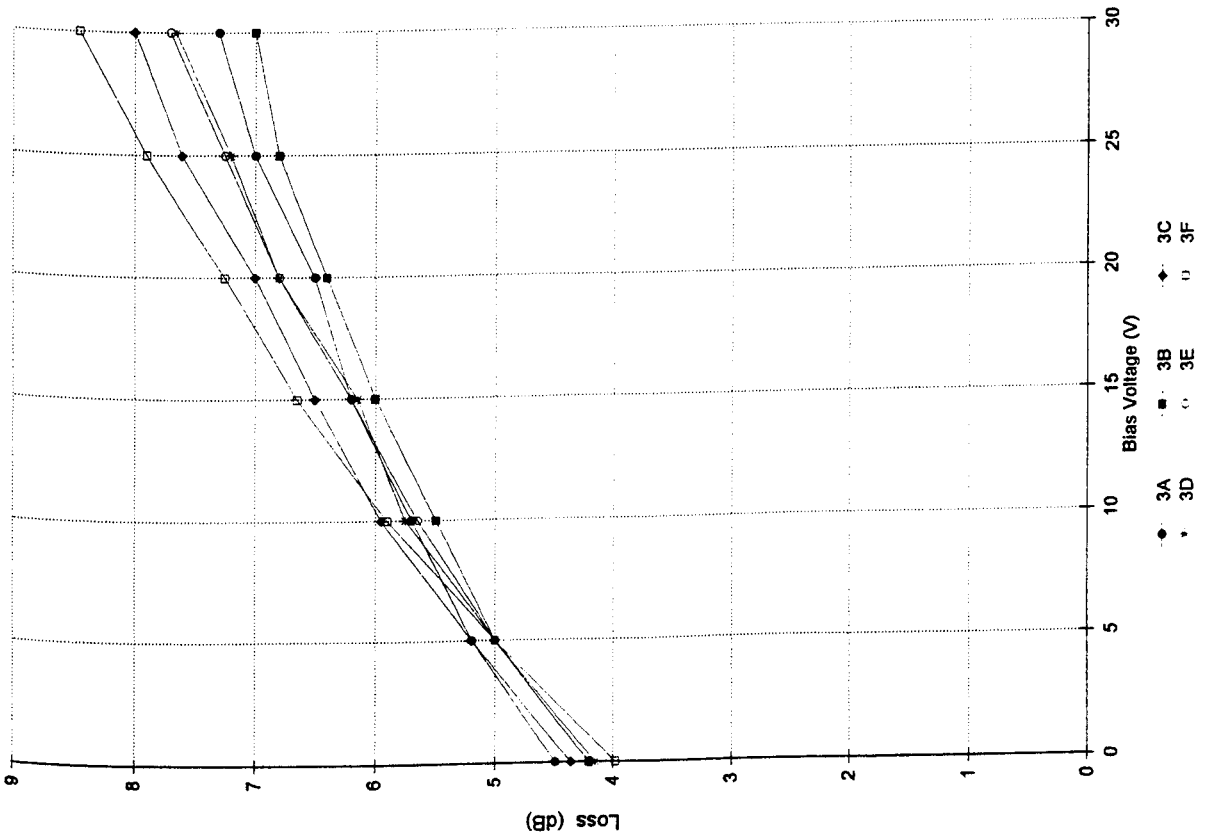


Figure 4.27(c) Insertion loss vs tuning voltage.

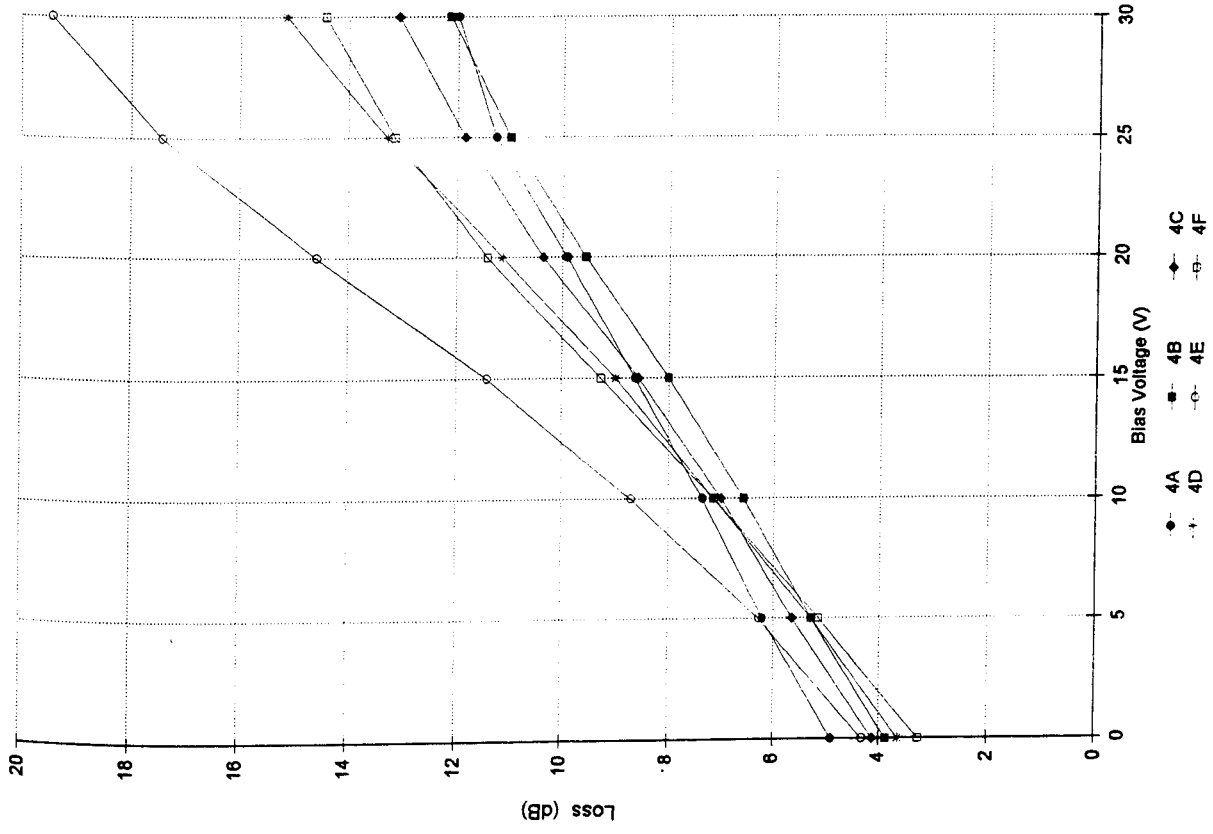


Figure 4.27(d) Insertion loss vs tuning voltage.

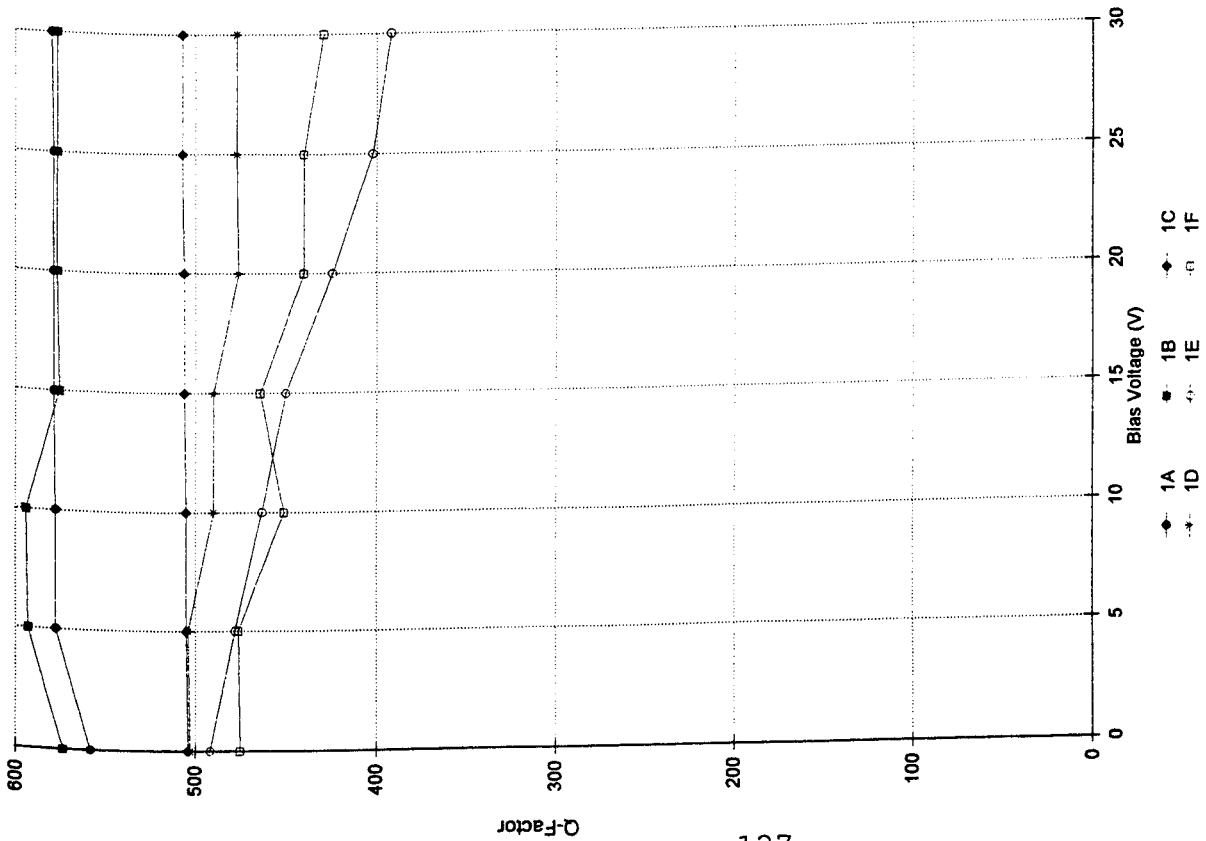


Figure 4.28(a) Loaded Q-factor vs tuning voltage.

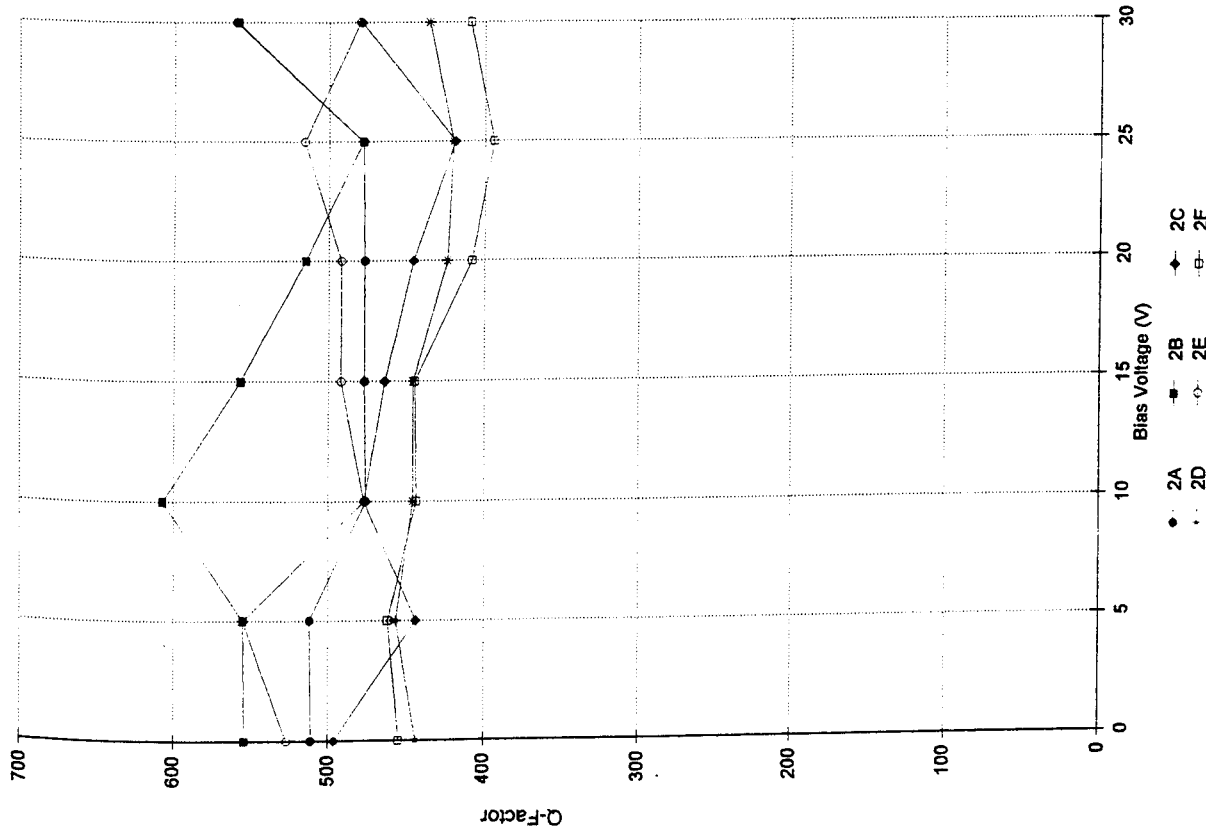


Figure 4.28(b) Loaded Q-factor vs tuning voltage.

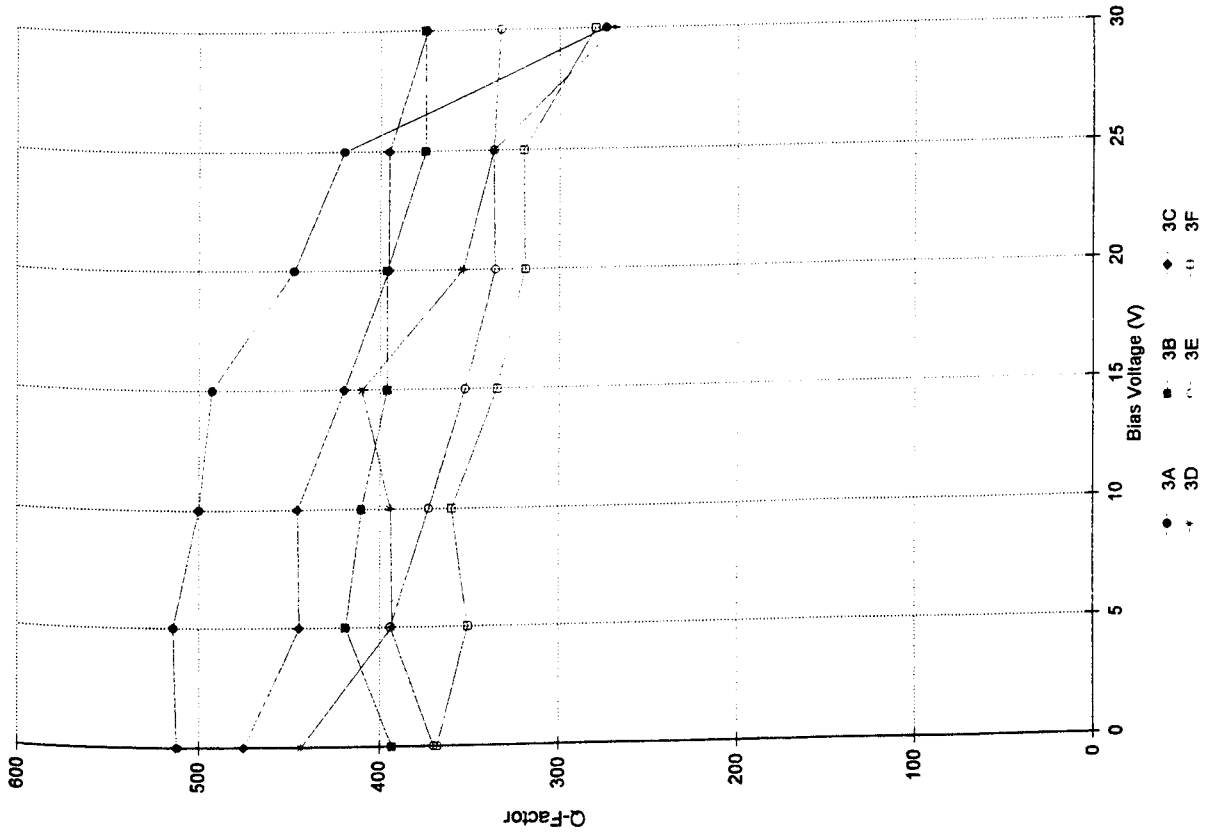


Figure 4.28(c) Loaded Q-factor vs tuning voltage.

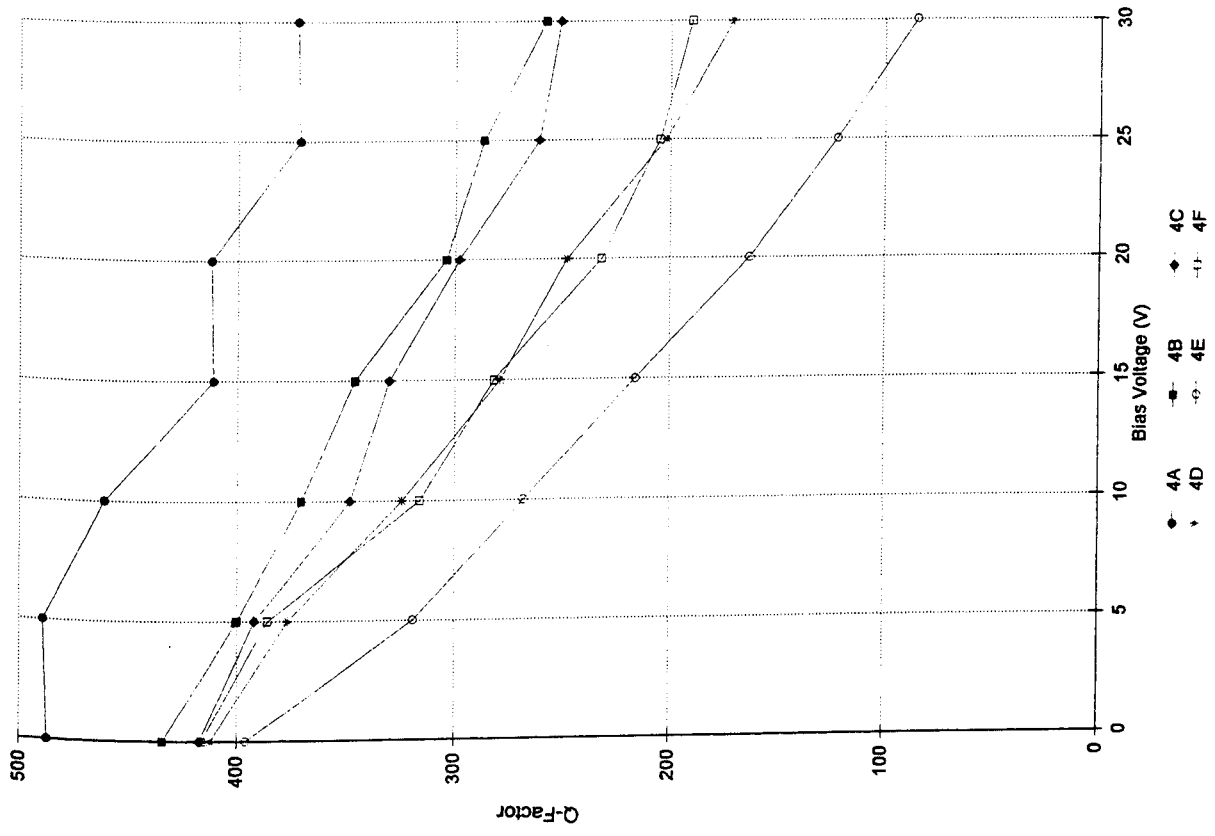


Figure 4.28(d) Loaded Q-factor vs tuning voltage.

Circuits 2A-2J

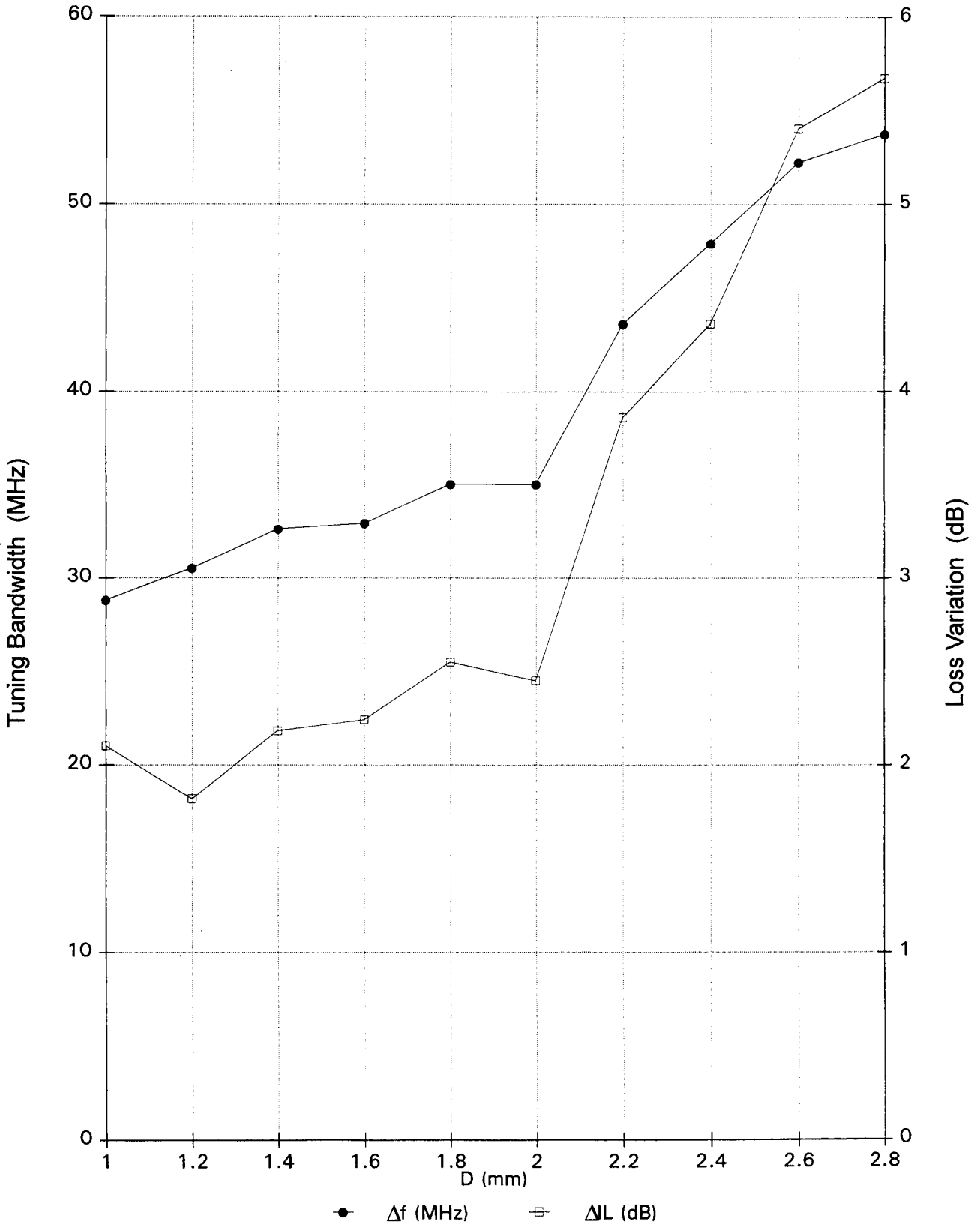


Figure 4.29 Tuning bandwidth & insertion loss vs distance D.

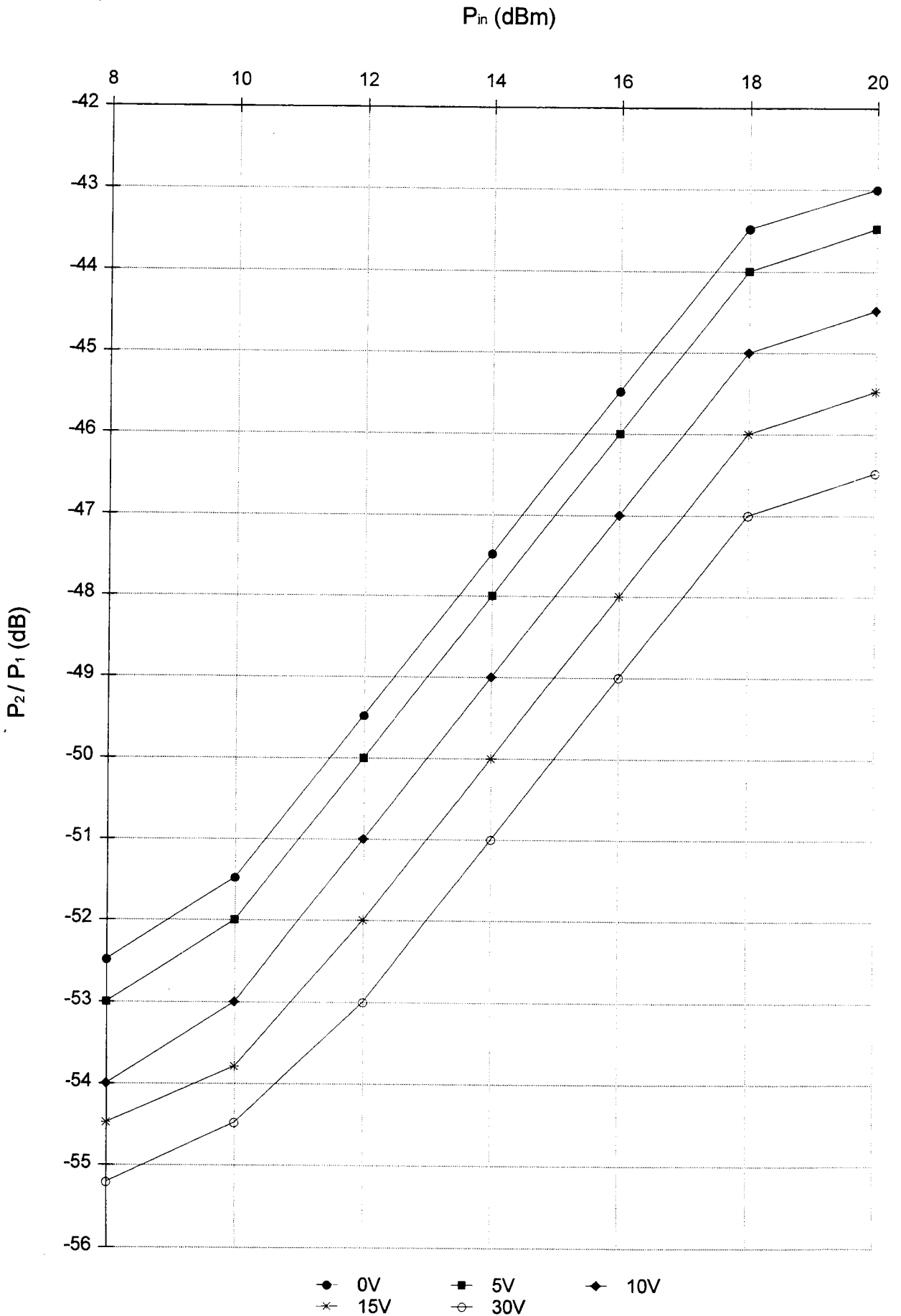


Figure 4.30 Ratio of second to first harmonic power levels vs input power.

Chapter 5

Electronically Tunable DR Bandpass Filters

5.0 Introduction

High performance bandpass filters play a very important role in the efficient utilisation and channelisation of an allocated frequency spectrum. Typically, at microwave frequencies, these filters are realized by using high-Q waveguide cavities because of the narrow bandwidth and low loss in the passband of individual filters which they can offer [1,2]. Because of the recent developments in low loss, temperature stable and high permittivity ceramics, the utilisation of these materials in the form of a dielectric resonator has been challenging the conventional cavity resonator in filter designs [3-6]. The major advantages of the dielectric resonator loaded filter is to reduce the volume by a factor of about $\sqrt{\epsilon_r}$ compared with a metallic cavity filter. In addition to their small size and light weight, this type of filter also provides better tolerance for mechanical design because most of the fields inside the cavity are concentrated in the high permittivity material such that a small change in the dimension of the enclosure has insignificant effects on the resonators properties. Dielectric resonators are also compatible with a microstrip environment, which eliminates the need for microstrip to waveguide adapters.

This chapter is mainly concerned with application of the

methods and results presented in the previous chapters to the design of low cost electronically tunable bandpass filters using dielectric resonators.

A variety of microwave systems require electronically tunable microwave filters that can be tuned over a wide band in a short time (typically 0.5GHz/ms [7]). An example of such a system is an electronic surveillance system receiver that searches for a short duration signal over a wide band. Spectrum analysers and a variety of other test instruments, as well as automated test setups, also require fast electronically tunable filters. A commonly used method of realising electronically tuned microwave filters is to use yttrium iron garnet (YIG) resonators [8]. YIG filters offer high selectivity as well as a wide tuning range. However, the tuning speed of the YIG filters is severely limited by the magnetic hysteresis effect. On the other hand, variation of the depletion layer capacitance of a varactor diode with the reverse bias is free of any hysteresis effect. Hence, fast electronically tunable microwave filters can be realised using varactors as the tuning element with the selectivity offered by the high-Q dielectric resonators.

In this chapter, two methods are developed, based on the general circuit theory which allows the user to determine the number of dielectric resonators, and the values of the coupling coefficients between adjacent resonators and between resonators and microstrip line. This information is necessary to design a

microwave bandpass filter based upon Chebyshev or Butterworth low-pass prototype which form the basis for the majority of microwave filter designs. Since microwave filter theory is well known and widely documented it will not be repeated here, however, the interested reader is referred to reference [9].

In the first method, the design synthesis is based upon the equivalent circuit model of coupled DRs which is directly related to the low-pass prototype elements. In the second method, admittance inverters are introduced into the equivalent circuit, converting the ladder-type bandpass filter into the type which contains only parallel-tuned circuits. In such filters, each resonator resonates at a single mode having a resonant frequency which is equal to the centre frequency of the filter. Design formulas are then derived which relate the low-pass prototype lumped elements to the DR filter and which allows the determination of the coupling coefficient between adjacent resonators. These values can then be related to the physical dimensions of the filter by comparing them with either the experimental or theoretical values of coupling obtained in Chapter 3.

5.1 Important Definitions

The performance of tunable bandpass or band-stop filters may be described by the same criteria as used for high quality fixed components, namely: low-insertion loss, high selectivity, high dynamic range and additionally by certain parameters relevant

only to tunable filters. The most important of them are:

1. Tuning range - defined as the difference between the lowest and highest midband frequency which is achievable within acceptable limits for insertion loss, bandwidth, and response distortion.
2. Tuning speed - defined as the frequency shift which is necessary to change the filter response to another steady state by unit time.
3. Tuning linearity - the maximum deviation of the centre frequency versus a parameter which enforces the tuning (voltage, or resonator length variation) from a best fit straight line over the specified operating range.
4. Tuning sensitivity or tuning efficiency - this can be written as:

$$\eta[\Delta f_o] = \frac{f_o(X_2) - f_o(X_1)}{X_2 - X_1} \quad (5.0)$$

where $f_o(X_2)$ and $f_o(X_1)$ are centre frequencies corresponding to X_2 and X_1 , respectively. X is the variable enforcing the tuning.

5.2 Equivalent Structure of a DR Coupled Filter

A loss less cylindrical DR can be represented by its equivalent model shown in Figure 5.1(a). Figure 5.1(b) shows the equivalent model of a loss free open circuited transmission

line when the line length is even multiples of $\lambda_g/4$.

The structure of a microstrip filter using cylindrical DRs can be represented by a cascade of several DRs coupled by input and output microstrip lines as shown in Figure 5.1(c). The coupling between DRs and between a DR and microstrip are represented by mutual inductances.

However, since two networks coupled by a capacitor are equivalent to two networks coupled by an inductance, Figure 5.1(d), it is possible to simplify the DR filter to that shown in Figure 5.1(e). In the next section this circuit will be shown to equate to a bandpass filter and hence the low-pass prototype elements.

5.3 Proposed Design Method 1

The first stage in this approach is to relate a coupled DR bandpass filter to the low-pass prototype lumped elements. Figure 5.2(a) shows a typical low-pass filter whilst Figure 5.2(b) shows its equivalent frequency transformed bandpass structure. To illustrate the transformation of this structure to that obtained by coupled DRs in Figure 5.1(e), consider a typical bandpass section such as shown in Figure 5.2(c). Splitting capacitor C_1 into two equal parts and inserting an ideal transformer of turns ratio n_{1-1} leads to the schematic of Figure 5.2(d). Recognising that $2C_1$ and the ideal transformer can be replaced by Norton's equivalent capacitive π configuration, Figure 5.3, results in the network of

Figure 5.2(e), where an additional ideal transformer of turns ratio n_{i+1} has been placed at the opposite end of the series inductance. Since n_{i+1} will be less than unity, this means that the negative shunt capacitance $2C_i(1 - 1/n_{i+1})$ can be combined with the positive capacitance C_{i-1} , which is in a corresponding parallel position, to give a positive equivalent capacitance. In addition, by a proper selection of n_{i+1} , the magnitudes of these two capacitances may be made equal, in which case they cancel and may be replaced by an open circuit. In a similar manner, the second transformer and series capacitance combination can be replaced by a capacitive π (see Figure 5.2(f)) and n_{i+1} chosen such that the shunt capacitance on the right vanishes. The resulting network is given in Figure 5.2(g). The derivation of the element value expressions in Figure 5.2(g) may be found in reference [10], and these are given by:

$$t = \frac{1 + C_{i-1}/2C_i}{1 + C_{i-1}/2C_i} \quad (5.1)$$

$$L'_i = \frac{L_i}{(1 + C_{i-1}/2C_i)^2} \quad (5.2)$$

$$C''_{i-1} = 2C_i + C_{i-1} \quad (5.3)$$

$$C'_{i-1} = C_{i-1}(1 + C_{i-1}/2C_i)/t \quad (5.4)$$

$$C'_{i-1} = C_{i-1}(1 + C_{i-1}/2C_i) \quad (5.5)$$

$$C''_{i-1} = 2C_i(1 + C_{i-1}/2C_i)/t \quad (5.6)$$

The π configuration in Figure 5.2(g) is further converted to

its equivalent T structure as shown in Figure 5.2(h). Figure 5.4(a) to 5.4(d) summaries this transformation sequence resulting from the low-pass prototype structure.

A section of Figure 5.4(d), Figure 5.5(a), is now further transformed by first inserting the Norton's transformation in the position of the plane AA' resulting in the schematic of Figure 5.5(c). A second transformer is inserted on the right side of the parallel LC resonant circuit at plane BB'. The transformer inserted is replaced by its equivalent structure as shown in Figure 5.5(d). Further simplification assuming the turns ratio $n_{i-1}=n_{i+1}$ results in the final structure shown in Figure 5.5(e).

In practice n can have any value that makes the components of the final section physically realisable. For example, n must be greater than one, or the capacitance $C_{i-1}(n-1)/n$ will not be realisable. A convenient value of n is that value which makes all the shunt capacitances equal i.e.:

$$\left(\frac{n-1}{n}\right)C_{i-1} = \frac{C_i}{n^2} - \frac{2(n-1)}{n^2}C_{i-1}$$

$$\therefore n = \frac{1}{2} \left(\sqrt{\frac{2C_i}{C_{i-1}} + 5} - 1 \right) \quad (5.7)$$

The above equation assumes $C_{i-1}=C_{i+1}$ which is usually the case. The element value in Figure 5.5 can be expressed by the

following equations:

$$C_{i-1}''' = C_{i-1} \left(\frac{n-1}{n} \right) \quad (5.8)$$

$$L_i' = n^2 L_i \quad (5.9)$$

$$C_{i-1} = \frac{C_{i-1}}{n} \quad (5.10)$$

$$C_{i-1}' = \frac{C_{i-1}}{n} \quad (5.11)$$

$$C_i'' = \frac{C_i}{n^2} - \frac{(n-1)}{n^2} (C_{i-1} + C_{i-1}') \quad (5.12)$$

$$C_{i-1}''' = C_{i-1} \frac{(n-1)}{n} \quad (5.13)$$

The complete transformation sequence is shown in Figure 5.6. By inspection we can see that the final structure is exactly equivalent to that represented in Figure 5.1(e). This equivalence allows us to determine the coupling coefficient between adjacent resonators and between resonator and input/output lines from the values of the low-pass prototype elements when the centre frequency and filter bandwidth are specified.

Referring to Figure 5.7, the coupling coefficients between the various sections are generally defined by [11]:

$$k'_{j,j+1} = \frac{C_{j,j+1}}{\sqrt{C_j C_{j+1}}} \quad j=1, \dots, n-1 \quad (5.14)$$

where $C_{j,j+1}$ are the series capacitors and C_j, C_{j+1} are shunt capacitors. Since the metal cavity housing the microstrip filter circuit is evanescent in nature a correction factor is

introduced in Equation (5.14) which is given by $F = (-9.257 \cdot k'_{j,j+1} + 0.148) / a \cdot b$ [10], where a and b are the width and height dimensions, respectively, of the metal enclosure. This relationship was determined experimentally and the new coupling coefficient is now given by $k_{j,j+1} = F \cdot k'_{j,j+1}$. The un-normalised coupling coefficient is represented by [11]:

$$K_{j,j+1} = \frac{\Delta f}{f_o} k_{j,j+1} \quad (5.15)$$

where Δf is the 3dB bandwidth and f_o is the centre frequency.

C_{12} , $C_{n-1,n}$ are the coupling capacitors between the input and output line and the DR. These define the input and output coupling coefficients K_{12} and $K_{n-1,n}$. C_{23} coupling capacitor defines the coupling between the inner second and third resonators represented by K_{23} .

From the above relationships the inter-resonator coupling coefficient values can be determined. The corresponding locations of the resonators can be obtained from either the measured or theoretical coupling data for inter-resonator and end resonator coupling as discussed earlier in Chapter 3.

To verify the validity of the proposed technique a fixed-frequency dielectric resonator bandpass filter was designed and its performance simulated using Touchstone.

The design procedure consists of the usual steps:

1. Select a normalised low-pass prototype filter which satisfies the necessary frequency response criterion.

2. Transformation of this prototype network to the required filter with the specified centre and/or band-edge frequencies.
3. Simulation and realisation of the network using dielectric resonators.

5.3.1 Design 1

The filter specifications selected are:

Centre frequency: $f_o=3270\text{MHz}$
 3dB Bandwidth: $\Delta f=30\text{MHz}$
 Number of DRs: $N=3$
 Response: Butterworth maximally flat
 Input/Output impedance: $Z_o=50\Omega$
 Resonator material: $(\text{ZrSn})\text{TiO}_4$, $\epsilon_r=36$
 Resonator dimensions: $D=17.145\text{mm}$, $H=7.722\text{mm}$
 Substrate: Cu217 , $\epsilon_r=2.17$, $h=0.794\text{mm}$

The desired $N=3$ prototype parameters are [9]:

$$g_0=1, g_1=1, g_2=2, g_3=1, g_4=1 \text{ and } \omega_1'=1$$

The third-order low-pass Butterworth filter shown in Figure 5.8(a) is first transformed into the bandpass structure of Figure 5.8(b) and successive transformations lead to the final structure in Figure 5.8(c). The lumped-elements have been scaled by using the following formulas:

$$L' = \frac{R'}{2\pi f'} L \quad (5.16)$$

$$C' = \frac{1}{R' 2\pi f'} C \quad (5.17)$$

where f' is the cut-off frequency and R' the input/output impedance.

The coupling parameters from Equations 5.14 and 5.15 are:

$$K_{12}=0.012$$

$$K_{23}=0.016$$

The simulated amplitude and return loss response of the filter is shown in Figure 5.9 verifying that the filter centre frequency and bandwidth are 3278MHz and 30MHz, respectively, as specified.

This method involves the computation of many expressions which can be very tedious. Secondly, the component values of the filter does not reflect the symmetry of the structure. Because of this and its complexity another method of designing dielectric filters was developed based on admittance inverters. This method was used to design and fabricate several filters as discussed next.

5.4 Proposed Design Method 2

In this method an admittance inverter is employed to realise the coupled DR filter shown in Figure 5.1(e). The first stage in this second approach is to demonstrate the practical use of

the capacitance inverter, in Figure 5.10(a) a normalised low-pass filter with a $N=5$ is shown. This constitutes the starting point of synthesis. To design a bandpass structure, the frequency transformation must be applied. In Figure 5.10(b) the circuit of the bandpass structure is shown. With reference to this figure the series resonant circuit is equivalent to an ideal inverter followed by parallel-resonant circuit and terminated by another ideal inverter. Thus, Figure 5.10(c) shows the third consecutive step of the procedure. In Figure 5.10(d) all inverters are substituted by capacitors, and Figure 5.10(e) shows the network after combining positive and negative capacitors. The coefficients $g_1, g_2, g_3, \text{ etc.}$, are ladder coefficients of the low-pass prototype.

The configuration shown in Figure 5.10(c) is intuitively pleasing; it is easy to visualise the response of the filter being controlled by the number of resonators, the coupling between them, and the terminations as seen by the end sections.

In practice an admittance inverter can be realised by using a quarter wavelength transmission line, but this is not a practical solution in the present case since a coupled DR filter is employed. However, the property of an admittance inverter can also be exhibited by a series inductor and a series capacitor albeit over a relatively narrow bandwidth. In the current case the series capacitor coupling ($C_{n-1,n}$), Figure 5.1(e), is achieved merely by the physical proximity of one resonator to another.

From the equivalent circuit of the DR coupled bandpass filter and its lumped-element counterpart the design equations are now derived. The admittance inverter constants, J_n , are first derived from the element values of a low-pass prototype. This will be performed for the case $N=3$ and then the results generalised.

With reference to Figure 5.11(a), and using the fact that all resonators resonate at the same frequency, $L_n C_n = 1/\omega_r^2$, the admittance, Y , seen just to the right of the J_3 inverter is:

$$Y = j\omega C + \frac{1}{j\omega L} + J_4^2 R_B = j\omega C \left(1 - \frac{\omega_r^2}{\omega^2} \right) + j_4^2 R_B \quad (5.18)$$

The admittance seen looking to the right at the plane AA' is J_3^2/Y and thus the admittance seen just to the right of J_2 is $j\omega C [1 - (\omega_r/\omega)^2] + J_3^2/Y$. By continuing this sequential operation it can be shown that:

$$Y_i = \frac{1}{(J_1 R_B)^2} \left(j\omega C \left[1 - \left(\frac{\omega_r}{\omega} \right)^2 \right] + \frac{J_2^2}{j\omega C \left[1 - \left(\frac{\omega_r}{\omega} \right)^2 \right] + \frac{J_3^2}{j\omega C \left[1 - \left(\frac{\omega_r}{\omega} \right)^2 \right] + J_4^2 R_B}} \right) \quad (5.19)$$

Relating the result above to the input admittance of a lumped-element bandpass filter of the type shown in Figure 5.10(b), it may be shown that:

$$Y_i = j\omega C'_1 [1 - (\omega_r/\omega)^2] + \frac{1}{j\omega L'_2 [1 - (\omega_r/\omega)^2] + \frac{1}{j\omega C'_3 [1 - (\omega_r/\omega)^2] + G_B}} \quad (5.20)$$

which is identical in form to Equation (5.19). Thus, the two circuits will be equivalent if the following conditions are met:

$$(J_1 R_B)^2 = \frac{C}{C'} \quad (5.21a) \quad (J_2 R_B)^2 = \frac{C^2 R_B^2}{L'_2 C'_1} \quad (5.21b)$$

$$(J_3 R_B)^2 = \frac{C^2 R_B^2}{L'_2 C'_3} \quad (5.21c) \quad (J_4 R_B)^2 = \frac{C}{C'_3} \quad (5.21d)$$

With the lumped-element bandpass filter having been designed via a reactance transformation of a low-pass prototype filter, we have:

$$C'_1 = \frac{g_1}{w\omega_o R_B} \quad (5.22a)$$

$$L'_2 = \frac{g_2 R_B}{w\omega_o} \quad (5.22b)$$

$$C'_3 = \frac{g_3}{w\omega_o R_B} \quad (5.22c)$$

where $w = (\omega_2 - \omega_1) / \omega_0$ is the fractional bandwidth of the filter,

and g_n is the value of the n th lumped element in the low-pass prototype circuit.

Using $LC=1/\omega_o^2$ and Equations (5.22) in (5.21) it may be shown that:

$$J_1 = \sqrt{\frac{C\omega_o}{g_1 R_B}} \quad (5.23a)$$

$$J_3 = \frac{C\omega_o}{\sqrt{g_2 g_3}} \quad (5.23b)$$

$$J_2 = \frac{C\omega_o}{\sqrt{g_1 g_2}} \quad (5.23c)$$

$$J_4 = \sqrt{\frac{C\omega_o}{g_3 R_B}} \quad (5.23d)$$

The generalisation of these results to the case of $n+1$ coupled resonators is, by induction, thus:

$$J_1 = \sqrt{\frac{C\omega_o}{g_1 R_B}} \quad (5.24a)$$

$$J_n = \frac{C\omega_o}{\sqrt{g_{n-1} g_n}} \quad (5.24b)$$

$$J_{n+1} = \sqrt{\frac{C\omega_o}{g_n g_{n+1} R_B}} \quad (5.24c)$$

Note that for a Butterworth design, or for a Chebyshev design with $N=\text{odd}$, $g_{n+1}=1$.

It is now possible to derive the corresponding coupling

capacitor equations for the admittance values. Looking left of the plane AA' in Figure 5.12(a) out toward C_{o1} and G_A in series, the admittance is:

$$Y = \frac{1}{\frac{1}{j\omega_o C_{o1}} + \frac{1}{G_A}} = \frac{\frac{\omega_o^2 C_{o1}^2}{G_A}}{1 + \left(\frac{\omega_o C_{o1}}{G_A}\right)^2} + j \frac{\omega_o C_{o1}}{1 + \left(\frac{\omega_o C_{o1}}{G_A}\right)^2} \quad (5.25)$$

Meanwhile, looking left of the plane BB' in Figure 5.12(b) into the J inverter the conductance

$$G = \frac{J_1^2}{G_A} \quad (5.26)$$

is seen.

Equating G in Equation (5.26) to the real part of Y in Equation (5.25) and solving for C_{o1} gives:

$$\frac{J_1^2}{G_A} = \frac{\frac{\omega_o^2 C_{o1}^2}{G_A}}{1 + \left(\frac{\omega_o C_{o1}}{G_A}\right)^2}$$

$$\frac{J_1^2}{G_A} \left[1 + \left(\frac{\omega_o C_{o1}}{G_A}\right)^2 \right] = \frac{\omega_o^2 C_{o1}^2}{G_A}$$

$$\frac{J_1^2}{G_A} + \frac{(\omega_o C_{o1})^2}{G_A} \left[\left(\frac{J_1}{G_A} \right)^2 - 1 \right] = 0$$

$$\therefore C_{o1} = \frac{J_1}{\omega_o \sqrt{1 - \left(\frac{J_1}{G_A} \right)^2}} \quad (5.27a)$$

Similarly we can derive the intermediate and end coupling capacitor equations and which are:

$$C_{j,j-1} = \frac{J_{j,j-1}}{\omega_o} \quad \text{for } j=1 \text{ to } n-1 \quad (5.27b)$$

$$C_{n,n-1} = \frac{J_{n,n-1}}{\omega_o \sqrt{1 + \left(\frac{J_{n,n-1}}{G_B} \right)^2}} \quad (5.27c)$$

The imaginary part of Y in Equation (5.25) can be dealt with satisfactorily by replacing it by a shunt capacitive susceptance $\omega_o C_{o1}^e$ of the same size which then leads to:

$$C_{o1}^e = \frac{C_{o1}}{1 + \left(\frac{\omega_o C_{o1}}{G_A} \right)^2} \quad (5.28)$$

Since C_{o1}^e effectively increases the shunt capacitance of resonator 1, this amount should be subtracted from C_1 when

computing the net shunt capacitance to be used in constructing resonator 1. Of course, the same reasoning applies for design of the $C_{n,n+1}$ coupling at the other end of the filter. The effective value of the end coupling capacitor is:

$$C_{n,n+1}^e = \frac{C_{n,n+1}}{1 + \left(\frac{\omega_o C_{n,n+1}}{G_B} \right)^2} \quad (5.29)$$

Finally, the node capacitors are calculated as the difference between the resonator capacitance and the two adjacent coupling capacitor.

$$C_1 = C - C_{o1}^e - C_{12} \quad (5.30a)$$

$$C_k = C - C_{k-1,k} - C_{k,k+1} \quad \text{for } k=2 \text{ to } n-1 \quad (5.30b)$$

$$C_n = C - C_{n-1,n} - C_{n,n+1}^e \quad (5.30c)$$

The design is then completed by calculating the coupling parameters using Equations 5.14 and 5.15.

5.4.1 Design Procedure

Now that the preliminary details have been addressed, the calculation of actual component values to build the DR filter according to the procedure outlined below may be performed as follows.

1. Choose source and load resistances and the inductance or capacitance of each resonator. Assume that the same value

of inductor, L , is to be used in each resonator. Figure 5.13 shows the schematic of a generic bandpass filter with each component defined. Once the resonator inductance has been selected, the resonant capacitance is calculated using $C=1/\omega_o^2L$.

2. Next the admittances of the end coupling capacitors and the admittance inverters are determined using the previously calculated values of resonator capacitance and normalised low-pass elements using Equations (5.24a) to (5.24c).
3. After the admittance values have been found, the corresponding capacitor values are calculated using Equations (5.27a) to (5.27c).
4. The effective value of the end coupling capacitors is found next using Equations (5.28) and (5.29).
5. Next, the node capacitors are calculated as the difference between the resonator capacitance and the two adjacent coupling capacitors using Equations (5.30a) to (5.30c).
6. Finally, the coupling coefficients between adjacent resonators are calculated using Equations (5.14) and (5.15).

This completes the design of the filter.

5.4.2 Design 2

Now that the design procedure has been established, three filters are now designed and analysed. The design

specifications of these filters are:

BPF-1

Centre frequency: $f_o=3.26\text{GHz}$
3dB Bandwidth: $\Delta f=12\text{MHz}$
Ripple: $L_{ar}=0.01\text{dB}$
Minimum attenuation: $20\text{dB @ } f=f_o \pm 0.06 \text{ GHz}$
Input/Output impedance: $Z_o=50\Omega$
Resonator material: $(\text{ZrSn})\text{TiO}_4$, $\epsilon_r=36$
Resonator dimensions: $D=17.145\text{mm}$, $H=7.722\text{mm}$
Substrate: Cu217 , $\epsilon_r=2.17$, $h=0.794\text{mm}$

BPF-2

Centre frequency: $f_o=3.26\text{GHz}$
3dB Bandwidth: $\Delta f=14\text{MHz}$
Ripple: $L_{ar}=0.01\text{dB}$
Minimum attenuation: $25\text{dB @ } f=f_o \pm 0.035 \text{ GHz}$
Input/Output impedance: $Z_o=50\Omega$
Resonator material: $(\text{ZrSn})\text{TiO}_4$, $\epsilon_r=36$
Resonator dimensions: $D=17.145\text{mm}$, $H=7.722\text{mm}$
Substrate: Cu217 , $\epsilon_r=2.17$, $h=0.794\text{mm}$

BPF-3

Centre frequency: $f_o=3.26\text{GHz}$
3dB Bandwidth: $\Delta f=18\text{MHz}$
Ripple: $L_{ar}=0.01\text{dB}$
Minimum attenuation: $25\text{dB @ } f=f_o \pm 0.025 \text{ GHz}$
Input/Output impedance: $Z_o=50\Omega$
Resonator material: $(\text{ZrSn})\text{TiO}_4$, $\epsilon_r=36$
Resonator dimensions: $D=17.145\text{mm}$, $H=7.722\text{mm}$
Substrate: Cu217 , $\epsilon_r=2.17$, $h=0.794\text{mm}$

All these would, of course, be Chebyshev filters. The number of DRS needed to meet the attenuation requirements can be determined by [9]:

$$\frac{\omega'}{\omega_1} = \frac{1}{w} \left(\frac{\omega}{\omega_o} - \frac{\omega_o}{\omega} \right) \quad (5.31)$$

where ω_o , ω and w are the centre frequency, variable frequency and fractional bandwidth, respectively. Thus, filters BPF-1 requires two dielectric pucks, BPF-2 requires three pucks and BPF-3 requires four pucks. From here onwards these filters will be referred to as 2-pole, 3-pole and 4-pole filters, respectively.

Since the number of poles has been determined, we can proceed directly to the normalised low-pass element values. These can be obtained from either tables or from the equations presented in reference [9]. After calculating or looking up these values, for a 2-pole (see Figure 5.14) we have:

$$g_o=1, g_1=0.4488, g_2=0.4077, g_3=1.1007$$

The fractional bandwidth which is the ratio of filter bandwidth to centre frequency is $w=0.00368$.

The resonator inductance is arbitrarily chosen to assume a value of 45nH. The resonant capacitance is calculated next as:

$$C = \frac{1}{\omega_o^2 L} = 0.05296 \text{ pF}$$

and the input coupling capacitance is then found:

$$J_{o1} = \sqrt{\frac{G_A C W \omega_o}{g_1}} = 4.218 \times 10^{-4}$$

$$C_{o1} = \frac{J_{o1}}{\omega_o \sqrt{1 - \left(\frac{J_{o1}}{G_A}\right)^2}} = 0.020597 \text{ pF}$$

$$C_{o1}^e = \frac{C_{o1}}{1 + \left(\frac{\omega_o C_{o1}}{G_A}\right)} = 0.020595 \text{ pF}$$

The coupling capacitors between the resonators are calculated next:

$$J_{12} = \frac{C W \omega_o}{\sqrt{g_1 g_2}} = 9.33 \times 10^{-6}$$

$$C_{12} = \frac{J_{12}}{\omega_o} = 0.0004556 \text{ pF}$$

Then the output coupling capacitor is determined:

$$J_{23} = \sqrt{\frac{G_B C W \omega_o}{g_2 g_3}} = 4.21 \times 10^{-4}$$

$$C_{23} = \frac{J_{23}}{\omega_o \sqrt{1 - \left(\frac{J_{23}}{G_B}\right)^2}} = 0.020597 \text{ pF}$$

$$C_{23}^e = \frac{C_{23}}{1 + \left(\frac{\omega_o C_{23}}{G_B}\right)} = 0.020587 \text{ pF}$$

Next, the node capacitors are found by taking the difference between the resonator capacitance and the coupling capacitors.

$$C_1 = C - C_{o1}^e - C_{12} = 0.03190 \text{ pF}$$

$$C_2 = C - C_{23}^e - C_{12} = 0.03191 \text{ pF}$$

Finally, the coupling coefficients between adjacent resonators are calculated using:

$$K_{12} = F \cdot \frac{\Delta f}{f_o} \frac{C_{12}}{\sqrt{C_1 C_2}} = 3.81 \times 10^{-4}$$

The resonator position corresponding to this coupling value is 46.0mm, determined from the inter-resonator coupling data, presented in Chapter 3.

The completed 2-pole filter is shown in Figure 5.15.

The 3-pole and 4-pole filter parameters are calculated similarly and these are:

3-pole BPF

$$C_{o1} = 0.01877\text{pF}$$

$$C_{o1}^e = 0.01876\text{pF}$$

$$C_{12} = 0.00029\text{pF}$$

$$C_{23} = 0.00029\text{pF}$$

$$C_{34} = 0.01877\text{pF}$$

$$C_{34}^e = 0.01876\text{pF}$$

$$C_1 = 0.03385\text{pF}$$

$$C_2 = 0.05232\text{pF}$$

$$C_3 = 0.03385\text{pF}$$

$$K_{12} = 9.98 \times 10^{-4}$$

$$K_{23} = 9.98 \times 10^{-4}$$

$$d_{12} = 37.0\text{mm}$$

$$d_{23} = 37.0\text{mm}$$

4-pole BPF

$$C_{o1} = 0.020018\text{pF}$$

$$C_{o1}^e = 0.020009\text{pF}$$

$$C_{12} = 0.00031547\text{pF}$$

$$C_{23} = 0.0002322\text{pF}$$

$$C_{34} = 0.0003161\text{pF}$$

$$C_{48} = 0.020018\text{pF}$$

$$C_{48}^e = 0.020009\text{pF}$$

$$C_1 = 0.03264\text{pF}$$

$$C_2 = 0.0524\text{pF}$$

$$C_3 = 0.0524\text{pF}$$

$$C_4 = 0.03263\text{pF}$$

$$K_{12} = 1.356 \times 10^{-3}$$

$$K_{23} = 7.20 \times 10^{-3}$$

$$K_{34} = 1.356 \times 10^{-3}$$

$$d_{12} = 34.4\text{mm}$$

$$d_{23} = 35.61\text{mm}$$

$$d_{34} = 34.4\text{mm}$$

The complete 3-pole and 4-pole filters are shown in Figure 5.16 and 5.17, respectively.

5.4.3 Evaluation of Designs

To verify the designs, the filters were first analysed using computer simulation with Touchstone and the designs were then fabricated. Figures 5.18 to 5.20 shows the plot of the filter amplitude and return loss response as well as a close-up of the passband response. Figures 5.21 to 5.23 shows the actual measured responses of these filters using a scalar network analyser.

Table 5.1 shows the comparison of the salient features of the computed and measured results to the design specifications. All these designs were based on virtually no passband insertion loss (ideal case). The computer simulation also showed no loss since Touchstone assumes ideal conditions and doesn't take into account practical conditions in which losses will definitely be encountered. The measured insertion loss was about 4dB in the worst case for the 2-pole design. This can be attributed to losses encountered in the DR and the tuning screws which were mounted above each resonator to eliminate interfering box modes.

Computed values of the centre frequency matched exactly to the design values. However, the measured values of the centre frequency were out by 2% in the worst case. This can be attributed entirely to the tuning screws shifting the resonant

frequency of the resonators [12]. This frequency change can be remedied by selecting resonators with a slightly lower than required resonant frequency.

The discrepancy in the 3dB bandwidth computed was due to the simplified model used in the analysis. Touchstone does not take into account the resonators high-Q in its simulation. The measured bandwidth is below by 6.7% (worst case) for the 2-pole and by only 0.35% for the 3-pole filter.

During the process of positioning the DRs in the circuit it was observed that the outer most resonators (i.e. those closest to the input and output lines) determine the amount of power coupled in the system. That is, the tighter the coupling the lower the passband insertion loss and vice-versa. Moreover, the inner resonators determined the amount of passband ripple, the spacing between the resonators determined the level of the passband ripple.

The exact location of the resonators was extremely vital in determining the filter response. The slightest disturbance in the resonators position had a profound change in the filter response. Therefore positioning of the resonators correctly in the circuit is a very time consuming process.

The experimental results correlate with the theoretically predicted results validating the proposed design procedure. Moreover, the measured results show the lack of neighbouring spurious passbands around the desired passband. Hence, electronically tunable DR bandpass filters were designed and

implemented using this design technique as discussed in the next section.

5.5 Tunable DR Filter Designs

Electronically tunable DR bandpass filters were designed and realised based on the design technique outlined above. The design specifications of these filters were identical to the 2-pole, 3-pole, and 4-pole filters outlined above. The tuning configuration employed consisted of two semi-circular microstrip tracks loaded with commercially available GaAs varactor diodes; SMV1400-04 manufactured by Alpha Ind. Inc., as discussed in Chapter 4. The tuning configurations were constructed directly on the substrate below each resonator and they all had a common bias supply. The layout of these filters are shown in Figures 5.24 to 5.26. The corresponding measured transmission responses are shown in Figures 5.27 to 5.29.

5.5.1 Evaluation of Designs

Table 5.2 compares the salient features of the measured response to the design specifications.

The final designs produced were moderately lossy, as expected. This can be attributed to losses encountered in the resonator, the tuning circuit, and the tuning screws. The measured insertion loss was about 5dB in the worst case at a bias of 0V.

The measured value of the centre frequency was up by 2.46%

in the worst case. This is mainly due to the tuning screws located above the resonators and the tuning circuit just below them, since the resonant frequency of the resonator operating in the TE_{016} mode is highly sensitive to the proximity of the ground plane. This problem can be overcome by selecting resonators with a marginally lower than required resonant frequency.

The measured 3dB bandwidth is below that required by 34.7% in the worst case for the 4-pole design and by only 3.75% for the 2-pole design. From experimental observations it was discovered that the large discrepancy in the bandwidth was due to the non-uniform height alignment of the tuning screws above the resonators. The depth of especially the outer two screws had an adverse effect of comprising the filter bandwidth. The bandwidth, however, could easily be improved by choosing an appropriately sized enclosure whose modes are far away from the desired operating frequency, hence, making the use of the tuning screws superfluous.

The tuning characteristics of the filters are shown in Figures 5.30 to 5.32. Table 5.3 lists some of the characteristics of these filters. The measured graphs indicate almost linear frequency tuning performance over the tuning range for 5V to 25V bias. The tuning non-linearity is marginal and discernable near 0V bias. It is evident from Table 5.3 that the 3-pole filter exhibits the largest tuning range and the highest tuning sensitivity of 38.8MHz and 1.293MHz,

respectively. However, this is at the expense of large variation in the passband insertion loss of 12.49dB as compared to only 0.75dB obtained for the 2-pole design. The 3dB bandwidth of these filters are almost constant over the entire tuning range. The photographs of the tunable filters are shown in Figures 5.33 to 5.35.

5.6 Conclusions

Novel design techniques for symmetrical DR filters have been developed and explicit design formulae are presented. One of these techniques has been used in the design of both fixed frequency and electronically tuned DR filters. Computer analysis of the filters was presented and this agrees closely with the measured performances of experimental designs. The design technique employed enables filters to be tuned across relatively wide tuning bandwidths with almost constant passband and high isolation in the stopbands. Compared to conventional cavity resonator filters, these devices offer drastic reduction in volume and weight. Moreover, the bandpass design lends itself to an inexpensive and reproducible manufacturing process.

References

1. Riblet, H.J., "A Unified Discussion of High-Q Waveguide Filter Design Theory," IRE Trans. PGMTT, vol.MTT-6, Oct.1958, pp359-368.
2. Atia, A.E. and Williams, A.E., "Narrow-Bandpass Waveguide Filters," IEEE Trans. on Microwave Theory & Techniques, vol. MTT-20, April 1972, pp258-265.
3. Harrison, W.H., "A Miniature High-Q Bandpass Filter Employing Dielectric Resonators," IEEE Trans. on Microwave Theory & Techniques, vol. MTT-16, April 1968, pp210-218.
4. Cohn, S.B., "Microwave Filters Containing High-Q Dielectric Resonators," IEEE Trans. on Microwave Theory & Techniques, vol. MTT-16, April 1968, pp218-227.
5. Plourde J.K. and Linn, D.F., "Microwave Dielectric Resonator Filters Using Ba₂Ti₂O₂₀ Ceramics," IEEE Trans. on Microwave Theory & Techniques, vol. MTT-27, March 1979, pp233-238.
6. Atia, A.E. and Bonetti, R.R., "Generalised Dielectric Resonator Filters," COMSAT Technical Review, vol.11, Autumn 1981, pp321-343.
7. Uher, J., Hoefler, J.R., "Tunable Microwave and Millimeter-Wave Band-Pass Filters," IEEE Trans. on Microwave Theory & Techniques, vol. MTT-39, No.4, April 1991, pp643-652.
8. Carter, P. S., "Magnetically-Tunable Microwave Filters Using Single-Crystal Yttrium-Iron Garnet Resonators," IRE Trans. on Microwave Theory & Techniques, May 1961, pp252-

260.

9. Matthaei, G., Young, L., and Jones, E.M.T., "Microwave Filters, Impedance-Matching Networks, and Coupling Structures," McGraw-Hill, 1964.
10. Virdee, B., Internal Research Report, 1994.
11. Humpherys, D.S., "The Analysis, Design, and Synthesis of Electrical Filters," Prentice-Hall, 1970.
12. Kajfez, D., Guillon, P., "Dielectric Resonators," Artech House, Inc., 1986.

Table 5.1 Comparison of Fixed Frequency DR Filter Performance

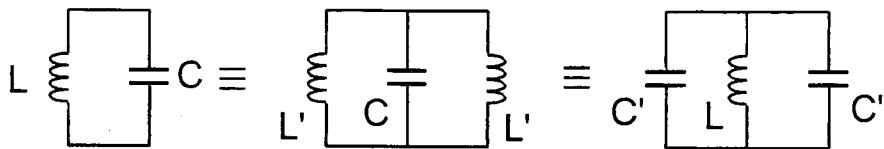
Filter	Design Specifications			Computed			Measured		
	Passband IL(dB)	fo(GHz)	3dB BW (MHz)	Passband IL(dB)	fo(GHz)	3dB BW (MHz)	Passband IL(dB)	fo(GHz)	3dB BW (MHz)
2-pole	0.01	3.26	12.0	0.0	3.260	39.7	4.13	3.3286	11.20
3-pole	0.01	3.26	14.0	0.0	3.262	26.4	3.27	3.3104	13.95
4-pole	0.01	3.26	18.0	0.0	3.260	26.6	4.00	3.3084	17.55

Table 5.2 Comparison of Electronically Tuned DR Filter Performance

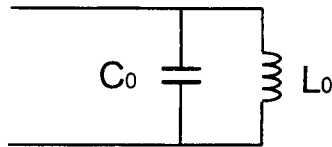
Filter	Design Specifications			Measured		
	Passband IL(dB) @ 0V	fo(GHz) @ 0V	3dB BW (MHz) @ 0V	Passband IL(dB) @ 0V	fo(GHz) @ 0V	3dB BW (MHz) @ 0V
2-pole	0.01	3.26	12.0	4.13	3.3283	11.55
3-pole	0.01	3.26	14.0	5.21	3.3401	12.37
4-pole	0.01	3.26	18.0	5.06	3.3347	11.76

Table 5.3 Characteristics of Electronically Tuned Filters

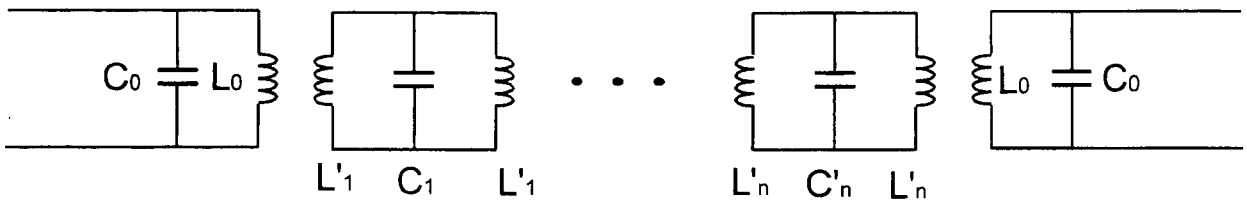
Tunable Filter	Δf (MHz) 0-30V	η (MHz/V) 0-30V	ΔIL (dB) 0-30V	Δf 3dB BW (MHz)
2-pole	20.0	0.667	0.75	1.5
3-pole	38.8	1.293	12.49	0.9
4-pole	24.0	0.800	2.07	1.6



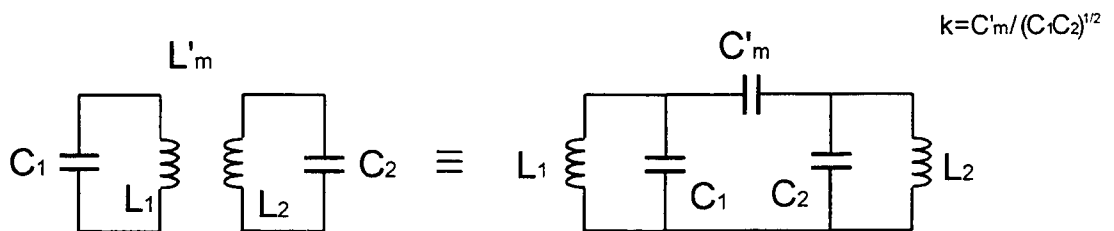
(a) Equivalent model of a loss-less DR.



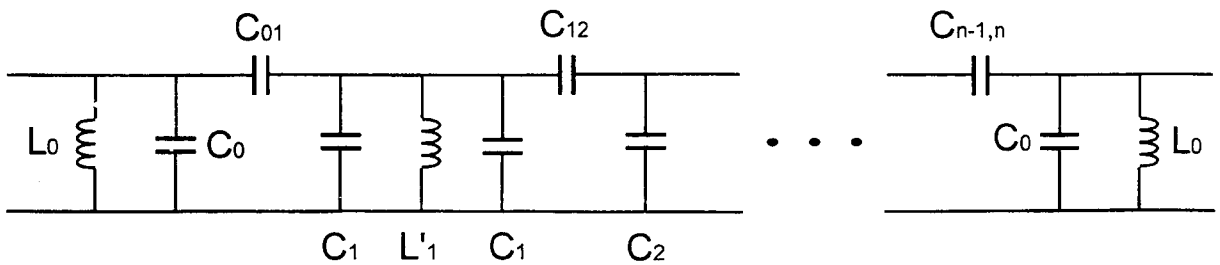
(b) Equivalent model of a loss-free open-circuited $\lambda_g/4$ transmission line.



(c) Equivalent model of cascaded DRs coupled to an input/output line.

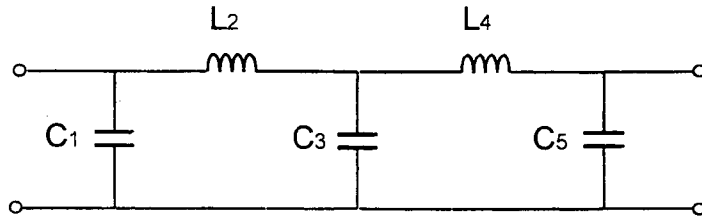


(d) Equivalent networks.

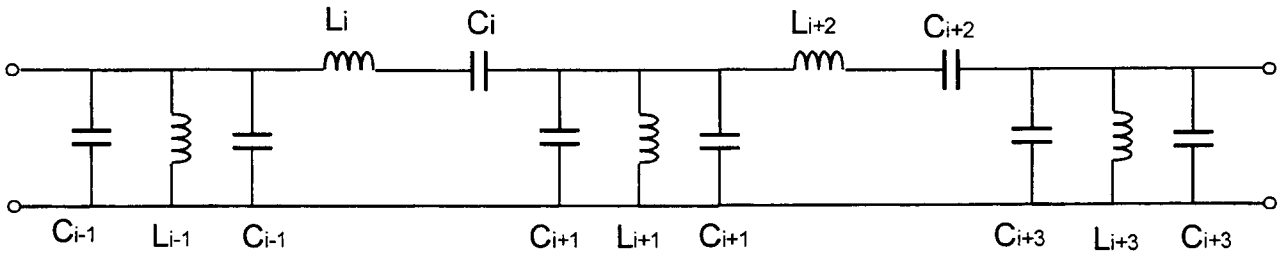


(e) Simplified equivalent circuit of (c).

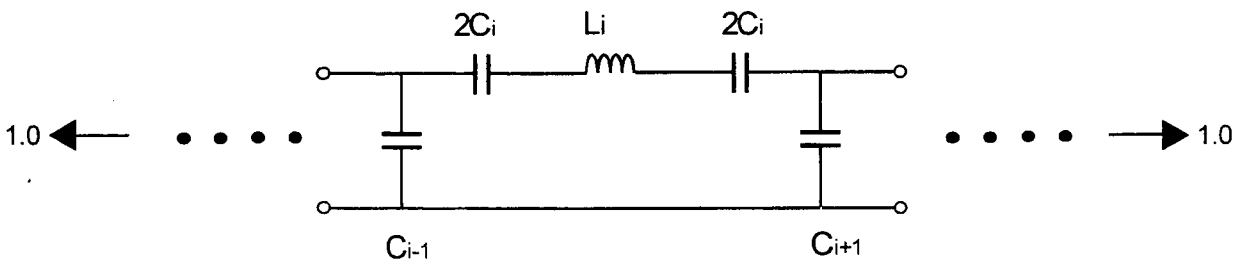
Figure 5.1



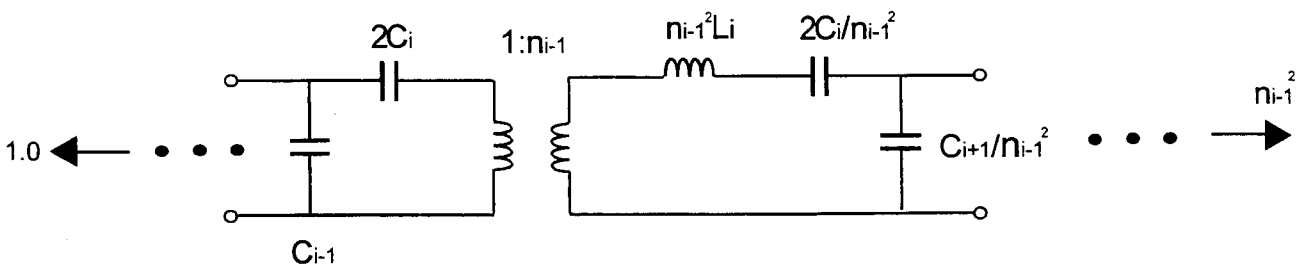
(a) Low-pass filter .



(b) Low-pass filter transformed to bandpass filter.



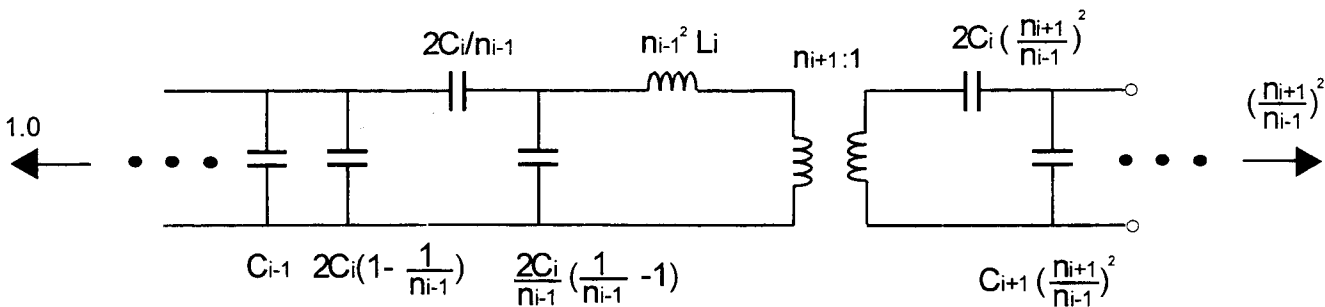
(c) A section of the bandpass filter.



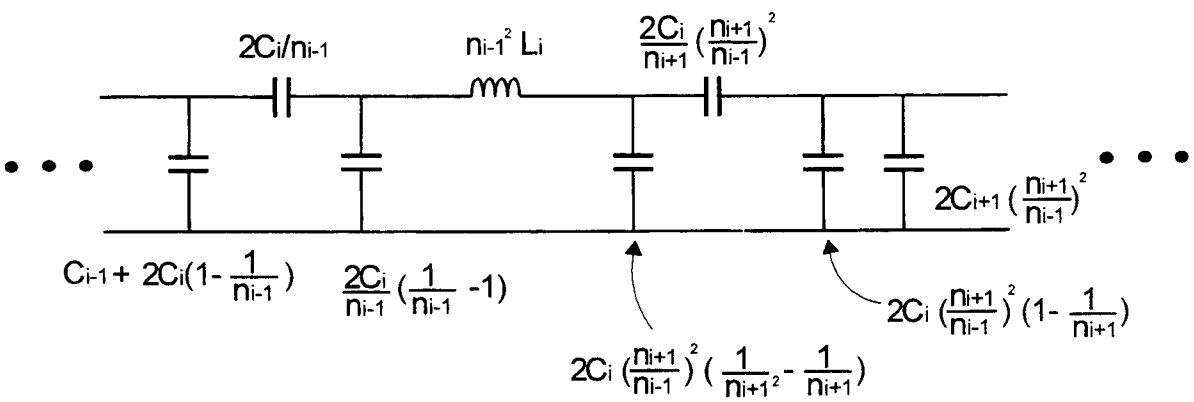
(d) Impedance transformation using an ideal transformer.

cont.

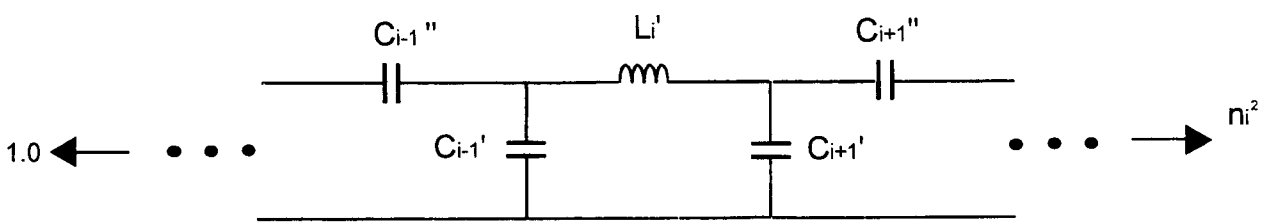
Figure 5.2 A bandpass filter section (b) and steps (c) to (g), leading to an equivalent section (h).



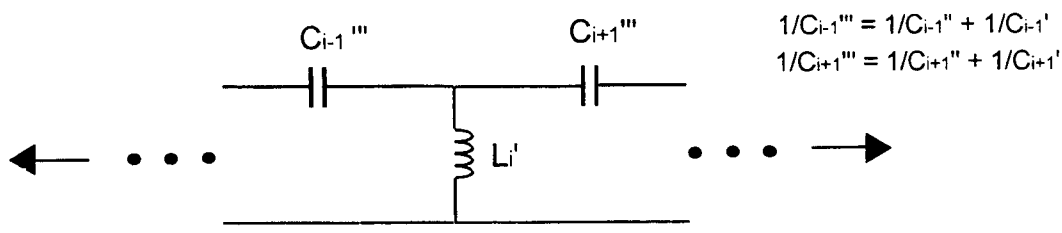
(e) Impedance transformation using equivalent π -section and ideal transformer.



(f) Bandpass section with internal impedance transformation.



(g) Simplified equivalent π -section of (c).



(h) Equivalent T-section of (c).

Figure 5.2 A bandpass filter section (b) and steps (c) to (g), leading to an equivalent section (h).

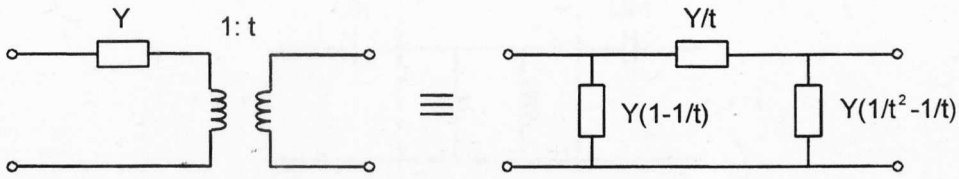
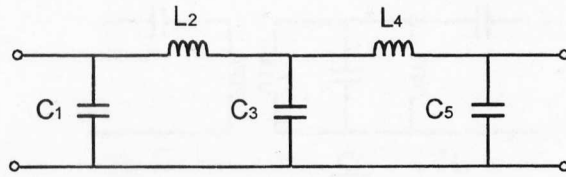
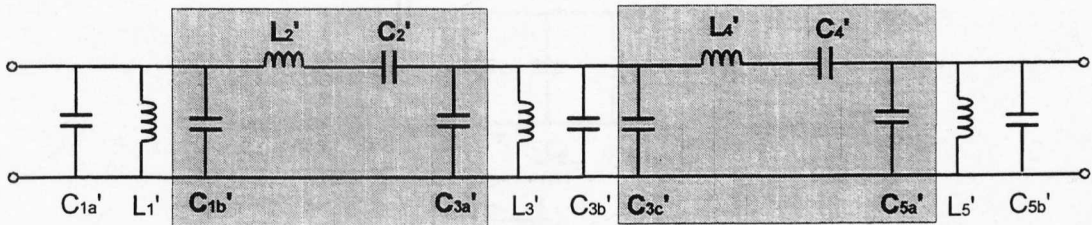


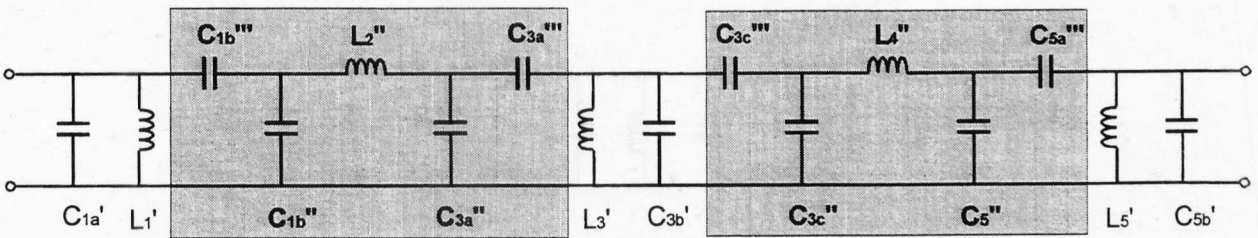
Figure 5.3 Network section containing an ideal transformer and its nonmagnetically coupled Norton equivalent.



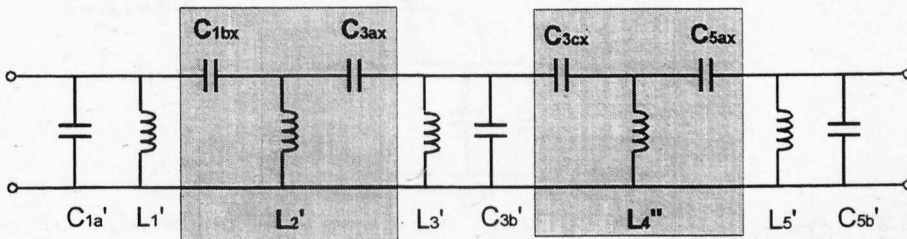
(a) Low-pass prototype filter.



(b) Bandpass filter.

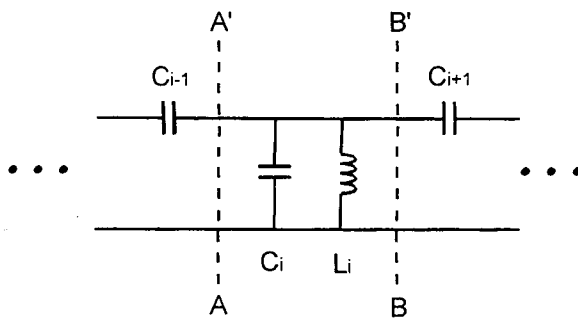


(c) Shaded section in (b) replaced with equivalent π -section.

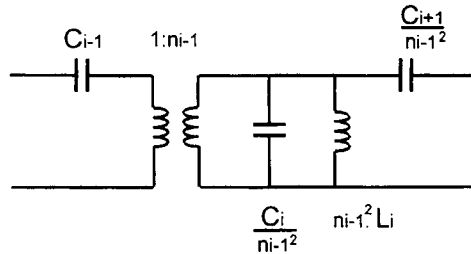


(d) Shaded section in (c) replaced with equivalent T-section.

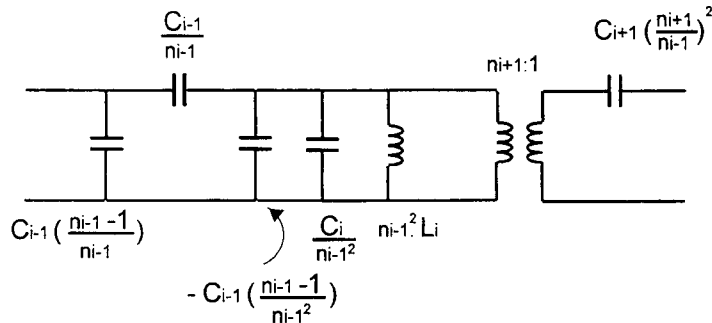
Figure 5.4



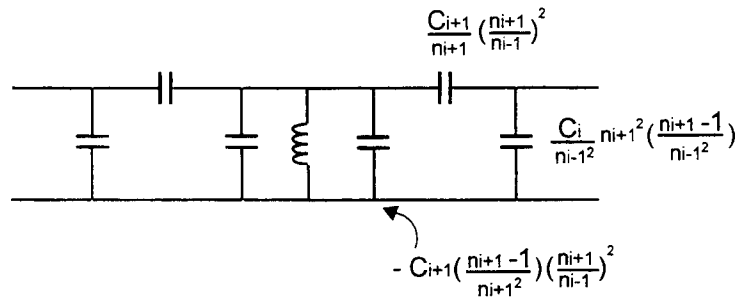
(a) Section of bandpass filter in Figure 5.4(d).



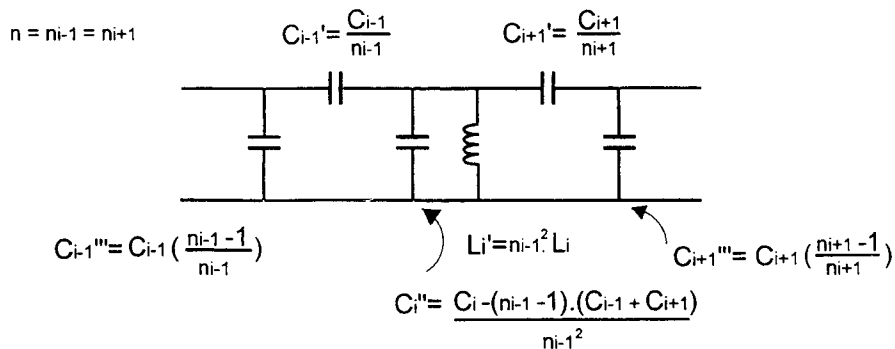
(b) Impedance transformation using ideal transformer at plane AA'.



(c) Impedance transformation using equivalent π -section & ideal transformer at plane BB'.

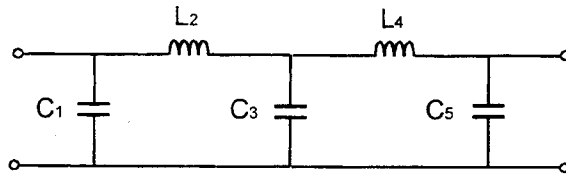


(d) Bandpass section with internal impedance transformation.

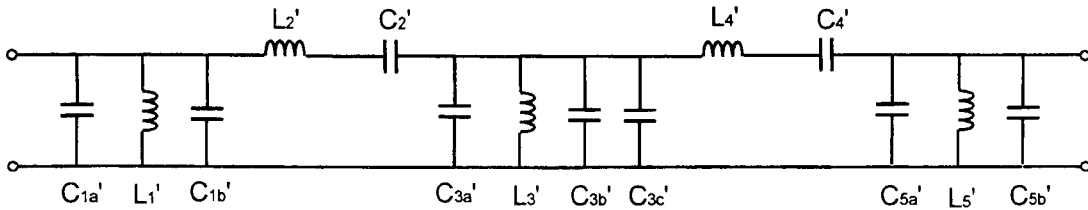


(e) Equivalent representation of (a).

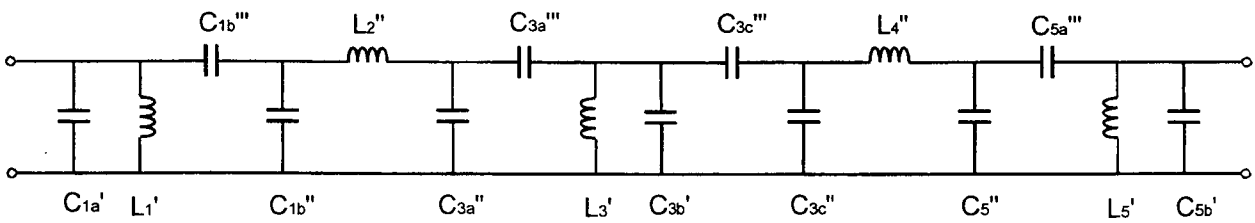
Figure 5.5



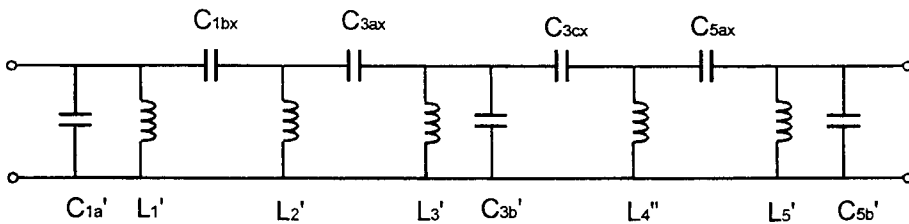
(a)



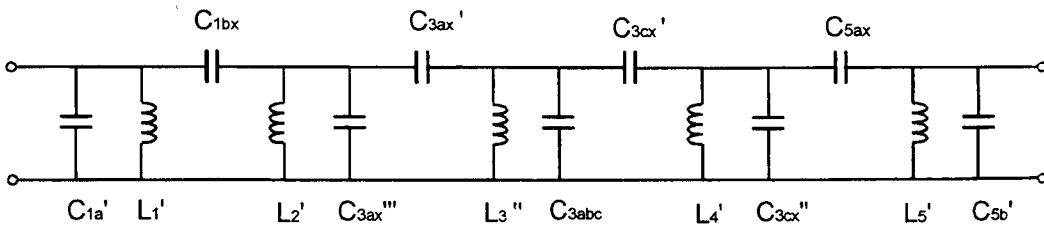
(b)



(c)



(d)



(e)

Figure 5.6 Summary of steps indicating the transformation of bandpass filter (b) to its final equivalent circuit (e).

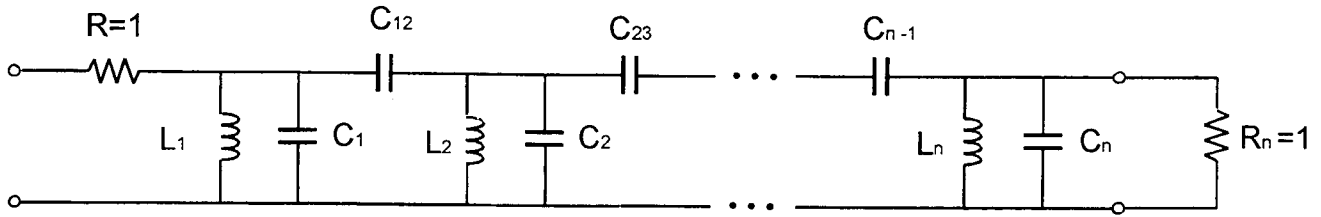
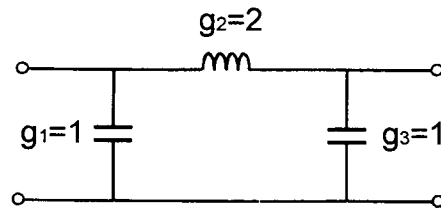
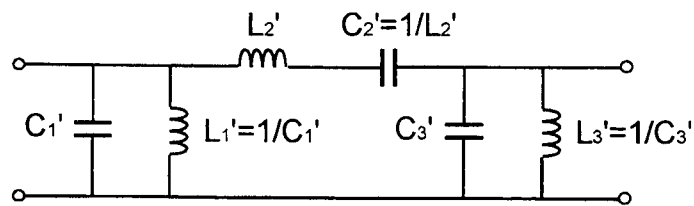


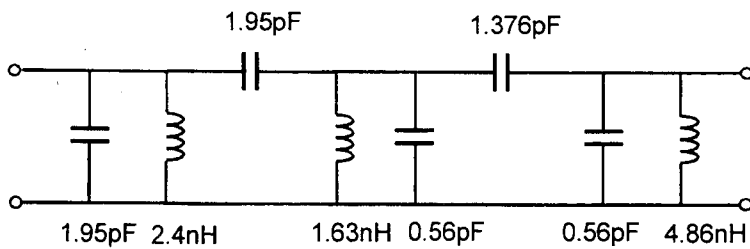
Figure 5.7 Capacitively coupled bandpass filter.



(a) Low-pass prototype filter.



(b) Bandpass filter.



(c) Equivalent bandpass filter structure.

Figure 5.8

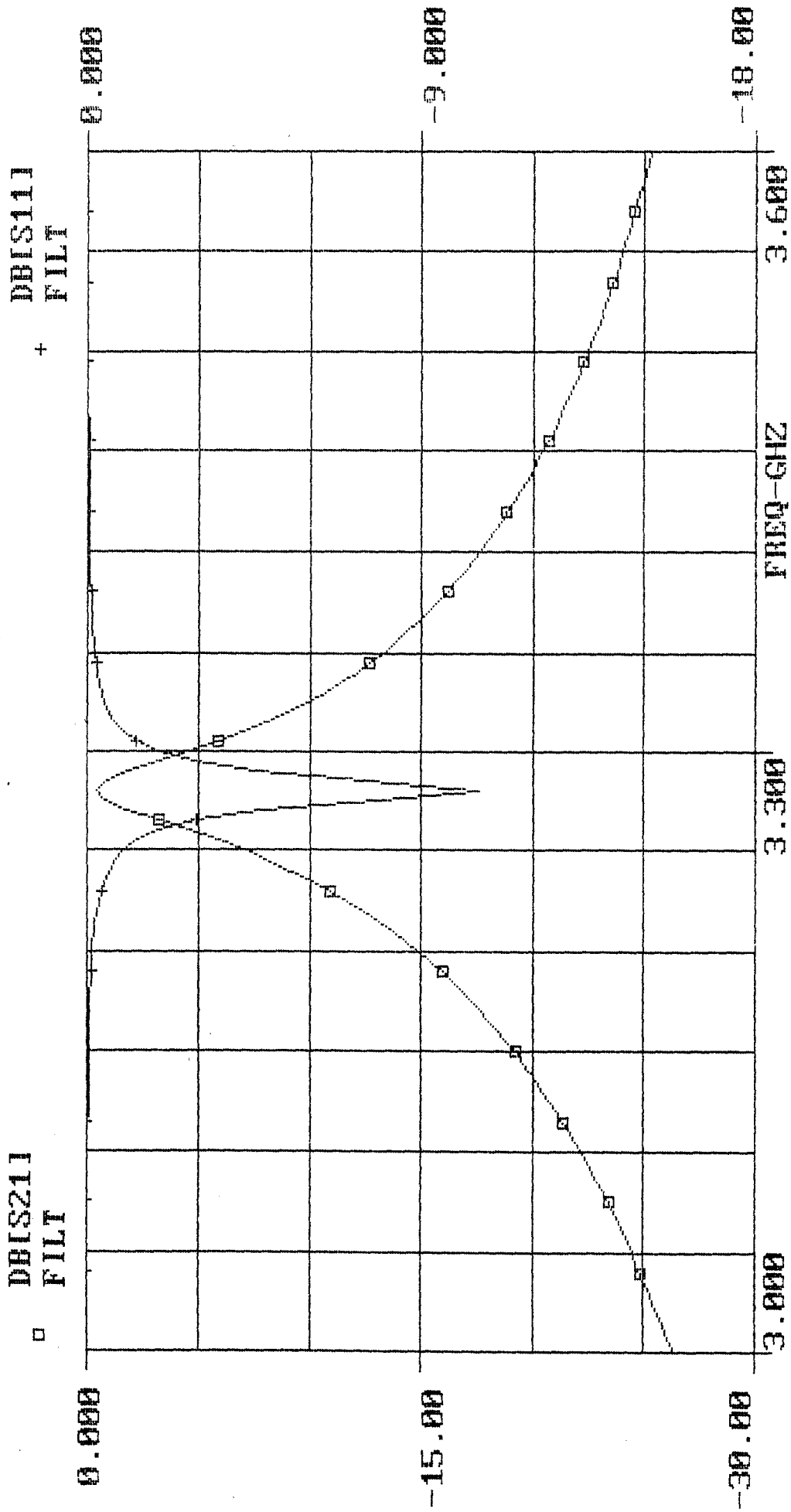
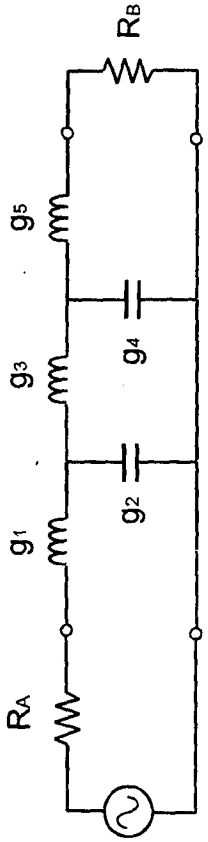
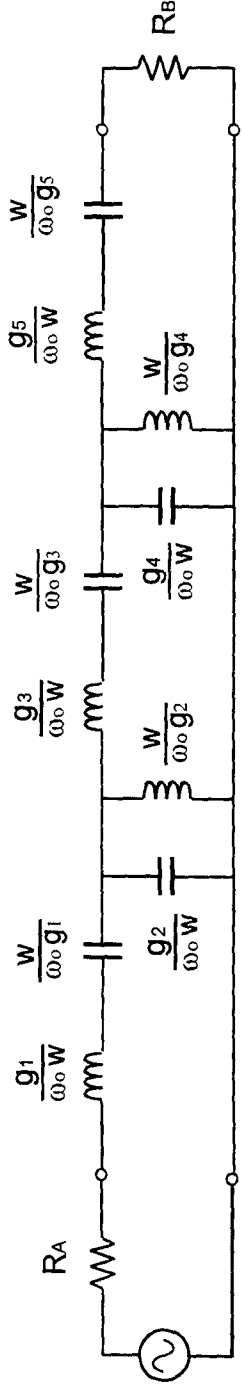


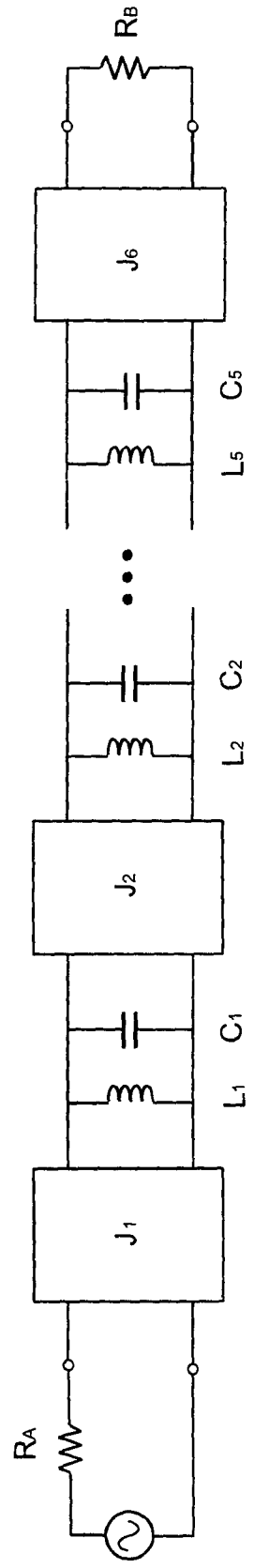
Figure 5.9 Computed response of a 3-pole DR BPF.



(a) Low-pass prototype filter.



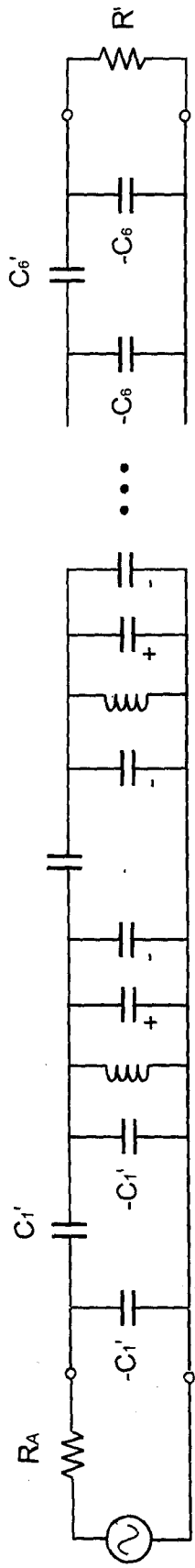
(b) Transformed bandpass filter.



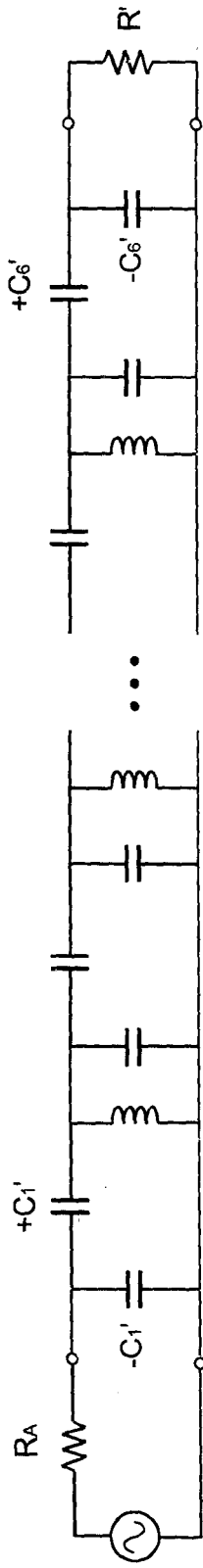
(c) Equivalent admittance inverter structure of a bandpass filter.

cont.

Figure 5.10



(d) Inverters in (c) are substituted by capacitors.



(e) Final schematic of transformed bandpass filter.

Figure 5.10 Transformation of conventional bandpass structure into narrowband structure with aid of inverters.

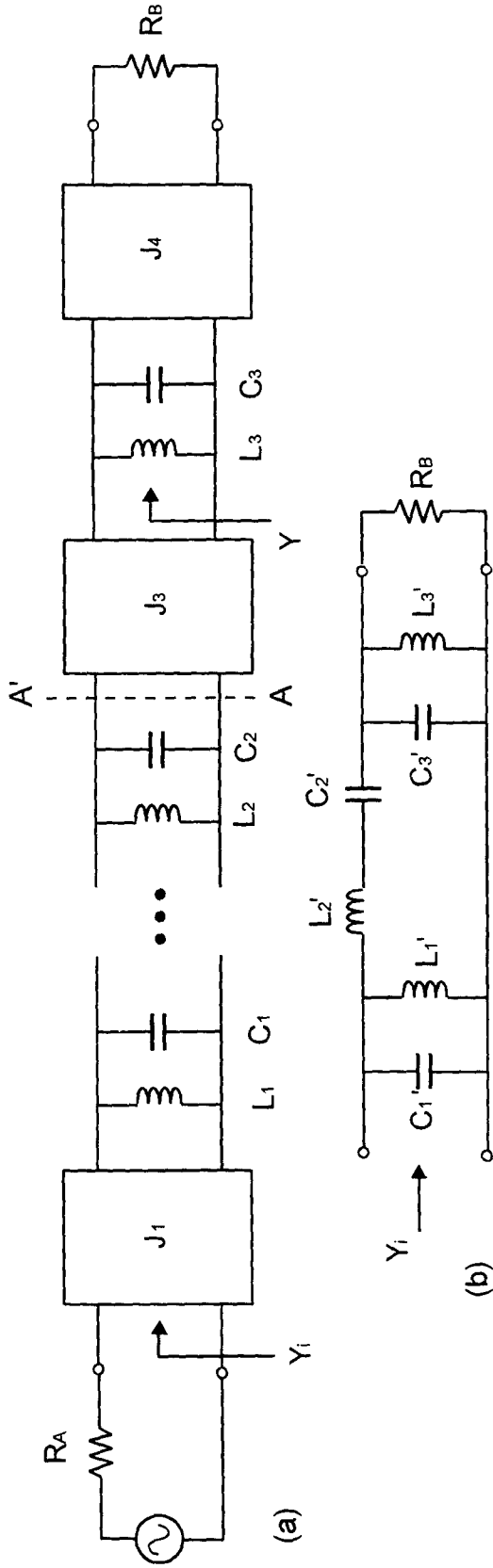
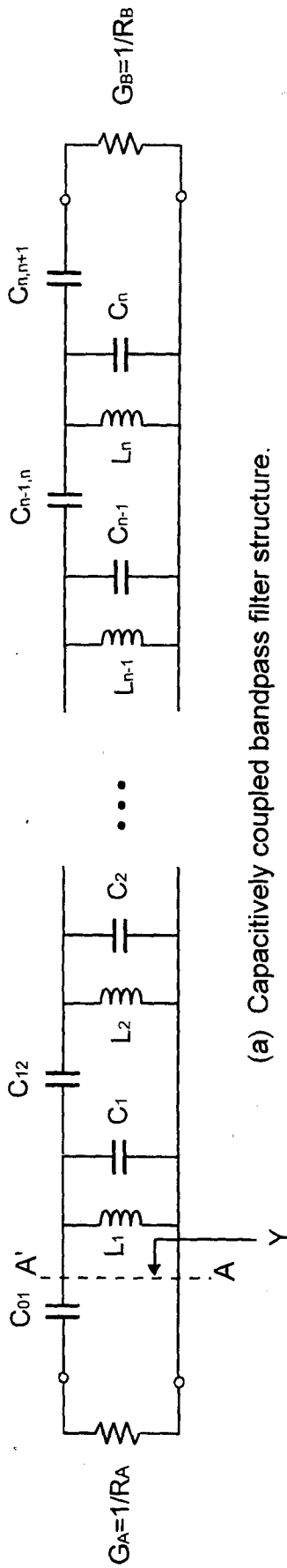
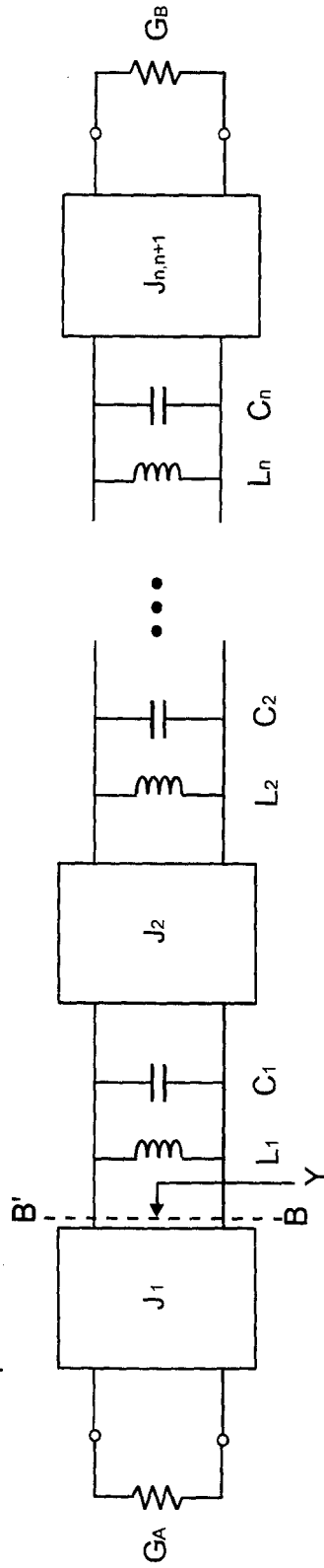


Figure 5.11 (a) Equivalent filter circuit using DRs and admittance inverters, (b) Equivalent lumped element bandpass filters.



(a) Capacitively coupled bandpass filter structure.



(b) Equivalent admittance inverter bandpass filter structure.

Figure 5.12

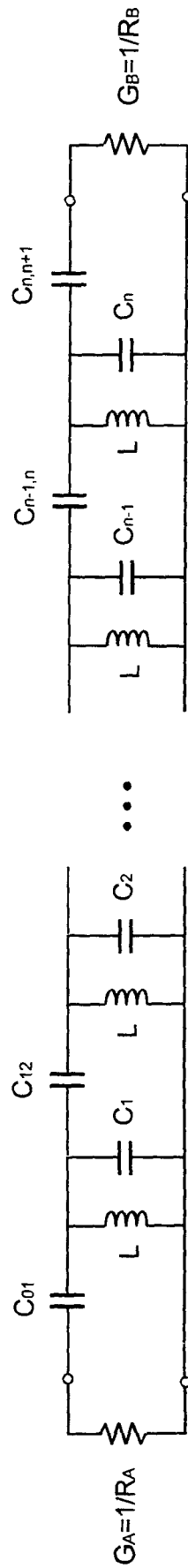


Figure 5.13 Generic bandpass filter.

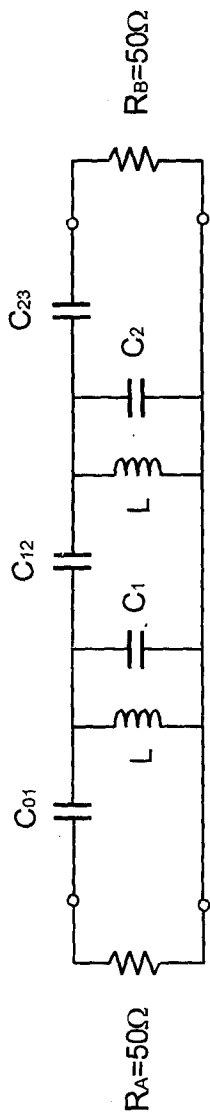


Figure 5.14 Uncalculated, capacitively coupled, 2-pole bandpass filter.

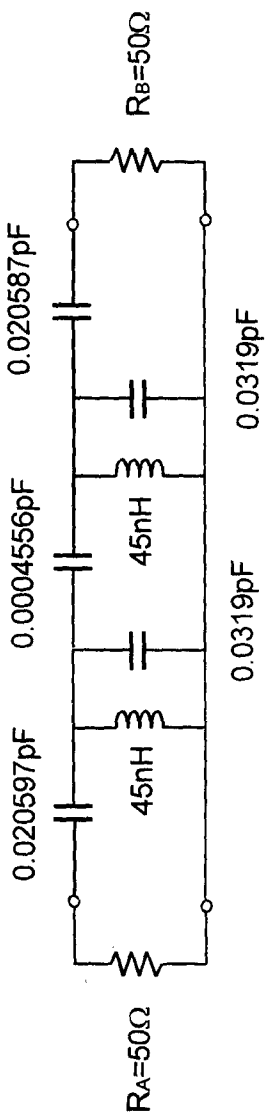


Figure 5.15 Completed 2-pole filter.

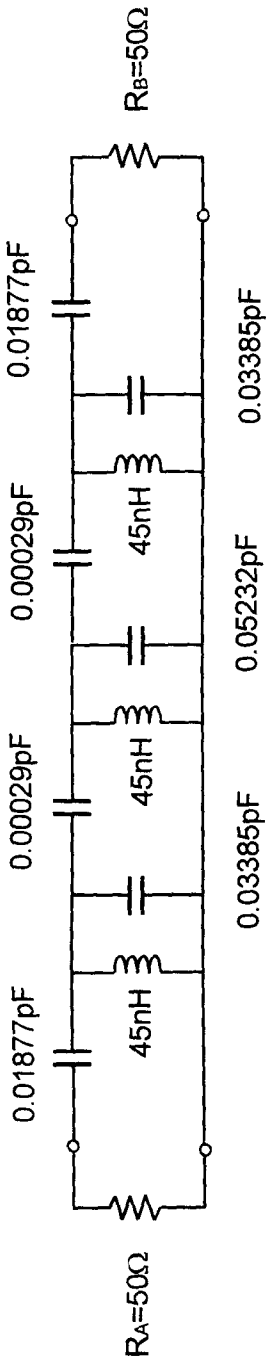


Figure 5.16

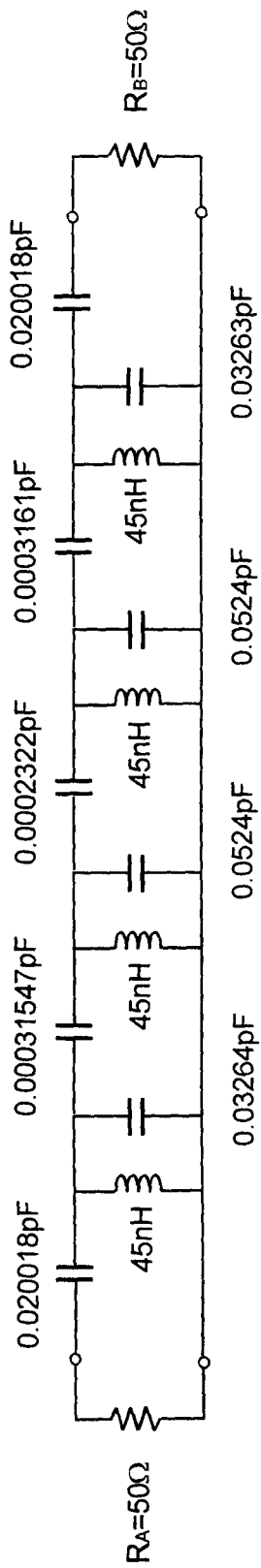


Figure 5.17

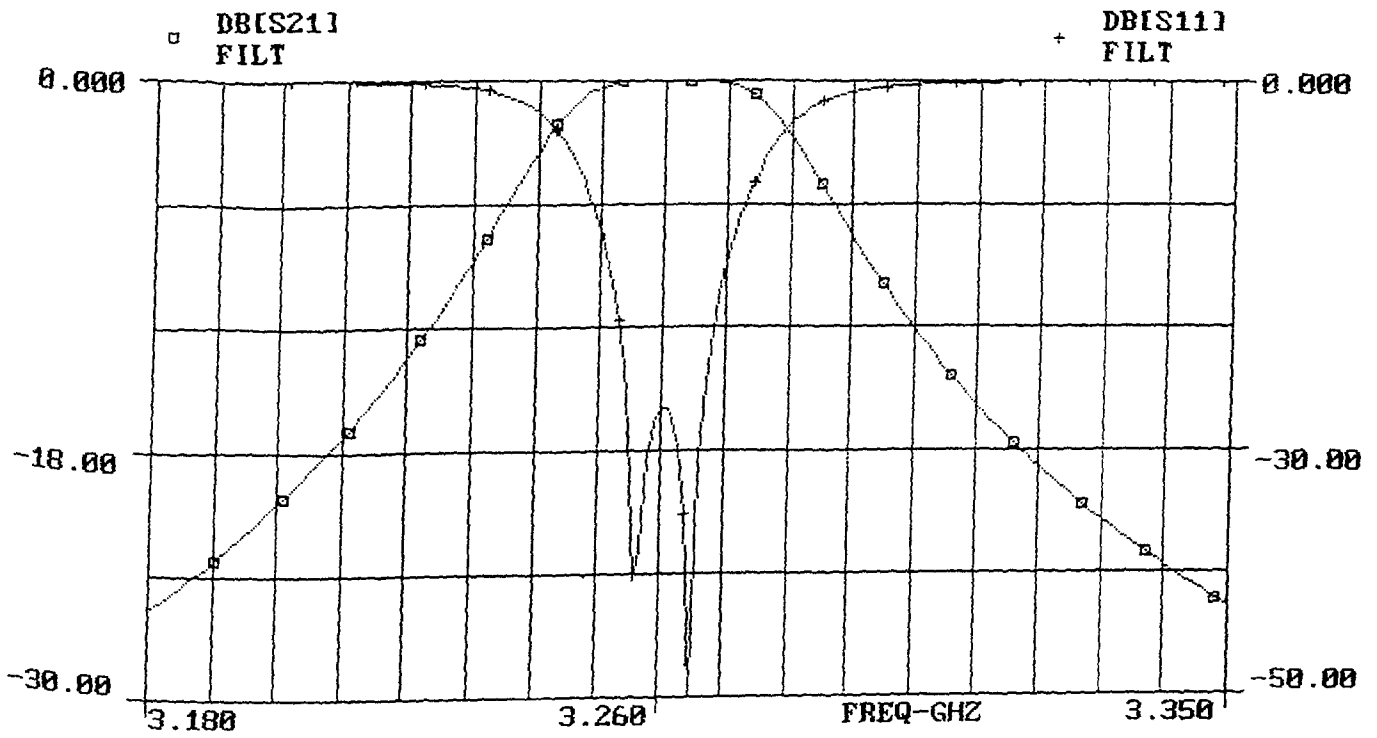


Figure 5.18(a) Computed wideband response of a 2-pole DR BPF.

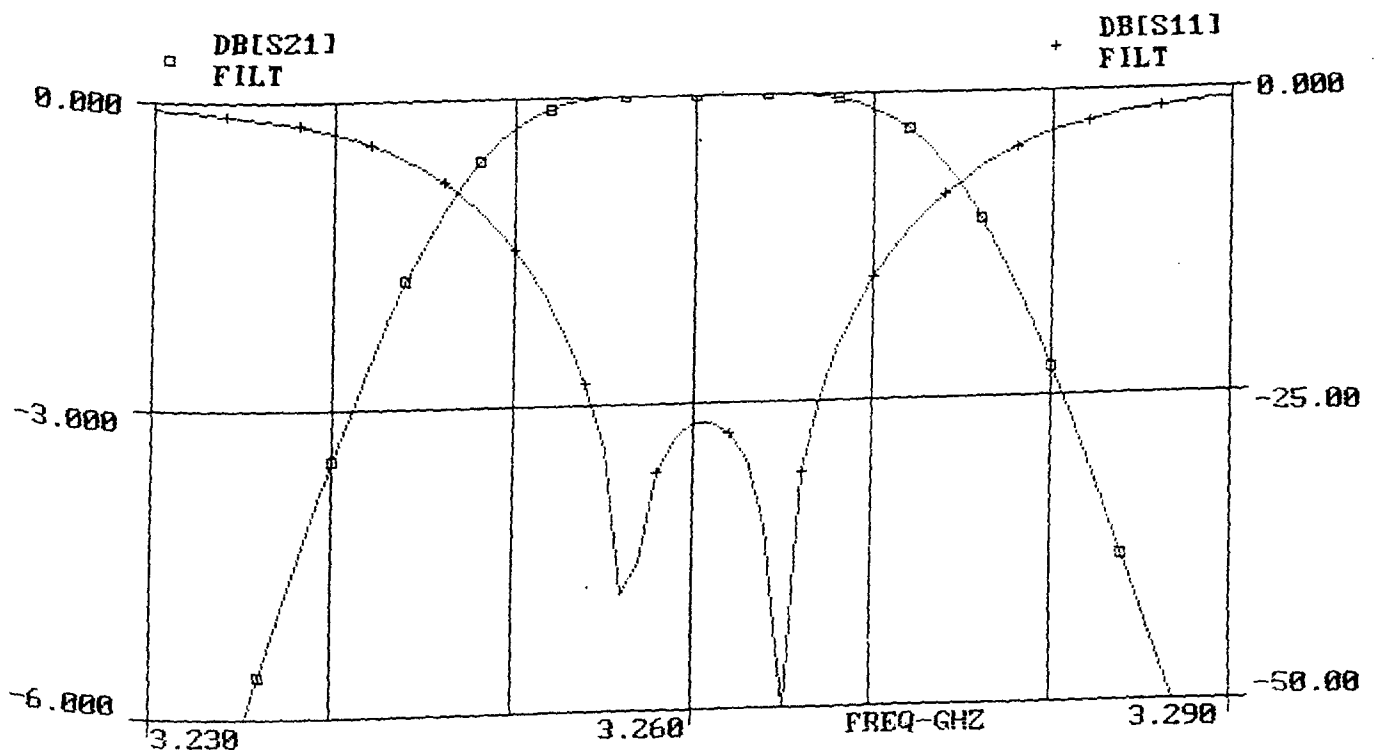


Figure 5.18(b) Computed passband response of a 2-pole DR BPF.

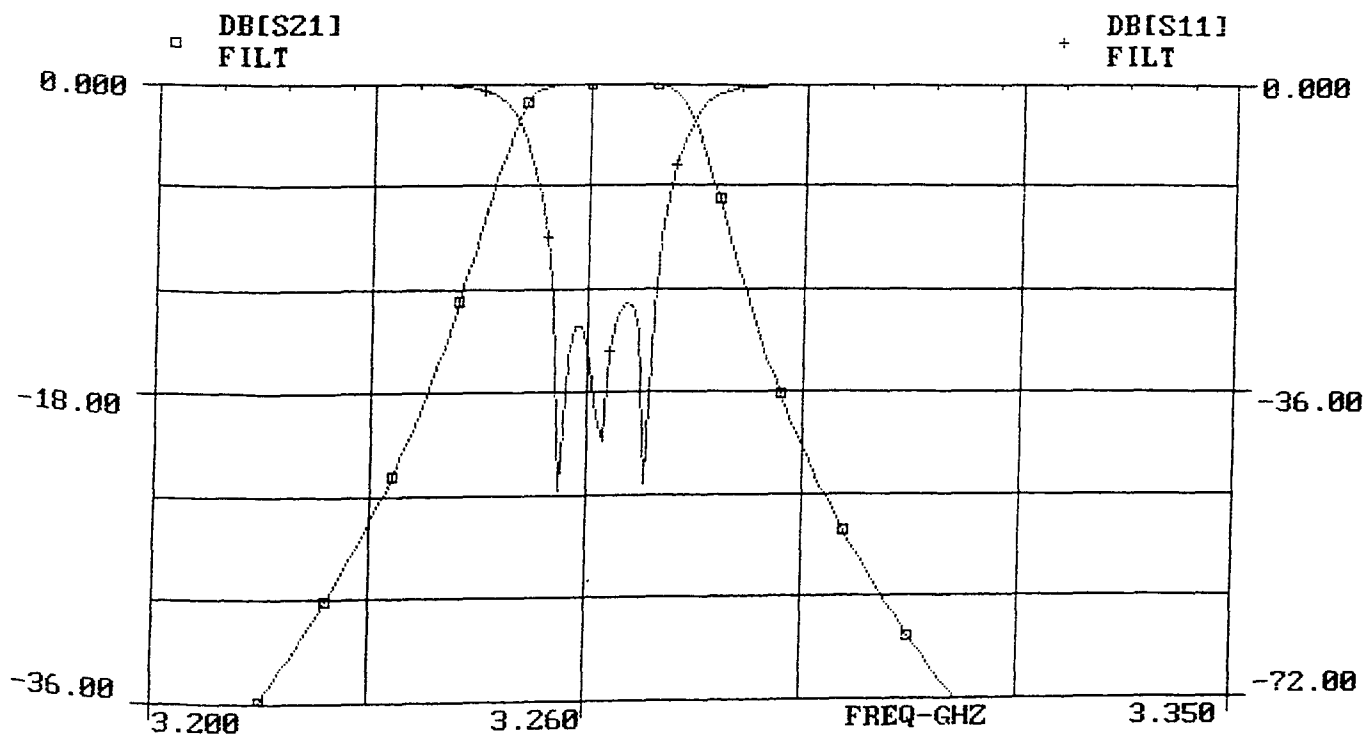


Figure 5.19(a) Computed wideband response of a 3-pole DR BPF.

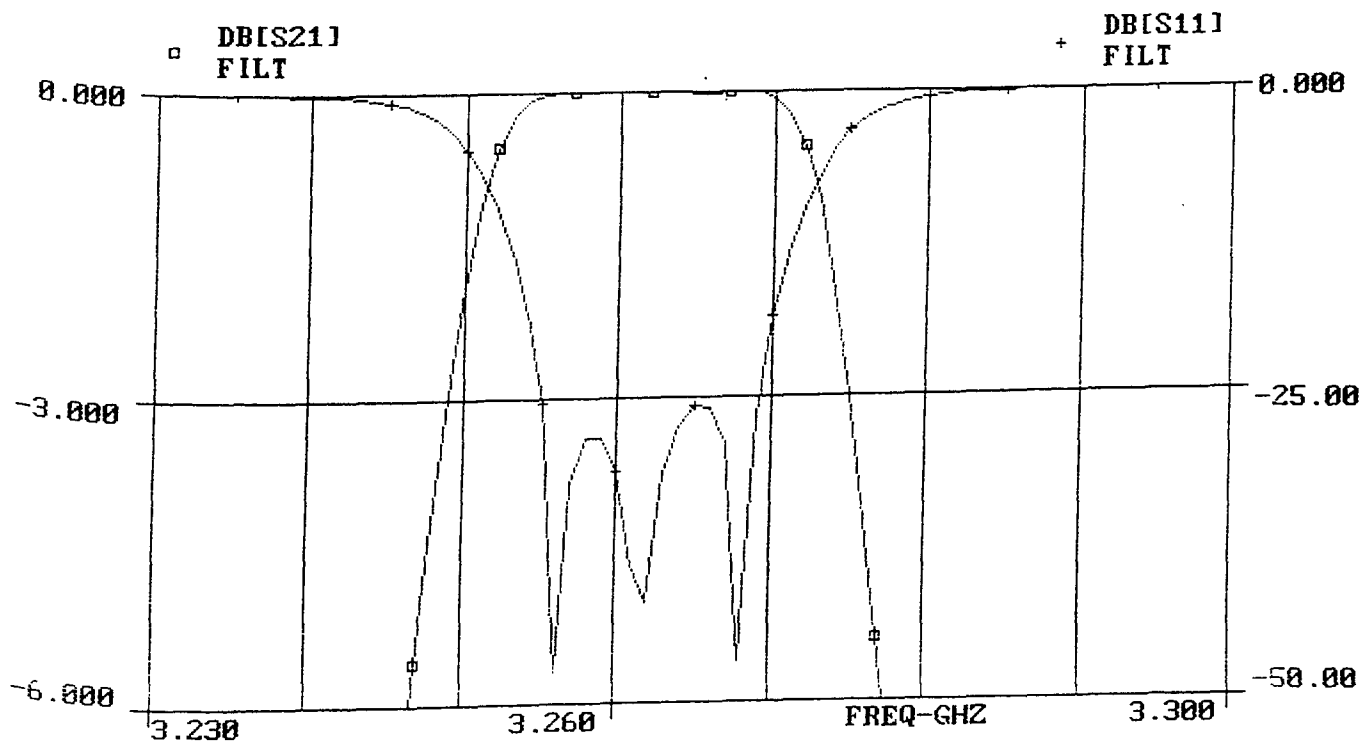


Figure 5.19(b) Computed passband response of a 3-pole DR BPF.

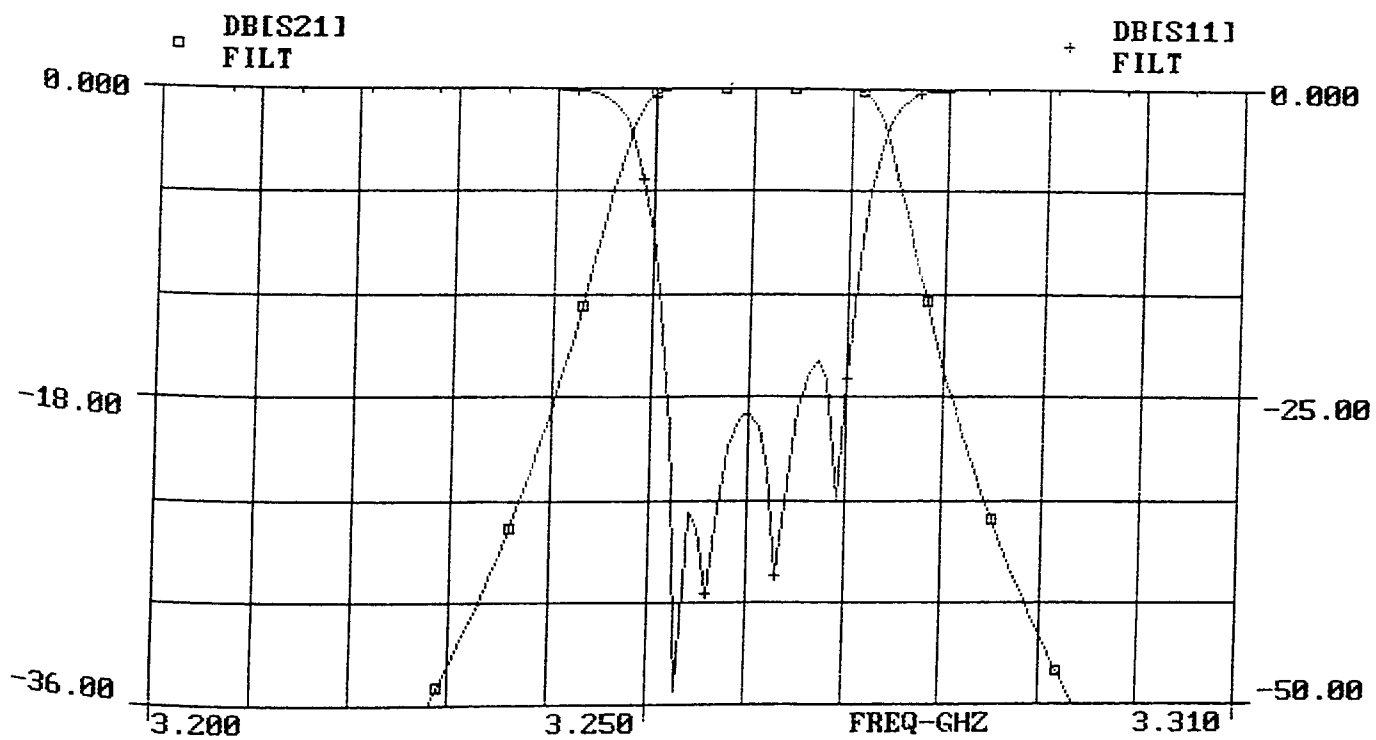


Figure 5.20(a) Computed wideband response of a 4-pole DR BPF.

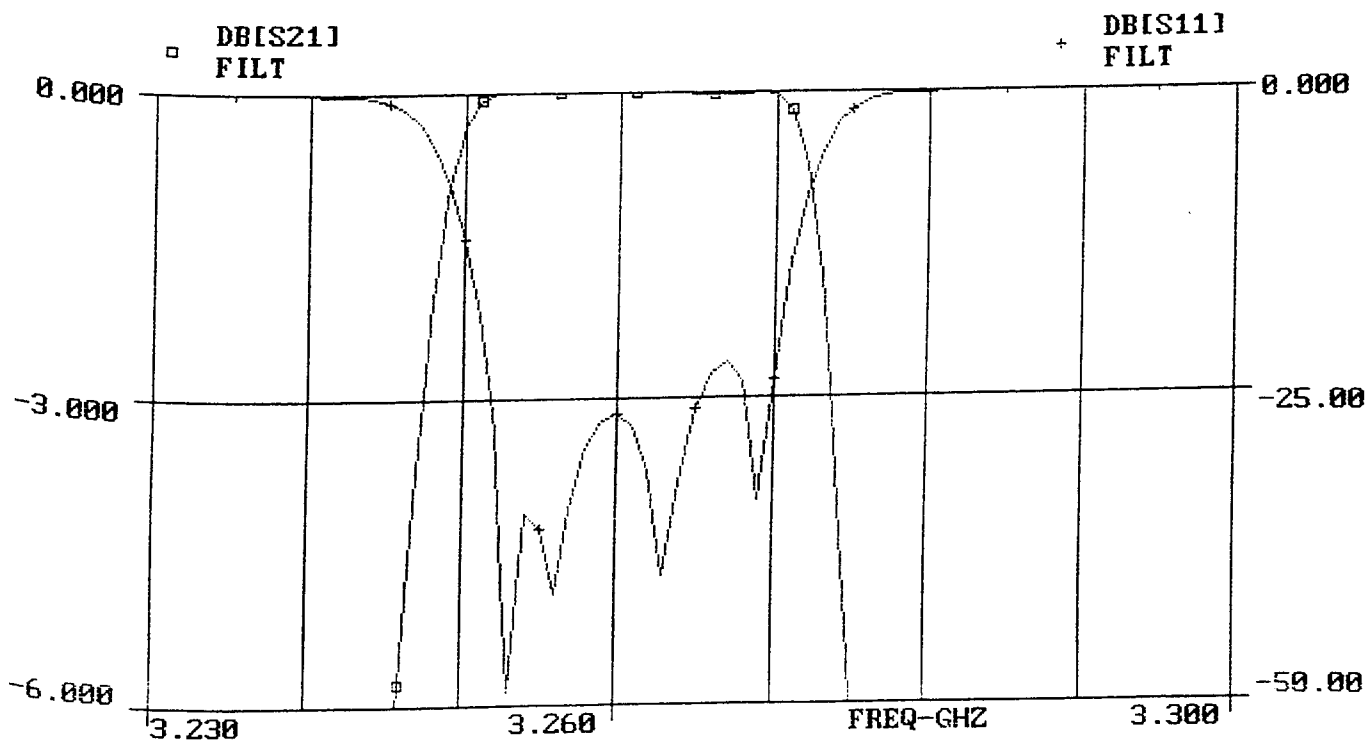


Figure 5.20(b) Computed passband response of a 4-pole DR BPF.

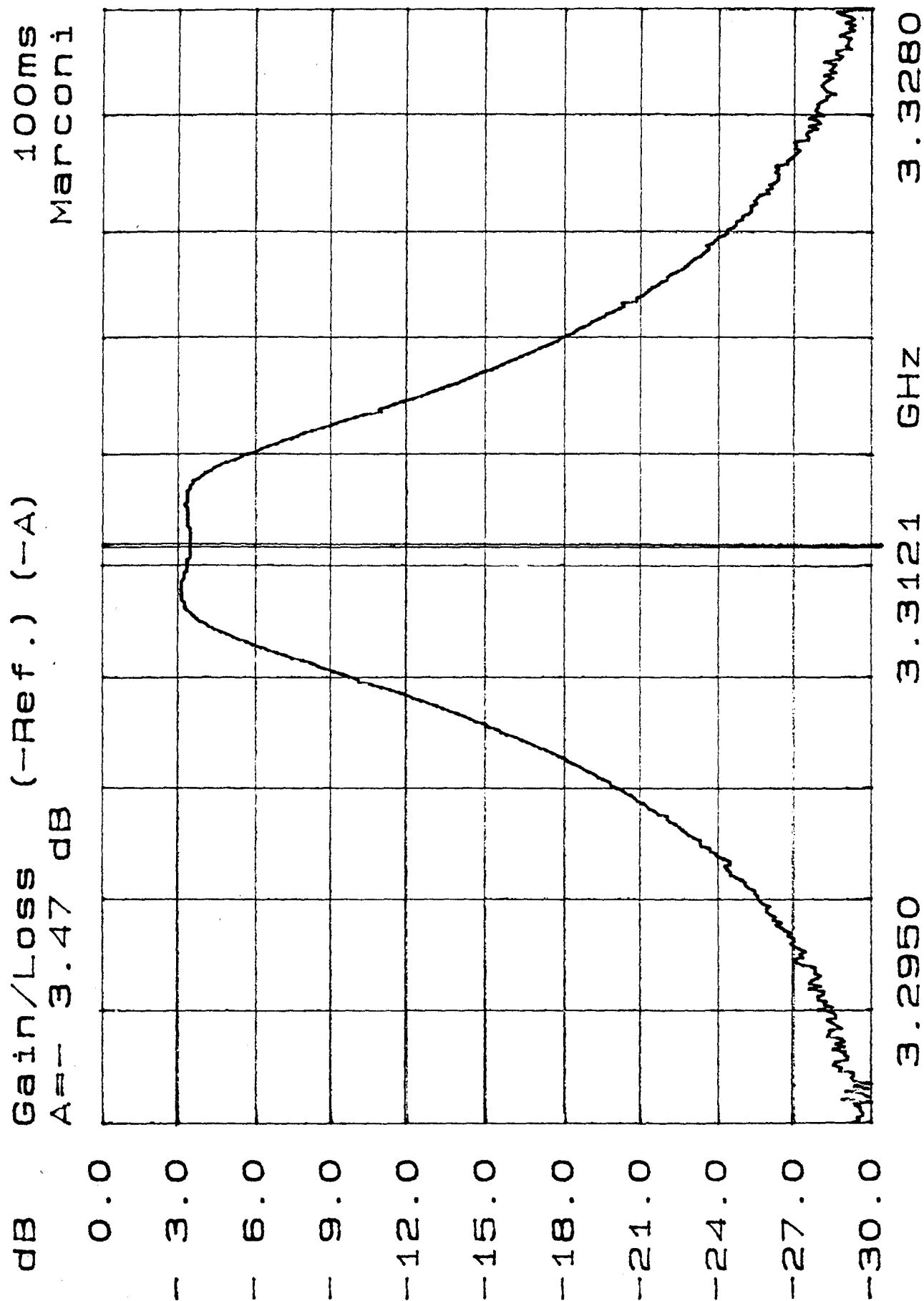


Figure 5.21 Measured response of a 2-pole DR BPF.

Gain/Loss (-Ref.) (-A)
A=-3.27 dB

100ms
Marconi

dB

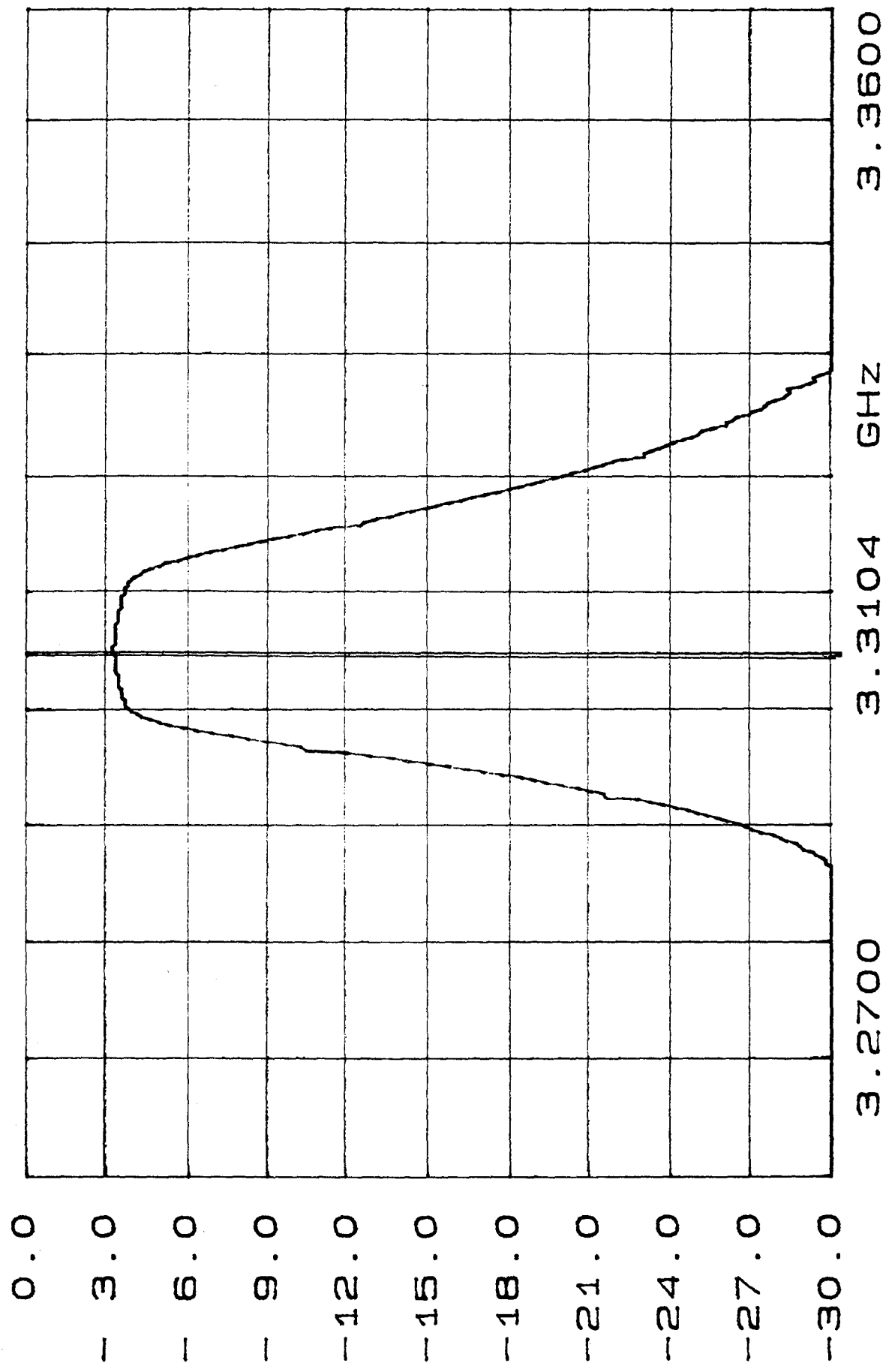


Figure 5.22 Measured response of a 3-pole DR BPF.

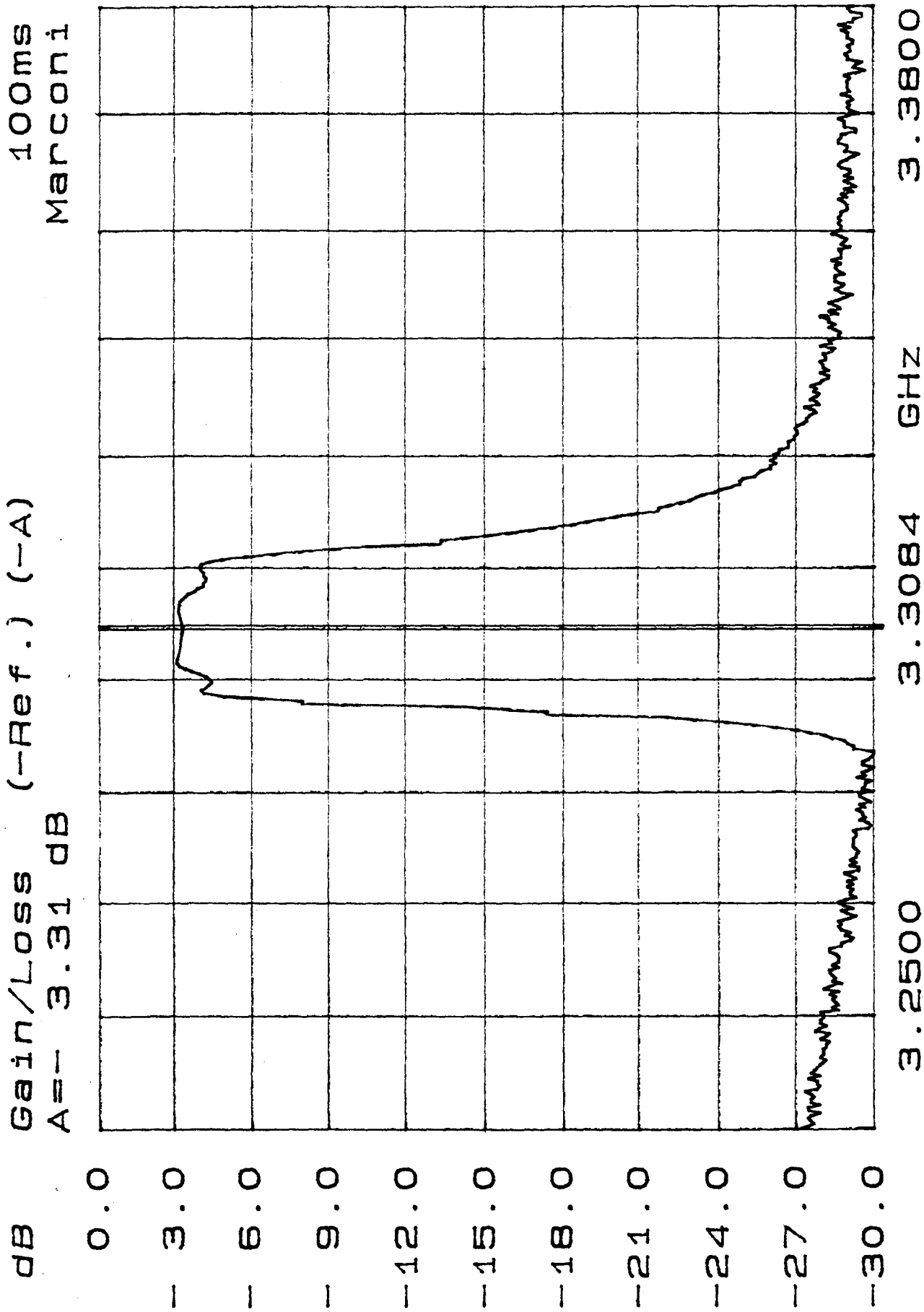


Figure 5.23 Measured response of a 4-pole DR BPF.

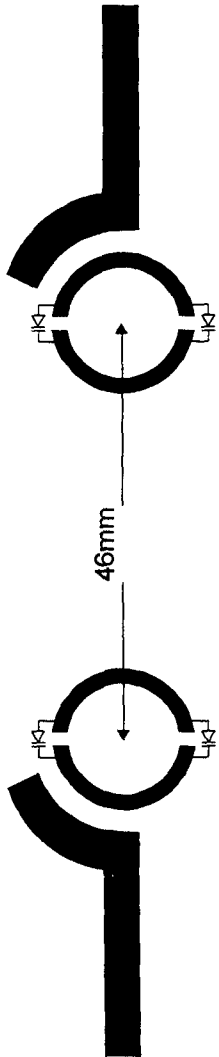


Figure 5.24 2-port DR BPF layout drawing.

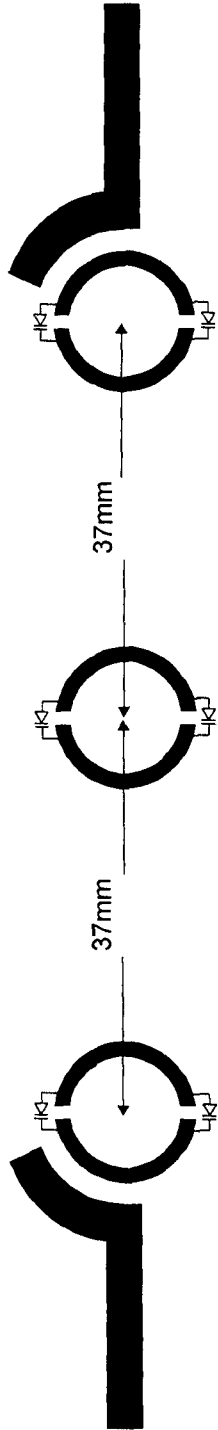


Figure 5.25 3-port DR BPF layout drawing.

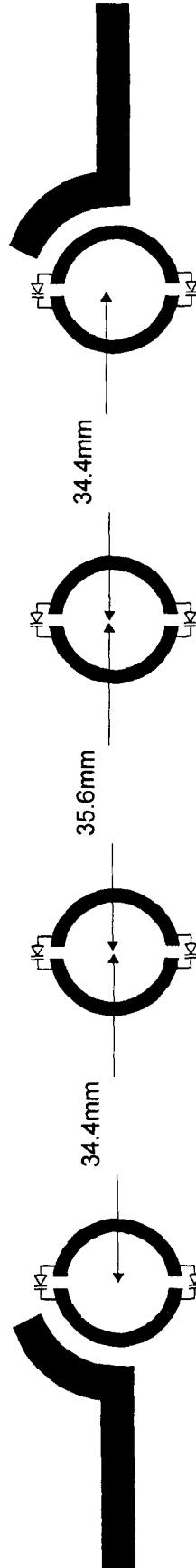


Figure 5.26 4-port DR BPF layout drawing.

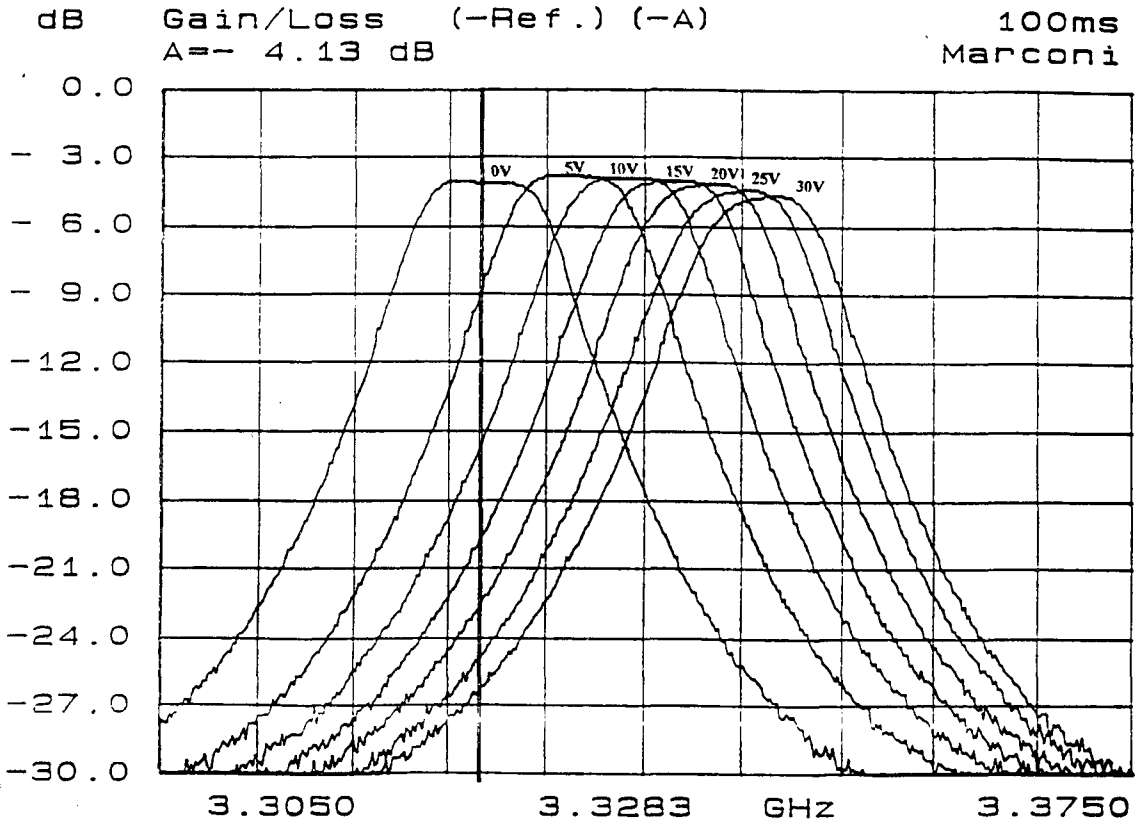
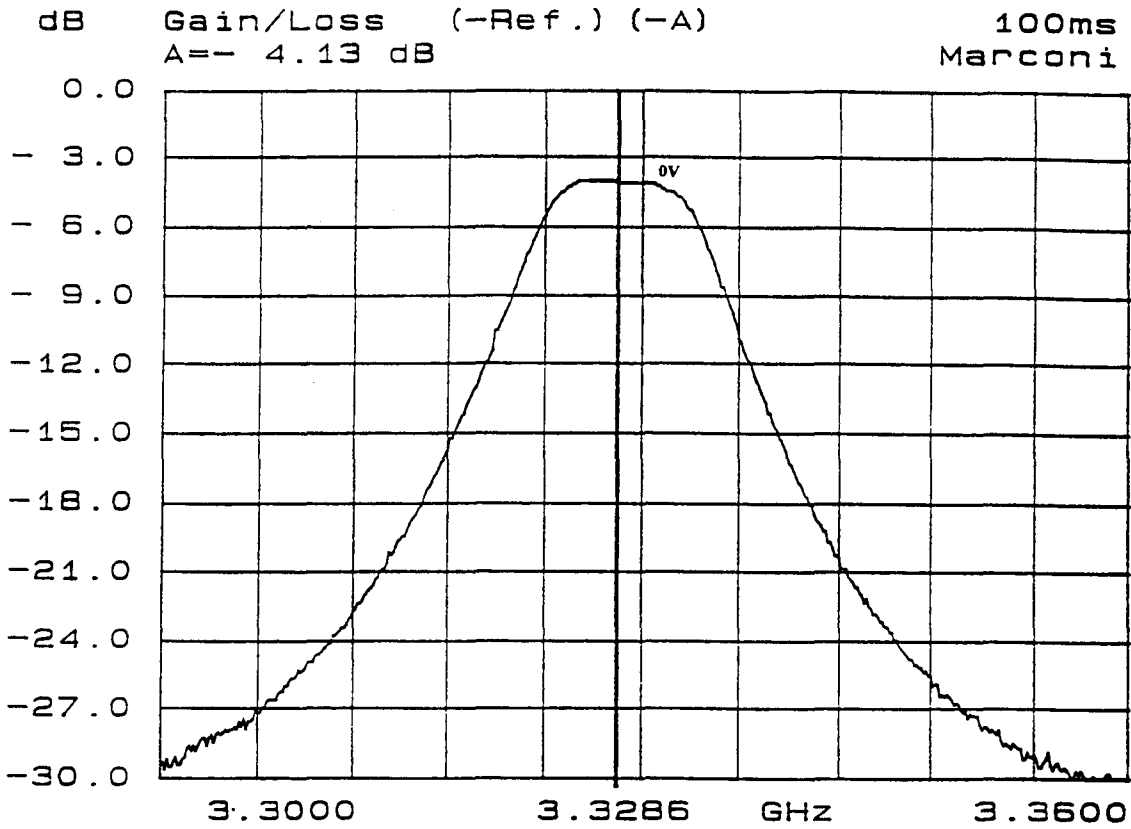


Figure 5.27 Measured response of electronically tuned 2-pole DR BPF.

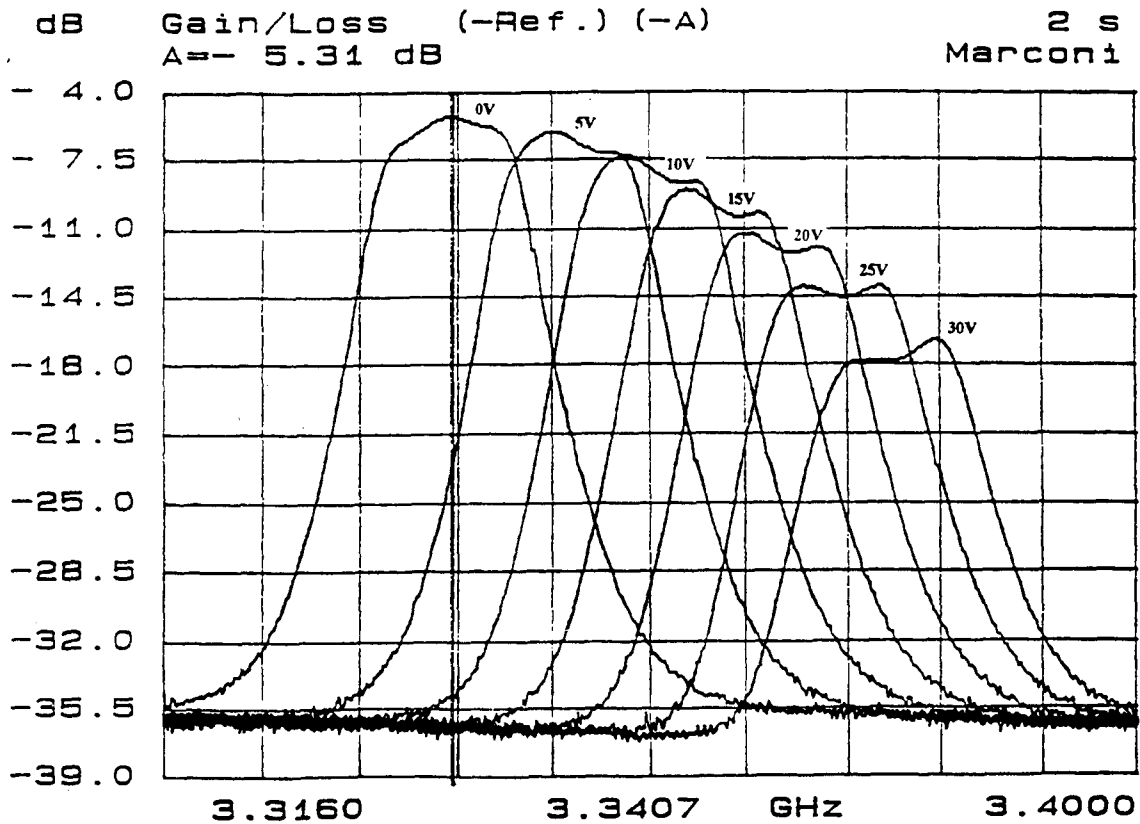
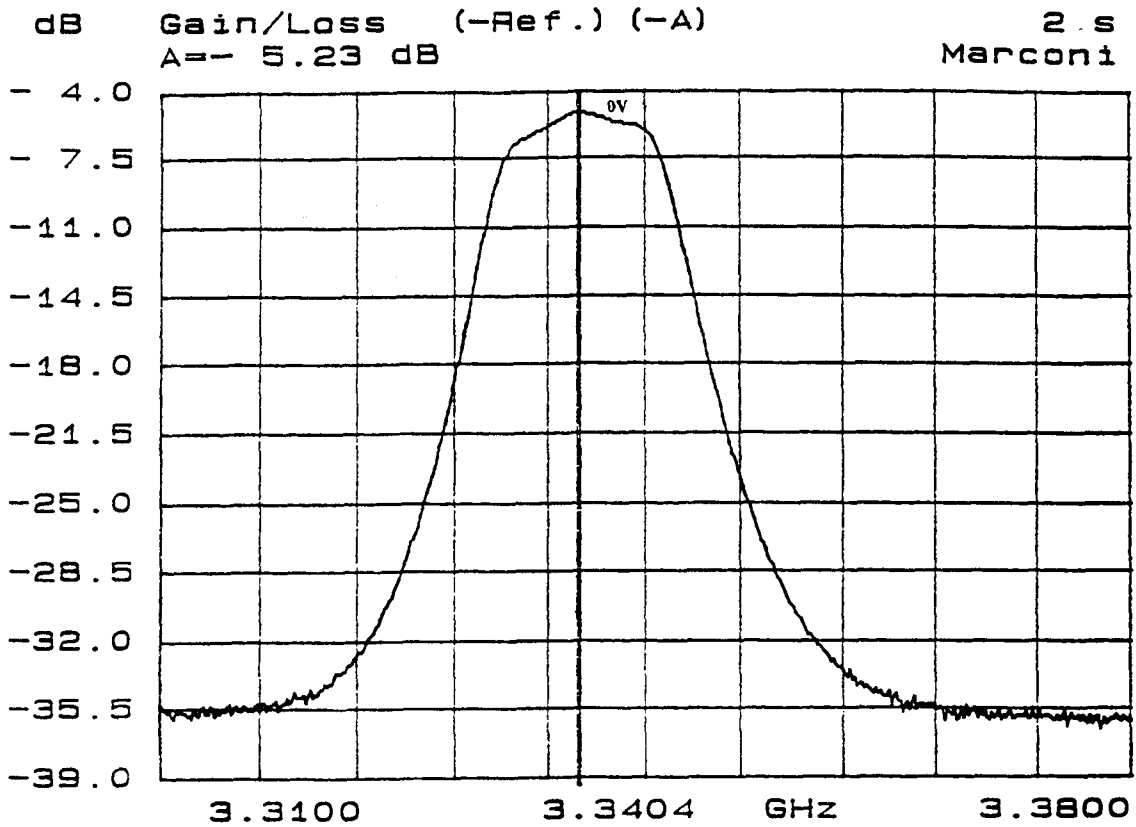


Figure 5.28 Measured response of electronically tuned 3-pole DR BPF.

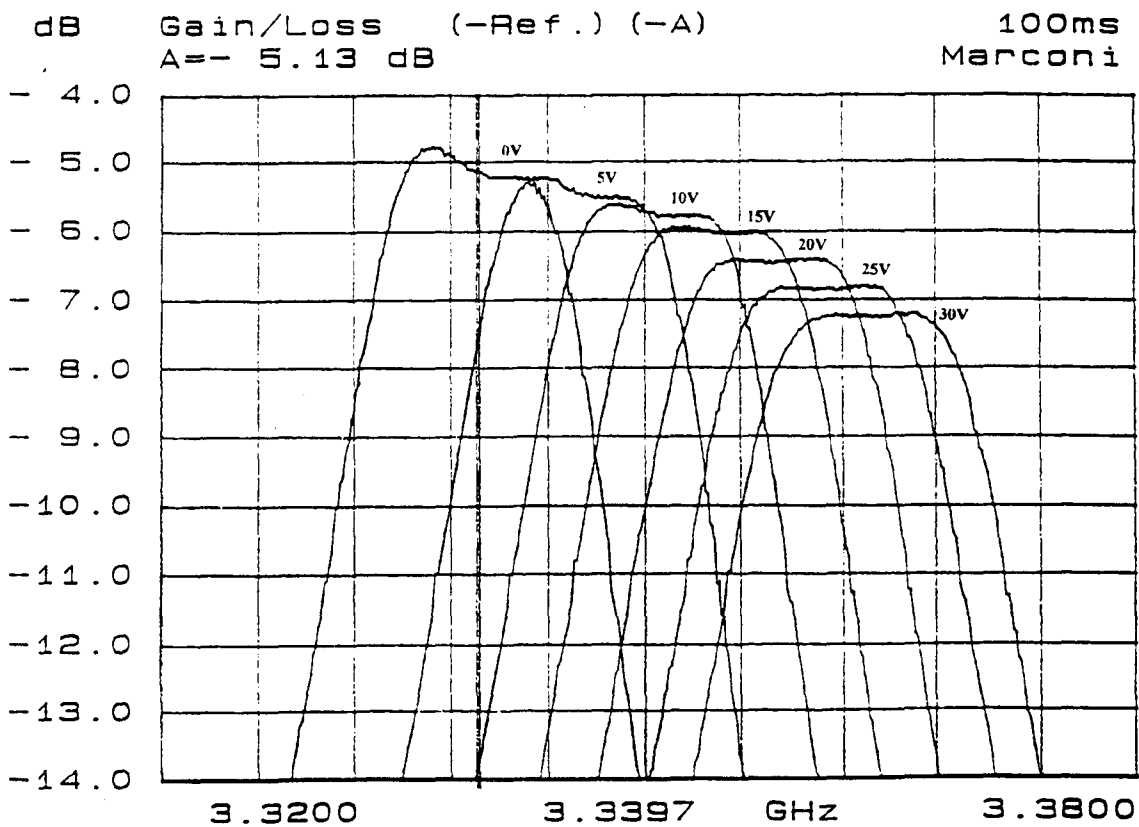
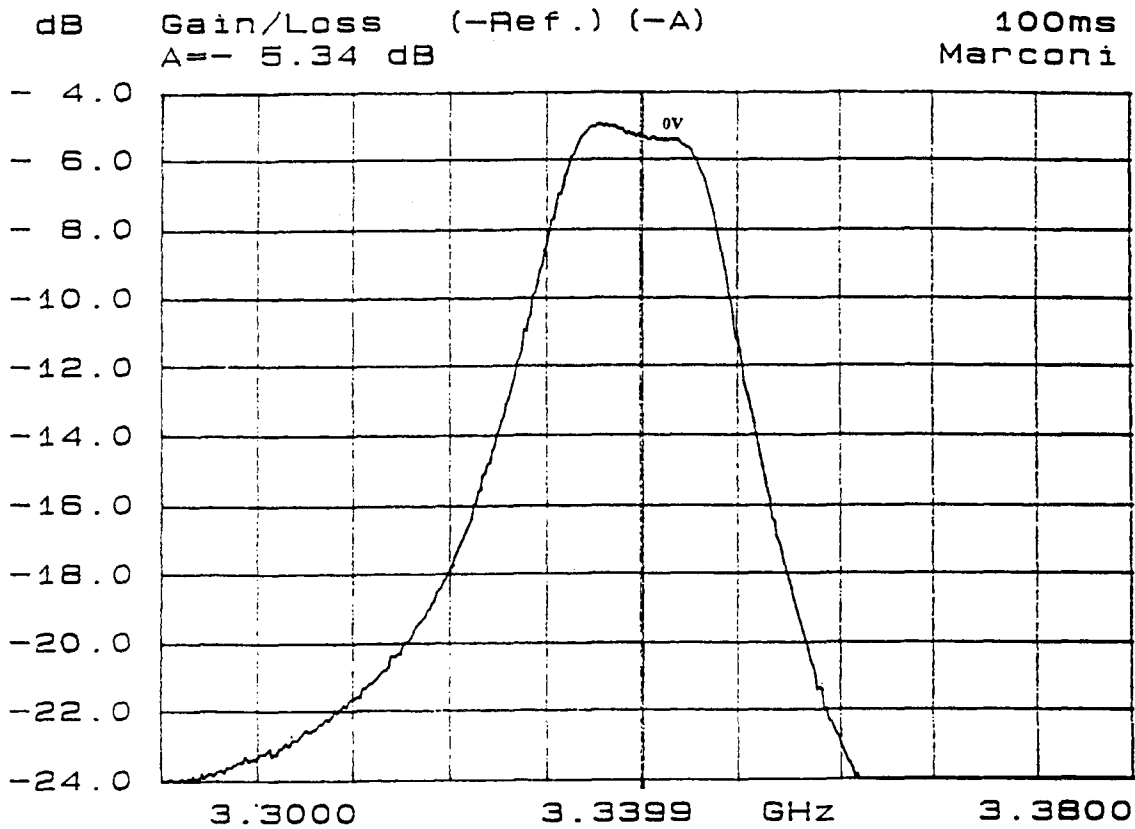


Figure 5.29 Measured response of electronically tuned 4-pole DR BPF.

2-Pole BPF

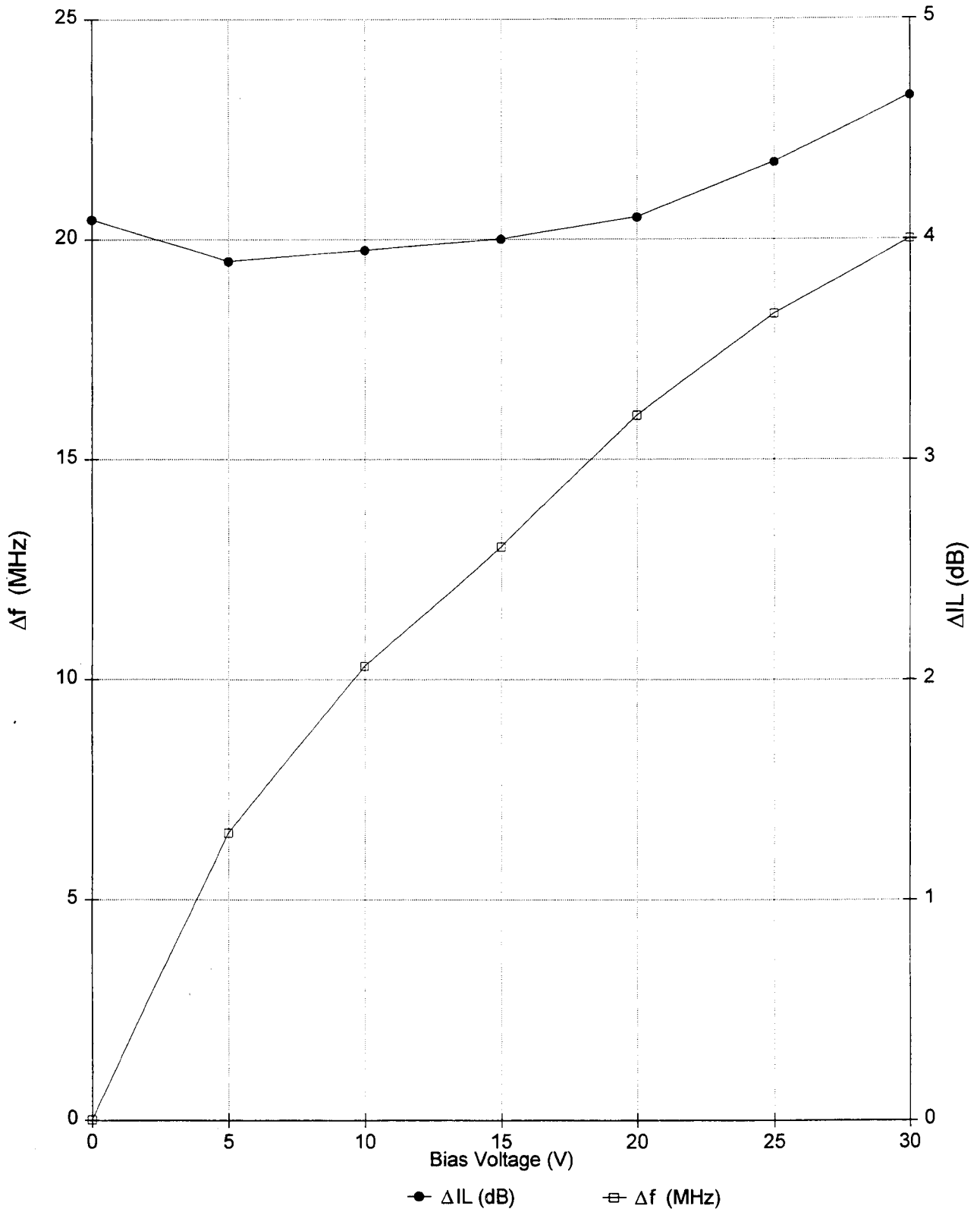


Figure 5.30 Tuning range & passband insertion loss variation as a function of bias voltage of a 2-pole BPF.

3-Pole BPF

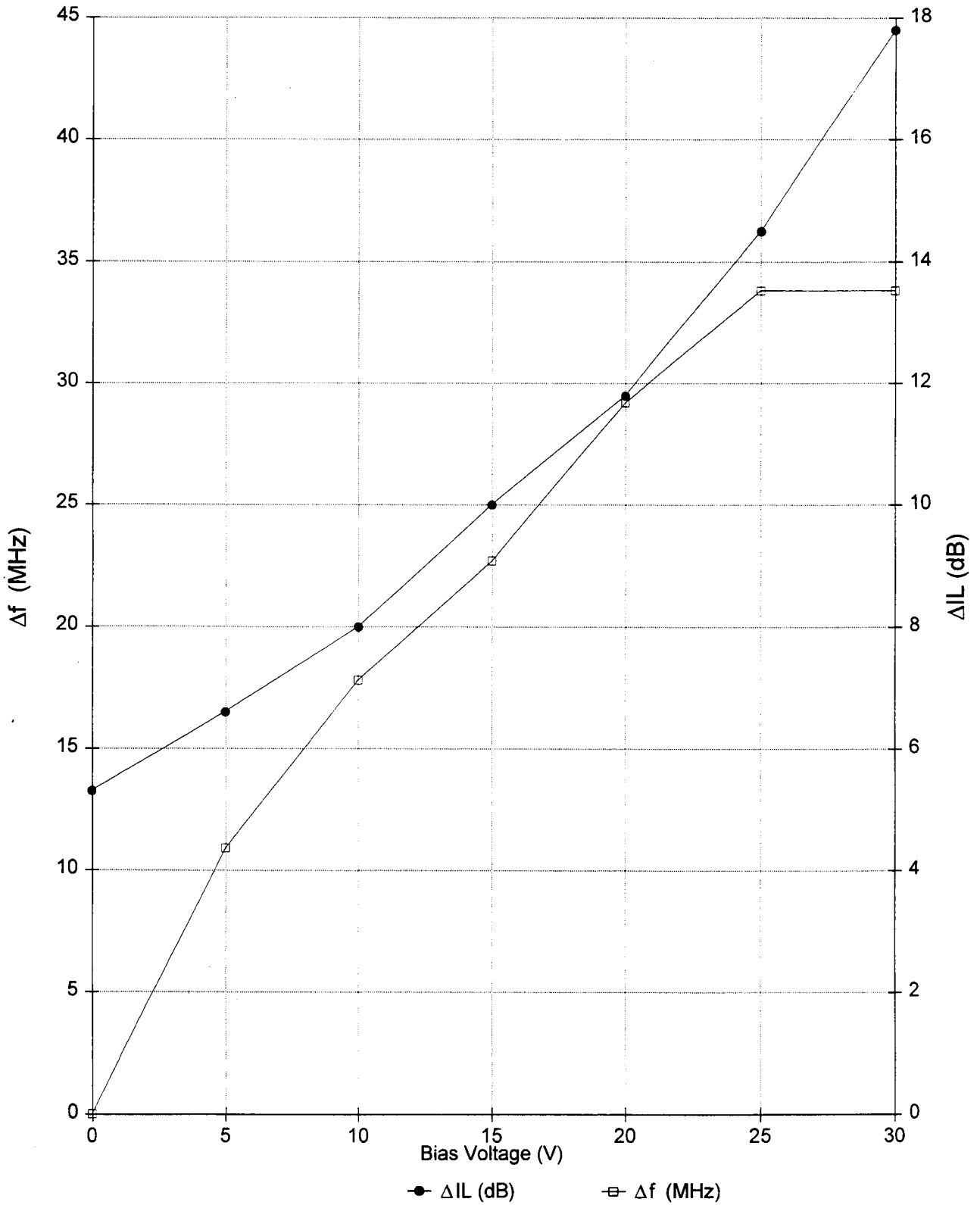


Figure 5.31 Tuning range & passband insertion loss variation as a function of bias voltage of a 3-pole BPF.

4-Pole BPF

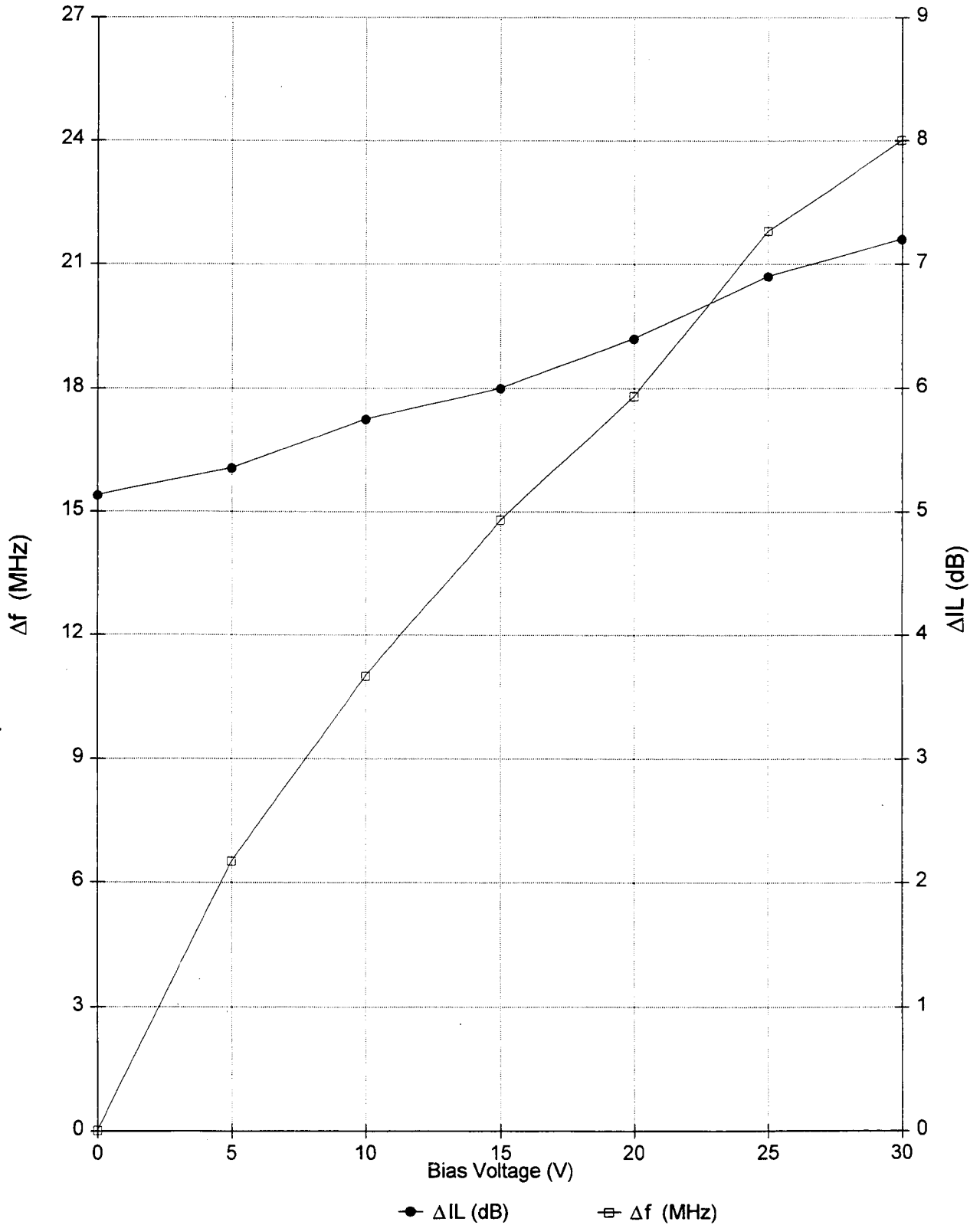


Figure 5.32 Tuning range & passband insertion loss variation as a function of bias voltage of a 4-pole BPF.

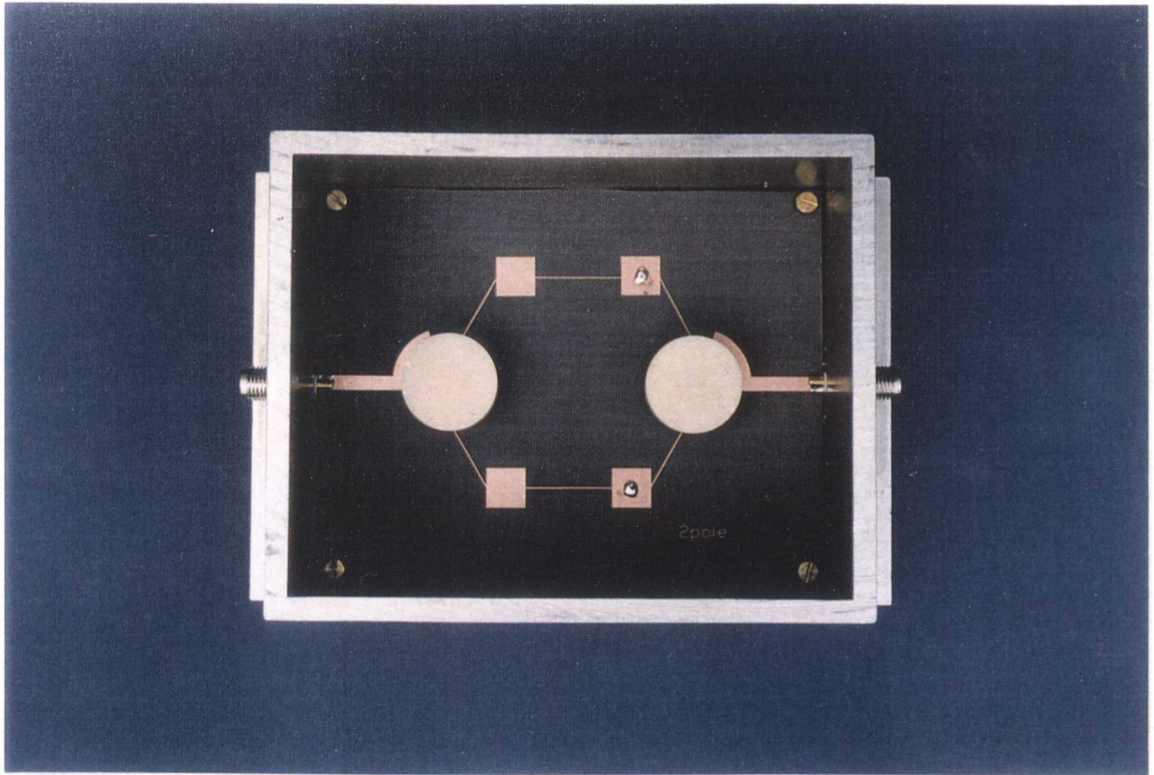


Figure 5.33 Photograph of an electronically tunable 2-pole DR BPF.

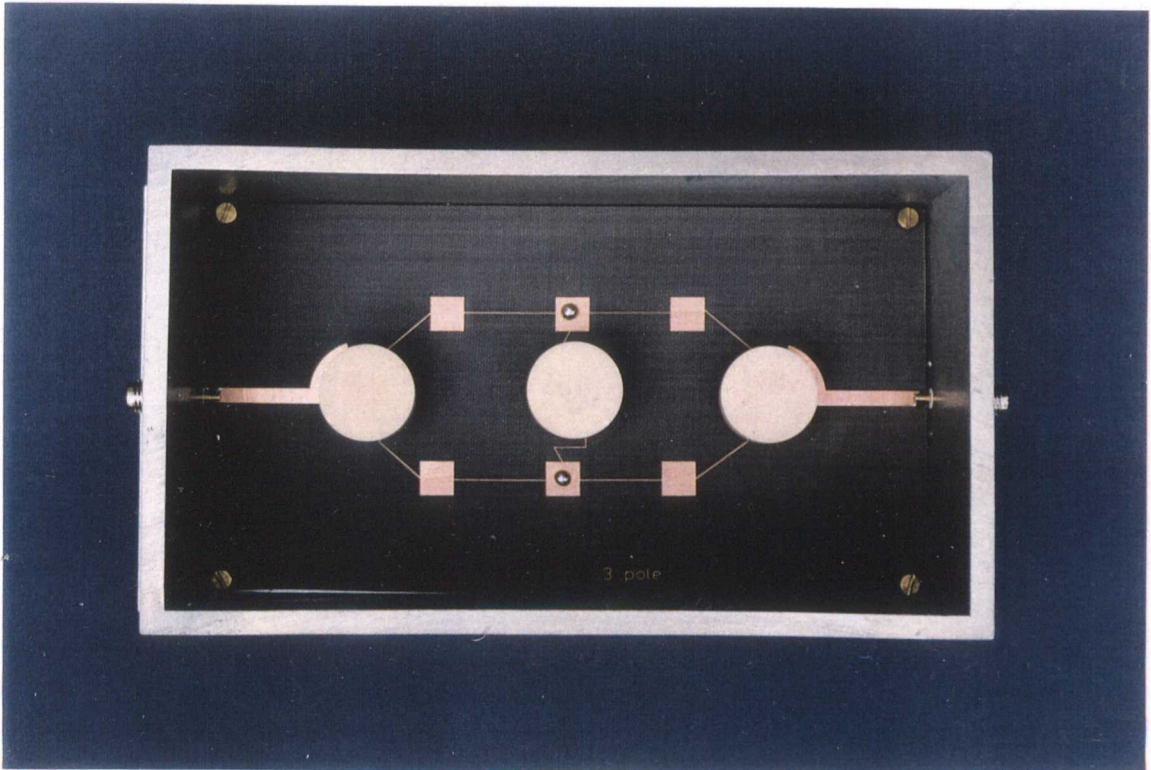


Figure 5.34 Photograph of an electronically tunable 3-pole DR BPF.

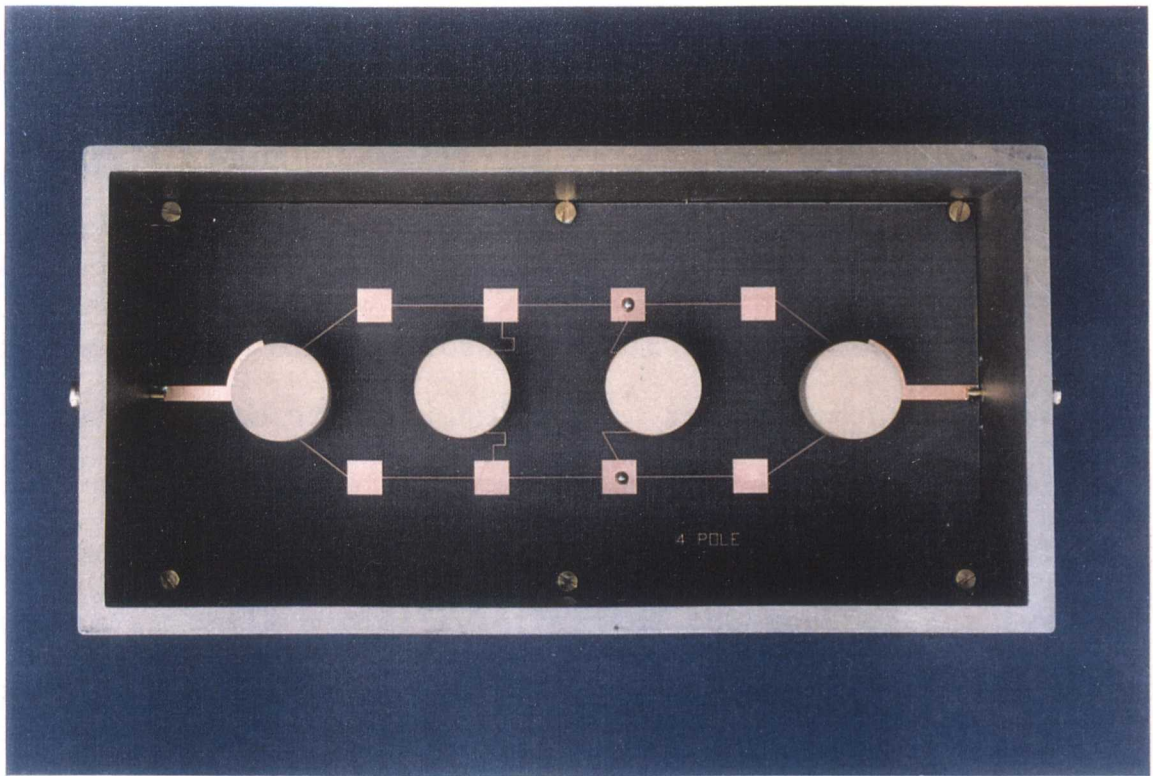


Figure 5.35 Photograph of an electronically tunable 4-pole DR BPF.

Chapter 6

Electronically Tunable DR Bandstop Filters

6.0 Introduction

Bandstop filters are important constituents of modern systems. Applications include communication, radar, countermeasures, etc. Such filters are the complement of bandpass filters and are used to selectively reject a relatively narrow band of frequencies while minimally affecting the rest of the system bandwidth.

Tunable bandstop filters are of interest for applications where it is desired to blank out an interfering signal, using electronic control to adjust the blanking frequency. One application with considerable potential for this type of device is in combination with a swept-frequency superheterodyne receiver where a narrow-band, electronically tunable bandstop filter could be used to eliminate the image response.

There is an extensive list of literature available which covers the synthesis of bandstop filters suitable for most types of transmission line, from strip line to waveguide, employing ferrimagnetic YIG resonators and tuning diodes [1-4]. There is, however, only a limited number of publications on bandstop filters employing DRs [5] and, to the authors knowledge, no previous work has been published on tunable DR bandstop filters.

This chapter presents a design procedure and experimental

results of a novel electronically tunable bandstop filter implemented using DRs in the S-band. The main requirements for a tunable bandstop DR filter are a good passband maintained over a broad bandwidth; narrow stopbands and a tuning mechanism which can easily be incorporated into the circuit. These requirements necessitate the use of a structure employing a through transmission line to achieve a good passband performance, and a means of coupling the resonator with the main line to achieve the required narrow stop-band bandwidths.

The tuning configuration employed in the current work consists of a microstrip loop loaded with GaAs varactor diodes coupled to a DR device, Figure 6.1. As with the approach adopted in section 4.8, the tuning circuit is selected to produce optimum variation in the DRs fundamental resonant frequency TE_{016} without significantly degrading its quality factor. A formula is (section 6.2) derived expressing the required Q_{ex} values of the resonators in terms of the elements of a low-pass prototype filter. Several fixed frequency and tunable bandstop filters were designed and tested. Agreement between measured and theoretical performance is excellent. The designs were constructed on Cu217 dielectric substrate with $\epsilon_r=2.17$ and thickness=0.794mm. The varactor diodes used were SMV1400-04 manufactured by Alpha Ind. Inc. and the DR was a Transtech D8500 series with $D=17.145\text{mm}$ and $h=7.722\text{mm}$ made of $(\text{ZrSn})\text{TiO}_4$ with $\epsilon_r=36$.

6.1 Tuning Configuration

Several novel microstrip tuning configurations have been investigated to establish one which perturbs profoundly the resonance frequency of a cylindrical dielectric resonator operating in its TE_{016} -mode without significantly degrading its Q-factor. The results of this study are reported in Chapter 4. The configuration which was found to be most apt for obtaining relatively large tuning bandwidths consisted basically of two semi-circular annular conductive tracks loaded with a pair of GaAs varactor diodes, Figure 6.1. The diameter of this loop and the width of the tracks were judiciously chosen for maximum tuning without unacceptable Q degradation. The dielectric puck is mounted directly above the tuning configuration and is supported by a low loss, low permittivity electrically insulating material in order to reduce ohmic losses and minimise degradation of resonator Q. The presence of the varactor diodes introduces an inductive component into the circuit so formed, and this inductance modifies the electromagnetic field associated with the DR, thereby altering its resonance frequency. This effect is quite appreciable as the experimental results show in Figure 6.2. The frequency of resonance can be readily altered over a range exceeding 60MHz centred around 3.29GHz. However, as expected the variation with bias voltage is not linear but is steeper in the area in which the applied bias is near to zero, Figure 6.2. This configuration was employed in the design of electronically

tunable bandstop filters discussed in the following section.

6.2 DR Bandstop Filter Design

The design of a single pole DR bandstop filter can easily be realised by placing a dielectric puck in the field of a propagating transmission line. In the vicinity of resonance the puck will introduce a high "Q" of reflection loss characteristic of a bandstop response. The bandwidth of this response is determined primarily by the degree of coupling of the resonator to the transmission line. For effective coupling, the magnetic-dipole of the resonator should be in the direction of the magnetic field of the transmission line, as shown in Figure 6.3.

By analysing a DR coupled with a microstrip line, as is the case in the DR bandstop filter configuration, we can obtain a general formula for external Q. From Chapter 3 and section 3.2.1, a DR may be represented by an equivalent resonant loop composed of an inductor tuned to resonance by a series capacitor, Figure 6.4.

The resonant loop couples an impedance $Z=jX$ in series with the line, as in Figure 6.4(b). Applying elementary circuit theory to Figure 6.4(a) yields the anti-resonant reactance function:

$$X = \frac{Z}{j} = \frac{-(\omega L_m)^2}{\omega L \left(1 - \frac{\omega_o^2}{\omega^2} \right)} \quad (6.1)$$

where L_m is the mutual inductance between the loop and the line, and $\omega_o^2 = 1/LC$. At ω_o , X is infinity, and a rejection peak occurs.

A narrow-bandwidth approximation for X is as follows:

$$X = \frac{(\omega_o L_m)^2}{2\omega L \left(\frac{f - f_o}{f_o} \right)} \quad (6.2)$$

At the 3dB points

$$X_{3dB} = \pm 2Z_o \quad (6.3)$$

and

$$\frac{f_{3dB}^{\pm}}{f_o} = 1 \pm \frac{(\omega_o L_m)^2}{4\omega_o L Z_o} \quad (6.4)$$

Hence

$$Q_{ex} = \frac{f_o}{f_{3dB}^+ - f_{3dB}^-} = \frac{2\omega_o L Z_o}{(\omega_o L_m)^2} \quad (6.5)$$

However, in terms of the elements of a low-pass prototype filter, the design of multipole DR bandstop filters exhibiting prescribed insertion loss characteristics, requires more specific design equations than those employed in circuits utilising distributed inductor and capacitor (e.g. see Young, et al [3]). It is now shown that for narrow bandwidth DR filters, the external Q_s of the individual resonators can be

expressed directly in terms of the elements of the low-pass prototype filter and the parameters of the frequency transformation.

In the circuit of Figure 6.5 the low-pass prototype structure is realised by DRs coupled in series with the transmission line at intervals equal to an odd multiple of a quarter guide wavelength. Young [3] defines a susceptance slope function by,

$$b_i = \frac{\omega_o}{2} \left. \frac{dB_i}{d\omega} \right|_{\omega = \omega_o} \quad (6.6)$$

where B_i is the susceptance of the i th resonator. For the constant admittance line structure of Figure 6.3, it has been shown that [3]:

$$\frac{b_i}{Y_o} = \frac{1}{\omega'_1 w g_i} \quad (6.7)$$

At the 3dB bandwidth points of an individual resonator, the susceptance in series with the line is equal to $-Y_o/2$ or $+Y_o/2$, while at ω_o the susceptance is zero. Thus, the admittance, dB, is equal to $Y_o/2$ when $d\omega$ corresponds to half of the 3dB bandwidth. From Equation (6.6),

$$b_i = Q_{\text{exi}} \frac{Y_o}{2} \quad (6.8)$$

where $Q_{exi} = \omega_0/2d\omega$ is the external Q of the i th resonator. Substituting Equation (6.8) in Equation (6.7), yields:

$$Q_{exi} = \frac{2}{\omega_1' w g_i} \quad (6.9)$$

The element values $g_i = g_1, g_2, \dots, g_n$ apply to the prototype low-pass filter whose response function is to be simulated by the bandstop filter. $\omega' = 2\pi f'$ is the frequency function for the low-pass filter, and $w = (f_2 - f_1)/f_0$ is the relative bandwidth of the bandstop filter. As shown in Figure 6.6, ω', ω_1 and ω_2 apply to corresponding response points of the low-pass and bandstop functions. Values of g_i for maximally flat and equal-ripple response functions may be found in reference [3].

It can be seen from Equation (6.9) that relatively small changes in Q_{ex} will affect the bandwidth of the filter. Such changes can be introduced by including tuning screws. To demonstrate this and to determine the degree of its effect upon the characteristics of a single resonator, measurements were made using the arrangement shown in Figure 6.7. The DR is mounted on the microstrip substrate, and the tuning screw is located directly above the resonator, supported by the top cover. The measured results of the resonant frequency and Q_{ex} as a function of distance H is given in Figure 6.8. From this we can conclude that increasing the distance beyond 21mm does not affect the frequency in any appreciable way. The lowest

frequency is about 3.3062GHz. When the distance H is reduced to less than about 7mm, frequency starts increasing rapidly. However, by bringing the metal surface of the tuning screw close to the resonator produces appreciable surface currents, which in turn reduce the external Q factor of the resonator. It was observed from the measurements that from zero insertion of the screw to the point of contact the overall Q_{ex} decreased to about 370.

Experimental observations [8] confirm that the distances between adjacent resonators need to be odd multiples of $\lambda_g/4$ otherwise excessive fringing field coupling between resonators degrades the response.

There are two possible ways of incorporating the dielectric puck onto the substrate to realise a bandstop response, as illustrated in Figure 6.9. Whilst it might be envisaged that the coupling between adjacent resonators to be more severe for resonators placed on the same side of the microstrip line than for those placed on the opposite sides never-the-less this particular point does require investigation. Thus to establish the best configuration for implementing tunable filters, bandstop filters were constructed using both configurations. From hereon these two configurations will be referred to as Type 1 and Type 2. In Type 1, the adjacent resonators are placed on opposite sides of the line, whereas in Type 2 pucks are placed on the same side of the line.

6.2.1 Design Specification of Fixed Frequency DR Bandstop Filters

Three Bandstop filters were designed to the following specifications:

Design 1.

2-Pole

Centre Frequency, f_o : 3.22GHz

Pass-Band Ripple: 0.5dB

3dB Rejection Bandwidth: 14.0MHz

Design 2.

3-Pole

Centre Frequency, f_o : 3.22GHz

Pass-Band Ripple: 0.5dB

3dB Rejection Bandwidth: 20.0MHz

Design 3.

4-Pole

Centre Frequency, f_o : 3.22GHz

Pass-Band Ripple: 0.5dB

3dB Rejection Bandwidth: 25.0MHz

The physical design and construction of each of these filters was very similar.

From Equation (6.9), and by use of tables of element values for 0.5dB ripple case, given in reference [3], the external Q of each resonator was calculated for the prescribed filter characteristics. These Q values corresponding to the above designs are tabulated in Table 6.1.

The size and location of the resonators relative to the microstrip line can be obtained either by analytic or experimental techniques described in Chapter 3. The resonators were placed on the substrate $\lambda_g/4$ intervals and with spacing from the microstrip line to yield the required resonator Q_{ex} values. The use of tuning screws above each resonator was also necessary to eliminate interfering enclosure modes which degraded the overall response of the filters. The consequence of this, however, was a slight increase in the filter centre frequency. Minor adjustments were required in the position of the resonators and the tuning screws in order to obtain the desired filter performance.

6.2.2 Measured Performance of the Bandstop Filters

The measured frequency responses of these bandstop filters are shown in Figure 6.10 to 6.12. Table 6.2 compares the experimental performance of the filters with the theoretical characteristics. Agreement between measured and theoretical performance is excellent. From these results it is interesting to note that adding more resonators will generally cause the peak attenuation to become larger, and the bandwidth at 20dB attenuation level to be greater. There does not appear to be any appreciable difference in the characteristics between the two types of configurations. Hence, Type 2 configuration was therefore chosen in the design for electronically tunable

bandstop filters since all the resonators are located on the same side of the microstrip line which makes the design of the bias for the tuning circuit considerably easier.

For designs requiring specific minimum attenuation in the stop-band, we need to determine the number of resonators to achieve this performance by using the following equation [3]:

$$\left| \frac{\omega'}{\omega_1} \right| = \left| \frac{w}{\left(\frac{\omega}{\omega_o} \right) - \left(\frac{\omega_o}{\omega} \right)} \right| \quad (6.10)$$

where ω/ω_o corresponds to the prescribed upper minimum attenuation point. Then by referring to the filter attenuation characteristics in reference [3] the number of resonators required can be obtained.

6.3 Tunable DR Bandstop Filter Design

Based on the design principles outlined in section 6.2, 2- and 4-pole tunable bandstop filters were realised. Figure 6.13 shows the 4-pole filter circuit including the tuning part. The d.c. bias voltage is applied to the tuning diodes through a low-pass filter. The design specification for the two filters are given in Table 6.3.

The measured performance of these filters are shown in Figures 6.14 and 6.15. Table 6.4 summarizes the salient features of the responses. Included here are also frequency

bandwidths which were measured directly. The 3dB bandwidth stays constant over the tuning range for both filters, however, the 20dB bandwidth tends to decrease. The tuning bandwidth of the 4-pole filter is considerably larger than that of the 2-pole design, furthermore, it is also evident from the responses that the rejection at the centre frequency of the 2-pole filter tends to decline with bias voltage. This is mainly attributed to the larger losses introduced by the tuning screws which were mounted above each resonator to eliminate interfering enclosure modes. It is envisaged that by using an appropriate enclosure the tuning bandwidth of the 2-pole may be improved.

Comparing the design parameters with the corresponding measured ones, the agreement is seen to be very good, indicating the reliability and the accuracy of the above design procedure.

6.4 Conclusions

A design procedure for realising bandstop filters with DRs has been presented. Application of this procedure to several experimental bandstop filters yielded very good correlation between theoretical and experimental performance. This technique has also been used successfully to realise novel electronically tunable DR bandstop filters. By cascading several such devices that are switchable, tunable filters that operate over a very large frequency band (i.e. several hundred MHz) can be obtained.

References

1. Philip S. Carter, "Side-Wall-Coupled, Strip-Transmission-Line Magnetically Tunable Filters Employing Ferrimagnetic YIG Resonators", IEEE Trans. on Microwave Theory & Techniques, May 1965, pp306-315.
2. George L. Matthaei, "Magnetically Tunable Band-Stop Filters", IEEE Trans. on Microwave Theory & Techniques, March 1965, pp203-212.
3. L.Young, G.L.Matthaei, E.M.T.Jones, "Microwave Band-Stop Filters with Narrow Stop Bands", IRE Trans. on Microwave Theory & Techniques, Nov.1962, pp416-427.
4. I.C.Hunter and J.D.Rhodes, "Electronically Tunable Microwave Band-Stop Filters", IEEE Trans. on Microwave Theory & Techniques, Sept. 1982.
5. P.Guillon, S.Mekerta, Y.Garault, "A Dielectric Resonator Bandstop Filter", IEEE MTT-S Int. Microwave Symp. Digest, June 1981, pp170-173.
6. B.Virdee, "Investigation of Different Microstrip Topologies for Tuning DR TE_{018} Resonant Frequency", 1994 Asia Pacific Microwave Conference, Tokyo, Japan, Dec. 1994.
7. K.Z.Guo, L.A.Trinogga, T.H.Edgar, "DR Coupling: Improvement to an Existing Approach", Electronics Letters, 3rd March 1988, Vol.24, No.5, pp285-287.
8. Virdee, B., "Novel Electronically Tunable DR Bandstop Filter," 1995 SMBO/IEEE MTT-S Int. Microwave and Optoelectronics Conf., Rio de Janeiro, July 24-27, Brazil.

Table 6.1

Design	External Q values
2-Pole	$Q_{ex1}=327.89, Q_{ex2}=652.56$
3-Pole	$Q_{ex1}=Q_{ex3}=201.72,$ $Q_{ex2}=293.61$
4-Pole	$Q_{ex1}=154.22, Q_{ex2}=216.0,$ $Q_{ex3}=108.87, Q_{ex4}=305.97$

Table 6.2

Type 1 Configuration

Filter	Measured fo (GHz)	Design fo(GHz)	Measured Rejection @ fo (dB)	Measured Δf-3dB (MHz)	Design Δf-3dB (MHz)	Measured Δf-20dB (MHz)
2-Pole	3.2435	3.22	27.20	13.65	15.0	0.9
3-Pole	3.2633	3.22	22.91	20.00	20.0	1.5
4-Pole	3.2637	3.22	31.36	25.65	25.0	2.1

Type 2 Configuration

Filter	Measured fo (GHz)	Design fo(GHz)	Measured Rejection @ fo (dB)	Measured Δf-3dB (MHz)	Design Δf-3dB (MHz)	Measured Δf-20dB (MHz)
2-Pole	3.2312	3.22	28.95	14.00	15.0	1.00
3-Pole	3.2272	3.22	31.55	20.50	20.0	1.50
4-Pole	3.2331	3.22	31.35	25.93	25.0	2.22

Table 6.3 Design Specifications.

Filter	Centre Frequency fo (GHz)	Pass-Band Ripple (dB)	3dB Rejection Bandwidth (MHz)
2-Pole	3.30	0.5	32.0
4-Pole	3.30	0.5	50.0

Table 6.4 Measured Characteristics.

Filter	2-Pole	4-Pole
Centre Frequency fo(GHz) @ 0 volts	3.3397	3.3456
Δf-3dB (MHz) @ 0 volts	33.0	50.025
Δf-3dB (MHz) @ 30 volts	33.0	49.30
Δf-20dB (MHz) @ 0 volts	2.40	10.87
Δf-20dB (MHz) @ 30 volts	1.50	4.35
Tuning Δf (MHz) 0 to 30 volts	20.7	58.0
Rejection @ fo (dB)	>20	>28

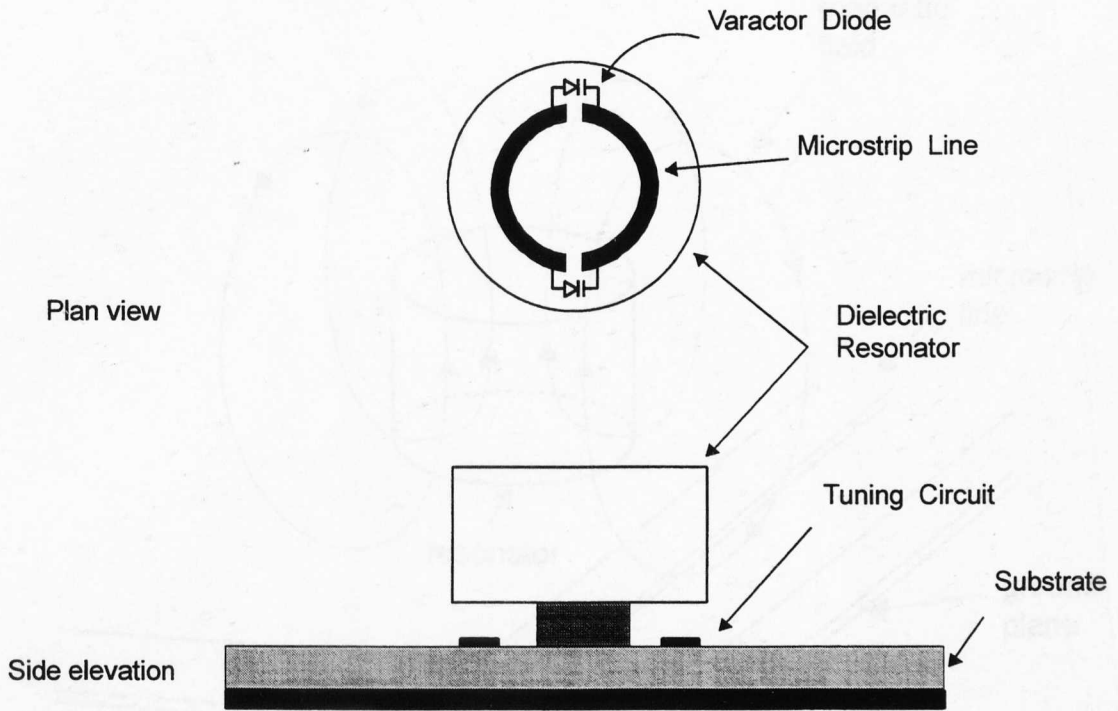


Figure 6.1 Tuning configuration.

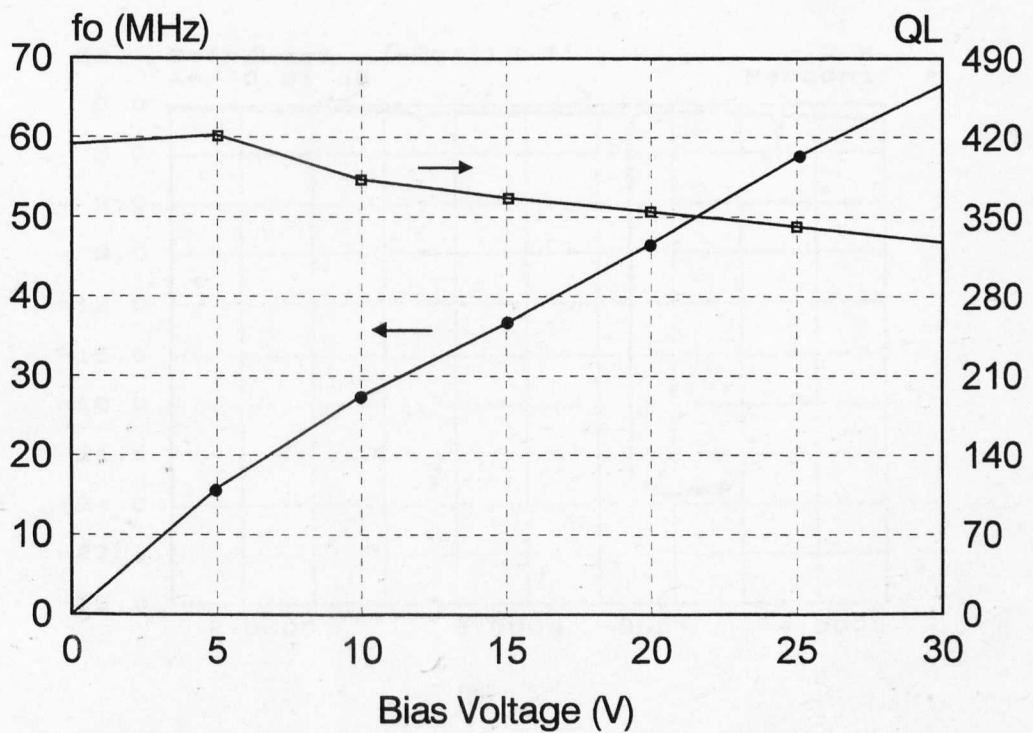
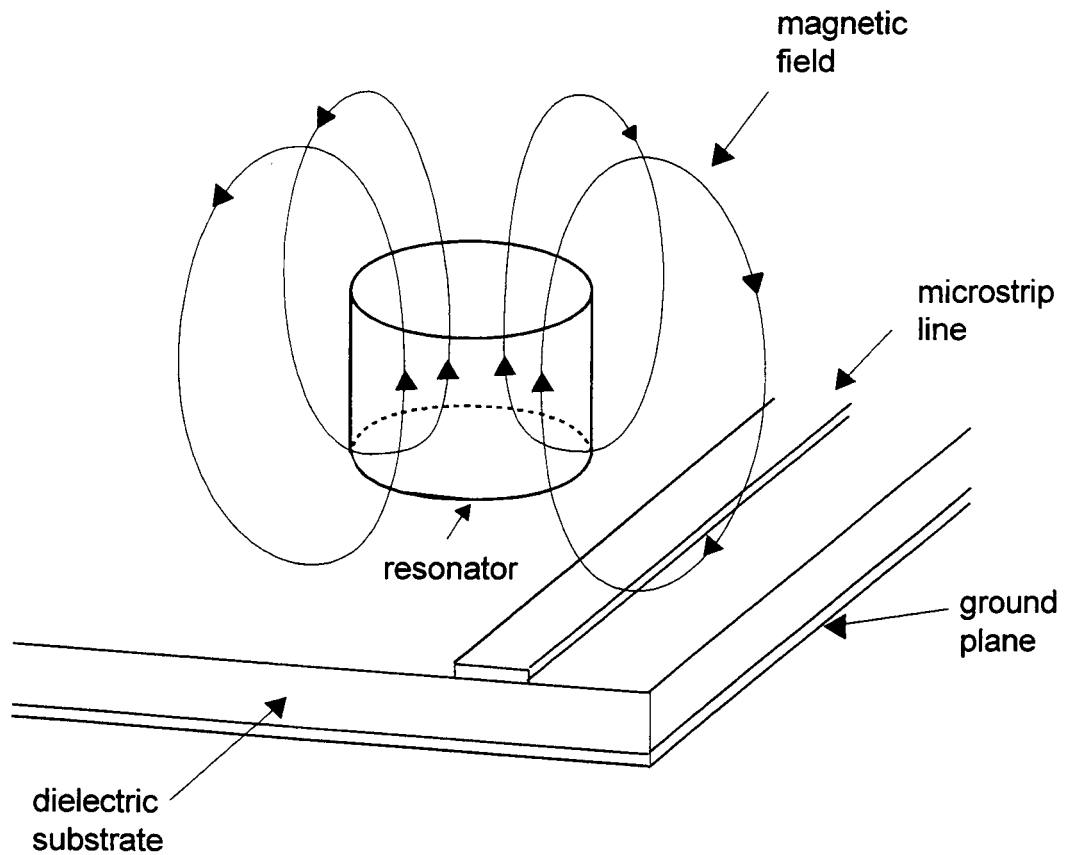
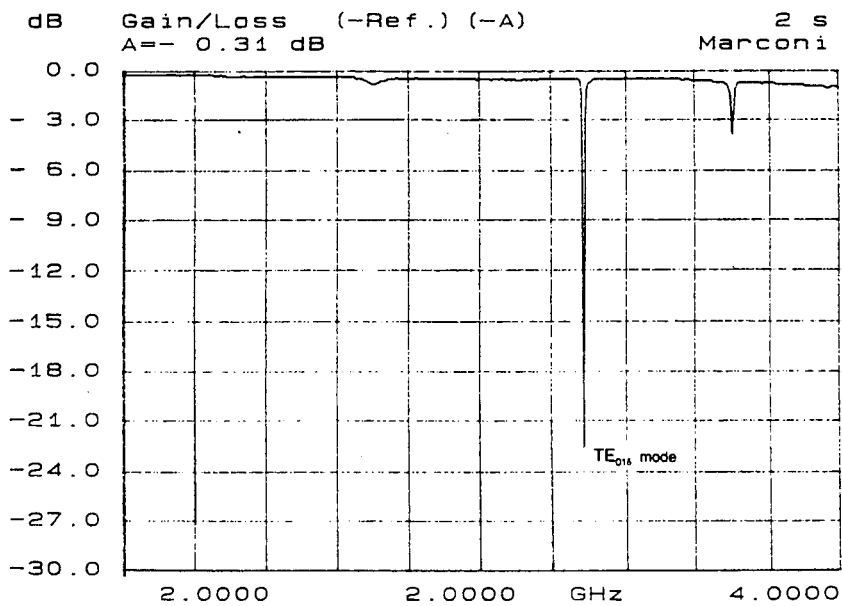


Figure 6.2 DR resonance frequency & loaded Q-factor as a function of varactor bias voltage.



(a)



(b)

Figure 6.3 (a) Configuration for coupling the DR TE_{016} mode to a microstrip line, and (b) The corresponding transmission response.

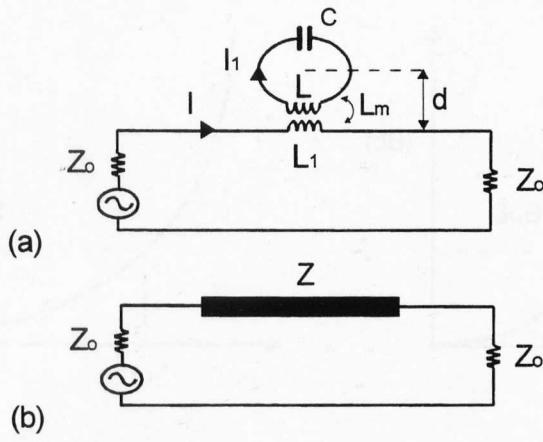
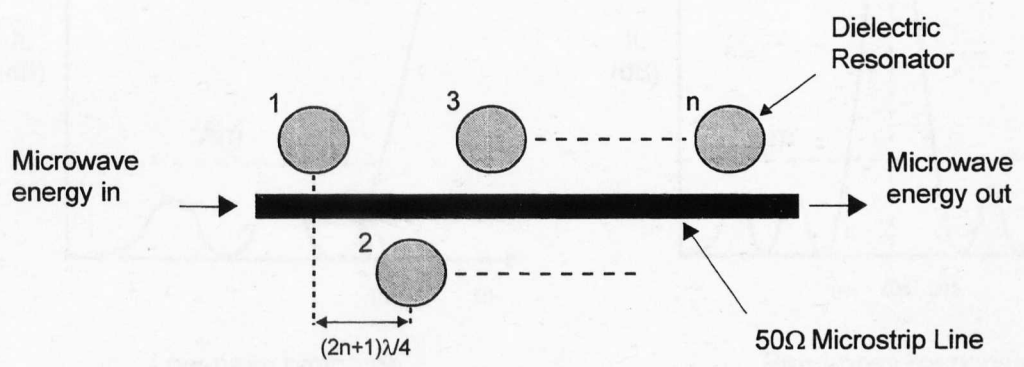
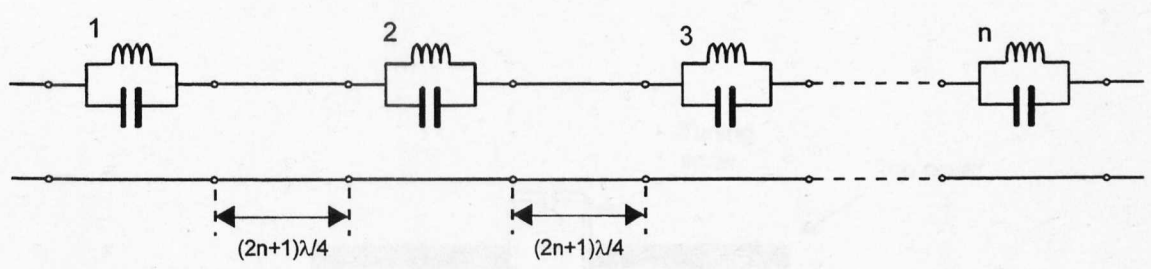


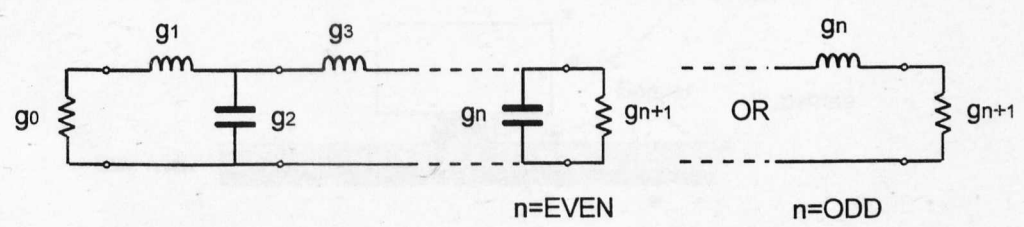
Figure 6.4 Equivalent circuit representing the coupling between transmission line and dielectric resonator.



(a) DR Bandstop filter.



(b) Equivalent circuit for (a)



(c) Low-pass prototype of (b)

Figure 6.5

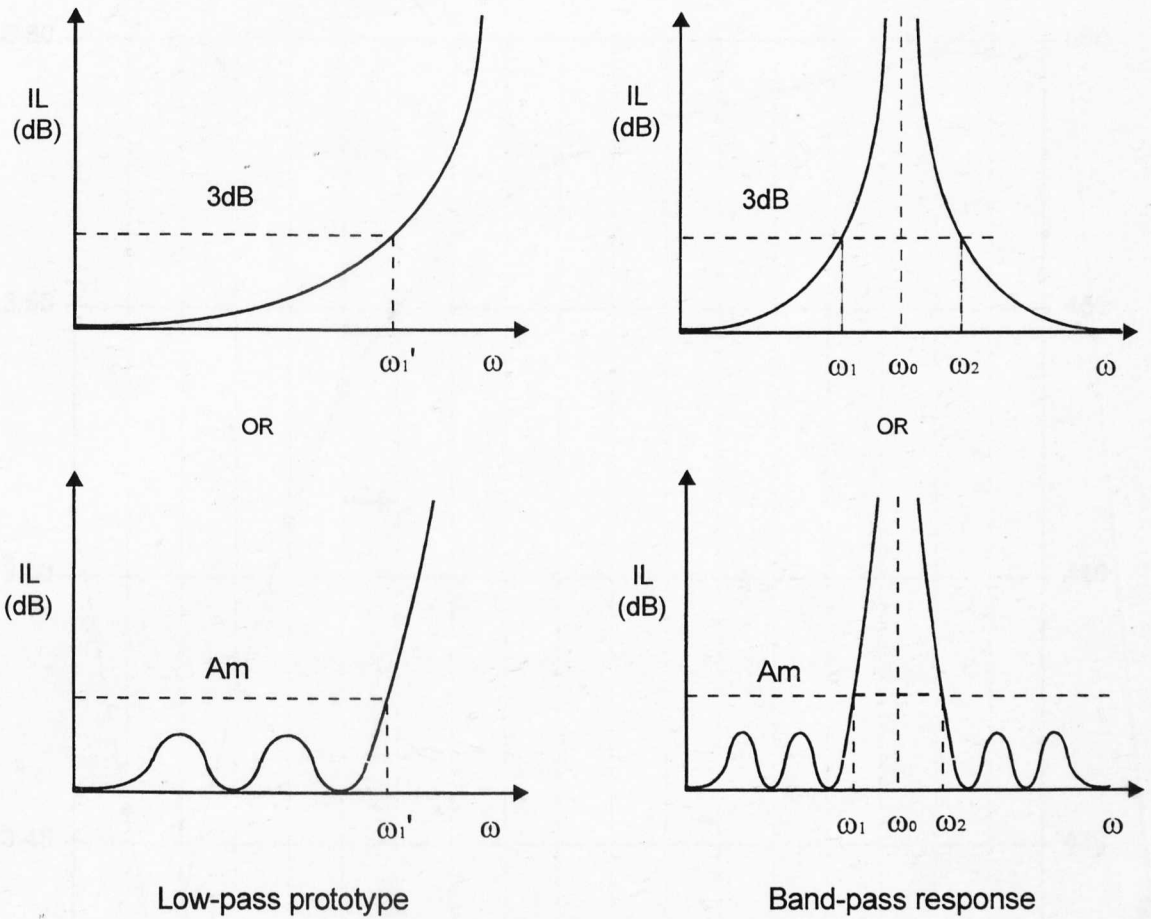


Figure 6.6 Ideal filter characteristics.

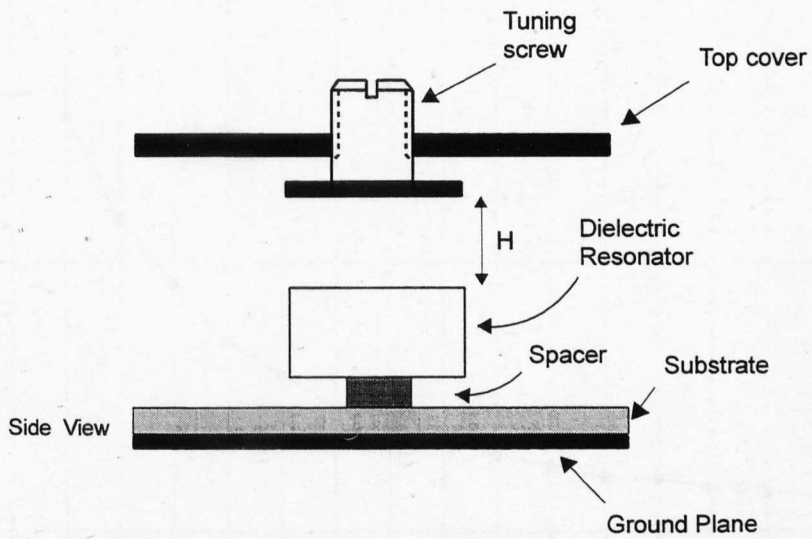


Figure 6.7 Test-fixture to measure resonant frequency & loaded Q-factor as a function of H .

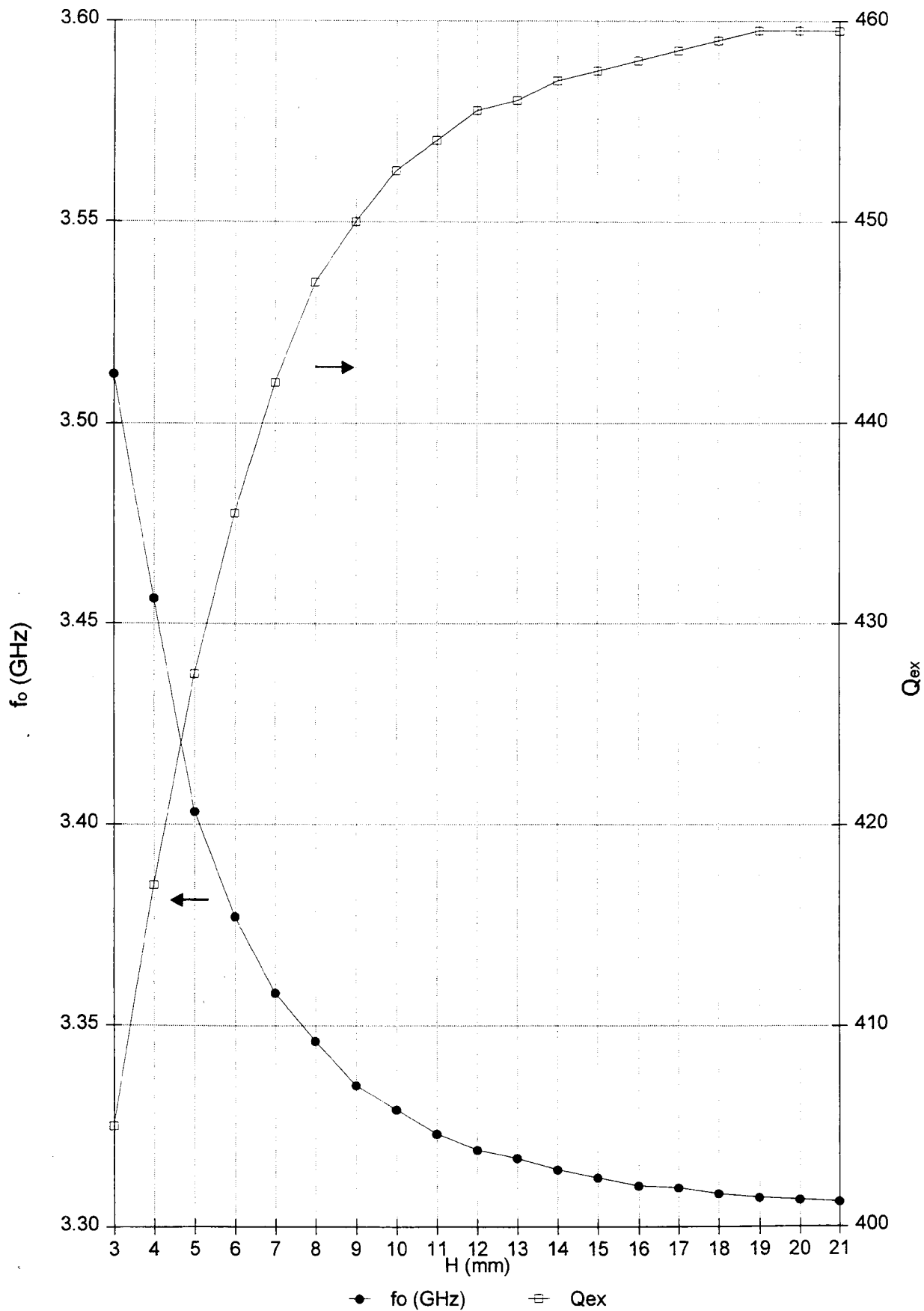


Figure 6.8 Measured change in resonant frequency and Q_{ex} as a function of H .

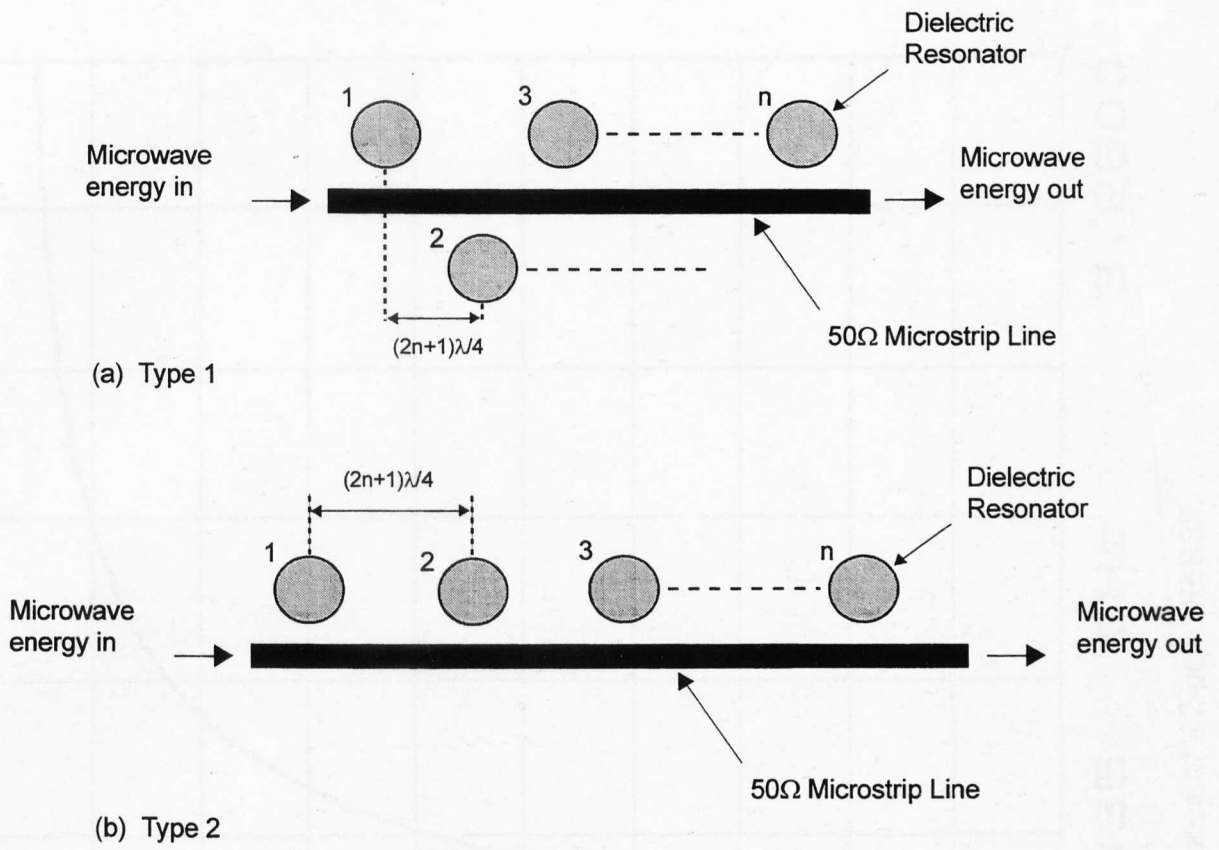


Figure 6.9 DR bandstop filter configurations.

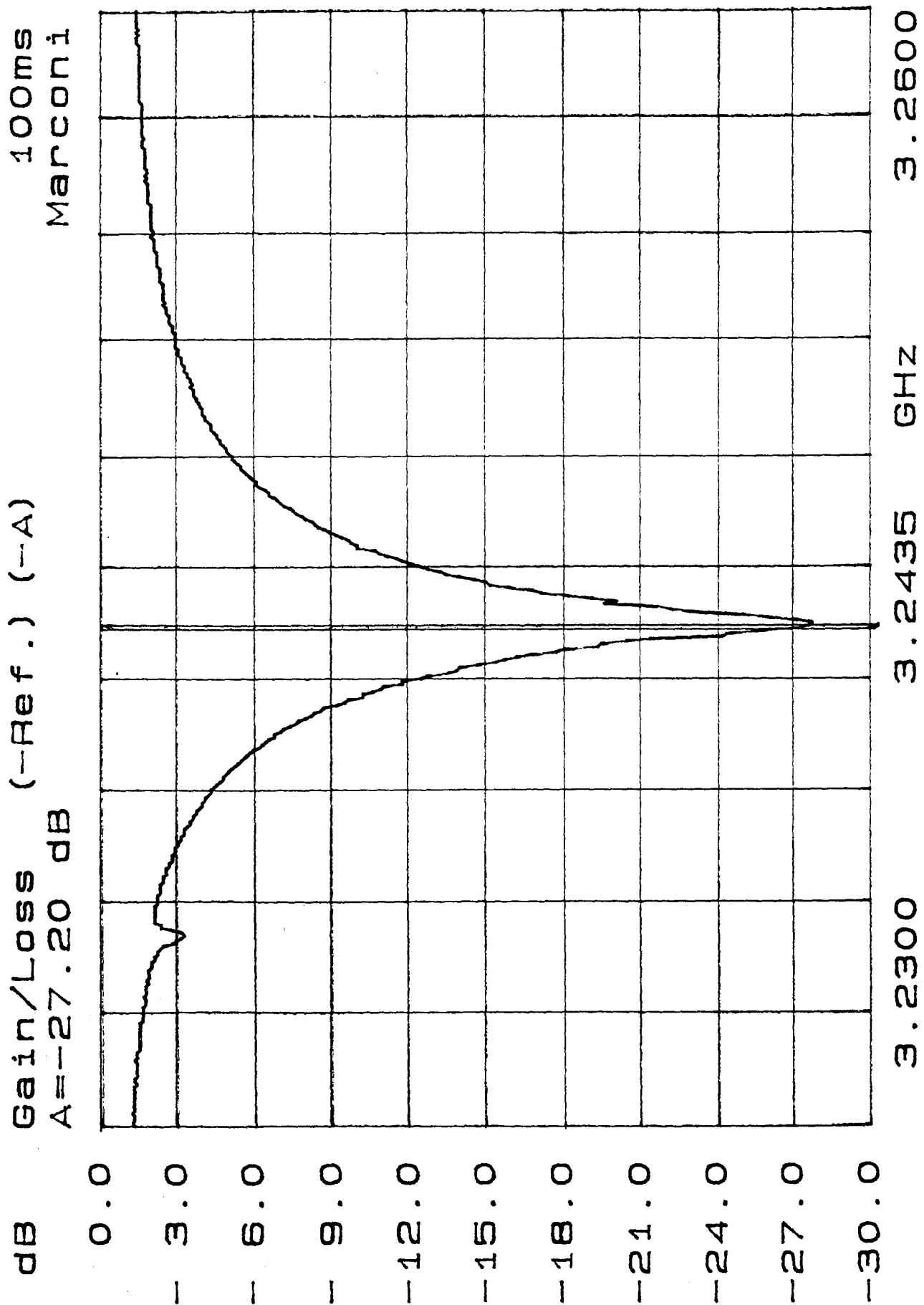


Figure 6.10 Measured response of a 2-pole DR BSF.

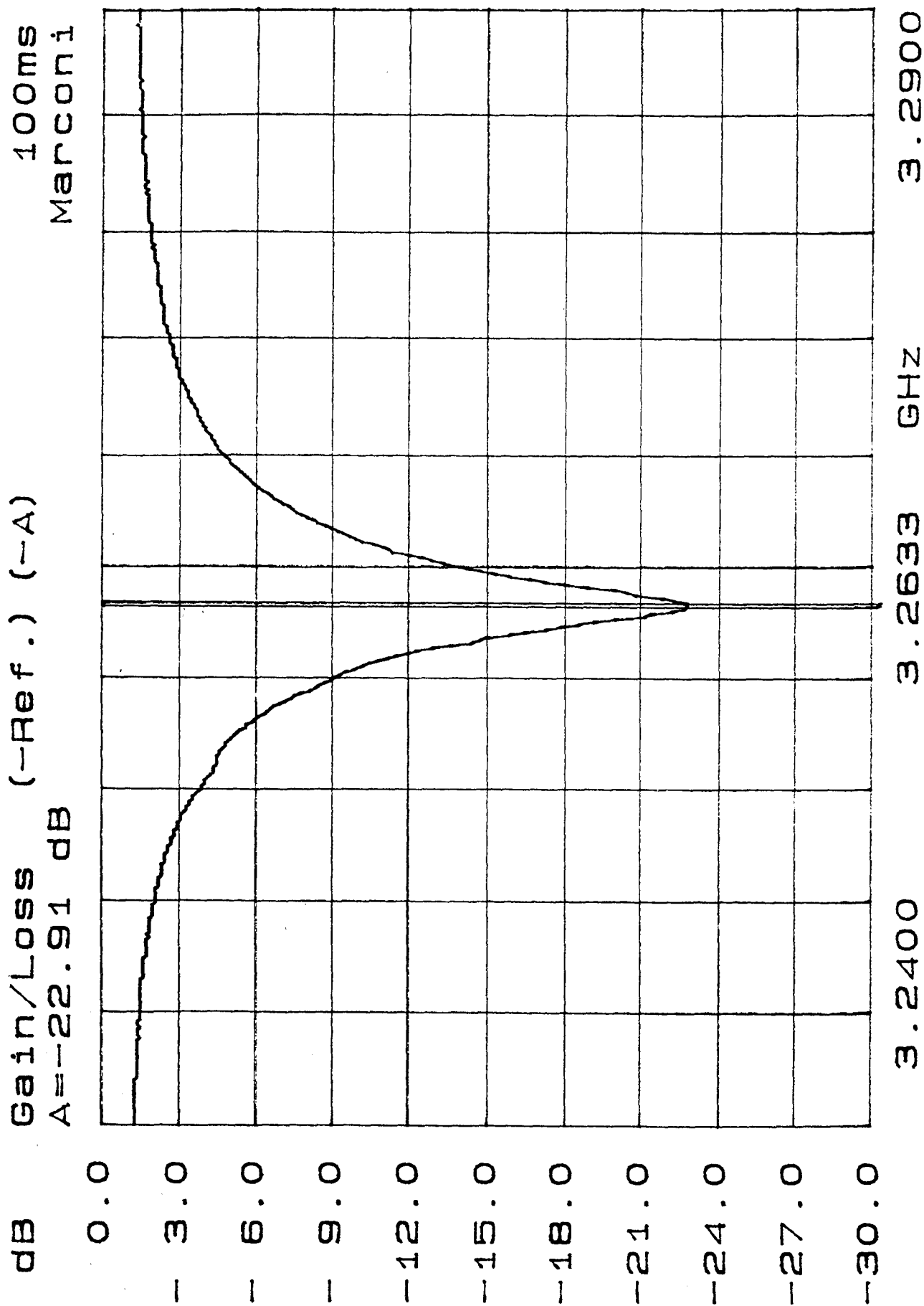


Figure 6.11 Measured response of a 3-pole DR BSF.

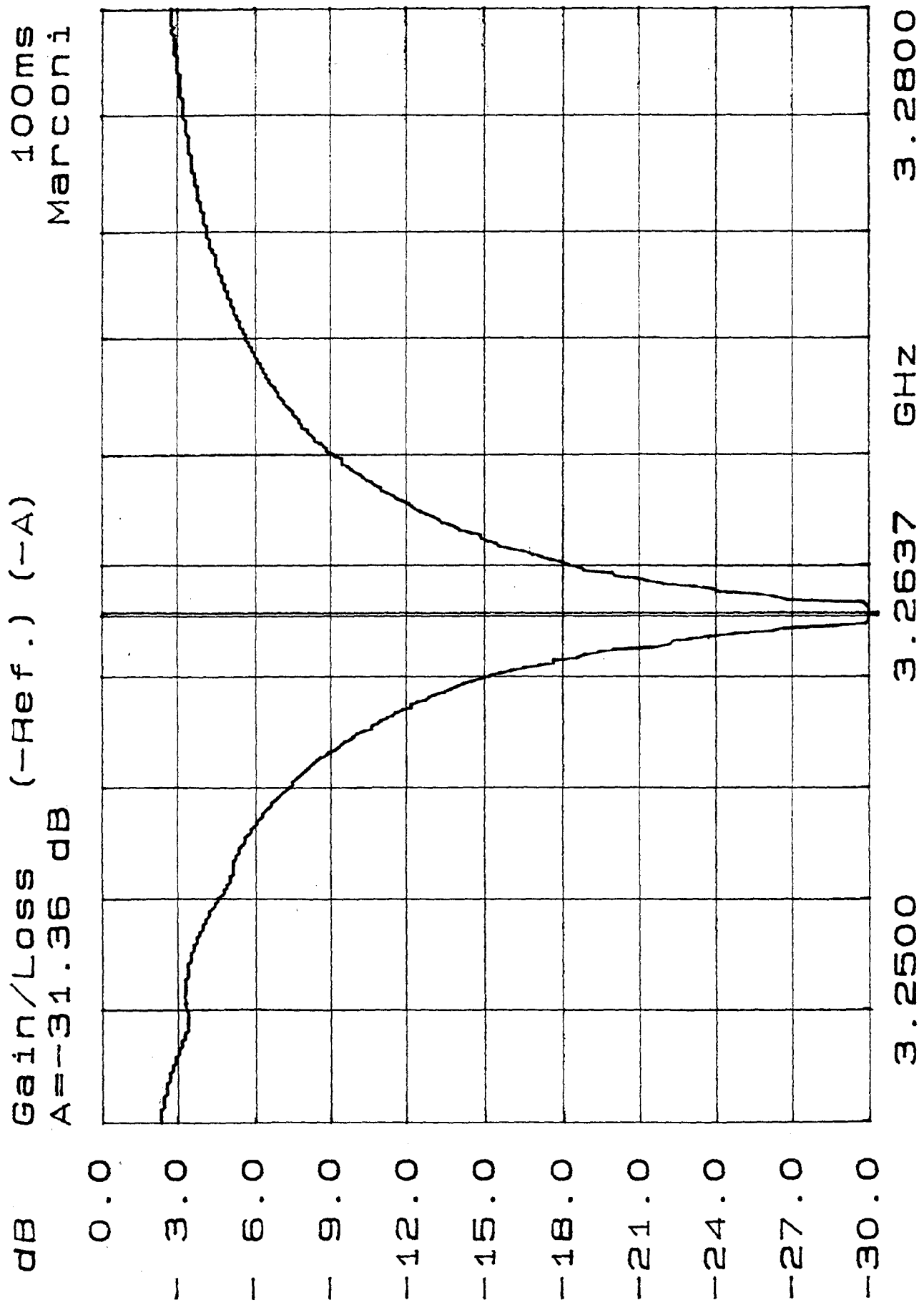


Figure 6.12 Measured response of a 4-pole DR BSF.

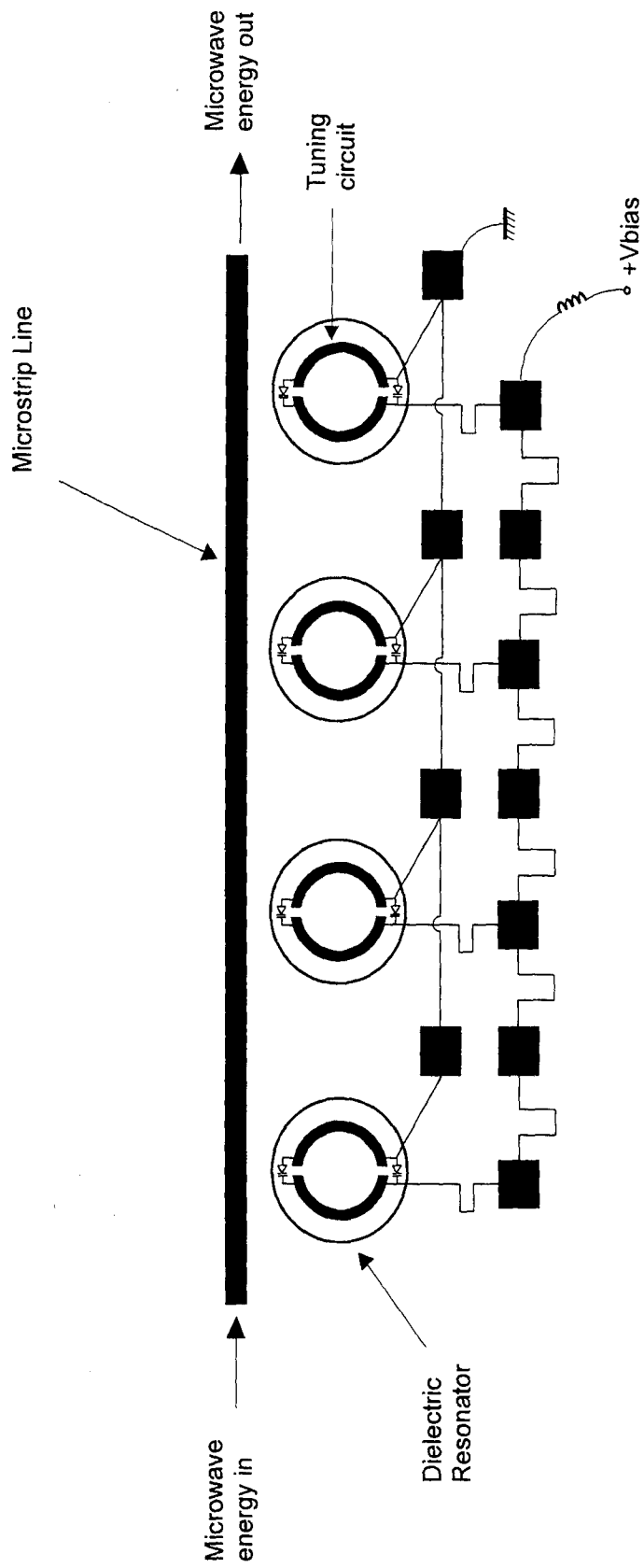


Figure 6.13 Tunable 4-pole DR bandstop filter layout drawing.

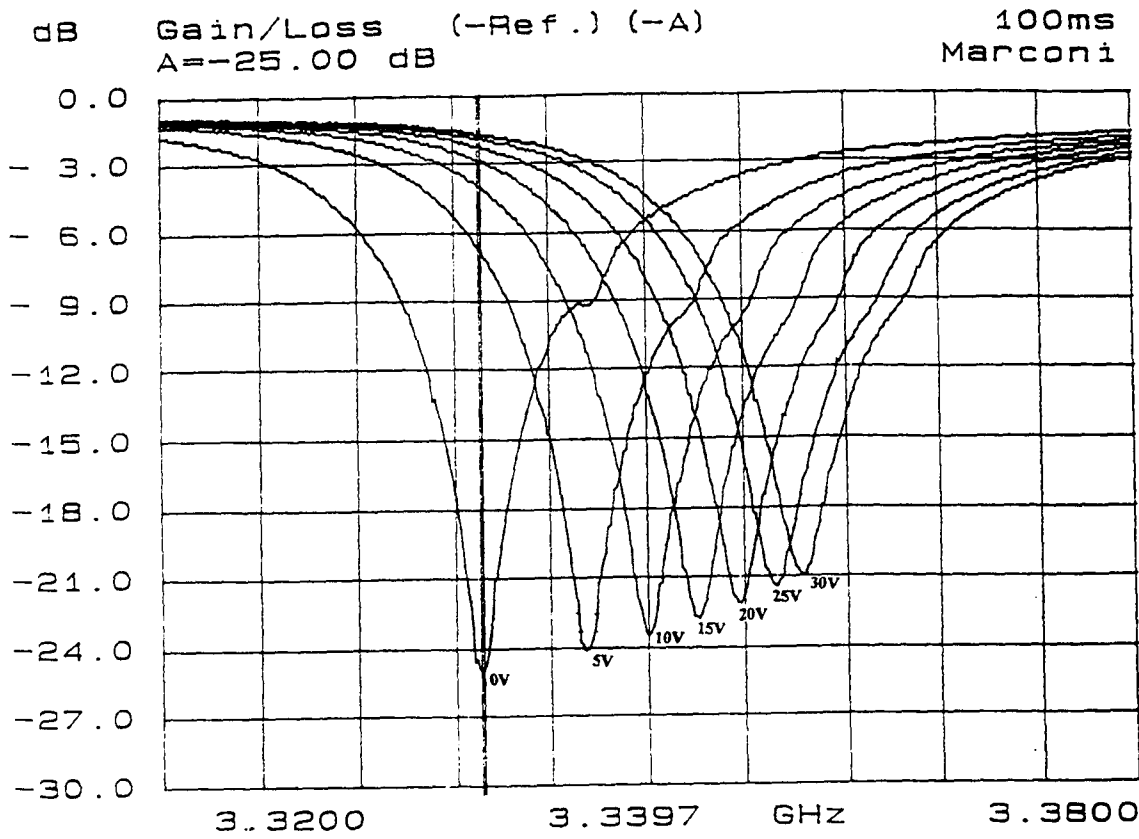


Figure 6.14 Measured response of electronically tuned 2-pole DR BSF.

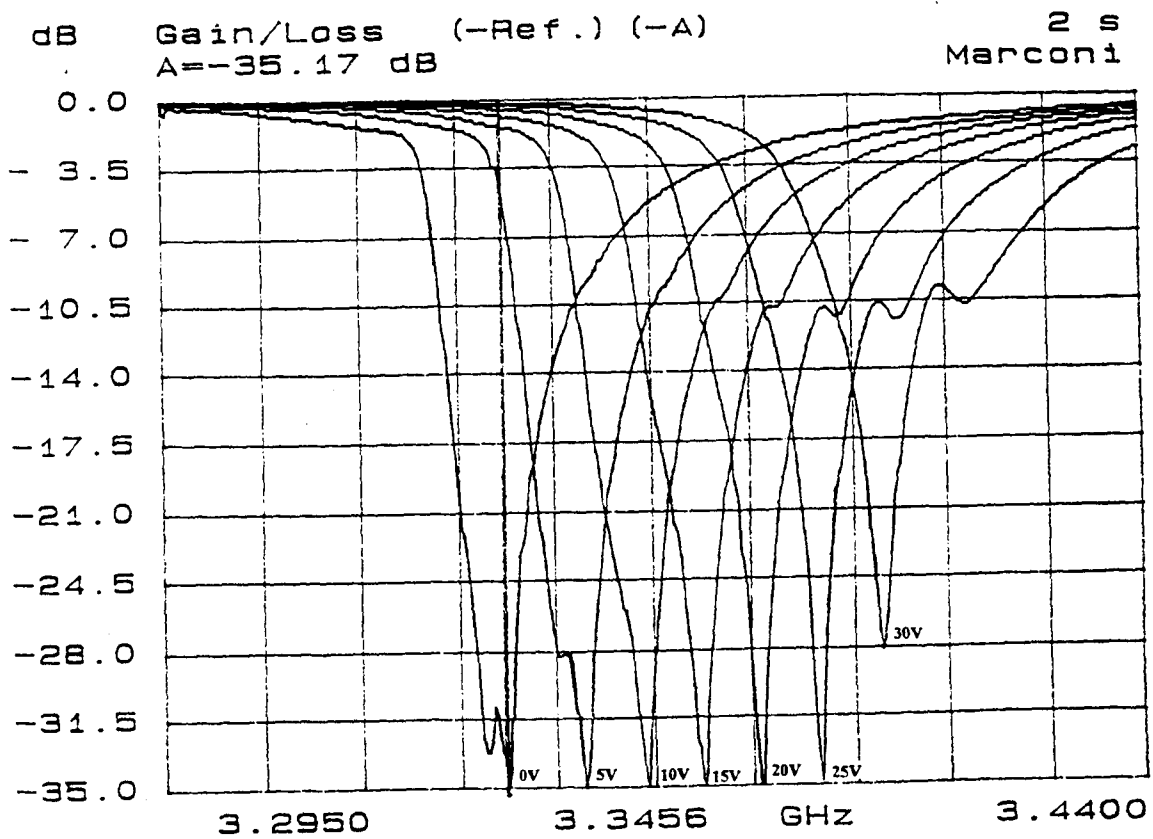


Figure 6.15 Measured response of electronically tuned 4-pole DR BSF.

Chapter 7

General Conclusions and Suggestions for Future Work

7.0 Conclusions

The importance of filters in high frequency systems design and microwave engineering is inevitably increasing with restrictions on use of the frequency spectrum. This is especially true for applications in cellular radio base stations, where filters with relatively very small passbands (typically 15MHz) are necessary for channel selection. Of particular importance in the development of the future generations of adaptive cellular radio systems is the need for electronically tunable filters to allow dynamic frequency allocation to occur over relatively wide bands. Consequently, electronic tunable filters currently represent a topic for development where the emphasis must be towards wide band, small size and low cost components.

This thesis has been devoted to a study of the design and realisation of electronically tunable microwave dielectric resonator filters. In particular, both bandpass and bandstop filters, with narrow passband and stopbands, respectively, together with relatively broad tuning bandwidths have been investigated. Dielectric resonators have been employed as the frequency selective element because of their comparable performance to waveguide resonators with an appreciable reduction in size, and the additional possibility of

temperature stabilisation and MIC integration.

The lack of suitable theoretical design information has resulted research in a more accurate expression representing the coupling coefficient which exists between a pair of identical DRs situated on a substrate and enclosed in a metal enclosure. Accurate knowledge of this coupling coefficient is essential in any practical filter design using DRs. Moreover, because of the large number of parameters involved, it is not feasible to obtain a quantity of experimental data adequate for all needs. In chapter three a generalised formula for the coupling coefficient between two magnetic dipole resonators is developed for the case of dielectric resonators placed in a microstrip environment and enclosed in a metallic housing. The structure under analysis was divided into several sub-regions in accordance with dimensional and/or material discontinuities. Electromagnetic field expressions in each sub-region were then derived and simplified according to the boundary conditions among the subregions and orthogonality properties of the fields. Expressions were then derived for the magnetic dipole moment and stored energy of the dielectric resonator which were used to compute the coupling coefficient between two dielectric resonators. A computer program, DRCOUP, was developed to predict the coupling coefficient. The computed values exhibit good agreement with the measured values.

The second phase of the work was concerned with, first selecting an appropriate tuning mechanism and then, developing

a tuning configuration which would yield optimum tuning bandwidth of the DR resonant frequency operating in the $TE_{01\delta}$ mode without degrading its Q-factor.

The mechanism chosen for tuning the resonator was a GaAs chip varactor diode whose choice was mainly based on its low response time, low cost, and small size.

The effects of the resonator support spacer height and the input/output coupling structure on the performance of the DR were also investigated. It was found that variation of the coupling arc radius and length had an insignificant effect on the DR resonant frequency. However, it was found that the resonant frequency depended on the spacer height which, along with the coupling arc radius and length, influenced both the passband insertion loss and Q-factor of the resonator. Specifically, it was found that the insertion loss increased and the Q-factor improved with rise in spacer height, and with a reduction in the coupling arc length. However, both these parameters deteriorated with an increase in the coupling arc radius.

Based upon these observations and supported by the new theoretical studies, several novel configurations were developed, (chapter four). It was found from measurements that although some of these configurations provided tuning bandwidths in excess of 60MHz, there was however, unacceptable variation in the resonator passband insertion loss. The configuration which exhibited a good overall performance

basically consisted of two semi-circular microstrip tracks loaded with varactor diodes.

The proximity of this tuning loop to the input/output lines and the effect of the track width on the performance of the configuration was also investigated. The measurements showed that both the tuning range and loss tend to rise proportionally with weaker coupling with the input/output lines. Since the Q-factor and loss are inversely related to each other, a trade-off between Q or tuning bandwidth and loss was inevitable. One of the configurations produced the largest tuning range of 187.6MHz at S-band (=5.63% bandwidth), however, the accompanying variation in Q and loss characteristics over this range were considered unacceptably high for filter application. It must be noted that this tuning bandwidth surpasses any other tuning method reported to date (i.e. 3% by ferrite tuning). The configuration chosen for use in the filter designs yielded a more modest tuning of 1.3%. This configuration was selected for its relatively low-loss and high-Q performance. This configuration too exceeded any tuning bandwidth reported to date with the exception of ferrite tuning. It should be noted that ferrite tuning has limited use for many applications due to its slower tuning rates.

The main advantage of the new techniques described in this thesis is the ease of tuning through a planar network. The tuning method greatly simplifies the implementation of dielectric resonators in high volume production circuits by

eliminating the need for the design of a complex mechanical tuning structure. It also allows use of dielectric resonators at much higher microwave and mm-wave frequencies, as well as in monolithic integrated circuits, where mechanical tolerances previously made tuning them expensive and impractical. Moreover, the tuning configuration is not susceptible to mechanical vibrations which could degrade its performance.

Once the tuning circuit was established, the next phase of the research was to develop a design technique for realising direct coupled DR microwave bandpass filters having a Butterworth or Chebyshev response. Two new methods were developed based on the general circuit theory which allows the determination of the number of DRs, the values of the coupling coefficients between adjacent resonators and between resonators and microstrip line.

The design synthesis of the first method is based on the equivalent circuit model of coupled DRs, whereas, the second method is based on admittance inverters. Both these methods were directly related to the low-pass prototype elements. Design formulas were derived which relate the low-pass prototype lumped-elements to the filter specifications and which allow the determination of the coupling coefficient values between adjacent resonators. These values can then be related to the physical dimensions of the filter by comparing them with either experimental or theoretical values of coupling. Computer analysis of the filter is presented enabling

their performance to be predicted.

Experimental filters were constructed in the S-band to verify one of the proposed techniques. Comparison of the measured performance with the design specifications showed that the filter centre frequency and 3dB bandwidth agreed very well, the discrepancy in the worst case is by 2% and 6.7%, respectively. On the whole, the experimental results correlated with the theoretically predicted results validating the design procedure. Based on this design technique, several novel electronically tuned DR bandpass filters were designed and implemented at S-band. The tuning bandwidth of these filters exceeded 20MHz over the bias range of 0V to 30V. The maximum tuning bandwidth measured was 38.8MHz for the 3-pole filter. The 3dB bandwidth of these filters remained almost constant throughout the tuning range. The tuning performance of the filters was also virtually linear over the tuning range.

The designs are compact, tunable over a relatively wide range of centre frequencies, while intrinsically exhibiting relatively low pass-band loss, and suitability for operation in demanding environments and represent a significant development in electronically tunable filters.

In chapter six the design and physical realisation of fixed and novel varactor tuned bandstop dielectric resonator filters is described. It is shown that dielectric resonators coupled to a propagating transmission line will exhibit bandstop characteristics. The bandwidth of this effect is

determined by the degree of coupling of the resonator to the transmission line. From experimentation it was verified that for reproducible and reliable design of bandstop filters the resonators should be coupled to the line at odd quarter wavelength intervals. In this chapter a formula was been derived which expresses the external Q of each dielectric resonator in a bandstop filter in terms of the element values of the normalised low-pass prototype and the parameters of the frequency transformation. Based on this expression, several fixed frequency and novel electronically tunable bandstop filters were designed and tested. The tuning bandwidth of these filters exceed 20MHz and the largest obtained is 58MHz produced by the 4-pole filter, which also represented a significant development in bandstop filter design. The rejection at the centre frequency of these filters remains constant and over 20dB throughout the entire tuning range. Experimental results show good agreement with theory. Moreover, the bandstop filter response can be easily adjusted to exhibit its prescribed response. Each resonator can be independently aligned so that the coupling from the main transmission line to that resonator yields the specified external Q .

In summary, new design and construction techniques for low cost fixed and electronically tunable microwave dielectric resonator bandpass and bandstop filters have been presented. Experimental devices have been constructed which exhibit relatively low loss and wide tuning bandwidth in excess of what

has been hitherto obtained by other researchers. In addition, these designs possess the important property of retaining almost constant passband or stopband bandwidth across the entire tuning bandwidth.

7.1 Suggestions for Future Work

The introduction of the tuning mechanism described in this work may be expected to cause some temperature instability of the overall system. Of particular importance is the possibility of adverse variation of centre frequency and bandwidth response with temperature. Knowledge of any such instability is of great interest, particularly if the tuned dielectric resonator is to be used in a hostile environmental medium, such as airborne or spaceborne systems. Analysis and quantification of the temperature stability of the dielectric resonator, with or without, tuning mechanism requires a further systematic investigation.

One of the main reasons behind the choice of the varactor diode as a tuning element is its rapid response time. Such a property is vital for many applications where a high speed tuning is required. These applications may include frequency hopping techniques, dynamic frequency allocation, etc... A thorough investigation of the tuning rates of varactor tuned filter is required with particular reference to variations in ambient temperature and spurious signal generation at the high tuning rates.

Finally, to achieve the broadest tuning range possible, a varactor capacitance ratio should be a maximum. Varactors used in the current work suffer from relatively large parasitic capacitances which reduces the varactor capacitance ratio. It is envisaged that the use of beam lead varactors, manufactured with low parasitic capacitance (and inductance) should be investigated.

Publications

1. Virdee, B., "Investigation of Different Microstrip Topologies for Tuning DR $TE_{01\delta}$ mode Resonant Frequency," 1994 Asia-Pacific Microwave Conference-APMC'94, December 6-9, 1994, Nippon Convention Centre (Makahari Messe), Tokyo, Japan.
2. Virdee, B., "Novel Electronically Tunable DR Bandstop Filter," 1995 SMBO/IEEE MTT-S International Microwave and Optoelectronics Conference, Rio de Janeiro, July 24-27, Brazil.

Appendix A

Program DRCOUP for computing the coupling coefficient between a pair of DRs.

```
CLS
REM *****
REM                               DRCOUP
REM  This program computes the DR resonant frequency, Q-factor,
REM  and the coupling coefficient between a pair of DRs.
REM
REM *****
DIM ER(8), NUM(8), DEN(8), MM(8)
DIM XX(3), KK(3), ALF(2), FIH(2), LL(3), FCT(3), GCT(3)
REM      lengths should be entered in mm
DATA 36,8.57,7.72
DATA 1.5,1,1,30,2.17,0.794
LMODE = 0
READ ER(6), A, L
READ ER(1), LL(1), ER(2), LL(2), ER(7), LL(3)
ER(3) = 1
ER(4) = 1
ER(5) = ER(2)
ER(8) = ER(7)
PRINT "*****"
PRINT "      DRCOUP "; DATE$, TIME$
PRINT "*****"
PRINT "input data"
PRINT "er="; ER(6); "a="; A; "L="; L; "lmode="; LMODE
PRINT "er1="; ER(1); "L1="; LL(1)
PRINT "er2="; ER(2); "L2="; LL(2)
PRINT "er7="; ER(7); "L3="; LL(3)
PI = 3.141593
NQ = 0
REM *****2-dimensional search for the solution *****
REM ***** of the transcendental equation *****
XX(2) = 2.9
IF ER(2) - ER(1) > 0 THEN EMAX = ER(2) ELSE EMAX = ER(1)
kmin = XX(2) / SQR(ER(6) - ER(4))
kmax = XX(2) / SQR(EMAX)
KK(2) = (9 * kmin + kmax) / 10
DXX = .00001
DKK = .00001
LB3: ITER = 0
```

```

PRINT "searching for the eigenvalue..."
LB9: XX(1) = XX(2) + DXX
KK(1) = KK(2)
XX(3) = XX(2)
KK(3) = KK(2) + DKK
FOR ITI = 1 TO 3
X = XX(ITI)
KO = KK(ITI)
KO2 = KO * KO
XIT2 = X * X
GOSUB LB1
RA = KO2 * (ER(6) - ER(4)) - XIT2
IF RA > 0 GOTO LB2
STEPX = STEPX / 2
STEPK = STEPK / 2
XX(2) = XX(2) - STEPX
KK(2) = KK(2) - STEPK
PRINT "STEP TOO LARGE, START AGAIN WITH 1/2 SMALLER STEP"
GOTO LB3
LB2: YY = SQR(RA)
KC4A = YY
GOSUB LB4
FCT(ITI) = JOB + YY * KOB / X
BA = SQR(KO2 * ER(6) - XIT2)
FOR JIT = 1 TO 2
ALF(JIT) = SQR(XIT2 - KO2 * ER(JIT))
POW = ALF(JIT) * LL(JIT) / A
IF POW > 8 GOTO LB5
EP = EXP(POW)
EI = 1 / EP
AGU = (EP + EI) / (EP - EI)
GOTO LB6
LB5: AGU = 1
LB6: AGU = AGU * ALF(JIT) / BA
FIH(JIT) = ATN(AGU)
NEXT JIT
GCT(ITI) = FIH(1) + FIH(2) - BA * L / A + LMODE * PI
NEXT ITI
AL = (FCT(1) - FCT(2)) / DXX
AU = (GCT(1) - GCT(2)) / DKK
BL = (FCT(3) - FCT(2)) / DXX
BU = (GCT(3) - GCT(2)) / DKK
CL = FCT(2) - AL * XX(2) - BL * KK(2)
CU = GCT(2) - AU * XX(2) - BU * KK(2)
DENO = AU * BL - AL * BU
XNEW = (CL * BU - CU * BL) / DENO

```

```

KNEW = (CU * AL - CL * AU) / DENO
STEPX = XNEW - XX(2)
STEPK = KNEW - KK(2)
STEP2 = STEPX ^ 2 + STEPK ^ 2
PRINT ITER + 1, "koa=", KK(2), "eigx=", XX(2)
XX(2) = XNEW
KK(2) = KNEW
IF STEP2 < 1E-12 THEN GOTO LB7
ITER = ITER + 1
IF ITER > 10 THEN GOTO LB8
GOTO LB9
PRINT ""
LB8: PRINT "SOLUTION NOT FOUND AFTER 10 ITERATIONS"
GOTO LB10
REM if the search is successful, re-evalute the constants
LB7: KOA = KK(2)
FIR = KOA * 150 / (PI * A)
PRINT ""
PRINT "Itoh & Rudokas model"
PRINT "freq(I&R)=", FIR, "GHz"
EIGX = XX(2)
KOA2 = KOA * KOA
EIG2 = EIGX * EIGX
RADIC = EIG2 - KOA2 * ER(1)
AL1A = SQR(RADIC)
RADI = EIG2 - KOA2 * ER(2)
AL2A = SQR(RADI)
RADA = KOA2 * ER(6) - EIG2
BA = SQR(RADA)
AL1L1 = AL1A * LL(1) / A
AL2L2 = AL2A * LL(2) / A
IF AL1L1 > 8 THEN GOTO LB12
Z1 = EXP(AL1L1)
ZI1 = 1 / Z1
CT1 = (Z1 + ZI1) / (Z1 - ZI1)
SIH1 = (Z1 - ZI1) * .5
GOTO LB11
LB12: CT1 = 1
LB11: IF AL2L2 > 8 THEN GOTO LB13
Z2 = EXP(AL2L2)
ZI2 = 1 / Z2
CT2 = (Z2 + ZI2) / (Z2 - ZI2)
SIH2 = (Z2 - ZI2) * .5
GOTO LB14
LB13: CT2 = 1
LB14: ARG1 = AL1A * CT1 / BA

```

```

ARG2 = AL2A * CT2 / BA
TH1 = ATN(ARG1)
TH2 = ATN(ARG2)
REM ***** variational formula *****
KC4A2 = RADA - KOA2 * ER(4)
KC4A = SQR(KC4A2)
GOSUB LB4
X = EIGX
GOSUB LB1
JOB2 = JOB * JOB
TRX = JOB2 - 2 * JOB / EIGX + 1
KOB2 = KOB * KOB
PRX = KOB2 + 2 * KOB / KC4A - 1
SIF1 = SIN(TH1 * 2)
SIF2 = SIN(TH2 * 2)
THET = (SIF1 + SIF2) * .5 / (TH1 + TH2 + LMODE * PI)
CO12 = A * (COS(TH1) ^ 2) / AL1A
IF AL1L1 > 8 THEN GOTO LB15
SECN = AL1L1 / (SIH1 * SIH1)
PARM1 = CT1 - SECN
GOTO LB16
LB15: PARM1 = 1
LB16: COPAM1 = CO12 * PARM1
CO22 = A * (COS(TH2) ^ 2) / AL2A
IF AL2L2 > 8 THEN GOTO LB17
SECN = AL2L2 / (SIH2 * SIH2)
PARM2 = CT2 - SECN
GOTO LB18
LB17: PARM2 = 1
LB18: COPAM2 = CO22 * PARM2
B = BA / A
AL1 = AL1A / A
RADI7 = EIG2 - KOA2 * ER(7)
AL7 = (SQR(RADI7)) / A
AL7L3 = AL7 * LL(3)
Z3 = EXP(AL7L3)
ZI3 = 1 / Z3
CT7 = (Z3 + ZI3) / (Z3 - ZI3)
SIH3 = (Z3 - ZI3) * .5
ALB = ATN(B / AL1)
AAA1 = 2 * (COS(TH1)) * (COS(ALB))
BBB1 = 2 * (SIN(TH1)) * (SIN(ALB))
RBBT = SQR((B ^ 2) + (AL1 ^ 2))
RBB = RBBT / AL1
RR1 = SQR((BBB1 ^ 2) - (AAA1 ^ 2))
BB1AA1 = AAA1 / BBB1

```

```

BBAA = (1 + BB1AA1) / (1 - BB1AA1)
ALTT = (LOG(BBAA)) / LOG(EXP(1))
ALT1 = .5 * ALTT
AL1L1AL = AL1L1 - ALT1
ZAL1 = EXP(AL1L1AL)
ZALI1 = 1 / ZAL1
REM CTAL=(ZAL1+ZALI1)/(ZAL1-ZALI1)
COSAL = (ZAL1 + ZALI1) * .5
SHAL = (ZAL1 - ZALI1) * .5
CO7 = (COSAL ^ 2) / AL7
SECN7 = AL7L3 / (SIH3 * SIH3)
PARM7 = CT7 - SECN7
COPAM7 = CO7 * PARM7
ZALT1 = EXP(ALT1)
ZALTI1 = 1 / ZALT1
CTALT = (ZALT1 + ZALTI1) / (ZALT1 - ZALTI1)
SHALT = (ZALT1 - ZALTI1) * .5
THET2 = (2 * SHALT * CTALT) + (2 * CTAL * SHAL)
NUM(1) = ER(1) * LL(1) * ((RBB * RR1) ^ 2) * TRX * ((THET2 / (2 * AL1L1)) + 1)
NUM(2) = ER(2) * COPAM2 * TRX
DEN(3) = ER(3) * LL(1) * ((RBB * RR1) ^ 2) * PRX * ((THET2 / (2 * AL1L1)) + 1)
NUM(3) = -(RADIC + KC4A2) / KOA2 * DEN(3) / ER(3)
NUM(4) = ER(4) * L * (1 + THET) * PRX
DEN(5) = ER(5) * PRX * COPAM2
NUM(5) = -(RADI + KC4A2) / KOA2 * DEN(5) / ER(5)
NUM(6) = ER(6) * L * (1 + THET) * TRX
DEN(7) = ER(7) * ((RBB * RR1) ^ 2) * COPAM7 * TRX
NUM(7) = DEN(7)
DEN(8) = ER(8) * ((RBB * RR1) ^ 2) * COPAM7 * PRX
DEN(1) = NUM(1)
DEN(2) = NUM(2)
DEN(4) = NUM(4)
DEN(6) = NUM(6)
DENSUM = 0
SURVER = -BA * A * (SIF1 + SIF2) * PRX / KOA2
SURHOR = X * JOB * 2 * (COPAM1 + COPAM2) / KOA2
NUMSUM = SURHOR + SURVER
FOR J = 1 TO 6
DENSUM = DENSUM + DEN(J)
NUMSUM = NUMSUM + NUM(J)
NEXT J
VARKOA = KOA * SQR(NUMSUM / DENSUM)
VARFRE = VARKOA * 150 / (PI * A)
PRINT ""
PRINT "variational result"
PRINT "freq(var)=", VARFRE, "GHz"

```

```

IF NQ = 1 THEN RETURN
PRINT ""
PRINT "want the percent error in frequency? (y or n)"
INPUT A$
IF A$ = "y" THEN GOSUB LB27
PRINT "want to compute the Q factor? (y or n)"
INPUT B$
IF B$ = "y" THEN GOSUB LB19
PRINT ""
PRINT "want to compute the coupling ? (y or n)"
INPUT C$
IF C$ = "y" THEN GOSUB LB20
LB10: END
LB27: REM ***** percent error *****
PRINT "enter the exact frequency in GHz"
INPUT EXCFRE
PERC = 100 * (VARFRE / EXCFRE - 1)
PRINT USING "+###.## -%"; PERC
RETURN
LB1: REM ***** function JOB=JO(X)/J1(X) *****
XMXO = X - 2.4048
TEM = (.0282 * XMXO - .1177) * XMXO + .2571
TEM = (TEM * XMXO - .716) * XMXO + 1.4282
JOB = TEM * XMXO / (X - 3.8317)
RETURN
LB4: REM ***** function KOB=KO(KC4A)/K1(KC4A) *****
KI = 1 / KC4A
TEM = (.00445 * KI - .02679) * KI + .06539
TEM = (TEM * KI - .11226) * KI + .49907
KOB = 1 / (1 + TEM * KI)
RETURN
LB19: REM ***** q factor *****
NQ = 1
FO = VARFRE
PRINT ""
PRINT "shield : copper, aluminium, brass, or other? (c,a,b,or o)"
INPUT A$
IF A$ = "c" THEN SIGMA = 5.8E+07
IF A$ = "a" THEN SIGMA = 3.72E+07
IF A$ = "b" THEN SIGMA = 1.57E+07
IF A$ <> "o" GOTO LB21
PRINT "enter conductivity in siemens/metre"
INPUT SIGMA
IF SIGMA < .1 GOTO LB22
LB21: SKIN = 50 / (SQR(FO * SIGMA) * PI)
PRINT ""

```

```

PRINT "skin depth=", 1000 * SKIN, "microns"
LL(1) = LL(1) - SKIN
LL(2) = LL(2) - SKIN
GOSUB LB3
DF = VARFRE - FO
IF DF / FO < .000001 GOTO LB23
Q = FO / DF
PRINT "Q(due to shield losses)=", Q
RETURN
LB23: PRINT "insignificant losses in the shield, quit"
RETURN
LB22: PRINT "conductivity too small, quit"
RETURN
REM *****
REM   The following subroutine computes the coupling coefficient
REM   between two DRs.
LB20: REM ***** coupling *****
Z2 = EXP(AL2L2)
ZI2 = 1 / Z2
CT2 = (Z2 + ZI2) / (Z2 - ZI2)
SIH2 = (Z2 - ZI2) * .5
COVS1 = COS(TH1) / SIH1
COVS2 = COS(TH2) / SIH2
THET1 = (1 / AL1) * (SHAL + SHALT)
AL2L22 = AL2L2 / 2
AL2I2 = EXP(AL2L22)
AL2I12 = 1 / AL2I2
SIH22 = (AL2I2 - AL2I12) * .5
AL7L32 = AL7L3 / 2
AL7I2 = EXP(AL7L32)
AL7I12 = 1 / AL7I2
SIH72 = (AL7I2 - AL7I12) * .5
AL2 = AL2A / A
GG2 = (2 / AL2) * (SIH22 ^ 2)
GG7 = (2 / AL7) * (SIH72 ^ 2)
THET12 = (SIN(TH1) + SIN(TH2)) / (TH1 + TH2 + LMODE * PI)
KP2 = KC4A / A
KP1 = EIGX / A
TRXC = (A / X) * ((2 / X) - JOB)
PRXC = (A / KC4A) * ((2 / KC4A) + KOB)
ERR1 = (RADIC - EIG2) / KOA2
ERR7 = (((RADI7 * A) ^ 2) - EIG2) / KOA2
EO = 8.854E-12
MM(1) = ER(1) * (1 / KP1) * RBB * RR1 * TRXC * THET1
MM(2) = ER(2) * (1 / KP1) * COVS2 * TRXC * GG2
MM(3) = EO * (1 / KP2) * RBB * RR1 * PRXC * THET1 * KCC1

```

```

MM(4) = ER(4) * (1 / KP2) * PRXC * THET12 * L
MM(5) = EO * (1 / KP2) * COVS2 * PRXC * GG2 * ERR1
MM(6) = ER(6) * (1 / KP1) * TRXC * THET12 * L
MM(7) = ER(7) * (1 / KP1) * RBB * RR1 * (COSAL / SIH3) * TRXC * GG7
MM(8) = EO * (1 / KP2) * RBB * RR1 * (COSAL / SIH3) * PRXC * GG7 * ERR7
MMSUM = 0
FOR J = 1 TO 8
MMSUM = MMSUM + MM(J)
NEXT J
PRINT ""
PRINT "input width of enclosure A in mm"
INPUT AA1: AA = AA1
PRINT ""
PRINT "input height of enclosure B in mm"
INPUT BB2: BB = BB2
PRINT ""
CC = 2.16
SS1 = 1.85
FCTE10 = ((1.5E+08) / AA) / 1E+09
T1 = 8.69 * SQR(PI * (FIR * 1E+09) * EO / 3.72E+07)
T2 = 1 + 2 * (BB / AA) * (FCTE10 / FIR) ^ 2
B1 = BB * SQR(1 - (FCTE10 / FIR) ^ 2)
AL4 = T1 * T2 / B1
SS = 0
LB26: FOR II = 1 TO 9
SS = SS + .5
S = SS1 * SS
REM calculations at z=L/2 (centre of DR)
ZZ = L / 2
KP2P = KP2 * S
K1KP2P = (SQR(PI / (2 * KP2P))) * (EXP(-KP2P)) * (1 + (3 / (8 * KP2P)) - (5 / (2 * (8 *
KP2P) ^ 2)))
K1KP2A = (SQR(PI / (2 * KC4A))) * (EXP(-KC4A)) * (1 + (3 / (8 * KC4A)) - (5 / (2 * (8 *
KC4A) ^ 2)))
CF = -CC * (EXP(-AL4 * S)) / (BB * AA)
CCOEF = CF * B * (K1KP2P / K1KP2A) * SIN((B * ZZ) - TH1) * MMSUM / (.5 *
DENSUM)
PRINT "S="; SS * 10
PRINT "CCOEF="; CCOEF
NEXT II
LB24: END

```